


UNIVERSITY OF BIRMINGHAM

# NUMERICAL AND EXPERIMENTAL DEVELOPMENT OF AN EFFICIENT ADSORPTION DESALINATION AND COOLING SYSTEM

**By**
**Ibrahim A A Albaik**

A thesis submitted to the University of Birmingham
for the degree of

**Doctor of Philosophy**

Department of Mechanical Engineering
School of Engineering
College of Engineering and Physical Sciences
The University of Birmingham
Oct - 2022

UNIVERSITY OF
BIRMINGHAM

## University of Birmingham Research Archive

### e-theses repository

This unpublished thesis/dissertation is copyright of the author and/or third parties. The intellectual property rights of the author or third parties in respect of this work are as defined by The Copyright Designs and Patents Act 1988 or as modified by any successor legislation.

Any use made of information contained in this thesis/dissertation must be in accordance with that legislation and must be properly acknowledged. Further distribution or reproduction in any format is prohibited without the permission of the copyright holder.

# ABSTRACT

In this Ph.D. thesis, different methods for enhancing the performace of heat powered adsorption system for water desalination and cooling are investigated through numerical and experimental works. These enhancement methods include: (i) optimizing the geometric design of the adsorber bed heat exchangers for both packing or coating with the adsorbent material , (ii) determining the best method of connecting the heat exchanger modules of the adsorber bed and the best vapor gap between them to reduce the mass transfer resistance, (iii) using metal-organic framework (MOF) adsorbent materials namely aluminium fumarate and a newly developed composite zirconium fumarate (MOF-801) / graphene to replace the conventional adsorbent materials, (iv) reducing the dead volume in the condenser and evaporator chambers to enhance the compactness of the adsorption system and (v) integrating the adsorption system with different desalination technology to increase the water recovery, and reduce the specific energy consumption.

After optimizing the geometrical design of the heat exchanger in the adsorber bed, a comparative study between a packed rectangular-finned tube and a coated wire-finned tube is conducted. Results showed that the coated wire-finned tube enhanced the adsorption system specific daily water production (SDWP) and specific cooling power (SCP) by 82% compared to the packed rectangular finned tube, while it lowered the system coefficient of performance (COP) by 52%. In terms of the specific volumetric daily water production (SVDWP), the adsorption system with coated wire-finned adsorber beds has SVDWP lower than the system with packed one by 21%. Integrating the adsorption system with a Batch Reverse Osmosis (BRO) desalination system using packed rectangular-finned tube adsorption system and a wide range of water salinity, it is found that the water recovery can be increased to 96.9% and 65.3% when brackish water and seawater are fed to the hybrid system respectively. Finally, using a newly developed composite zirconium MOF (MOF-801) material with graphene nanoplatelets enhanced the SDWP and SCP by 40% due to its higher thermal conductivity and faster kinetics compared to the neat MOF.

# ACKNOWLEDGEMENT

*First and foremost, all praise is due to **Allah** for reasons too numerous to mention, and especially for giving me the power to believe in myself and to be patient throughout these long years as a student to achieve many great successes.*

*I would like to extend my appreciation to the **University of Birmingham** who believed in me when I was awarded a school scholarship to study my Ph.D. after being awarded the Ratcliffe Prize as the best postgraduate student in the Engineering School during my Master's study.*

*I am grateful to **Dr. Raya Al-Dadah** for her supervision, great suggestions, and guidance, for reviewing the scientific papers, and for introducing me to the adsorption systems using Metal-Organic Frameworks (MOFs).*

*I am speechless! It is really hard to find the words to express my deep sense of gratitude to my great and distinguished **parents** for their endless love, daily support, faith, encouragement, and motivation, which is the key to success in completing this thesisl. I would like to thank all my **brothers and sisters** during this journey, and a special appreciation goes to my brother, **Hussam** for his financial support.*

*My special thanks with respect go to **Dr. İsmail Solmaz**, who took it upon himself to guide me through my research and in teaching me the partial differential equations. His support was huge in publishing the first two journal papers during COVID. I would like also to extend my appreciation to **Dr. Mahmoud Elsheniti** who also had great input in guiding me to model the adsorption system with different ideas.*

*I would like to thank my friend, **Abdulbari Beloufi** for his support during my study, particularly during the tough times as massive pressure on my shoulders was released because of him. I would also like to thank him for his support in the proofreading of several scientific papers.*

*I would like to take this opportunity to offer my gratitude to my friend, **Dr. Kamal Diab**, for his support during my study and for his great experience that helped me a lot and increased my background knowledge in MOFs. We had a great achievement together in adsorption systems during working in the labs for infinite hours. I believe that one day he will be nominated for Noble Prize in Chemistry and he will invite me to celebrate this achievement.*

# TABLE OF CONTENTS

ABSTRACT ..... I

ACKNOWLEDGEMENT ..... II

TABLE OF CONTENTS ..... III

LIST OF FIGURES ..... VII

LIST OF TABLES ..... XVI

NOMENCLATURE ..... XVII

LIST OF PUBLICATIONS ..... XX

1. Chapter 1: Introduction ..... 1

1.1. Introduction ..... 1

1.2. Aim and objectives ..... 4

1.3. Thesis outlines ..... 5

2. Chapter 2: Literature review ..... 8

2.1. Overview of the cooling and desalination adsorption systems ..... 8

2.2. Isotherms, kinetics and heat of adsorption ..... 9

2.2.1. Adsorption isotherms: ..... 9

2.2.2. Adsorption kinetics: ..... 11

2.2.3. The heat of adsorption: ..... 13

2.2.4. Adsorbent material characterizations ..... 14

2.3. Conventional adsorbent materials and metal-organic frameworks ..... 14

2.3.1. Enhancing the thermal conductivity ..... 19

2.4. Packing and coating the adsorbent materials ..... 22

2.5. Heat exchangers used in adsorber beds ..... 24

2.6. Low Pressure (LP) Evaporator and Condenser ..... 28

2.6.1. Falling film evaporator ..... 28

2.6.2. Flooded and Capillary-assisted Evaporators ..... 28

2.7. Review of mathematical modelling ..... 31

2.7.1. The thermodynamic model ..... 31
2.7.2. Lumped parameter models ..... 32
2.7.3. The heat and mass transfer model ..... 34
2.8. Integration of the adsorption systems with different system for different applications ..... 43
2.8.1. Solar driven multigeneration integrated systems ..... 43
2.8.2. Integration of adsorption system with Organic Rankine Cycle ..... 44
2.8.3. Integration of adsorption system with other desalinations systems ..... 47
2.9. Summary ..... 52
3. Chapter 3: Modelling of the wire-finned tube heat exchanger using the coupled solution approach 54
3.1. Abstract ..... 55
3.2. Brief introduction ..... 55
3.3. Model description ..... 56
3.4. Results and Discussions ..... 64
3.4.1. Optimisation of wire finned coated heat exchanger geometry ..... 71
*3.4.2.* Effect of operating conditions ..... 79
3.5. Conclusions ..... 80
4. Chapter 4: Effect of adsorber bed heat exchanger modules connection method on a scaled-up adsorption system – Numerical and Experimental investigations ..... 82
4.1. Abstract ..... 82
4.2. Brief introduction and purpose of the study ..... 83
4.3. Method (Numerical Model): ..... 84
4.4. Results and discussion (Numerical model): ..... 88
4.4.1. Effect of vapor gap between heat exchanger modules ..... 91
*4.4.2.* Heat exchanger modules connection (series and parallel) ..... 93
4.5. Experimental testing of a scaled-up adsorption system ..... 97
4.6. Experimental results and discussion: ..... 102
4.7. Conclusions: ..... 112
5. Chapter 5: Experimental study of multiple coated wire finned tube heat exchanger modules in a scaled-up adsorption system ..... 114

5.1. Introduction ..... 114
5.2. Preparation of MOF adsorbent material coating for the adsorption heat pump desalination and cooling unit ..... 115
5.3. Characterization of MOF adsorbent material coating ..... 115
5.4. Coating the heat exchanger for adsorber beds ..... 117
5.5. Assembly of the coated MOF adsorption system ..... 118
5.6. The testing procedure of the coated MOF adsorption system ..... 123
5.7. Results and discussions ..... 124
5.7.1. Performance of coated wire finned adsorption system ..... 124
*5.7.2.* Effect of half cycle time and operating temperatures ..... 126
*5.7.3.* Effect of Evaporator and condenser dead volume ..... 130
*5.7.4.* Comparative study between packed rectangular and coated wire finned tube heat exchanger ..... 132
5.8. Conclusions: ..... 135
6. Chapter 6: Hybrid Batch Reverse Osmose-Adsorption desalination system ..... 137
6.1. introduction ..... 137
6.2. Abstract ..... 138
6.3. Purpose of the study ..... 139
6.4. Description of BRO-AD hybrid system ..... 139
6.5. Mathematical modelling ..... 143
6.6. Results and discussion ..... 151
6.6.1. Base case analysis for BRO-AD hybrid system ..... 151
*6.6.2.* Effects of feed salinity and temperature ..... 157
*6.6.3.* Comparative analysis of energy consumption, water production rate, and cooling power generation in conventional BRO, conventional AD, and BRO-AD hybrid systems ..... 165
*6.6.4.* Implementation for ZLD or MLD system ..... 171
6.7. Conclusions ..... 172
7. Chapter 7: Newly developed zirconium-based MOF ..... 174
7.1. Introduction: ..... 174
7.2. Abstract ..... 175

7.3. Purpose of the study ..... 175
7.4. Materials ..... 176
7.5. Methodology ..... 177
7.5.1. Nitrogen isotherms ..... 177
*7.5.2.* water isotherms, kinetics and heat of adsorption ..... 178
7.6. Results and discussion ..... 183
7.7. Conclusions ..... 188
8. Chapter 8: Conclusions and future work ..... 189
8.1. Introduction ..... 189
8.2. Conclusions ..... 190
8.3. Future work and recommendations ..... 193
9. References ..... 194
10. Appendix A: Experimental setup for the packed finned tube adsorption system ..... 209
11. Appendix B: Experimental setup for the coated finned tube adsorption system ..... 214
12. Appendix C: CAD Drawings ..... 221
13. Appendix D: Electrical and control connection of the adsorption system ..... 225
14. Appendix E: Repeatability test ..... 228
15. Appendix F: Calibrations ..... 229
16. Appendix G: Uncertainty calculations ..... 233

# LIST OF FIGURES

Figure 1-1. Adsorption cooling and desalination system [7]…….2

Figure 2-1. Schematic diagram of the adsorption heat pump/cooling/desalination cycle [14] ..... 9

Figure 2-2. Isosteric cycle diagram of adsorption heat pump/cooling cycle [16] ..... 9

Figure 2-3. diffusion phases from bulk gas to solid surfaces [35] ..... 12

Figure 2-4. Water isotherms at different relative pressures for the conventional adsorbent materials [52,53] ..... 15

Figure 2-5. Maximum water uptake for different MOF groups [44,56,60–62] ..... 16

Figure 2-6. Different adsorption isotherm types [63] ..... 17

Figure 2-7. Recent water isotherms at different relative pressure at equilibrium conditions [56,67,69–71] ..... 19

Figure 2-8. Plate-finned shell and tube in adsorber bed [96] ..... 25

Figure 2-9. Plate-fin heat exchanger in adsorber bed [98] ..... 25

Figure 2-10. vapor channels in rectangular heat exchanger [99] ..... 26

Figure 2-11. Packed and coated finned plated-tubes aluminum heat exchanger [88] ..... 27

Figure 2-12. Aluminium foam heat exchanger [102] ..... 27

Figure 2-13. The 1st configuration of the Integrated ORC-Adsorption systems [156] ..... 45

Figure 2-14. The 2nd configuration of the Integrated ORC-Adsorption systems [156] ..... 45

Figure 2-15. The 3rd configuration of the Integrated ORC-Adsorption systems [156] ..... 46

Figure 2-16. The 4th configuration of the Integrated ORC-Adsorption systems [158] ..... 46

Figure 2-17. Integrating the adsorption system with MED [164] ..... 48

Figure 2-18. Integrating the adsorption system with HDH [165] ..... 49

Figure 2-19. Integrating the adsorption system with RO [162] ..... 50

Figure 3-1. (a) Wire finned tube, (b) Coated wire finned tube, (c) packed wire finned tube, (d) 3D combined packed and coated wire finned tube model. ..... 58

Figure 3-2. The number of fins at different tube diameters in the wire-finned tube. ..... 59

Figure 3-3. Boundary Condition of the wire-finned tube model ..... 62

Figure 3-4. Mesh sensitivity study ..... 63
Figure 3-5. Validation of the current numerical model with published experimental works from literature [186] (a) adsorbent temperature with time and (b) the effect of chilled water inlet temperature on SCP-wire finned tube with 2mm fin spacing, fin thickness of 1mm, fin height of 7mm, tube diameter of 10mm. ..... 65
Figure 3-6. Packed wire finned tube with tube diameter of 22mm and fin height of 20mm - Adsorption process after 250 seconds at $T_{evap}$ = 15 ºC, $T_{cond}$ = 30 ºC, $T_{des}$ = 90 ºC and $T_{ads}$ = 30ºC (a) vapor pressure (Pa), (b) temperature (K) and (c) water uptake ($kg.kg^{-1}$). ..... 66
Figure 3-7. Coated wire finned tube with tube diameter of 22mm and fin height of 20mm - Adsorption process at $T_{evap}$ = 15ºC, $T_{cond}$ = 30ºC, $T_{des}$ = 90ºC and $T_{ads}$ = 30ºC (a) vapor pressure after 50 seconds (Pa), (b) temperature after 50 seconds (K) and (c) water uptake after 250 seconds ($kg.kg^{-1}$). ..... 67
Figure 3-8. Wire finned tube with tube diameter of 22mm and fin height of 20mm - Adsorption process after 250 seconds at $T_{evap}$ = 15 ºC, $T_{cond}$ = 30 ºC , $T_{des}$ = 90 ºC and $T_{ads}$ = 30 ºC (a) Vapor pressure (Pa), (b) Temperature (K) and (c) Water uptake ($kg.kg^{-1}$)..... 68
Figure 3-9. Pressure and temperature variation in combined packed and coated wire finned tube in the X-direction using tube diameter of 22mm and fin height of 20mm. ..... 69
Figure 3-10. Water uptake variation in combined packed and coated wire finned tube in the Y-direction using tube diameter of 22mm and fin height of 20mm. ..... 69
Figure 3-11. Effect of packed, coated and combined wire finned tube on SCP and SDWP using tube diameter of 22mm, fin height of 20mm. ..... 70
Figure 3-12. Effects of packed, coated, and combined wire finned tube on SCP and SDWP using tube diameter of 22mm, fin height of 10mm. ..... 71
Figure 3-13. Effect of fin height on (a) SDWP and (b) SCP using different tube diameters and fin numbers. ..... 72
Figure 3-14. Coated wire finned heat exchanger module (a) module geometry, (b) module after coating. ..... 73
Figure 3-15. (a) Daily water production and (b) cooling power per module at different coated wire finned tube geometry. ..... 74

Figure 3-16. (a) Required adsorbent and (b) metal mass at different coated wire finned tube geometry. ..... 75
Figure 3-17. The bed height at different coated wire finned tube geometry..... 76
Figure 3-18. Effect of coating thickness on (a) SDWP and (b) SCP at different coated wire finned geometries. ..... 77
Figure 3-19. Required (a) adsorbent and (b) metal mass at different coating thickness. ..... 78
Figure 3-20. Bed height at different coating thickness. ..... 79
Figure 3-21. Effect of evaporation and water heating temperatures on the (a) SDWP and (b) SCP using tube diameter of 22mm and fin height of 20mm and coating thickness of 0.5mm. ..... 80
Figure 4-1. Computational domains of the packed finned tube heat exchanger (a) 2D *Axisymmetric* circular fins without vapor domain, (b)2D *Axisymmetric* circular fins with vapor domain and (c)3D rectangular fins..... 85
Figure 4-2. Mesh sensitivity analysis..... 87
Figure 4-3. The boundary condition of the 2D axisymmetric model..... 88
Figure 4-4. Outer surface temperature of the adsorbent material at pipe length of 20cm ($t_{cycle}$ = 250 sec, $t_{switching}$ = 40 sec, $T_{ad}$ = 25$^{o}$C, $T_{des}$ = 85 $^{o}$C at water flow rate of 27L/day, $T_{chilled}$ = 24$^{o}$C and $T_{cond}$ = 25$^{o}$C) ..... 89
Figure 4-5. 2D axisymmetry and 3D models after 250 seconds of cooling (a) Vapor pressure distributions (Pa), (b) temperature distributions (K), and (c) water uptake (kg/kg). ($t_{cycle}$ = 250 sec, $t_{switching}$ = 40 sec, $T_{ad}$ = 25$^{o}$C, $T_{des}$ = 85 $^{o}$C at water flow rate of 27L/day, $T_{evaporator}$ = 24$^{o}$C and $T_{condenser}$ = 25$^{o}$C) ..... 90
Figure 4-6. Effect of vapor gap between heat exchanger module on vapor pressure variation (a) 2mm vapor gap, (b) 4mm vapor gap and (c) 5mm vapor gap. ($T_{ad}$ =30 $^{o}$C, $T_{des}$ = 90 $^{o}$C, $T_{evaporator}$ = 15$^{o}$C and $T_{condenser}$ = 30$^{o}$C) ..... 92
Figure 4-7. Effect of module length on the vapor gap distance between the modules ..... 93
Figure 4-8. Packed heat exchanger modules configurations (a)Scenario 1, (b)Scenario 2 and (c)Scenario 3 ..... 94

Figure 4-9. Packed heat exchanger modules scenarios effect on required heating power and water flow rate (Tad =30 $^{o}$C, Tdes = 90 $^{o}$C, Tevaporator = 15$^{o}$C and Tcondenser = 30$^{o}$C) ..... 95

Figure 4-10. Packed heat exchanger modules scenarios effect on SCP and COP ($T_{ad}$ =30 $^{o}$C, $T_{des}$ = 90 $^{o}$C, $T_{evaporator}$ = 15$^{o}$C and $T_{condenser}$ = 30$^{o}$C) ..... 96

Figure 4-11. Scaled-up adsorption system components ..... 97

Figure 4-12. Schematic diagram of the adsorption system ..... 98

Figure 4-13. (a) single packed heat exchanger module, (b) the heat exchanger modules connection and (c) adsorber bed assembly ..... 99

Figure 4-14. Stainless coil for the evaporator ..... 100

Figure 4-15. Experimental reading of the Water temperature profiles in each component in the adsorption system ($t_{half\ cycle}$ = 250 sec, $t_{switching}$ = 40 sec, $T_{ad}$ = 25$^{o}$C, $T_{des}$ = 85 $^{o}$C, $T_{chilled}$ = 24$^{o}$C and $T_{cond}$ = 25$^{o}$C) ..... 104

Figure 4-16. Model validation by using adsorbent temperature ($t_{cycle}$ = 250 sec, $t_{switching}$ = 40 sec, $T_{ad}$ = 25$^{o}$C, $T_{des}$ = 85 $^{o}$C at water flow rate of 27L/day, $T_{chilled}$ = 24$^{o}$C and $T_{cond}$ = 25$^{o}$C) ..... 105

Figure 4-17. Model validation by using SDWP values at different operating conditions ..... 105

Figure 4-18. Effect of half-cycle time on DWP, SDWP, CP and SCP ($t_{switching}$ = 40 sec, $T_{ad}$ = 25$^{o}$C, $T_{des}$ = 85 $^{o}$C, $T_{chilled}$ = 24$^{o}$C and $T_{cond}$ = 25$^{o}$C at desorption water flow rate of 27 L/day) ..... 106

Figure 4-19. Effect of half-cycle time on DWP, SDWP, CP and SCP ($t_{switching}$ = 40 sec, $T_{ad}$ = 30$^{o}$C, Tdes = 60$^{o}$C, $T_{evap}$ = 20$^{o}$C and $T_{cond}$ = 12.5$^{o}$C at water desorption flow rate of 17L/day) ..... 107

Figure 4-20. Effect of the half cycle time on the COP of the adsorption system (Tad = 25$^{o}$C, $T_{des}$ = 85 $^{o}$C at water flow rate of 27L/day, $T_{chilled}$ = 24$^{o}$C and $T_{cond}$ = 25$^{o}$C) ..... 108

Figure 4-21. Effect of adsorption cooling water inlet temperature on DWP, SDWP, CP and SCP ($t_{half\ cycle}$ = 350 sec, $t_{switching}$ = 40 sec, $T_{des}$ = 60$^{o}$C, $T_{evap}$= 20$^{o}$C, $T_{cond}$ = 12.5$^{o}$C at water desorption flow rate of 17L/day) ..... 108

Figure 4-22. Effect of evaporator water inlet temperature on DWP and SDWP (thalf cycle = 350 sec, tswitching = 40 sec, $T_{ad}$ = 30$^{o}$C, $T_{des}$ = 60$^{o}$C at water desorption flow rate of 17L/day) (a) $T_{cond}$ = 20$^{o}$C (b)$T_{cond}$ = 12.5$^{o}$C ..... 109

Figure 4-23. Comparison between conventional adsorbent and MOF materials and aluminum fumarate at a desorption temperature of 65$^{o}$C using different chilled water temperature ..... 110

Figure 4-24. Effect of Feeding water salinity on the SDWP ($t_{cycle}$ = 250 sec, $t_{switching}$ = 40 sec, $T_{ad}$ = 25$^{o}$C, $T_{des}$ = 85$^{o}$C at water flow rate of 27L/day, $T_{chilled}$ = 24$^{o}$C and $T_{cond}$ = 25$^{o}$C) ..... 111

Figure 4-25. Effect of Feeding water salinity on the specific electrical energy consumption ($t_{cycle}$ = 250 sec, $t_{switching}$ = 40 sec, $T_{ad}$ = 25$^{o}$C, $T_{des}$ = 85 $^{o}$C at water flow rate of 27L/day, $T_{chilled}$ = 24$^{o}$C and $T_{cond}$ = 25$^{o}$C) ..... 112

Figure 5-1. Aluminum fumarate preparation for coating (a) distilled water mixed with a binder (b) mixing distilled water and binder with adsorbent material powder ..... 115

Figure 5-2. Water cyclic performance at different coating thicknesses ..... 116

Figure 5-3. (a) adsorbent material spraying and (b) initial drying before placing the heat exchanger in the oven ..... 118

Figure 5-4. Two-bed adsorption heat pump system for desalination and cooling ..... 119

Figure 5-5. (a) Plastic carrier of the heat exchanger and (b) Connecting the coated wire finned tube heat exchanger modules by soldering ..... 121

Figure 5-6. Placing the heat exchanger modules inside the adsorber bed ..... 121

Figure 5-7. Copper coils placed inside the chambers (a) condenser and (b) flooded evaporator ..... 123

Figure 5-8. Temperature variation with time ($T_{cooling}$ = 25$^{o}$C, $T_{heating}$ = 90$^{o}$C, $T_{chilled}$ = 23$^{o}$C and $t_{halfcycle}$ = 200 sec) ..... 126

Figure 5-9. Effect of half cycle time on daily water production and specific daily water production. ($T_{des}$ =90$^{o}$C, $T_{chilled}$ = 23$^{o}$C, $T_{cond}$ = 25$^{o}$C, $T_{ads}$ = 25$^{o}$C) ..... 127

Figure 5-10. Effect of inlet heating temperature (desorption temperature) on daily water production and specific daily water production ($t_{half\ cycle}$ =200 sec, $T_{chilled}$ = 23$^{o}$C, $T_{cond}$ = 25$^{o}$C, $T_{ads}$ = 25$^{o}$C) ..... 128

*Figure 5-11. Effect of chilled water inlet temperature (in evaporator) on daily water production and specific daily water production ($t_{half\ cycle}$ =200 sec, $T_{des}$ = 90$^{o}$C, $T_{cond}$ = 25$^{o}$C, $T_{ads}$ = 25$^{o}$C)* ..... 129

Figure 5-12. Effect of adsorber inlet cooling water temperature on daily water production and specific daily water production (half-cycle time=200 sec, Tdes = 90$^{o}$C, Tcond = 25$^{o}$C, Tchilled = 23$^{o}$C) ..... 130

*Figure 5-13. Evaporator chamber (a) 12.5% occupied, (b) 25% occupied, (c) 37.5% occupied and (d) 50% occupied* ..... 131

*Figure 5-14. Effect of the dead volume in the evaporator and condenser chambers on the water production* ..... 132

Figure 5-15. The temperature profile of inlet/outlet to/from the adsorber bed (a) packed heat exchanger and (b) coated heat exchanger ..... 133

Figure 5-16. Comparative study between the packed rectangular finned heat exchanger and the coated wire finned one (thalf cycle =200 sec, Tdes = 90°C, Tcond = 25°C, Tchilled = 23°C) (a) COP, (b) SDWP and (c) SCP ..... 134

Figure 5-17. Specific volumetric daily water production in the adsorber bed between the packed and coated adsorption system ..... 135

*Figure 6-1. Schematic illustrations of BRO-AD hybrid process.* ..... 141

Figure 6-2. Operating strategy for continuous water production in BRO-AD hybrid system. ..... 142

Figure 6-3. Effects of feed concentration on the performances of BRO-AD hybrid system for brackish water desalination. RO membrane: LG-BW440R (high-rejection membrane) from LG Chem. (a) SECelec and SECheat, (b) recovery and water production rate in each unit, (c) permeate quality and peak pressure at RO unit, and (d) cooling power and COP. ..... 159

Figure 6-4. Effects of feed concentration on the performances of BRO-AD hybrid system for brackish water desalination. RO membrane: XLE-440 (high-flux membrane) from Dupont. (a) $SEC_{elec}$ and $SEC_{heat}$, (b) recovery and water production rate in each unit, (c) permeate quality and peak pressure at RO unit, and (d) cooling power and COP. ..... 160

Figure 6-5. Effects of feed concentration on the performances of BRO-AD hybrid system for seawater desalination. RO membrane: LG-SW440R (high-rejection membrane) from LG Chem. (a) $SEC_{elec}$ and $SEC_{heat}$, (b) recovery and water production rate in each unit, (c) permeate quality and peak pressure at RO unit, and (d) cooling power and COP. ..... 162

Figure 6-6. Effects of feed temperature on the performances of BRO-AD hybrid system for brackish water desalination. RO membrane: LG-BW440R (high-rejection membrane) from LG Chem. (a)

$SEC_{elec}$ and $SEC_{heat}$, (b) recovery and water production rate in each unit, (c) permeate quality and peak pressure at RO unit, and (d) cooling power and COP. ..... 163
Figure 6-7. Effects of feed temperature on the performances of BRO-AD hybrid system for seawater desalination. RO membrane: LG-SW440R (high-rejection membrane) from LG Chem. (a) $SEC_{elec}$ and $SEC_{heat}$, (b) recovery and water production rate in each unit, (c) permeate quality and peak pressure at RO unit, and (d) cooling power and COP. ..... 165
Figure 6-8. Comparative analysis results in conventional AD, BRO, and BRO-AD hybrid systems. Two cases (3 g/L and 35 g/L) are selected as representative cases for brackish water and seawater desalination, respectively. (a) $SEC_{elec}$ and $SEC_{heat}$ for brackish water desalination, (b) $SEC_{elec}$ and $SEC_{heat}$ for seawater desalination, (c) permeate water quality and peak pressure at RO system for brackish water desalination, (d) permeate water quality and peak pressure at RO system for seawater desalination, I cooling power and required mass of absorbent for brackish water desalination, and (f) cooling power and required mass of absorbent for seawater desalination. ..... 168
Figure 6-9. Comparative analysis results in conventional AD, BRO, and BRO-AD hybrid systems depending on feed concentration at brackish water desalination. (a) SECelec (solid line) and SECheat (dotted line), (b) peak pressure in RO system (maximum durable pressure of BWRO membrane is denoted as dotted black line), (c) permeate water quality, and (d) cooling power (solid line) and required mass of absorbent (dotted line). ..... 170
*Figure 6-10. Comparative analysis results in conventional AD, BRO, and BRO-AD hybrid systems depending on feed concentration at seawater desalination. (a) SECelec (solid line) and SECheat (dotted line), (b) peak pressure in RO system (maximum durable pressure of SWRO membrane is denoted as dotted black line), (c) permeate water quality, and (d) cooling power (solid line) and required mass of absorbent (dotted line).* ..... 171
Figure 7-1.Optical pictures for (a) MOF 801 soaked in ethanol, (b) MOF 801 after drying (c) MOF 801-G10% soaked in ethanol and (d) MOF 801-G10% after drying ..... 177
Figure 7-2. BET Nitrogen isotherms of MOF-801 particles and MOF-801/graphene composite ..... 178
Figure 7-3. Water kinetics at different adsorption temperatures and relative pressures using MOF-801 ..... 179

Figure 7-4. Water kinetics at different adsorption temperatures and relative pressures using MOF-801-G10% ..... 179
Figure 7-5. Water uptake at different relative pressures and adsorption temperatures (a) MOF-801 and (b) MOF-801-G10% ..... 181
Figure 7-6. Water uptake at different vapor pressures (a) MOF-801 and (b) MOF-801-G10%..... 182
Figure 7-7. The relation between $1T$ and $ln\ (Pvapour)$ at different water uptake (a) MOF-801 and (b) MOF-801-G10% ..... 183
Figure 7-8. Temperature variation with time in each component in the adsorption system with time using different adsorbent materials ($t_{halfcycle}$ = 400 sec, $t_{switch}$ = 40 sec, $T_{chilled}$ = 23ºC, $T_{heating}$ = 90ºC, and $T_{cooling}$ = 25ºC) ..... 184
Figure 7-9. Heat variation with time in each component in the adsorption system with time using different adsorbent materials ($t_{halfcycle}$ = 400 sec, $t_{switch}$ = 40 sec, $T_{chilled}$ = 23ºC, $T_{heating}$ = 90ºC, and $T_{cooling}$ = 25ºC) ..... 185
Figure 7-10. The Effect of half cycle time on (a)SCP and (b) COP using MOF 801 and MOF 801-G10% ..... 185
Figure 7-11. Effect of inlet chilled water temperature in the evaporator on the SDWP at inlet adsorption water temperature of (a) 25ºC, (b) 30ºC, (c) 35ºC and (d) 40ºC..... 186
Figure 7-12. Effect of inlet heating water temperature (desorption) in the bed on the SDWP at inlet chilled water temperature of (a) 5ºC, (b) 10ºC, (c) 15ºC and (d) 20ºC..... 187
Figure 7-13. Comparison between the presented MOFs and other MOFs in the literature ($T_{chilled}$ = 10ºC and $T_{cooling}$ = 30ºC) ..... 188
Figure 10-1. Two-bed packed adsorption desalination and cooling system ..... 209
Figure 10-2. Adsorber bed and its connections in packed adsorption system ..... 210
Figure 10-3. detailed water connections to the adsorber bed in packed adsorption system ..... 211
Figure 10-4. Evaporator and condenser and their connections in packed adsorption system..... 212
Figure 10-5. Datal logger, and power & control boxes in packed adsorption system ..... 213
Figure 11-1 . Heat exchanger coils connections in evaporator and condenser ..... 214
Figure 11-2. Hot and cold water sources for the adsorption system..... 215

Figure 11-3. Coated wire finned tube heat exchanger modules preparations ..... 216
Figure 11-4. Carrying the adsorber bed and pressure test of the coated wire finned tube heat exchanger modules ..... 217
Figure 11-5. Pressure test of the heat exchanger coils of the condenser ..... 218
Figure 11-6. Actuator connections of the electrical solenoid ball valve ..... 219
Figure 11-7. Data logger panel (box) with its connections to RTD and K-type thermocouples ..... 220
Figure 12-1. 3D isometric drawing of the adsorption system ..... 221
Figure 12-2. Top view of the adsorption system ..... 221
Figure 12-3. Front and side views of the adsorption system ..... 222
Figure 12-4. Drawing of the adsorber bed with the coated heat exchanger modules ..... 223
Figure 12-5. Top view of the packed rectangular finned tube heat exchanger modules in the adsorber bed ..... 224
Figure 12-6. Top view of the coated wire finned tube heat exchanger modules in the adsorber bed ..... 224
Figure 13-1. Power and control wiring of the solenoid valves ..... 225
Figure 13-2. Control panel wiring with pressure transducers and solenoid valves ..... 226
Figure 13-3. Summary of the electrical wiring of the adsorption system ..... 227
Figure 14-1. Repeatability test by measuring the inlet and outlet cold/hot water temperature to the 2nd adsorber bed ..... 228
Figure 15-1. Temperature sensor calibrations ..... 229
Figure 15-2. Calibration of the condenser temperature sensors ..... 230
Figure 15-3. Calibration of the evaporator temperature sensors ..... 231
Figure 15-4. Calibration of the adsorber bed temperature sensors ..... 232

# LIST OF TABLES

Table 2-1. Literature review on enhancing the thermal conductivity of adsorbent materials ..... 21

Table 2-2. Literature review on using coating in the adsorption system ..... 23

Table 2-3. Literature review in experimental works using different low-pressure evaporator design . 30

Table 2-4. Literature review in adsorption modelling ..... 38

Table 2-5. Literature review in effect of water salinity in the adsorption desalination systems. ..... 51

Table 3-1. Coated wire finned tube dimensions. ..... 59

Table 3-2. Input geometry ..... 64

Table 3-3. Input operating conditions ..... 64

Table 3-4. Heat exchanger module dimensions (coating thickness = 0.3mm) ..... 73

*Table 4-1. Thermophysical properties of adsorbent material, tube and fins* ..... 86

Table 4-2. input parameter of adsorber bed, condenser and evaporator ..... 102

Table 4-3. Operating conditions of the adsorption desalination system ..... 102

Table 5-1. Coating layers procedure to obtain 0.75mm coating thickness ..... 117

Table 5-2. Heat exchanger modules dimensions ..... 122

Table 5-3. Operating conditions ..... 125

*Table 6-1. Thermophysical properties of the AD system* ..... 147

Table 6-2. Operating conditions of AD unit. ..... 148

*Table 6-3. Simulation results at the base case of BRO-AD hybrid system (brackish water desalination, RO membrane: XLE-440 (high-flux membrane) from Dupont)* ..... 154

*Table 6-4. Simulation results at the base case of BRO-AD hybrid system (brackish water desalination, RO membrane: LG-BW440R (high-rejection membrane) from LG Chem.)* ..... 155

*Table 6-5. Simulation results at the base case of BRO-AD hybrid system (seawater desalination, RO membrane: LG-SW440R (high-rejection membrane) from LG Chem.)* ..... 157

Table 7-1. Simulated LDF constants ..... 180

Table 7-2. Isosteric heat of adsorption ..... 183

# NOMENCLATURE

| Symbol | Definition | Units |
|---|---|---|
| $A$ | the adsorption potential | J. $mol^{-1}$ |
| $C_p$ | Specific heat | J. $K^{-1}$ .$kg^{-1}$ |
| $C_{p,tf}$ | Specific heat of thermal fluid | J. $K^{-1}$ .$kg^{-1}$ |
| $C_{p,sf}$ | Specific heat of solid fin | J. $K^{-1}$ .$kg^{-1}$ |
| $C_{p,mt}$ | Specific heat of metal tube | J. $K^{-1}$ .$kg^{-1}$ |
| $d_p$ | Particle diameter | m |
| $Ea$ | Activation energy | J. $mol^{-1}$ |
| $\Delta H_{ads}$ | Isosteric heat of adsorption | J. $mol^{-1}$ |
| $h_{fg}$ | Heat of evaporation | J. $mol^{-1}$ |
| $K_d$ | Permeability | $m^2$ |
| $ko$ | pre-exponential constant | $s^{-1}$ |
| $k_{tf}$ | Thermal conductivity of thermal fluid | W. $m^{-1}$.$K^{-1}$ |
| $k_t$ | Turbulent thermal conductivity of thermal fluid | W. $m^{-1}$.$K^{-1}$ |
| $k_{sf}$ | Thermal conductivity of solid fin | W. $m^{-1}$.$K^{-1}$ |
| $k_{mt}$ | Thermal conductivity of metal tube | W. $m^{-1}$.$K^{-1}$ |
| $k_{ads}$ | Thermal conductivity of adsorbent | W. $m^{-1}$.$K^{-1}$ |
| $k_{eff,ads}$ | Effective thermal conductivity of adsorbent | W. $m^{-1}$.$K^{-1}$ |
| $T_{ads}$ | Adsorption water temperature | $^oC$ |
| $T_{des}$ | Desorption water temperature | $^oC$ |
| $T_{cond}$ | Condensation temperature | $^oC$ |
| $T_{evap}$ | Evaporation temperature | $^oC$ |
| $T_{tf}$ | Thermal fluid temperature | K |
| $T_{sf}$ | Solid fin temperature | K |

| | | |
|---|---|---|
| $T_{mt}$ | Metal tube temperature | K |
| $T_{ads}$ | Adsorbent temperature | K |
| $t_{cycle}$ | Total time of the cycle | sec |
| $t_{adsorption}$ | Adsorption time | sec |
| $P_2$ | Vapor pressure | Pa |
| R | Ideal gas constant | J. $mol^{-1}$ .$kg^{-1}$ |
| $\rho_v$ | Vapor density | $kg.m^{-3}$ |
| $\rho_{tf}$ | Thermal fluid density | $kg.m^{-3}$ |
| $\rho_{sf}$ | Solid fin density | $kg.m^{-3}$ |
| $\rho_{mt}$ | Metal tube density | $kg.m^{-3}$ |
| $\rho_{ads}$ | Adsorbent density | $kg.m^{-3}$ |
| U | Thermal fluid velocity | $m.s^{-1}$ |
| $u_2$ | vapor velocity | $m.s^{-1}$ |
| X | Instantaneous water uptake | $kg.kg^{-1}$ |
| $X_{inf}$ | equilibrium water uptake | $kg.kg^{-1}$ |

***Subscripts***

| | |
|---|---|
| $ads$ | Adsorption |
| $AD$ | Adsorption desalination system |
| $b$ | Brine |
| $bed$ | Adsorber bed |
| $BRO$ | Batch reverse osmose |
| $cond$ | Condenser |
| $ch$ | Chilled water |
| $cw$ | Cold water |
| $des$ | Desorption |
| $evap$ | Evaporator |

| | | |
|---|---|---|
| $elec$ | Electrical | |
| $hw$ | Hot water | |
| $HX$ | Heat exchanger | |
| $in$ | Inlet | |
| $o$ | Outer | |
| $out$ | Outlet | |
| $S$ | Surface | |
| $w$ | Water | |

**Greek letters**

| | | |
|---|---|---|
| μ | Viscosity | $N.m^{-2}$ |
| $\mu_t$ | Turbulent viscosity | $N.m^{-2}$ |
| $\eta$ | Efficiency | |
| $\mu_v$ | Vapor viscosity | $N.m^{-2}$ |
| $\rho$ | density | $kg.m^{-3}$ |
| $\varepsilon_t$ | Total porosity | (-) |
| ξ | Minor loss coefficient | |

**Abbreviations**

| | |
|---|---|
| AF | Aluminium Fumarate |
| COP | Coefficient of performance |
| LDF | Linear Driving force |
| MOF | Metal Organic Framework |
| SCP | Specific cooling power |
| SDWP | Specific daily water production |
| SVDWP | Specific Volumetric Daily Water Production |
| *SEC* | Specific energy consumption |

# LIST OF PUBLICATIONS

The thesis consists of eight chapters which are published/under review in peer-reviewed journals and conferences as follows:

**Journal Publications:**

1. **I. Albaik**, R. Al-Dadah, S. Mahmoud, İ. Solmaz, Non-equilibrium numerical modelling of finned tube heat exchanger for adsorption desalination/cooling system using segregated solution approach, **Applied thermal engineering**. 183 (2021). https://doi.org/10.1016/j.applthermaleng.2020.116171. **(Impact factor: 6.46)**

2. **I. Albaik**, R. Al-Dadah, S. Mahmoud, M.K. Almesfer, M.A. Ismail, E. Elsayed, M. Saleh, A comparison between the packed and coated finned tube for adsorption system using aluminium fumarate: Numerical study, **Thermal science and engineering progress**. 22 (2021) 100859. https://doi.org/10.1016/j.tsep.2021.100859. **(Impact factor: 4.56)**

3. **I. Albaik,** R. Al-Dadah, S. Mahmoud, M. Ismail, M. Almesfer. Coated, packed and combined wire finned tube adsorption cooling and desalination system using metal-organic framework: Numerical study. **Energy** 2022;247:123506. https://doi.org/10.1016/j.energy.2022.123506. **(Impact factor: 8.85)**

4. **I. Albaik,** M. Badawy Elsheniti, R. Al-Dadah, S. Mahmoud, İ. Solmaz, Numerical and experimental investigation of multiple heat exchanger modules in cooling and desalination adsorption system using metal organic framework, **Energy conversion and management**. 251 (2022) 114934. https://doi.org/10.1016/j.enconman.2021.114934. **(Impact factor: 11.53)**

5. **I. Albaik**, K. Diab, M. Saleh, R. Al-Dadah, S. Mahmoud, M. F. El-Kady, İ. Solmaz and M. Elsheniti, 'MOF based Water Desalination and cooling Coated Adsorption System Integrated with Pre-treatment remediation unit', **Sustainable energy technologies and assessments** (accepted with corrections). **(Impact factor: 7.63)**

6. **I. Albaik,** Y. Alamri, M. Elsheniti, R. Al-Dadah, S. Mahmoud, M. Ismail. Assessment of a novel multi-generation solar CPV/T system combining adsorption and organic rankine cycle subsystems. **Solar Energy** 2022;236:455–72. https://doi.org/10.1016/j.solener.2022.03.024. **(Impact factor: 7.18)**

7. K. Park, **I. Albaik,** P. A. Davies, R. Al-Dadah, S. Mahmoud, M. A. Ismail and M. K. Almesfer, Batch reverse osmosis (BRO)-adsorption desalination (AD) hybrid system for multipurpose desalination and minimal liquid discharge, **Desalination**, 2022 https://doi.org/10.1016/j.desal.2022.115945. **(Equal contribution with the first author) (Impact factor: 11.21)**

8. K. E. Diab, **I. Albaik**, R. Al-Dadah, S. Mahmoud, M. A. Ismail, M. K. Almesfer, M. F. El-Kady, A. Abd El-moneim, Enhancing the thermophysical Properties and Water Kinetics of Zirconium Metal-Organic Frameworks for more Efficient Sorption-driven Applications, **Microporous and Mesoporous Materials**, 2022 (accepted). **(Impact factor: 5.87)**

9. **I. Albaik,** K. E. Diab, R. Al-Dadah, S. Mahmoud, M. A. Ismail, M. K. Almesfer, M. F. El-Kady, Zirconium Metal Organic Framework / Graphene Nanoplatelets Composite for More Efficient Cooling and Desalination Adsorption System (under review).

## Conference Publications:

1. **I. Albaik,** K. Diab, R. Al-Dadah, S. Mahmoud, M. A. Ismail, Coating Thickness Effect on the Cyclic Performance of Aluminum and Zirconium Metal-Organic Frameworks for heat pump application, International Conference on Applied Energy, Thailand/Virtual, 2021.

# Chapter 1: Introduction

## 1.1. Introduction

About 70% of the planet is occupied by water with seawater representing 97.5% of this quantity [1]. The salinity (Total dissolved solid) of the seawater is more than 40,000 ppm and only a third of the seawater quantity is accessible and can be utilized directly [2]. The number of seawater desalination plants with different technologies is increasing dramatically, particularly in developing countries, desert areas (Gulf counties) and coastal countries. However, the cooling demand in these areas, which are characterized by long and hot summers is another crucial aspect that should be considered alongside the water demand. Several water desalination technologies have been developed in recent decades and can be classified mainly into four types; (1) pressure activated, (2) thermally activated, (3) chemically activated and (4) adsorption technology [3]. Most of the above mentioned regions use thermally activated technologies, due to the abundant amount of solar and waste heat, while the pressure-activated desalination system is the most widely used in the world.

Recently, adsorption technology has received considerable attention for water desalination applications due to its low electrical energy consumption compared to pressure and thermally driven desalination technologies [4]. Adsorption is a process in which the molecules of the adsorbate (gas or liquid) adhere to solid adsorbent particle surfaces. This process takes place based on the Van der Waals forces and is known as physisorption. If the adsorption process involves a chemical reaction it is called chemisorption [5]. The ability to use low temperature heat sources is another advantage of this technology, as it can operate in a temperature range of 70-100$^{o}$C [6]. Adsorption desalination systems can handle a feeding water with extremely high salinity (up to 67,000 ppm) compared to the reverse osmose (RO) and multiple effect distillation (MED) that can work with feeding water salinity up to 45,000 ppm. It can also produce a very high water quality compared to other technologies with a salinity of less than 10ppm [3]. The adsorption system can also be used as an energy storage system by storing the solar energy during the day to be used at night. Moreover, adsorption technology can provide cooling in addition to desalinated water. Thermally driven adsorption chillers (TDC) are another approach compared to the conventional vapor compression refrigeration systems, as it provides cooling

using low-grade energy such as waste heat from industrial processes. TDC can also provide cooling without CO2 emissions, using environmentally friendly refrigerants such as water. However, the coefficient of performance (COP), the specific daily water production (SDWP) and, the specific cooling power (SCP) of the commercially available adsorption systems are low due to the low water uptake of the conventional adsorbent material used.

The adsorption system consists of four main components: two adsorber beds, an evaporator and a condenser as shown in **figure 1-1**. The saline water is fed in the evaporator under vacuum conditions. Firstly, the adsorption cycle takes place by adsorbing the water vapor at a low saturation temperature (5-30$^{o}$C) using the adsorbent material inside the adsorber bed. Subsequqently, the water vapor will be released from the bed during the desorption process by heating the adsorbent material,after which all the freshwater will be condensed and collected from the condenser.

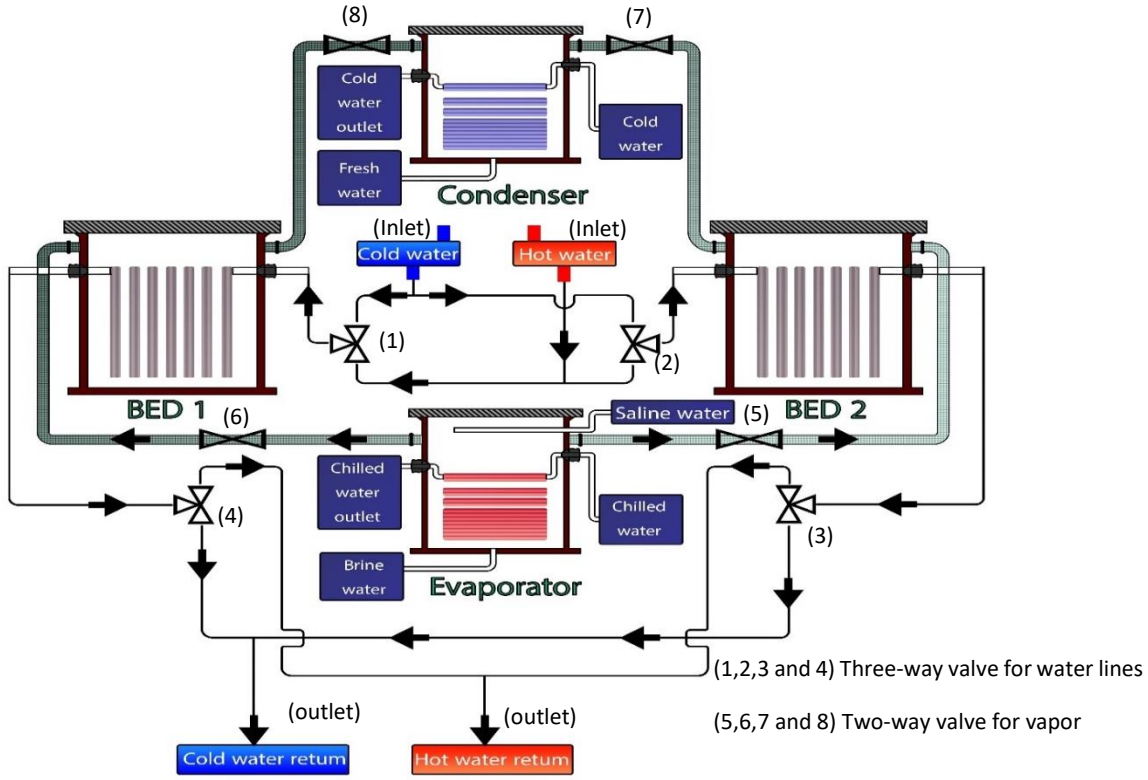



Figure 1-1. Adsorption cooling and desalination system [7]

The adsorber bed is the main component that affects the system performance, which contains the adsorbent material integrated into heat exchangers. The adsorbent material is normally packed inside the heat exchanger in the form of granular particles (pellets) and needs to be restrained using fine metal

mesh. Recently, coating the adsorbent material onto the adsorber bed heat exchangers showed better performance compared to the packed ones as it enhances the heat transfer through the thin adsorbent material coating layer [8,9]. However, the coated layer thickness is very sensitive as it influences the vapor mass transfer resistance as a result of mixing the binder agent with the adsorbent material, which can block the pores of the adsorbent material. Thus, a critical investigation should be carried out to obtain the optimum coating layer thickness that provides the optimum mass and heat transfer.

Numerical models to simulate the heat and mass transfer in adsorber beds are powerful tools to optimize the design of the adsorption system and lead to enhancing its SDWP and SCP. The performance of the adsorber bed is negatively affected by the poor heat and mass transfer due to the low thermal conductivity and high mass transfer resistance of the adsorbent material. Many attempts have been carried out to investigate the internal (intraparticle) and external (interparticle) mass transfer resistance of the water vapor flow through the voids between the adsorbent particles [10,11]. The heat and mass transfer models including the internal and external mass transfer resistances in two and three-dimensional geometries are the most advanced as they can solve the high degree of non-linearity of the partial differential equations especially when the model requires a huge computational domain to solve. Although several studies were carried out on the geometrical design of the heat exchanger in the bed as mentioned above, most of these studies focus only on a very limited computational domain in the heat exchanger ignoring the effect of studying the domain of the adsorber bed such as the position of the inlet/outlet vapor to the bed, the gap between heat exchangers modules, the computational cost, the simplicity of the model and unique heat exchanger geometry with higher performance.

On the other hand, an effective evaporator and condenser are essential to utilize the adsorbent material effectively as the cooling energy is obtained from the evaporator, while the distilled water is extracted from the condenser. The design of these components is a challenge as they are working under vacuum pressure and a low saturation temperature [12].

Recently, to enhance the performance of adsorption systems, metal-organic framework (MOF) materials have been investigated to replace conventional adsorbent materials (such as silica gel and Zeolite) due to their chemical stability and unsurpassed porosity [13]. MOFs also provide high water

uptake; tuneable hydrophilicity and narrow pore size distributions which can provide an extremely sharp loading step compared to the silica gel [13,14]. Aluminum fumarate MOF material is considered a good alternative for conventional adsorbent materials as it provides good water uptake and low desorption temperature (less than 90$^{o}$C), which is a very good candidate to be applied for different applications using low-grade heat sources [15]. However, this material has low performance at low relative pressure. Thus, further investigations for other MOFs that can provide high water uptake at low relative pressure with low desorption temperature is needed to improve the system performance. Additionally, improving the thermal conductivity of MOFs without affecting the water uptake capacity is also another key factor that recent studies have been struggling with.

Finally, integrating the adsorption system with other systems to overcome the high electrical consumption and provide higher hybrid system performance using low-grade energy increases the potential of using the adsorption system for large-scale applications. Therefore, achieving higher system performance by investigating the type of MOF used, the method of applying the MOF (coating or packing), improving the design of the components (adsorber bed, evaporator and condenser), and integrating other technologies are all needed to be investigated using numerical simulations and experimental testing.

## 1.2. Aim and objectives

The aim of this Ph.D. work is to enhance the performance of the adsorption desalination and cooling system, through numerical simulation and experimental testing in terms of increasing water and cooling production and reducing energy consumption. To achieve this, the following objectives are considered:

a. Develop an effective numerical method to simulate the heat exchangers in the adsorber bed. This method should be able to predict the variation of pressure, water uptake and temperature distributions in the heat exchanger of the adsorber bed. Also, the model should incorporate variable boundary conditions to study the cyclic performance of the system.

b. Use the developed numerical model to investigate different geometrical design parameters including the tube fin type (rectangular or wire finned), the wire fin geometry ( diameter, height

and spacing), the gap between the heat exchanger modules and connection approach (parallel or series) between the modules.

c. Study the packed and coated heat exchanger with aluminum fumarate adsorbent material and find the best approach to be applied to the system.

d. Investigate the effect of multiple heat exchanger modules in the adsorber bed of the scaled-up adsorption desalination and cooling system on its performance.

e. Develop an effective compact evaporator and condenser design to be applied in the scaled-up adsorption systems.

f. Investigate newly developed MOFs as alternatives to aluminum fumarate, characterize their water adsorption uptake in terms of isotherms and kinetics, and use the adsorption system model to study their performance for cooling and water desalination applications. Furthermore, investigate the effect of enhancing the thermal conductivity of the MOFs on the system performance.

g. Integrate the adsorption system with different desalination/power generation/ water treatment systems to enhance the overall performance of the hybrid system.

## 1.3. Thesis outlines

The thesis is written in an alternative format approach in which each chapter contains one published/submitted journal paper integrated cohesively to address the research objectives. The thesis consists of eight chapters: the first one is the introduction and the second one is the literature review. The following five chapters contain peer-reviewed papers with the literature reviews removed and summarized in the literature review chapter (chapter 2). The detailed setup of the experimental works is provided in the appendices A and B.

Chapter 3 describes the modelling of a heat exchanger in the adsorber bed called a wire-finned tube, using the coupled solution approach. This chapter applied the coupled approach to developing a three dimensional model for complex geometry (wire-finned tube heat exchanger). Additionally,

packing, coating and combining the two techniques of applying the adsorbent material on the heat exchanger are also investigated. The same modelling approach is used in chapter 4 to build the adsorption system using different heat exchanger designs to study the performance of the system in terms of SDWP, SCP and COP.

Chapter 4 investigates multiple heat exchanger modules in a scaled-up adsorption system numerically and experimentally using the packing method with a rectangular-finned tube heat exchanger. This chapter applies the coupled solution approach to investigate a larger computational domain to study the full set of heat exchanger modules installed in the adsorber bed (a gap between the modules and connection type between the modules), which is then used to build the test rig with water production of 200L/day and cooling power of 5kW.

Chapter 5 optimizes the scaled-up adsorption system by applying the coated method on the wire-finned heat exchanger on a test rig with water production of over 260 L/day. It also provides a study of the evaporator and condenser design to optimize the compactness of their chambers by investigating the effect of the dead volume on water production. In this chapter, the design of the adsorption system is optimized by using a thicker coated layer on the heat exchanger surface to produce higher water production and cooling rate, compared to the packed approach. A comparative study is provided between the packed rectangular finned tube and coated wire finned tube in terms of the SDWP, SCP, COP and specific volumetric daily water production in the adsorber bed (SVDWP).

The conclusions from chapters 4 and 5 are considered in the design of the hybrid adsorption system in the next chapter. Chapter 6 describes the integration of the adsorption system with another desalination system to increase the overall performance of the integrated system using a packed rectangular-finned tube heat exchanger.

The optimizations of the adsorption system from chapter 3 to 5 are based on enhancing the design of the heat exchanger in the adsorber bed (the geometrical design, multiple heat exchangers, and the method of applying the adsorbent material on the heat exchanger (packing, coating, and combination between both)) and enhancing the compactness design of evaporator and condenser. Therefore, it is also

necessary to study the adsorbent material itself and how its performance can be optimized to be evaluated on the efficiency of the adsorption system.

Chapter 7 optimized the cooling and desalination adsorption system performance, using newly developed MOF material after enhancing the thermal conductivity of the MOFs. Finally, chapter 8 includes the conclusion followed by recommendations for future works

# Chapter 2: Literature review

## 2.1. Overview of the cooling and desalination adsorption systems

The thermodynamic cycle of adsorption heat pumps for cooling and water desalination consists of four steps as shown in Figure 2-1 and Figure 2-2, which are described as follows: Isosteric heating (I−II): when the adsorbent material is saturated with refrigerant/working fluid, the regeneration/desorption process is required. During this process, the adsorbent is heated up from $T_1$ to $T_2$, without releasing the working fluid to the condenser, thus the pressure in the adsorber chamber/bed will be increased from the evaporator pressure to the condenser pressure ($P_{ev}\ to\ P_{con}$).

Isobaric desorption (II−III): the heating is continued while the working fluid is released to the condenser, thus, the pressure during this step is constant. This step is continued until reaching the minimum working fluid uptake ($W_{min}$) by heating the adsorbent material at the desorption temperature ($T_{des}$). The working fluid is condensed and heat will be rejected in the condenser ($Q_{con}$) during the Isobaric desorption, while thermal energy is consumed during the isosteric and isobaric desorption ($Q_{des}$).

Isosteric cooling (III−IV): after regenerating the adsorbent, the adsorption process starts by cooling the adsorber chamber/bed from $T_{des}$ to $T_3$, while the pressure in the chamber decreases to $P_{ev}$ without adsorbing the working fluid from the evaporator.

Isobaric adsorption (IV−I): the cooling is continued, while the working fluid flows from the evaporator to the adsorber bed, as the adsorbent material adsorbs the working fluid at a constant pressure. This step will be finished after reaching $T_3$ and the maximum working fluid uptake ($W_{max}$). The adsorbed working fluid takes up energy from the environment in the evaporator at a low temperature for the evaporation process ($Q_{ev}$), while heat is released in the adsorber bed at an intermediate temperature level ($Q_{ads}$).

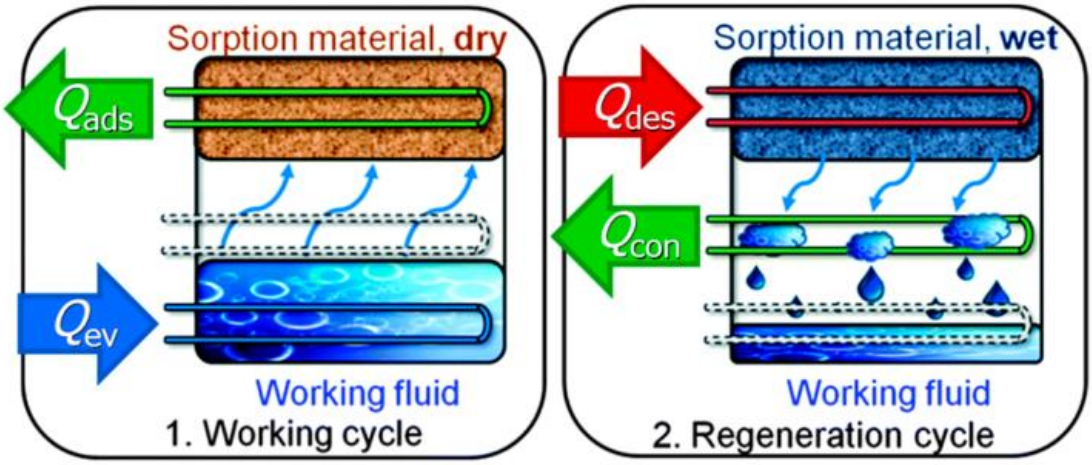



Figure 2-1. Schematic diagram of the adsorption heat pump/cooling/desalination cycle [14]

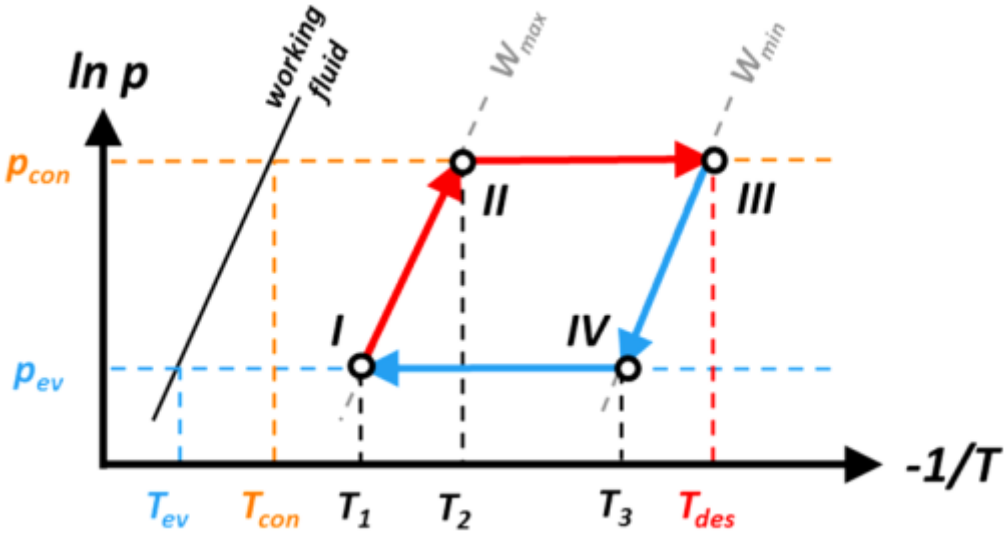



Figure 2-2. Isosteric cycle diagram of adsorption heat pump/cooling cycle [16]

## 2.2. Isotherms, kinetics and heat of adsorption

### 2.2.1. Adsorption isotherms:

Adsorption is a process in which the molecules of the adsorbate (gas or liquid) adhere to solid adsorbent particle surfaces. This process takes place under the Van der Waals forces and is known as physisorption, while it is called chemi-sorption if the process involves a chemical reaction [5]. Adsorption isotherms refer to the relation between the relative pressure/concentration and the adsorbent material gas/vapor capacity at equilibrium conditions and certain temperatures [17]. There are over thirteen isotherm models that are classified based on empirical models and Polanyi's theory [17].

Linear, Sips [18], Toth [19], and Freundlich [20] models are based on the empirical isotherms that are derived from the Langmuir theory [21] in which their characteristics (such as adsorption isotherm curves) do not represent a specific physical meaning. Dubinin-Astakhov (D-A) [22] and Dubinin-Radushkevich (D-R) [23] models are based on Polanyi's potential theory and are considered semi-empirical models. To summarize these models, the linear model represents the condition when the initial concentration of the gas/vapor is low, Freundlich model represents the physical adsorption or mono layer adsorption in which 50 percent of adsorption sites are occupied. The Sips model also represents the monolayer adsorption in which one molecule is adsorbed to 1/n sites. The Langmuir model represents the macroscopic homogeneous adsorption, while the D-A and D-R models are used to study the microstructure of adsorbents. Based on Wang and Guo [17], the most used models in the literature are the Langmuir, then Freundlich followed by Sips, linear, D-A, and D-R models. However, the isotherm types (I – VI) are also critical parameters in selecting the best model, especially when the isotherm type cannot be represented by one equation such as the S shape isotherms. It was found that for adsorbent materials that are widely used for water adsorption such as silica gel [24], zeolites, aluminum fumarate, MIL-101 Cr [25] , CPO-27 Ni [26], and MOF-801, the D-A, the modified D-A, and the modified Freundlich provide a very good fit to the experimental adsorption isotherms. The D-A model based on Polanyi's adsorption potential theory is considered using the following equation:

$$\boldsymbol{W_{inf} = W_m \exp(-\left(\frac{A}{E}\right)^n)} \qquad 2.1$$

$$\boldsymbol{A = -RT \ln\left(\frac{P}{P_o}\right)} \qquad 2.2$$

Where $W_{inf}$ is the equilibrium uptake, $W_m$ is the maximum uptake, $A$ is the adsorption potential, $E$ is the activation energy, $R$ is the gas constant, $T$is the adsorbent temperature, $\frac{P}{P_o}$ is the relative pressure (the ratio between the saturation pressure of the evaporator/condenser to the saturation pressure of the adsorbent material) and $n$ is a constant varying between 2 to 6 depending on the adsorbent material [27].

### 2.2.2. Adsorption kinetics:

The adsorption kinetics is the time variation of the adsorption process which represents how fast the material reaches the equilibrium uptake at a specific temperature and pressure. The faster the kinetics and lower the cycle time the better the adsorption system performance [28]. The kinetics are mainly a function of the mass transfer between the adsorbate (vapor) and adsorbent material and enhancement of the kinetics which leads to better system performance [29]. As mentioned earlier, the mass transfer includes both the intra-particle and inter-particle mass transfers. Intra-particle mass transfer represents the vapor flow through the adsorbent micro pores, while the vapor flow through the voids between the adsorbent particles is considered as the inter-particle mass transfer [11]. The heat transfer indirectly affects the kinetics, as faster cooling/heating of the adsorbent material leads to a faster adsorption rate. Particle size and porosity significantly affect the adsorption kinetics. When the adsorbent particle size decreases, the intra-particle mass transfer resistance will decrease, ultimately enhancing the adsorption rate and system performance. On the other hand, decreasing the particle size has a negative effect on the inter-particle mass transfer, since the voids between the particles (adsorbent granules) will decrease as the void channels become narrower [30]. The effect of the inter-particle mass transfer can be observed in packed adsorber beds with adsorbent granules, in which the pressure drop of the vapor flow through the bed is higher when smaller particle size is used. The particle size also has a significant effect on the heat transfer resistance. The adsorbent particles are cooled down or heated up during the adsorption or desorption processes using a heat exchanger with different configurations in which the contact thermal resistance is a function of the surface contact area between the metal surface and the particles. Therefore, large particle size has lower surface contact with the heat exchanger which leads to an increase in the thermal contact resistance [31]. The adsorbent porosity is also found to affect heat transfer through effective thermal conductivity. If the material has very high porosity, the effective thermal conductivity will decrease as the pores and voids have lower thermal conductivity compared to the adsorbent material [32].

The adsorption kinetic models are based on adsorption diffusion models which consists of film (surface) diffusion (inter-particle) and internal diffusion (intra-particle) [33]. The adsorbent particle

mentioned earlier is generally formed by compressing the micro/meso porous material into pellets (granules) with a wide range of shapes [34]. Before investigating the models, the mechanism of the mass transfer inside the adsorber bed phases can be classified into four; bulk gas, macro-pores, micro/mesopores, and solid surfaces as shown in **Figure** 2-3 [35].




Figure 2-3. diffusion phases from bulk gas to solid surfaces [35]

In micro/meso pores, firstly, the gas occupies the interstitial sites (the voids) between the pellets (granules) by axial dispersion. Then a film will be formed around the pellets in which the film diffusion occurs from the bulk gas to the pellets. Then the gas will enter the pellets and diffuse through the micro and mesopores. Finally, the gas will be adsorbed by the adsorbent surfaces. In macropores, the diffusion occurs through one or a combination of molecular diffusion, Knudsen diffusion, and viscous diffusion. The macropore size is larger than the molecular size of the gas/vapor, and molecular diffusion occurs through the random collision between the molecules. The Knudsen diffusion occurs if the molecular mean path is larger than the pore diameter, then another type of collision will be considered between the molecular and macropore walls. While viscous diffusion occurs when the flow through the macropores is due to the pressure gradient and it is negligible in the packed beds [35].

Several models have been developed to study the diffusion processes including the overall mass transfer coefficients such as; Linear driving force (LDF) model, solid diffusion model, Nakao and Suzuki model, and Vermeulen model. The LDF model proposed by Gleuckauf and Coates has been widely used due to its simplicity, and analytically and physically consistent [79, 80] for predicting adsorption kinetics [38,39] using the following equations:

$$\frac{\partial W}{\partial t} = K\,(W_{inf} - W) \qquad 2.3$$

$$\boldsymbol{K = \frac{F\, D_e}{R^2}} \qquad 2.4$$

Where $\frac{\partial W}{\partial t}$ is the rate of adsorption, $K$ is the overall mass transfer coefficient, $W_{inf}$ is the equilibrium uptake and $W$ is the instantaneous uptake, $F$ is the pellet constant which is 15 for a spherical shape, $D_e$ is the diffusion coefficient and $R$ is the particle radius.

This model assumes that the adsorption rate is proportional to the adsorbate (gas/vapor) concentrations between the inner and outer adsorbent particles [40]. Additionally, this model ignores the inter-particle mass transfer resistance since this mass transfer is much faster than the intra-particle mass transfer [41]. Therefore, this assumption is only valid with large particle sizes or small adsorbent thicknesses [42]. The calculation steps to determine the diffusion constants using the LDF model are widely known [29, 86]. Recently, a coating technique was developed where the powder adsorbent is mixed with a binder and the produced solution is coated on the heat exchanger surface. The coating of the adsorbent material resulted in reducing the thermal contact resistance [15], however, the binder can block the voids or the pores of the adsorbent which can lead to reconsidering calculating the LDF constants by using the experimental data to modify the constant values.

### 2.2.3. The heat of adsorption:

The heat of adsorption is a measure of the interaction strength between the adsorbate (gas/vapor) and the solid adsorbent. The change in the enthalpy, determined from the adsorption isotherms with a specific number of adsorbed molecules using two or more temperatures, is called the isosteric heat of adsorption [45]. It is used to determine the extent of the changes in the adsorbent temperature within the adsorber bed using the adsorption process (exothermic) and desorption process (endothermic) [46]. The heat of adsorption is derived either from the adsorption isotherms or, as differential heat of adsorption, determined experimentally using the Calorimetric method [47]. The isosteric heat of adsorption can be calculated using the Clausius-Clapeyron equation as follows [48]:

$$\frac{\delta(lnP_v)}{\delta\left({}^{1}/_{T_{ads}}\right)} = -\frac{Q_{ads}}{R} \qquad 2.5$$

Where $P_v$ is the vapor pressure, $T_{ads}$ is the adsorption temperature, $R$ is the specific gas constant and $Q_{ads}$ is the isosteric heat of adsorption.

### 2.2.4. Adsorbent material characterizations

To measure the adsorbent material properties, several devices are used including (i) Powder X-ray diffraction (PXRD) to study the crystallinity, phase purity, and structural characterization of the solid-state material to identify the characteristic pattern as each adsorbent has the fingerprint that distinguishes it from other adsorbent materials. (ii) Nitrogen adsorption at 77K, using Quantachrome NOVA surface area analyzer is used to identify the surface area, and pore volume of the adsorbent. (iii) Thermogravimetric Analysis (TGA) is used to study thermal stability by monitoring the mass change of adsorbent as a function of time and/or temperature. (iV) Dynamic vapor sorption (DVS) is used to measure the gravimetric water uptake as a function of temperature, relative pressure, and time as well as study the cyclic performance of the adsorbent material over running multiple cycles of adsorption and desorption processes. (V) Scanning electron microscopy (SEM) is used to evaluate the crystal size and morphology of the adsorbent material.

## 2.3. Conventional adsorbent materials and metal-organic frameworks

The performance of adsorption systems depends on the adsorbent material's adsorption and thermophysical properties which determine the ability of the adsorbent material to capture the water vapor during a specific cycle time [49]. The adsorption material is characterized by: (i) adsorption isotherm and kinetics, (ii) particle size, pore volume, and surface area, and (iii) thermal properties such as thermal conductivity. The high surface area and pore volume per unit mass/volume of adsorbent material are the main factors that need to be considered in selecting the material. Additionally, reaching the maximum water uptake inside the pores at the minimum cycle time is also a critical factor that affects the overall performance of the adsorption systems. The Brunauer Emmer Teller (BET) surface area per unit mass (SSA) of the conventional adsorbent materials such as silica gel, zeolite, and activated carbon varied between 150 $m^2/g$ to 3100 $m^2/g$. This range of surface area is considered relatively small and inadequate for adsorption applications [50,51]. However, silica gel and zeolite are still used for water adsorption application with relatively good specific daily water production (SDWP) (higher than

10L/kg/day). The limitations of these materials can be found in the undesirable water linear isotherms of silica gel between the relative pressure and water uptake and the limited maximum water uptake as shown in Figure 2-4. Additionally, the high desorption energy to regenerate the zeolite is also considered one of the limitations of using this material in water applications.

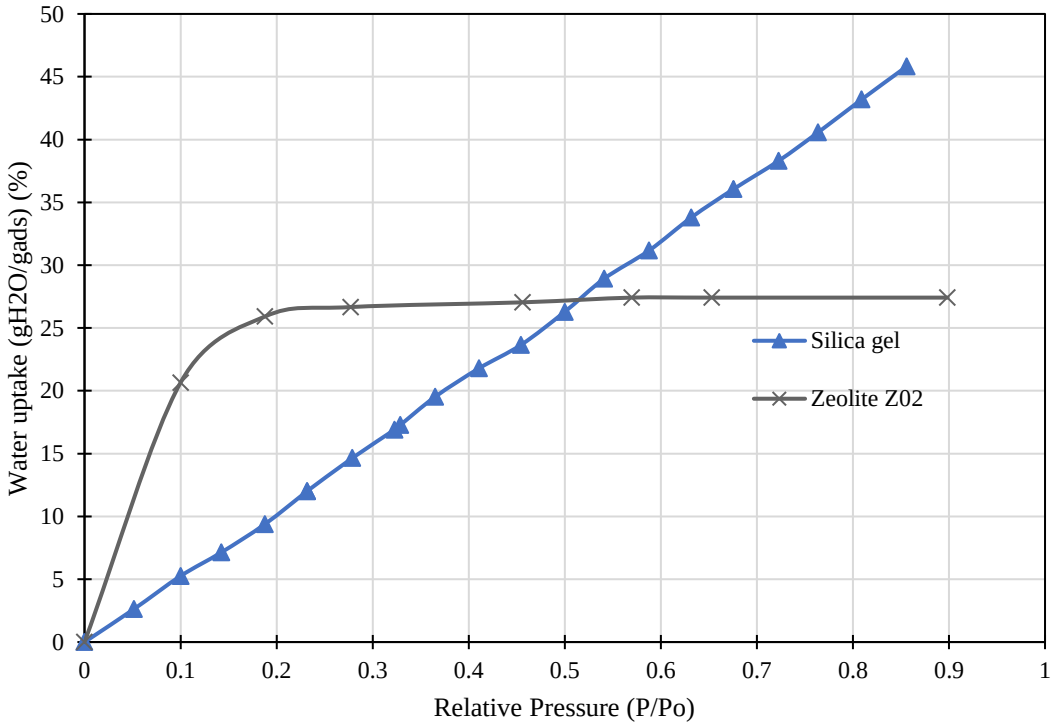



Figure 2-4. Water isotherms at different relative pressures for the conventional adsorbent materials [52,53]

These limitations encouraged the researchers to develop materials with a high surface area such as metal-organic framework materials (MOFs) which were firstly introduced by Yaghi et al. in 1996 [54]. MOFs are porous crystalline materials constructed from metal ions and organic ligands connected in a three-dimensional structure. Due to their unique adsorbent properties, large surface area, and tuneable adsorption behavior, MOFs are considered very promising materials [55] if the challenges that faced these materials are solved such as the stability issues and the long-time of the synthesis process. MOFs have been widely investigated for water sorption-based applications including seawater desalination [56], cooling [16], energy storage [57], humidity control in buildings [58], and water harvesting from the air [59]. Several topologies of MOFs have been investigated and developed based on the metal ions used in which each one shows unique adsorption characteristics which can be classified as follows;

aluminum (Al), zirconium (Zr), copper (Cu), chromium (Cr), iron (Fe) and nickel (Ni). These groups are presented in **Figure** 2-5 based on the maximum water uptake at the equilibrium condition. Cr-MOF has the largest water uptake amongst the MOF groups. However, this material is undesirable for cooling applications since the relative pressure at which the high water uptake is achieved is higher than 0.4 leading to poor cooling performance under the typical operating conditions of cooling systems like water chillers. Because of the large pore sizes of MIL-101 Cr, the capillary condensation occurs at a high range of relative pressure [16].

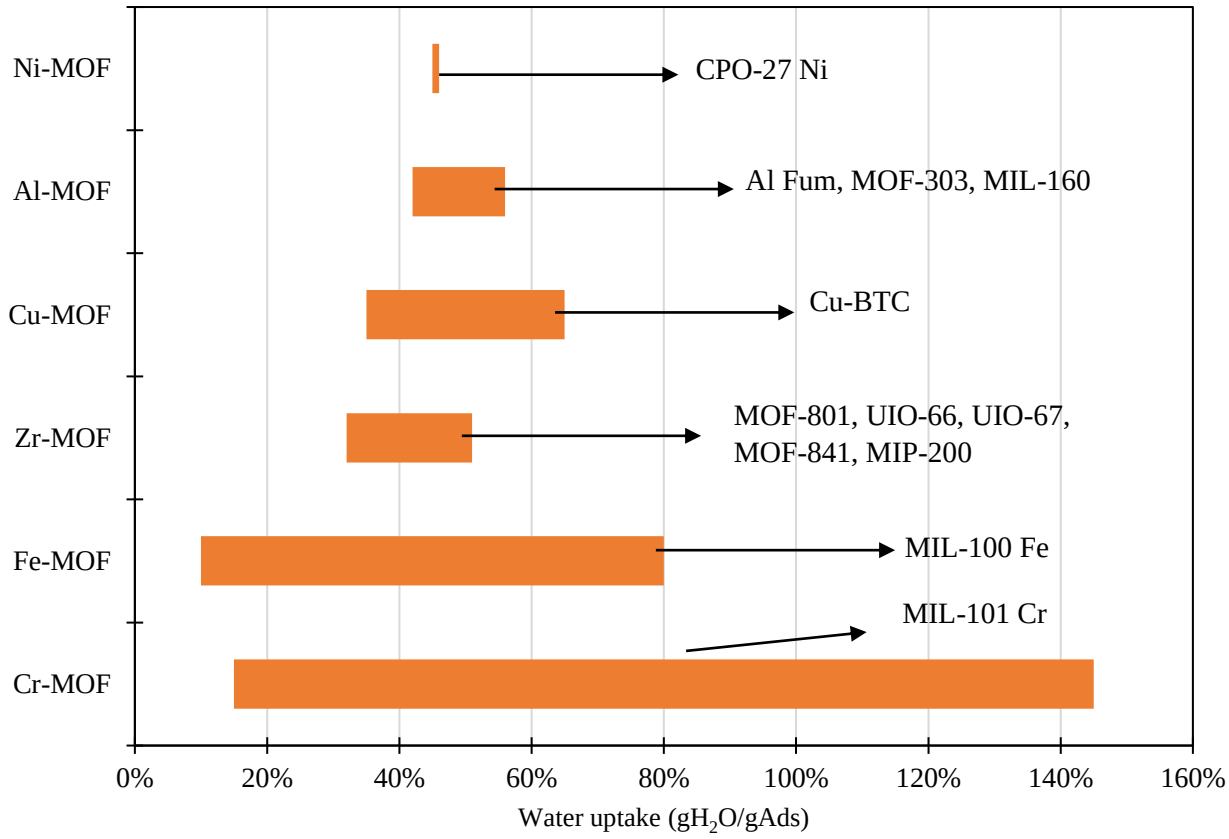



Figure 2-5. Maximum water uptake for different MOF groups [44,56,60–62]

There are six different types of adsorption isotherms, each having its advantages over the others and their application as presented in **Figure** 2-6**.**

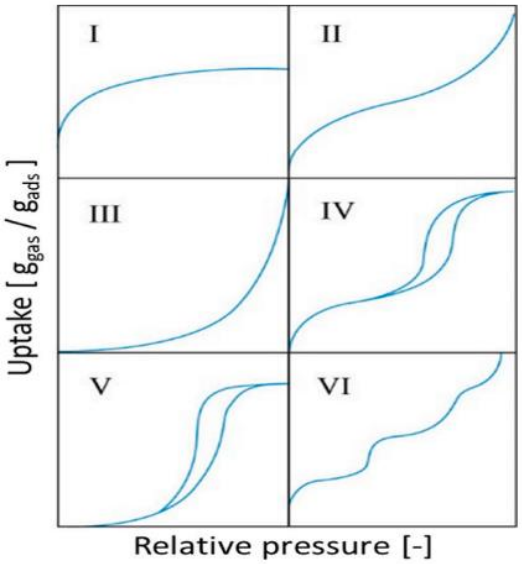



Figure 2-6. Different adsorption isotherm types [63]

For example, Type I is preferable for cooling applications as it has high water uptake at a low relative pressure (P/Po less than 0.3), which provides good cooling performance at evaporation temperature of less than 10$^{o}$C. CPO-27 Ni has type I isotherm since it shows maximum rapid water uptake at low relative pressure due to the irreversibility in adsorption of water molecules in the sites of the metal [64] (see Figure 2-7). While, for desalination application, the relative pressure has a wider range as types II, V, and IV, as well as type I, in which the low and high relative pressures can be used. Aluminum fumarate represents type V (S shape) as shown in Figure 2-7, where the desalination system becomes effective when the evaporation temperature is higher than 15$^{o}$C [65]. The performance of the cooling and desalination system is evaluated, based on the specific daily water production (SDWP), specific cooling power (SCP), and coefficient of performance (COP). The selection criteria of the adsorbent material for water adsorption applications can be summarized as follows:

A. The maximum water uptake that can be obtained at specific relative pressure/humidity at the equilibrium condition.

B. The kinetics: how fast the material can adsorb the water vapor until reaching the equilibrium condition.

C. The cyclic performance and stability, which is measured by maintaining a steady state of cyclic water uptake between the adsorption and desorption processes.

Burtch et al. [66] defined four different levels of stability: thermodynamic stability (exposure to the aqueous solution for a long time (at least 7 days exposed to pure water)), high kinetic stability (stable with high relative pressure), low kinetic stability (stable with low relative pressure) and unstable (the exposure to the humidity causes a loss in structural integrity). For example, it is reported that UIO-66-NH2 lost 38% of the water capacity after 40 cycles [14].

D. The scaling up production and cost of the adsorbent material.

E. The regeneration energy which mainly related to the isosteric heat of adsorption of the material.

MOF-841, MOF-801, and aluminum fumarate show high reversible water adsorption with isotherm of S shape, which resulted in moderate isosteric heat of adsorption. Therefore, these materials are considered good candidates for cooling and water desalination applications [16].

**Figure** 2-7 illustrates the water adsorption isotherms of different MOFs that were studied for water adsorption for cooling and water desalination applications. For cooling application, the required relative pressure (P/Po) is lower than 0.35 to produce cooling at low temperatures (less than 20$^{o}$C), while for water desalination application, the P/Po has a wider range as the evaporation temperature can be higher than 20$^{o}$C. As mentioned earlier, CPO-27 Ni has a very high water uptake at P/Po of only 0.1 which is around 0.4 $g_{H2O}/g_{Ads}$ as tested by Elsayed et al.[67]. It showed very good performance at an evaporation temperature of 5$^{o}$C. However, it requires a high regeneration temperature that exceeds 120$^{o}$C, making this material undesirable for cooling applications since it requires a high temperature. Youssef et al. [68] also tested this material but with an evaporator temperature of 25$^{o}$C, and they obtained a SCP of 228 W/kg. After increasing the evaporation temperature to 40$^{o}$C, they obtained a SDWP of 22.8 $L/kg_{ads}$/day at a desorption temperature of 95$^{o}$C. While with this range of evaporation temperature, the system cannot be considered for cooling application.

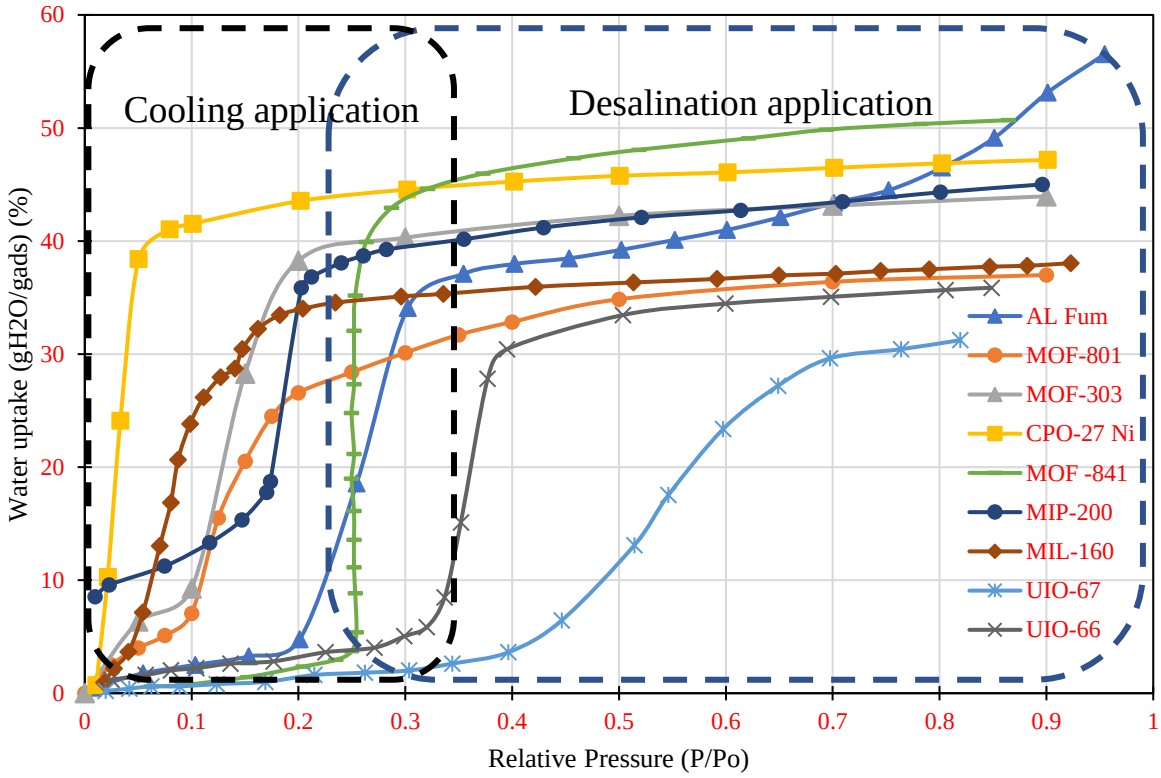



Figure 2-7. Recent water isotherms at different relative pressure at equilibrium conditions [56,67,69–71]

### 2.3.1. Enhancing the thermal conductivity

The adsorbent materials have low thermal conductivity and are considered insulating materials which require an effective heat exchanger, with more metal surfaces in contact with the adsorbent materials to effectively cool down/heat up the material during the adsorption/desorption process to overcome the low thermal conductivity. However, the metal mass should be restricted with the COP of the adsorption system since increasing the metal to adsorbent material mass ratio decreases the COP of the system. Therefore, enhancing the thermo-physical properties of MOFs to decrease the energy required for water desorption, enables maximum regeneration with minimal heat source temperature. Thus, finding ways to circumvent this intrinsic constraint is paramount to improving the temperature-actuated water sorption cycle efficiency. For example, creating composites of MOFs with excellent sorption characteristics and other materials with good heat transfer properties of having the potential of improving the adsorption system performance [72]. Several studies were carried out to enhance the thermal conductivity of the adsorbent materials by developing composites of such materials with

thermally conductive additives such as graphene oxide (GO) [73], few-layers of graphene (FLG) [74,75], functionalized carbon nanotubes (fCNT) [74], three-dimensional graphene (3dGR), expanded natural graphite (ENG) [76,77], and metal additives [78] as shown in Table 2-1. Many strategies have been developed to create the composite structure through different methods such as the synthesis process and the physical mixing. However, the reported studies usually have one or more of the following limitations; significant reduction in water uptake compared to the parent neat adsorbent materials, resulting in decreasing the performance of the adsorption systems as summarized in Table 2-1. Additionally, to the best of the author's knowledge, there was no reporting for a significant enhancement of the thermal conductivity in the composite structures with a maximum reported thermal conductivity of 1.6 W/m-K.

Table 2-1. Literature review on enhancing the thermal conductivity of adsorbent materials

| Ref | Adsorbent material (Parent) | Additives | additives weight percentage | Thermal conductivity of adsorbent material | Method | Thermal conductivity of composite | Limitations in study |
|---|---|---|---|---|---|---|---|
| [73] | MIL-101(Cr) | Graphene oxide (GrO) | 0.5 - 5% | 0.05 -0.1 W/m-K at 30 -200$^{o}$C | Synthesis process | A slight increase | GrO has relatively low thermal conductivity compared to other conductive materials - A significant reduction in water uptake if the additives weight percentage exceeds 2% - distortion of the crystal structure at 5% additives weight |
| | | | | | Physical mixing | 20-30% increase at 2%GrO and 250% increase at 5%GrO | |
| [78] | Silica gel | Aluminum, Copper, Brass, and Steel | 5 - 15% | 0.198 W/m-K | Physical mixing | 28% increase at 5%steel - 241% at 15%alumnuim | A negative impact on the chiller cooling capacity at a fin spacing ratio of lower than 1.2 |
| [79] | MOF-5 | Expanded natural graphite (ENG) | 5 - 10% | around 0.08 W/m-K at 25-55$^{o}$C | Physical mixing (uni-axial compression, custom die/compression geometry, layered microstructure fabrication | 2000% increase at 5%ENG using layered microstructure | Anisotropic microstructural in uni-axial compression - impact on the adsorption performance applications was not reported - more investigation needs to be clarified regarding the impact of the graphite on the water isotherms |
| [74] | Zeolite | Few-layer graphene (FLG), graphene oxide (GO), and functionalized carbon nanotubes (fCNT) | 3% | 0.27 - 0.37 W/m-K at density of 1.2 to 1.35 g/cm$^{3}$ | Physical mixing | 25% increase at 3%FLG | Negligible enhancement in thermal conductivity when GO and fCNTs were used -poor contact between fCNTs and zeolite - the impact of the composite on the water uptake at relative pressure higher than 0.2 was not reported |
| | Zeolite | three-dimensional graphene (3dGR) | - | 0.09- 0.3 W/m-K at density of 0.65 to 1.25 g/cm$^{3}$ | Physical mixing | 500% increase | Because of the high porosity of 3dGR, it has a relatively low thermal conductivity compared to the conductive material - synthesizing 3dGR needs more cost-effective procedures |
| [75] | MIL-101(Cr) | Few layers of graphene (FLG) | 5-25% | 0.1 W/m-K | Physical mixing (ball milling) | 650% and 1130% increase at 20 and 25%FLG respectively | Significant reduction in water uptake at relative pressure higher than 0.5 - Despite the high thermal conductivity of FLG, the physical mixing limits the enhancement of the thermal conductivity of the MOF composite |

## 2.4. Packing and coating the adsorbent materials

The vast majority of laboratory-scale adsorption systems developed by researchers and most commercially available systems use granular adsorbent material packed adsorber beds (GPAB) [78]. Until now, various attempts have been made in the literature to eliminate or reduce the heat and mass transfer limitations inside the GPAB. Li et al. [80] numerically investigated the effect of the spatial porosity distribution (stepwise and continuous polynomial distributions) of the GPAB on the adsorption process and cooling performance under the constant bed porosity case. Their findings revealed that an increase in the bed porosity from the cooling side to the steam side leads to a reduction in adsorption temperature hence, an enhancement in the adsorption uptake and the specific cooling power (SCP). Ellis et al. [81] performed a numerical study to optimize the geometrical parameters of an innovative star fin-type Fuji RD-type silica gel GPAB with metal additive. The authors pointed out that the adsorbent particle diameter and fin spacing have a great influence on SCP. Also, a 300 % enhancement in the SCP of the adsorption heat pump is observed by adding aluminum particles to the bed.

Recently, coating the heat exchanger surfaces with the adsorbent material which resulted in decreasing or removing the contact resistance between the adsorbent material and heat exchanger surfaces has been investigated and compared to packing the adsorbent material [13]. Thus, the coating can increase the SCP of the adsorption system as it provides a higher heat transfer rate through the coating layer. The coating layer thickness is very sensitive as it influences the vapor mass transfer resistance. Thus, a critical investigation should be carried out to obtain the optimum coating layer thickness that provides the optimum mass and heat transfer. Two strategies were developed to coat the adsorbent material namely using the binder agents or direct synthesis [82]. In direct synthesis, the adsorbent material is directly crystallized onto the heat exchanger surfaces, which can reduce the heat transfer resistance and cycle time of the adsorption/desorption process as the heat transfer at the interface between the heat exchanger surface and adsorbent material is high due to the very thin layer of the coating layer thickness [83]. However, with this coating process, the adsorption system performance might decrease due to the high metal-to-adsorbent mass ratio. Moreover, this technique has 100% of adsorbent material without using a binder agent. Thus, the coating layer is very brittle,

mechanically unstable, and difficult to achieve a homogenous and regular structure [84]. In binder-based coating, the adherent films with a reproducible and controllable thickness are easy to achieve. Compared to direct synthesis coating, this type of coating is simple since it has a simple process setup and conditions [82]. Thus, the binder agent strategy in the coating is preferable for developing adsorption systems. However, the binder agent reduces the water capacity of the adsorbent material as the binder agent can reach up to 25% of the coating layer mass, which decreases the performance of the adsorption system compared to the direct synthesis [85]. Table 2-2 summarizes research on the use of the coating in adsorption applications. It shows that the coated material surface can be stainless steel, graphitic support, aluminum sheet, and copper plates. In direct synthesis, the maximum coating layer thickness is only 310 µm, while it can be 690 µm when a binder agent is used.

Table 2-2. Literature review on using coating in the adsorption system

| References | Adsorbent type | Adsorbate pair | Coated surface (substrate) | Coating strategy | Coating thickness |
|---|---|---|---|---|---|
| [85] | Zeolite A and Zeolite X | water | Stainless steel plates | Direct synthesis | 38 and 230 µm |
| [86] | SAPO34 | water | Graphitic supports | Direct synthesis | 200, 210, and 310 µm |
| [87] | Aluminum fumarate | water | Aluminum sheet | Direct synthesis | 300 µm |
| [88] | SAPO-34 | water | Aluminum finned flat-tube heat exchanger | Binder agent (Silane 10%) | 100 µm |
| [89] | SAPO-34 | water | Aluminum sheet | Binder agent (Hydroxyethyl ether 5%) | 60-460 µm |
| [90] | Zeolite Y and SAPO-34 | water | Aluminum sheet | Binder agent (hydroxyethyl ether, 5-25%) | 102-290 µm |
| [91] | Silica gel | water | Copper plate | Binder agent (Polyvinylpyrrolidone (PVP)) | 200 – 690 µm |

## 2.5. Heat exchangers used in adsorber beds

The heat exchanger in the adsorber bed is a device that provides thermal contact for cooling or heating the adsorbent material during the adsorption and desorption process respectively. Several factors need to be considered in designing the heat exchanger. It was suggested that heat exchangers should have a high number of heat transfer units (NTU), minimum inert mass in the adsorber bed, and low Biot number to produce a good performance in adsorption systems [92]. A high ratio of the fluid channel radius to the thickness of the adsorbent and a low heat exchanger aspect ratio (ratio of the heat exchanger length to half of the heat exchanger width) is also reported to be specifications for a good heat exchanger design [93]. Low inert material alpha number, as well as the low fluid alpha number, are also observed for a good heat exchanger which can be defined as follows [94]: `

$$\alpha_{m-ads} = \frac{M_m Cp_m}{M_{ads} Cp_{ads}} \quad 2.6$$

$$\alpha_{f-ads} = \frac{M_f Cp_f}{M_{ads} Cp_{ads}} \quad 2.7$$

Where $\alpha_{m-ads}$ is the inert mass alpha number (heat capacitance ratio of thermal fluid to adsorbent mass) and $\alpha_{m-ads}$ is the fluid alpha number (heat capacitance ratio of bed inert mass to adsorbent mass).

The inert bed mass is the metal mass that can be calculated by multiplying the volume of the metal with the density. For example, if the metal is considered to be copper or aluminum, then the values of $M_m Cp_m$ for aluminum and copper are ($V_m\, \rho_m Cp_m = V_m \left(\frac{2700kg}{m3}\right)\left(\frac{910J}{kg*K}\right) = for\ alumnuim\ and\ V_m \left(\frac{8960kg}{m3}\right)\left(\frac{389J}{kg*K}\right)\ for\ copper$). The ratio of copper to aluminum $\left(\frac{\rho_{cu} Cp_{cu}}{\rho_{al} Cp_{al}}\right)$ is only 1.4 which can be compensated by the higher thermal conductivity of the copper over the aluminum of 1.6. Thus, the low weight of aluminum does not mean that it is always preferable over copper in heat exchanger design. On the other hand, copper is three times more expensive than aluminum.

Wang et al. [92] developed a plate-finned shell and tube heat exchanger as shown in Figure 2-8 that has a combined heat capacity ratio of the heat exchanger material and thermal fluid to adsorbent of 3.11,

which produced good adsorption system performance but can be reduced if oil is used as a thermal fluid [95].

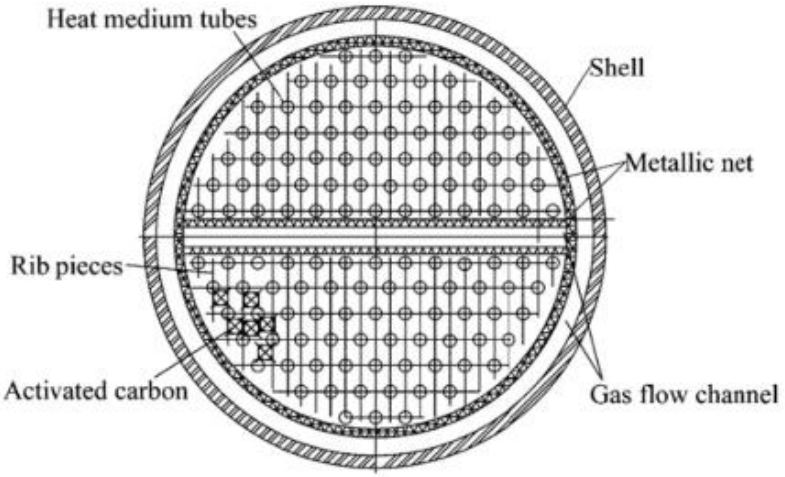



Figure 2-8. Plate-finned shell and tube in adsorber bed [96]

Critoph et al. [97] developed a similar heat exchanger which has multiple layers of 2mm monolithic carbon discs and 0.2mm of aluminum fins to enhance the heat transfer. However, this design has a drawback in that the penetration path for the vapor is insufficient to provide an effective mass transfer. Liu et al [98] introduced a vapor channel that is separated by wire gauze between two channels of adsorbent material to enhance the mass transfer and allow the vapor to flow freely as shown in Figure 2-9.

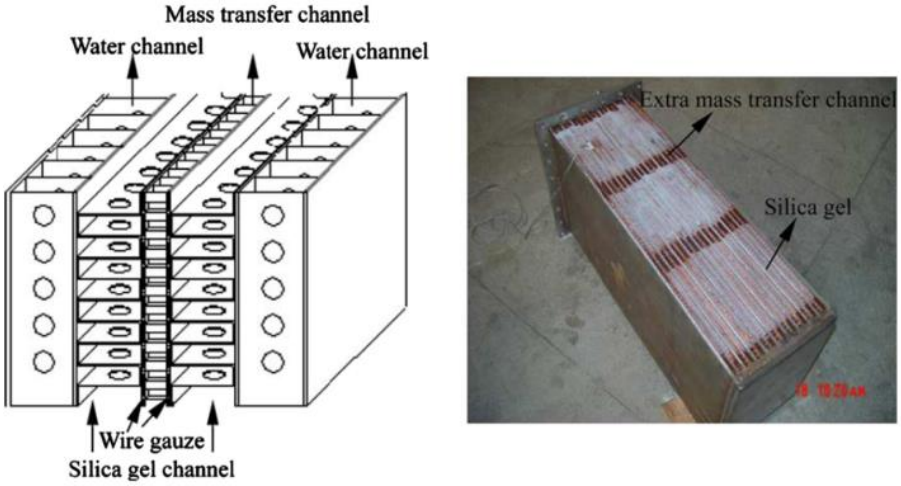



Figure 2-9. Plate-fin heat exchanger in adsorber bed [98]

Mohammed et al. [99] also developed a vapor channel/passage between two layers of adsorbent material that is in contact with metal plates in the form of a rectangular heat exchanger as shown in Figure 2-10. They concluded that this vapor channel is only needed if the adsorbent particle size is less than 0.5mm, while the channel can be removed with larger particle size.

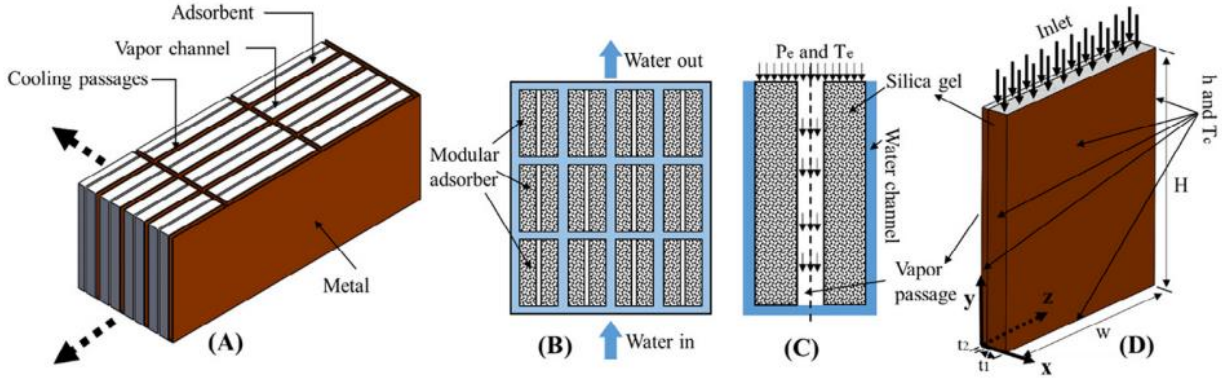



Figure 2-10. vapor channels in rectangular heat exchanger [99]

The low thermal conductivity of adsorbent materials is a critical issue that negatively affects the overall heat transfer performance of the heat exchangers used in the adsorber bed. Guilleminot et al. [100] developed a consolidated material consisting of metallic foam and zeolite to be used as an adsorbent with a better heat transfer. This design can reduce the heat exchanger size by 5-10 times compared to the conventional one. However, a significant reduction in the mass transfer is also observed as well as an increase in the cost [101]. These drawbacks are resolved by Restuccia et al. who proposed a new heat exchanger coated with a thin layer of zeolite that showed a remarkable improvement in the specific cooling power compared to the granular or powder adsorbent. However, a thin layer of coating requires a larger heat exchanger surface area which ultimately increases the overall size of the heat exchanger. An example of coating (coating thickness of 0.1mm) and packing a finned plated-tubes aluminum heat exchanger is shown in Figure 2-11. A very thin layer of coating provided an improvement in specific cooling power by 35% compared to the packing, while the coefficient of performance decreased by 40% as a result of using more heat exchanger surfaces [88].

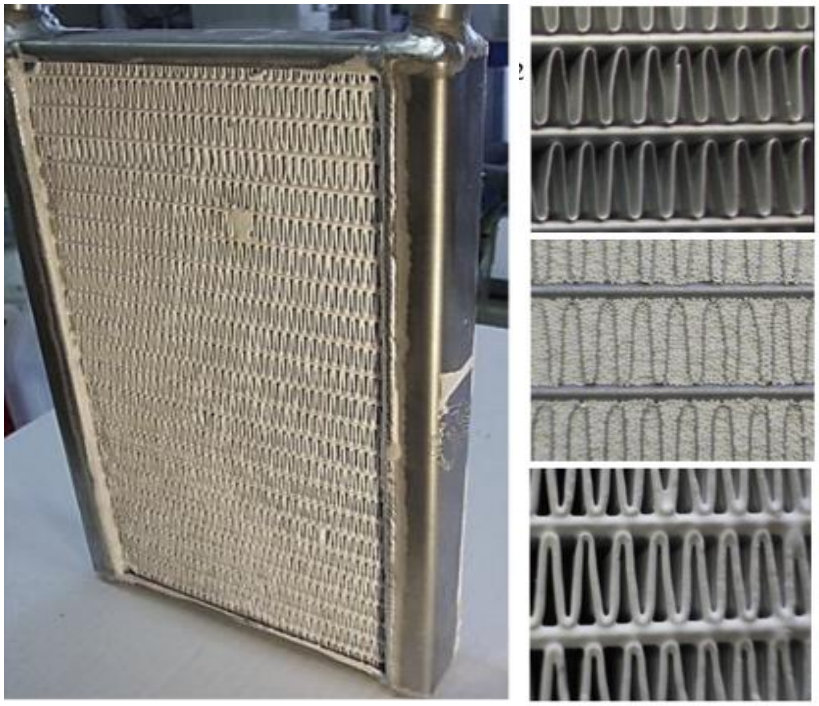


Figure 2-11. Packed and coated finned plated-tubes aluminum heat exchanger [88]

Mohammed et al. [102] developed nanoporous silica that has a high surface area with a large pore volume. The new silica is coated on ligaments of aluminum foam to be used as a heat exchanger in the adsorber bed as shown in Figure 2-12. The conventional silica RD is also used in this heat exchanger by packing instead of coating. The mass transfer is improved in this design and they observed that the new silica has better performance for desalination applications, while the conventional one is preferable in cooling applications.

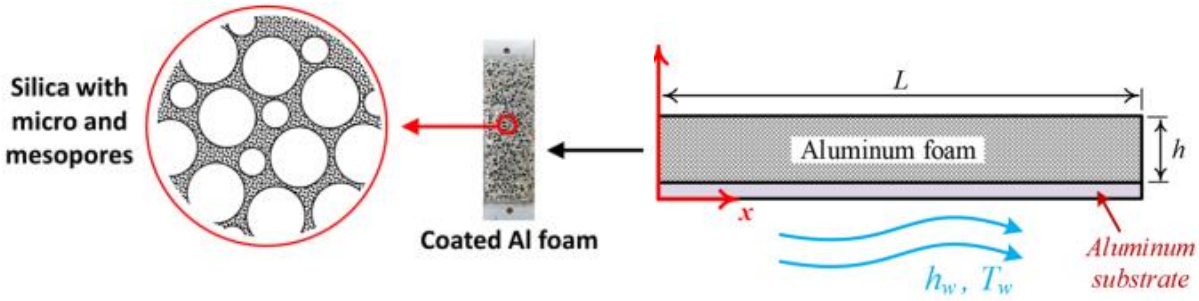



Figure 2-12. Aluminium foam heat exchanger [102]

## 2.6. Low Pressure (LP) Evaporator and Condenser

The evaporator is a critical component in the adsorption desalination or cooling system. Limited studies were carried out recently to investigate the optimum type of evaporator with a high heat transfer coefficient that can be operated under low saturation temperature and pressure, and can lead to a compact design of the adsorption system. Designing an effective and compact evaporator has been a challenge in recent years [12]. Low pressure (LP) evaporators are classified into three types; (i) falling film evaporators, (ii) capillary–assisted evaporators, and (iii) flooded (full, partially) evaporators.

### 2.6.1. Falling film evaporator

In falling film evaporator, the water (refrigerant) is sprayed over the outer surface of the tubes using nozzles and a circulation pump, where an equal distribution over the tube surfaces is essential to obtain the maximum boiling heat transfer coefficient. The main advantages of the falling film evaporator over the other types can be summarized as follows [103]:

- High heat transfer coefficient.
- Compact design because of high heat transfer coefficient.
- Requires short contact time between the surfaces and water droplets.
- Low probability to have salt sedimentation over the tube surfaces, which eases the cleaning of the tubes and prolong the life of the system.
- One-third reduction of working fluid requirements as compared with the flooded evaporator.

### 2.6.2. Flooded and Capillary-assisted Evaporators

Flooded evaporators are the simplest type of evaporator that operates on natural convection heat transfer. Thus, they have a low heat transfer coefficient and tend to be bulky. Over the last two decades, limited studies investigated the improvement of the flooded evaporator to increase its efficiency to be competitive with the falling film evaporator. The design of flooded evaporators is more challenging, compared to the design of flooded condensers. In the condensation process, the refrigerant accumulates at the outer of the shell, thus, the shell and tube heat exchanger is a preferred option for the condenser of the adsorption systems [44]. While in the LP flooded evaporator, the accumulation of the water in the shell creates a water column, which will increase the hydrostatic pressure in the evaporator. For

example, 10 cm of water column generates 0.98 kPa hydrostatic pressure, and if the saturation pressure in the shell is 2 kPa, the total pressure will increase to (0.98+2 = 2.98 kPa), which will increase the saturation temperature and the boiling point. The change in this temperature can sharply reduce the cooling power of the adsorption refrigeration system, which will lead to poor performance. The capillary-assisted evaporator is a novel solution to overcome the hydrostatic pressure effect in the flooded evaporator. This evaporator also utilizes the advantage of uniform fluid film distribution along the tube surfaces which will significantly enhance the overall heat transfer coefficient value to a higher value than that of the falling film evaporator [103]. Table 2-3 summarizes different low-pressure evaporators reported in the literature for application in adsorption systems. It shows that the overall heat transfer coefficient of some capillary-assisted evaporators is higher than the falling film one.

Table 2-3. Literature review in experimental works using different low-pressure evaporator design

| References | Evaporator Type | Tubes Geometry | Pipes material and refrigerant type | Adsorbent/adsorbate pair | Thermal fluid | Operating conditions | | Max Overall heat transfer coefficient W/(m2 .K) | Chilled water flow rate | Application | Studied parameter |
|---|---|---|---|---|---|---|---|---|---|---|---|
| | | | | | | Temperature | Pressure | | | | |
| [104] | Capillary-assisted on the outer surface of the tube | Outer diameter: 18 mm | Copper | NA/ water | Water | 5C and 15C | NA | 5000 | NA | the form of gravity heat pipe | dimensionless liquid level, superheating temperature, evaporating pressure, shape parameter (the ratio of the groove's depth to the width) |
| [105] | serpentine of horizontal tubes | Outer diameter: 12.7mm | stainless steel | LiBr/water | Water | NA | 1 KPa | NA | 0.046 kg/s | air-cooled absorption chiller of 2 kW for air-conditioning | pressure, flow rate, chilled water temperature |
| [106] | Falling film (Turbo-CAB (19 fpi and 26 fpi), Korodense, and smooth tubes) | Outer diameter: 15mm | Copper | NA/ water | Water | 11–18C | 0.85-1.15 Kpa | 3500 | 16.7 L/min | Three liquid circuits (falling film, heating water, and condensing water circuits) | tube type, chilled water temperature, evaporation pressure |
| [107] | capillary-assisted tubes and Plain tubes (Flooded evaporator) | Outer diameter: 19.05m, fins height: 1.47-0.5 mm | Copper Alloys C12200, water | NA/ water | water | 10–20C | 0.5–0.8 kPa | 1613 (Capillary assisted tube), 308 (Plain tube) | 2.4-2.7 Kg/min | adsorption cooling systems (By using only vacuum pump to activate the system) | capillary geometry, water height, chilled water flow rate |
| [108] | Capillary-assisted on the outer surface of the tube | Outer diameter: 18.8mm, 15mm | Copper | NA/ water | Water | 5-20 C | 8.7 - 23.4 mbar | 500 (uncoated plain tube), 3500 (uncoated finned tube), 4100 (Coated plain tube), 5500 (Coated fined tube) | 16 L/min | adsorption cooling systems (By using only a vacuum pump to activate the system) | filling level, chilled water temperature |
| [103] | Falling Film evaporator | Outer diameter: 16 mm | stainless steel | Silica gel/ water | water | 10 - 40 C | 0.93–3.60 kPa | 1025.45 | 48 L/min | Adsorption desalination | salt concentration, chilled water temperature, |

## 2.7. Review of mathematical modelling

Yong et al. [109] and Teng et al. [110] classified the mathematical models developed for simulating adsorption systems into three groups; (i) thermodynamic models, (ii) lumped parameters models, and (iii) heat and mass transfer models.

### 2.7.1. The thermodynamic model

Thermodynamic models are based on the first and second laws of thermodynamics while heat transfer is not considered in the equation. The first law is used to predict the performance of the cycle, while the second law describes the quality of the adsorption process [95]. To describe the adsorption heat pump/cooling/desalination cycle from a thermodynamic perspective, COP is used to describe the energetic efficiency defined as the useful output energy divided by the energy input [111,112]. For heating and cooling, the COP is calculated as follows:

$$COP_H = \frac{(Q_{con} + Q_{ads})}{Q_{des}} \quad 2.8$$

$$COP_C = \frac{(Q_{ev})}{Q_{des}} \quad 2.9$$

Where $COP_H$ is for heating and $COP_C$ is for cooling.

The evaporation energy ($Q_{ev}$) and the released energy from the condenser are calculated based on the enthalpy of the evaporation as shown in the following equations:

$$Q_{ev} = \frac{\Delta H_{vap}(T_{ev})\rho_{liq}M_{ads}\Delta W}{M_w} \quad 2.10$$

$$Q_{con} = \frac{\Delta H_{vap}H(T_{con})\rho_{liq}M_{ads}\Delta W}{M_w} \quad 2.11$$

Where $\Delta W$ is the working fluid capacity and $\Delta H_{vap}$ is the enthalpy of evaporation.

The $Q_{ev}$ can be considered identical with $Q_{con}$ since the difference between the condenser and evaporator temperatures is limited.. The regeneration energy ($Q_{des}$) is also similar to the adsorption energy ($Q_{ads}$). As the enthalpy of adsorption/desorption should be larger in magnitude than the enthalpy of evaporation/condensation, the $COP_H$ has a range between 1 to 2, while the $COP_C$ is always

lower than 1. The COP values can also be increased if multiple adsorber beds are used so that the part of the energy released from one bed can be used to regenerate another adsorber bed [53,54].

Gui and Wang[115] developed a thermodynamic model to investigate the COP of a practical three heat reservoirs models for air conditioning application and compared the model results with experimental values showing good agreement. Thu et al.[116] studied the adsorption cooling system using an entropy generation framework to investigate the heat dissipation losses in the cycle with a heat source temperature between 60 to 85°C. The model also included details of the evaporator such as the vapor mass transfer in the evaporator, the de-superheating of condensate from the condenser, flushing of chilled water through the evaporator tubes, and heat transfer to the chilled water. Critoph [117] developed a thermodynamic model using the following assumptions;(i) at the end of the adsorption cycle, the temperature is equal to the condenser temperature, (ii) the specific heat of the liquid is equal to 0.2% of the latent heat, (ii) constant heat sink and source temperatures and (iii) the specific heat of the refrigerant is assumed to be in the liquid phase, then the required sensible heat in desorption/heating process was considered to be equal to the required heating energy for the adsorbent material until reaching to the final temperature during the desorption process. To summarize the thermodynamic models, they are based on simple algebraic equations in steady state conditions using specific assumptions that make the system close to be ideal. On the other hand, it can provide a good prediction of the performance of the system with a rough estimation of the system quality.

### 2.7.2. Lumped parameter models

In lumped parameter models, the following assumptions are considered; (i) a uniform temperature in adsorbent material, (ii) the adsorbate is uniformly adsorbed, and (iii) thermodynamic equilibrium between different phases [109]. The first lumped model was developed by Sakoda and Sucuki which consists of one packed bed with silica gel, an evaporator and a condenser to study the performance of solar powered adsorption system [118]. The conservation of mass and energy equations in this model is written as follows:

$$\boldsymbol{M_{ads}\frac{dW}{\partial t}+\frac{dM_a}{\partial t}=0} \qquad 2.12$$

$$\boldsymbol{M_{ads}Cp_{ads}\frac{dT_s}{\partial t} = \pm M_{ads}Q_{ads}\frac{dW}{\partial t} - A_sU(T_s - T_f) + A_sQ} \quad 2.13$$

Where $M_{ads}$ is the adsorbent mass, $\frac{\partial W}{\partial t}$ is the rate of uptake, $M_a$is the adsorbate mass, $Q_{ads}$is the isosteric heat of adsorption, $T_s$ is the bed temperature, $A_s$ is the surface area of the heat exchanger, $U$ is the overall heat transfer coefficient, $T_f$ is the thermal fluid temperature (or atmospheric temperature) and $Q$ is the heat flux by radiation.

Cho and Kim [119] enhanced the lumped model by adding the sensible heat of the adsorbate, and the energy equation was modified as follows:

$$\begin{aligned}(\boldsymbol{M_{ads}Cp_{ads} + WM_{ads}Cp_a + M_{HX}Cp_{HX}})\frac{\boldsymbol{dT_s}}{\boldsymbol{\partial t}} = \\ \boldsymbol{\pm M_{ads}Q_{ads}\frac{dW}{\partial t} - E\dot{m}_fCp_f(T_s - T_f) + M_{ads}Cp_v(T_{eva} - T_s)}\end{aligned} \quad 2.14$$

Where $Cp_a$ is the specific heat of adsorbate, $M_{HX}$ is the heat exchanger mass, $Cp_{HX}$ is the specific heat of the heat exchanger, $E$ is the heat exchanger effectiveness, $Cp_f$ is the specific heat of the thermal fluid, $\dot{m}_f$ is the mass flow rate of the thermal fluid, and the last term on the right side of the equation is the sensible heat of adsorbate from the evaporator.

Cacciola et al. [120] applied the above lumped model for a two-bed system and they added a heat recovery scheme to the energy equation. Then, Sami and Tribes [121] modified the energy equation by including the thermal effect due to the adsorbate flow from the evaporator to the adsorber bed and compared the modeling results of the COP with experimental values showing good agreement (0.68 (simulation), 0.67$\pm$ 0.05 (experiment)).

Rezk and Al-Dadah [122] developed an empirical lumped parameter model to study a two-bed adsorption system incorporating a heat and mass transfer recovery scheme using Silica gel water. This model predicted the performance with an acceptable deviation, and they used the model to study the effect of the fin configurations of the packed heat exchanger on the adsorption system cooling and to identify the optimum half-cycle time. Basdanis et al.[123] modelled a solar-driven single-stage dual-bed adsorption cooling system using lumped parameter model with algebraic expression to investigate

the half cycle time that provides the maximum cooling power. This model was validated by Koronaki et al. [124] model who also developed a lumped parameter model to study the same system to investigate the effect of the solar collector type in the eastern Mediterranean area on the cooling power of the adsorption system and overall efficiency. Youssef et al. [68] applied the lumped parameter model in an adsorber bed to study the effect of the adsorption, desorption and evaporator water temperatures on water and cooling production of the adsorption system using Aluminium Fumarate, Silica gel and AQSOA-Z02 adsorbents. Their results showed that Aluminium Fumarate outperformed other adsorbents except at low evaporator temperature (10°C) and high desorption temperature (85°C). Elsayed et al. [25] used the same lumped parameter modelling method to investigate the adsorption system using MIL-101(Cr)/graphene oxide composites adsorbent. To summarize the lumped parameter models, transient ordinary differential equations are used to express the mass and energy equations. This model has a limitation to investigate the geometrical design of the adsorber bed in which the model cannot identify the best performance of the heat exchanger design (such as a rectangular and circular finned tube, wire finned tube and microchannel) in the bed. Chua et al. [125] upgraded the lumped parameter model to provide different temperatures in every discrete element of a finned tube in the adsorber bed and came up with the following energy equation:

$$(\boldsymbol{M_{ads}Cp_{ads} + M_{HX}Cp_{HX}})\frac{\boldsymbol{dT_{bed}}}{\boldsymbol{\partial t}} + \boldsymbol{WM_{ads}}\frac{\boldsymbol{dh_{ads}}}{\boldsymbol{\partial t}} =$$

$$\boldsymbol{M_{ads}}\frac{\boldsymbol{dW}}{\boldsymbol{\partial t}}\{\boldsymbol{\delta}[\boldsymbol{h_g(T_{eva})} - \boldsymbol{h_g(P_{eva}, T_{eva})} + \boldsymbol{Q_{ads}}] + (\boldsymbol{1-\delta})\boldsymbol{Q_{ads}}\} \qquad 2.15$$

$$- \boldsymbol{U_{cooling}}\frac{\boldsymbol{A_{bed}}}{\boldsymbol{N}}\sum_{\boldsymbol{i=1}}^{\boldsymbol{N}}(\boldsymbol{T_{bed} - T_i})$$

Where $h_{ads}$ is the partial enthalpy of adsorbate/refrigerant, $h_g$ is the specific enthalpy of vapor, $\delta$ is equal to 1 or 0 in the adsorption or desorption process, $U_{cooling}$ is the overall heat transfer coefficient of the adsorber bed and N is the number of discrete elements of the finned tube heat exchanger.

### 2.7.3. The heat and mass transfer model

All the above discussed models assume thermodynamic equilibrium conditions, which can be divided into thermal equilibrium and mass equilibrium. In local thermal equilibrium condition, the

temperatures of the vapor and adsorbent material are identical, while in the mass equilibrium condition, there is no mass transfer resistance between the vapor and adsorbent material. Thus, the amount of adsorbed vapor is directly related to the vapor pressure and adsorbent material temperature using the adsorption equilibrium equation. The local thermal equilibrium is no longer valid if the following exist: the adsorbent particles and voids are not small enough, significant heat generation in the process and a significant variation in the thermal properties or the convective term is critical [126]. In heat and mass transfer modelling, the heat and mass content is not only changing with time, they are also variable with space. Therefore, all the governing equations in this type of model are partial differential equations. The complexity of the model depends on the geometry of the heat exchanger of the adsorber bed (one [93,127], two [10,11,29], or three-dimensional [129] model), the assumptions made, the design of the modelled system and the numerical solution method used. This model is generally based on four equations; mass (continuity) conservation equation, energy balance equation, momentum equation and kinetic and isotherm equation of the adsorbent-adsorbate. The challenge in solving this type of equation is their nonlinearity and the variable initial and boundary conditions of the system if the model is used to simulate the adsorption, desorption and switching cycle (cyclic condition). The choice of the method of the solution depends on how complex the geometry of the heat exchanger used in the system. For example, if the heat exchanger geometry is simple and has a limited number of grids, the segregated solution approach is the most suitable method where the partial differential equations are solved separately and sequentially leading to low computational cost and number of iterations. The iterations are divided into inner and outer (Picard) iterations in order to minimize the error obtained from the nonlinearity of the equations [130]. Albaik et al. [65] used the segregated solution approach for modelling two-dimensional finned tube heat exchanger packed and coated with Aluminium Fumarate to conduct a parametric study of the fins configurations to obtain the best design that given the optimum performance in terms of the specific cooling power (SCP) and specific daily water production (SDWP). The model was validated with experimental results with good agreement. However, this method is limited if the complexity of the geometry and the computational domain size increases. In such case the coupled solution approach in which all the partial differential equations are solved simultaneously thus reducing the computational cost. Solving the equations of the adsorption system in the heat and mass

transfer model is classified into three methods; (i) finite volume method [33,34], (ii) finite difference method [132–134] and (iii) finite element method [135]. The finite difference is the simplest method to solve the parabolic equations and it is a powerful tool to handle the variation in the initial and boundary conditions of cyclic operation. The assumptions of the heat and mass transfer model are classified based on the thermophysical properties, heating source, evaporator and condenser, thermodynamic state and heat and mass transfer [109]. Part of the modelling using this approach ignores the mass transfer in the equation, which mean that the pressure through the adsorbent material is uniform. Sun et al.[114] developed a two-dimensional numerical model of the adsorption heat pump with a thermal wave heat regeneration assuming that the pressure is uniform. They observed that using this assumption is reasonable for high-pressure adsorbates such as ammonia. Guilleminot et al. [136] adopted using the uniform pressure approach to study the heat transfer in a finned reactor of a rectangular cross-section. The model is experimentally validated by neglecting the mass diffusion resistance, while the heat diffusion is considered through the heat conductivity of the adsorber bed and the heat transfer coefficient between the adsorber bed and fins.

The performance of the heat exchanger of the adsorber bed is affected negatively by the limitations in the mass and heat transfer due to the internal (intraparticle) and external (interparticle) mass transfer resistance and low thermal conductivity of adsorbent material. The uniform pressure assumption through the adsorbent is one of the external mass transfer resistance assumptions. If the pressure is variable, then the vapor flow velocity and pressure can be described using the Darcy law [137]. Another technique in expressing the vapor flow through the adsorbent voids is Ergun equations to describe the superficial velocity to include the inertial effects [138]. In internal mass transfer resistance, the linear driving force (LDF) model is the most popular model due to its simplicity and accuracy which assumes that the concentration profile is parabolic within the particle. The solid diffusion (SD) [127] model is also another approach for the internal mass transfer resistance expression obtained from Fick's law.

To sum up, several models with different assumptions were extensively investigated which mainly depend on the purpose of the study. The heat and mass transfer model including the internal and

external mass transfer resistances in two and three-dimensional geometries is the most complicated model due to its high degree of non-linearity of the partial differential equations especially when the model requires a huge computational domain to solve. There are several studies where this type of model is used to study the geometrical design of the heat exchanger in the adsorber bed. However, most of these studies focus only on a very limited computational domain in the heat exchanger ignoring the effect of studying the larger domain of the adsorber bed including the inlet/outlet vapor to the bed and the vapor domain of the bed. Additionally, there is a crucial significance of investigating the vapor domain in the adsorber bed with an extended computational domain in the packed finned tube heat exchanger to investigate the best pipe configuration when the pipe length is extended, so parallel and series pipe connections will be a major aspect that needs to be considered when adsorber bed has several of heat exchanger modules. Moreover, most of the mentioned studies only simulated half of the cycle to study the temperature, pressure and water uptake in adsorbent material which is insufficient to study the adsorption process as a system rather than as a piece of packed or coated heat exchanger pipe without considering the other component of the system such as the effect of the evaporator and condenser.

Table 2-4 summarizes the literature review of using the lumped parameter and heat and mass transfer models for the simulation of the adsorption system. It is observed that most of the studies assumed a thermal equilibrium between the solid adsorbent and adsorbate (fluid) in solving the energy equations regardless of the geometry of the heat exchanger in the adsorber bed, while Darcy's law is used to express the external mass transfer resistance (pressure drop).

Table 2-4. Literature review in adsorption modelling

| References | Heat exchanger type | Adsorbent type | Adsorbate pair | The adsorbent filling method in the heat exchanger | Dimension | Energy equation Temperature assumption | Internal mass transfer equation | External Mass Transfer Resistance Model | Method of solution | Software | Studied parameters | Validation |
|---|---|---|---|---|---|---|---|---|---|---|---|---|
| [139] | 12 radial fined tube (thermal fluid inside the tube) | Zeolite 13x | water | Packed | 3D | local thermal non-equilibrium model | LDF | Darcy's law | (alternating direction implicit), Finite volume method, Coupled heat and mass transfer model | NA | Cycle time | Validated experimentally (10.71% error in Qin, 13.2% in COP ) |
| [93] | Annular tubes (thermal fluid inside the tubes) | Silica gel | water | Packed | 2D | thermal equilibrium between solid and fluid | LDF | Uniform pressure | Finite difference scheme, alternating direction im-plicit (ADI) method | computer programming | The number of transfer units (NTU), Bed Biot number (Bi ), Heat exchanger thickness ratio (Hr), Aspect ratio (Ar) | Not validated |
| [127] | Annular tubes (vapour inside the tubes) | Monolithic Carbon | Ammonia | Packed | 1D | thermal equilibrium between solid and fluid | LDF, Equilibrium and Solid diffusion | Uniform pressure | DASSL intergration algorithm | NA | Diffusion coefficient to particle radius ratio | Not validated |
| [140] | glass and metal tube adsorber | Activated carbon | methanol | Packed | 2D | local thermal non-equilibrium model | Sakoda and Suzuki equation | Darcy's law | finite-difference approximation, line-by-line iterative method, three-diagonal matrix inversions algorithm | NA | cycle time, circumferential positions, solar insolation effect | (experimentally validated) |

| | | | | | | | | | | | | |
|---|---|---|---|---|---|---|---|---|---|---|---|---|
| [42] | cylindrical adsorbent bed (Vapor inside the cylinder) | Activated carbon, monolith activated carbon | methanol and ammonia | Packed | 1D | thermal equilibrium between solid and fluid | LDF | Darcy's law | finite volume method, implicit scheme, Coupled heat and mass transfer model | NA | Thermal conductivity, density ratio, heat transfer rate, Darcy number, dimensionless pressure difference | HT model is not valid and the use of the HMT model is mandatory (numerically validated) |
| [141] | cylindrical adsorbent bed (thermal fluid inside the tube) | zeolite NaX | water | Packed | 2D | thermal equilibrium between solid and fluid | LDF | Darcy's law | finite volume method, implicit method, Tri-Diagonal Matrix Algorithm (TDMA) | computer programming | NA | Not validated |
| [142] | cylindrical adsorbent bed (vapour inside the tube) | Activated carbon | Ammonia | Packed | 1D | thermal equilibrium between solid and fluid | LDF | Uniform pressure | finite differences technique, Tri-Diagonal Matrix Algorithm (TDMA) | FORTRAN (Coding) | mass flow rate, different storage tank volume, bed thickness, heat source temperature | validated in the isosteric heating phase, not valid for full cycle (experimentally) |
| [143] | fined(square and annular) tube (thermal fluid inside the tube) | Silica gel | water | Packed | 3D | thermal equilibrium between solid and fluid | LDF | Darcy's law | finite control volume method, alternating direction implicit method and tri diagonal matrix solver algorithm | NA | fins type, contact resistance effect | (experimentally validated) |
| [11] | annular fined tube (thermal fluid inside the tube) | Silica gel | water | Packed | 2D | thermal equilibrium between solid and fluid | LDF | Eurgen's equation | finite volume method, The alternating direction implicit (ADI) method and tri-diagonal matrix algorithm (TDMA) | NA | fins hegiht, fins number, cycle time, particle diameter | (experimentally validated) |

| | | | | | | | | | | | | |
|---|---|---|---|---|---|---|---|---|---|---|---|---|
| [131] | Annular tubes (thermal fluid inside the tubes) | Silica gel | water | Packed | 2D | local thermal non-equilibrium model | LDF | Darcy's law | Finite difference scheme, alternating direction im-plicit (ADI) method, (Thomas algorithm). | Matlab | Adsorbent bed length, bed thickness, convective heat transfer coefficient, material conductivity, | Not validated |
| [132] | annular fined tube (thermal fluid inside the tube) | composite sorbent SWS-1L | water | Packed | 3D | local thermal non-equilibrium model | LDF | Darcy's law | finite volume method, The alternating direction implicit (ADI) method and tri-diagonal matrix algorithm (TDMA) | NA | fin height for different fins spaces | (experimentally validated) |
| [78] | annular fined tube (thermal fluid inside the tube) | Silica gel | water | Packed | 0D | thermal equilibrium between solid and fluid | LDF | Uniform pressure | analytical solution (No differentail equations) | NA | fins spacing ratio, metal tube material | (experimentally validated) |
| [144] | Honeycomb Adsorption Bed | Silica gel | water | Packed | 3D | thermal equilibrium between solid and fluid | LDF | Darcy's law | Finite element method | COMSOL | honeycomb cell height, cell size, cooling water flow rates | Not validated |
| [128] | Annular tube (thermal fluid inside the tubes) | Silica gel | water | Packed | 2D | local thermal non-equilibrium model | LDF | Darcy's law | finite differences technique, The alternating direction implicit (ADI) method ,Tri-Diagonal Matrix Algorithm (TDMA) | NA | evaporator pressure, cooling source temperature, driving heat source temperature, condenser pressure | Not validated |

| | | | | | | | | | | | | |
|---|---|---|---|---|---|---|---|---|---|---|---|---|
| [10] | finless and finned tube-type adsorbent bed (thermal fluid inside the tube) | Silica gel | water | Packed | 2D | thermal equilibrium between solid and fluid | LDF | Darcy's law | Finite element method | COMSOL | base fin configuration, fins with larger thickness, fins with larger radius, fins closer to each other | (experimentally validated) (Max temperature difference 4.5K |
| [145] | WireWound Finned Tubes and Aluminium flat finned heat exchanger | Silica gel | water | Packed | 3D | NA | NA | NA | Finite element mehtod | CFD | NA | (experimentally validated) |
| [133] | flat-tube adsorbers | Silica gel | water | Packed | 0D | Lumped parameters (thermal equilibrium between solid and fluid) | LDF | Uniform pressure | Analytical solution (No differential equations) | NA | Cooling water temperature, fin spacing | (experimentally validated) |
| [99] | two layers of packed beads separated by vapor passage | Silica gel | water | Packed | 3D | local thermal non-equilibrium model. | LDF | Darcy–Brinkman equation | The continuity, momentum, and energy equations are coupled, using the finite volume technique, The standard SIMPLE algorithm | FORTRAN (Coding) | effective solid thermal conductivity, adsorbent thickness, particle diameter, vapor channel passage, bed height | (experimentally validated) maximum temperature error of 0.5% K |
| [146] | annular fined tube (thermal fluid inside the tube) | Activated carbon | ethanol | Packed | 2D | thermal equilibrium between solid and fluid | LDF | Applying the momentum equation (including the Darcy' law) | Finite element method | Fluent coupled model | Adsorbent thickness, heat of adsorption effect | (experimentally validated) |

| | | | | | | | | | | | | |
|---|---|---|---|---|---|---|---|---|---|---|---|---|
| [147] | trapezoidal aluminum finned flat-tube heat exchanger | composite sorbent SWS-1L | water | Packed | 3D | thermal equilibrium between solid and fluid | LDF | Darcy's law | finite volume method, The alternating direction implicit (ADI) method and tri-diagonal matrix algorithm (TDMA) | FORTRAN (Coding) | fins pitch , fins height, cycle time, bed length | (experimentally validated) (10% error in uptake curve) |
| [148] | annular and longitudinal finned tube (thermal fluid inside the tube) | zeolite-13x | water | Packed | 3D | local thermal non-equilibrium model | LDF | Darcy's law | finite volume method, The alternating direction implicit (ADI) method and tri-diagonal matrix algorithm (TDMA) | FORTRAN (Coding) | fins height and fins spacing | (experimentally validated) (17% difference) |
| [135] | annular fined tube (thermal fluid inside the tube) | Silica gel | water | Packed | 2D | thermal equilibrium between solid and fluid | LDF | Darcy's law | Finite element mehtod | COMSOL | cycle time, ratio between desorption and adsorption times, fins geometrical parameters | (experimentally validated) |
| [129] | Wire fin heat exchanger, rectangular finned, microchannel heat exchanger | aluminum fumarate | water | Packed | 3D | thermal equilibrium between solid and fluid (same temperature between adsorbent and gas) | LDF | Darcy's law | Finite element mehtod | COMSOL | fins height, wire fin spacing, tube diameter | (experimentally validated) |

## 2.8. Integration of the adsorption systems with different system for different applications

### 2.8.1. Solar driven multigeneration integrated systems

The adsorption cooling and desalination system is a thermally driven one in which heat is required to regenerate the adsorbent material during the desorption process. Solar energy is a renewable energy source that can be used to drive the adsorption system. The solar energy system can heat up the thermal fluid that passes through the heat exchangers of the adsorber bed, thus heating the adsorbent material. Many researchers have developed different solar systems which can be classified into; solar thermal energy, photovoltaic (PV) and combined photovoltaic thermal systems (PVT) [149]. In solar thermal energy, the solar radiation is converted to thermal energy only by using different solar collectors such as flat plates, parabolic troughs and evacuated tubes [150]. Solar thermal energy systems can be integrated with the adsorption system to provide the thermal energy required for the desorption process. In PVT systems, the generated heat besides the electrical power can be extracted by feeding cooling water to the cells. However, the extracted heat has a low temperature (less than 50$^{o}$C) which is insufficient to regenerate the adsorbent material during the desorption process.

Concentrated photovoltaics thermal (CPV/T) systems use multi-junction solar cells (MJSCs) receiving highly concentrated solar radiation via an optical element, thus producing electricity and thermal energy at a temperature suitable to drive the adsorption system [151]. The CPV/T has higher energy conversion efficiency compared with conventional PV due to intensifying the solar direct normal irradiance onto small multi-junction PV cells. Consequently, the CPV system requires an efficient cooling system using passive or active techniques, which has inspired many innovative investigations to integrate with a thermally driven system [152]. The design of such CPV/T systems should consider the operating temperature limit and the cost of the PV cell offered by manufacturers for different applications [153]. The produced thermal energy with a temperature of higher than 70$^{o}$C can be used to power the adsorption system for water desalination, heating and cooling products. Such solar-driven multi-generation system is primarily proposed to increase the overall energy conversion efficiency and

produce more than one useful output by integrating two or three subsystems. For instance, the overall measured efficiency for a CPV/T system was higher than 60% [154].

### 2.8.2. Integration of adsorption system with Organic Rankine Cycle

Since the adsorption system can be driven using low-grade thermal energy, it can also be integrated with another power generation system that is driven by thermal energy. The organic Rankine Cycle (ORC) is a cycle that uses thermal energy at a lower temperature (less than 100$^{o}$C) compared to the conventional Rankine Cycle to produce electricity. ORC utilizes an organic fluid such as n-pentane, butane, R134a, R290, and R245fa that can boil at low temperature compared to water [155]. However, the thermodynamic efficiency of the standard ORC is lower than the conventional one (less than 20%) as a result of working at lower temperatures. The ORC cycle consists mainly of an evaporator, condenser, pump and turbine/expander. The working fluid in the liquid phase is pressurized using a pump followed by heating the fluid in the evaporator to superheated vapor. Then, expansion (pressure drop) occurs in the turbine/expander to generate power. Finally, the fluid will be condensed and converted to liquid at constant pressure in the condenser. Several integrated adsorption-ORC systems with different configurations are studied in the literature to form a multigeneration system [156–159]. As both systems require a thermal energy source, this energy is fed to the evaporator of the ORC first, then the outlet will be used as an inlet to the adsorber bed for the regeneration process as shown in Figure 2-13, which represents one of the integrated system configurations.

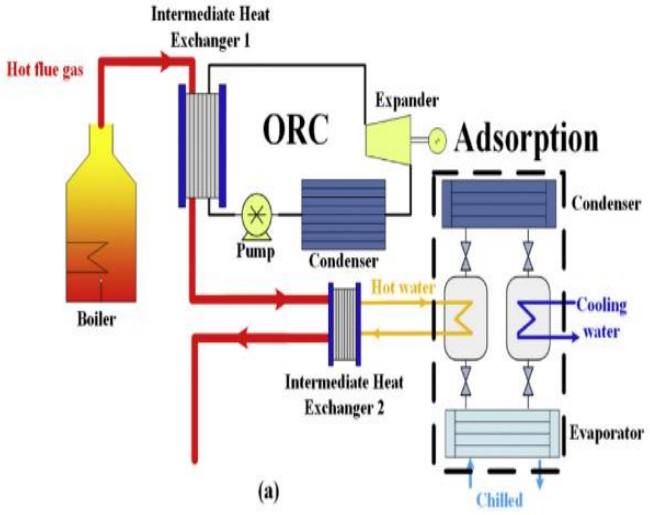



Figure 2-13. The 1st configuration of the Integrated ORC-Adsorption systems [156]

The 2nd configuration is to connect the thermal energy source to the evaporator of the ORC only, while feeding the thermal energy to the adsorber bed from the outlet water of the condenser of the ORC. This configuration has lower thermodynamic efficiency due to the high temperature in the condenser and low expansion ratio in the expander as shown in Figure 2-14.

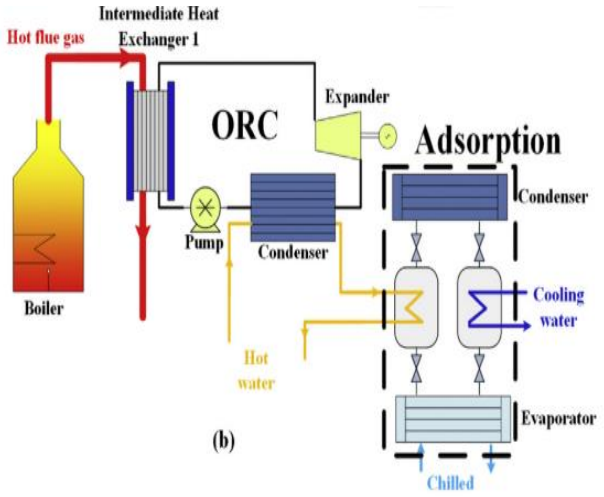



Figure 2-14. The 2nd configuration of the Integrated ORC-Adsorption systems [156]

In the third configuration, the heat supplied to the adsorber bed is extracted from the working fluid between the two expanders instead of the condenser, which allows increasing in the expansion ratio in the ORC expander to achieve higher thermal efficiency as shown in Figure 2-15.

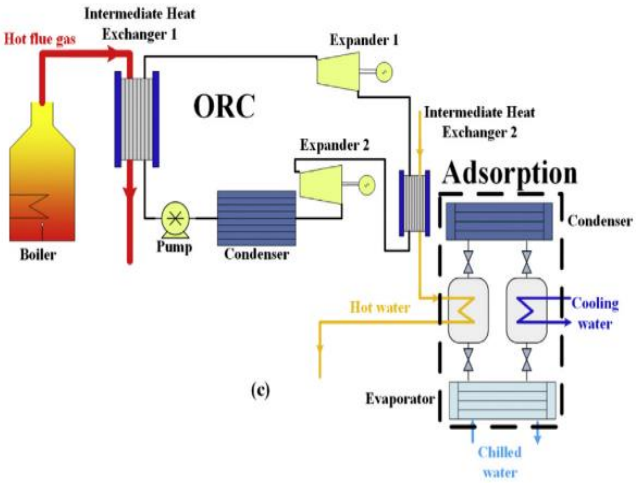



Figure 2-15. The 3rd configuration of the Integrated ORC-Adsorption systems [156]

In the 4th configuration, the heat supply for the evaporator of the ORC and the adsorber bed is the same as the 1st configuration, while the ORC condenser has a lower temperature as it utilizes the cooling effect of the adsorption system evaporator as shown in Figure 2-16.

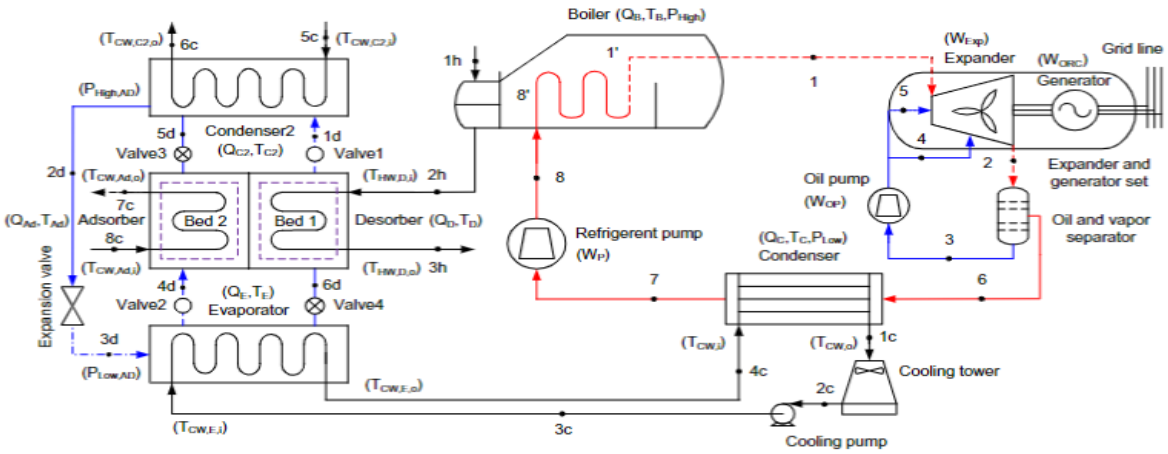



Figure 2-16. The 4th configuration of the Integrated ORC-Adsorption systems [158]

This configuration increased the ORC efficiency by approx. 12.5% [158]. All the above described configurations are based on using conventional adsorbent material (silica gel and zeolite), thus there is a need to investigate the use of MOFs in such systems to take the advantage of the high performance of these materials at lower heating temperature. Additionally, the adsorption systems in these configurations are only studied as a lumped model without considering the design details of the adsorber

bed such as the heat exchanger geometry and adsorbent material thicknesses. Moreover, different integrated ORC-adsorption system configurations are also required to obtain the best system performance.

### 2.8.3. Integration of adsorption system with other desalinations systems

With its double distillation process, adsorption desalination (AD) system can produce high-quality freshwater using low-grade thermal energy [160,161]. The AD system can generate a cooling effect at the evaporator, and high-quality freshwater less than 10 ppm at the condenser [162,163]. Additionally, the heat of adsorption generated during the water vapour adsorption can be extracted to be used as a heat source for different applications with a temperature of around 40$^{o}$C. During the condensation process, heat is rejected and can be also utilized with almost the same temperature rejected in the adsorption phase (around 40$^{o}$C). Therefore, AD can be effectively utilized for dual-purpose desalination by integrating the system with different conventional desalination systems that are mainly driven by thermal energy such as Multi Effect Desalination (MED) and Humidification-Dehumidification (HDH) or by pressure such as Reverse Osmose (RO) [160,162–166].

In MED, the evaporation process occurs at different stages as shown in Figure 2-17. Firstly, the seawater is preheated in the condenser that is connected with the last stage of evaporation process. The seawater is then sprayed at different stages to form a mist over the hot tube surfaces. The evaporated water rises up in order to be directed to the next stage as a heat source [167]. Normally, the top-brine to low-brine temperatures in the stages have a range between 65 to 40$^{o}$C [164]. Shahzad et al. [164] integrated this system with AD by taking the water vapour from the last stage as a vapour input to the adsorber bed, which means that the MED system acts as an evaporator to the AD. This allows the latter stage in MED to work at a temperature of 5$^{o}$C instead of 40$^{o}$C, which leads to have larger temperature range between the top-brine to low-brine. The water recovery is enhanced by this approach while the scaling and fouling effect caused by high concentration of brine water is reduced at lower saturation temperature compared to the conventional MED.

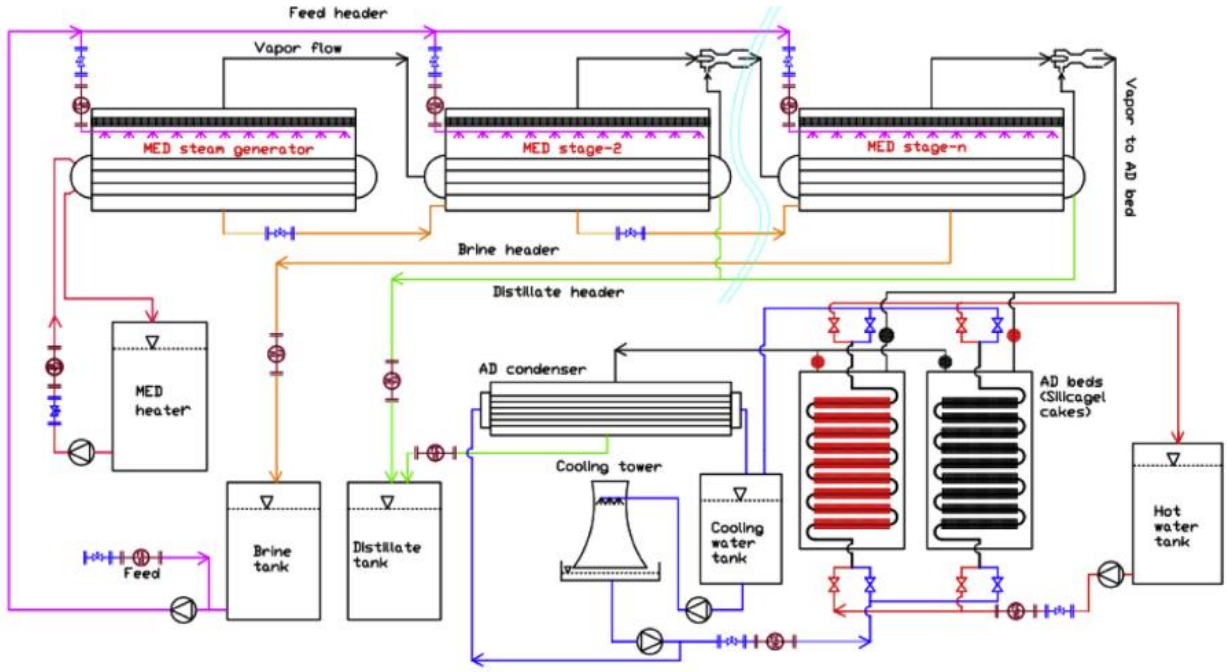



Figure 2-17. Integrating the adsorption system with MED [164]

In HDH, the seawater/saline water is evaporated by spraying the water through the air during the humidification process. Then it is condensed as distilled water in another chamber during the dehumidification process [168]. Ali et al. [165] developed a mathematical model to investigate the integration of this system with AD by extracting the generated heat either from the condenser or the adsorber bed of the AD in order to heat up the seawater fed to the HDH before entering the humidification process as shown in Figure 2-18. Two ejectors are added to the cycle to mix the vapours and liquids between the two systems to increase the production rate. They reported an overall maximum specific daily water production (SDWP) of 83.1 $m^3$/ton.

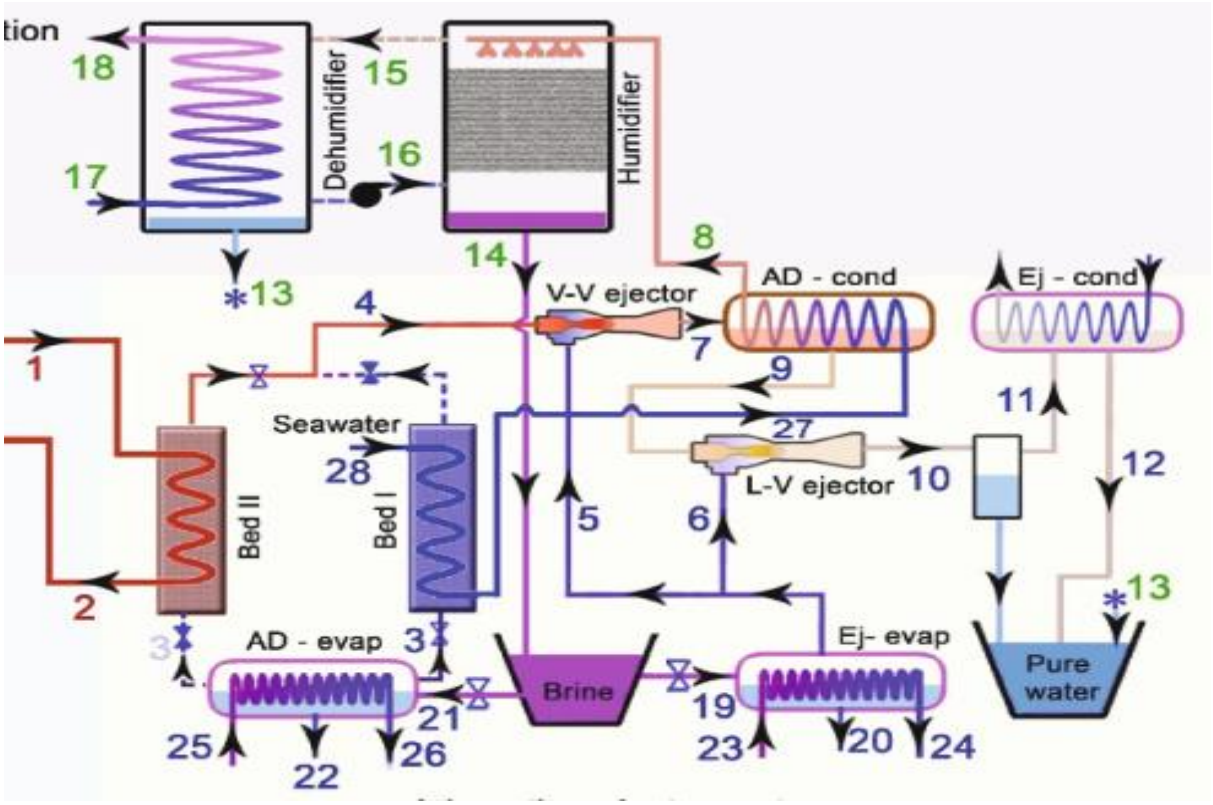



Figure 2-18. Integrating the adsorption system with HDH [165]

In RO, the process is opposite to the natural osmosis phenomenon in which the saline water is pressurized above the osmotic pressure in order to force the water through a semi permeable membrane so that the saline water is transferred from the high-water concentration to the lower concentration, while the salt remain in the membrane [169]. Normally, the conventional seawater RO has a water recovery of up to 50%, where the second half is considered as a brine water with high concentration. Since the performance of the AD system is not affected by feed concentration [162], the AD system can be integrated with the conventional desalination systems such as RO for brine management. The use of AD as a brine treatment subsequent to the conventional desalination system can further increase the overall recovery of the desalination system and minimise the volume of brine disposal. In addition, it is viable to develop a multipurpose desalination system that can simultaneously produce freshwater, high-quality distilled water, and cooling power. Thus, hybridisation with AD is an attractive solution for not only resolving the environmental problem of brine disposal but also obtaining valuable products (distilled water and cooling power) using low-grade thermal energy. Atab et al. [162] applied this approach of combining the brine water of the RO with the AD and adding a pressure exchange to reduce

the energy consumption as shown in Figure 2-19. They obtained a minimum specific energy consumption of 0.8kWh/m$^3$ using a brackish water feed.

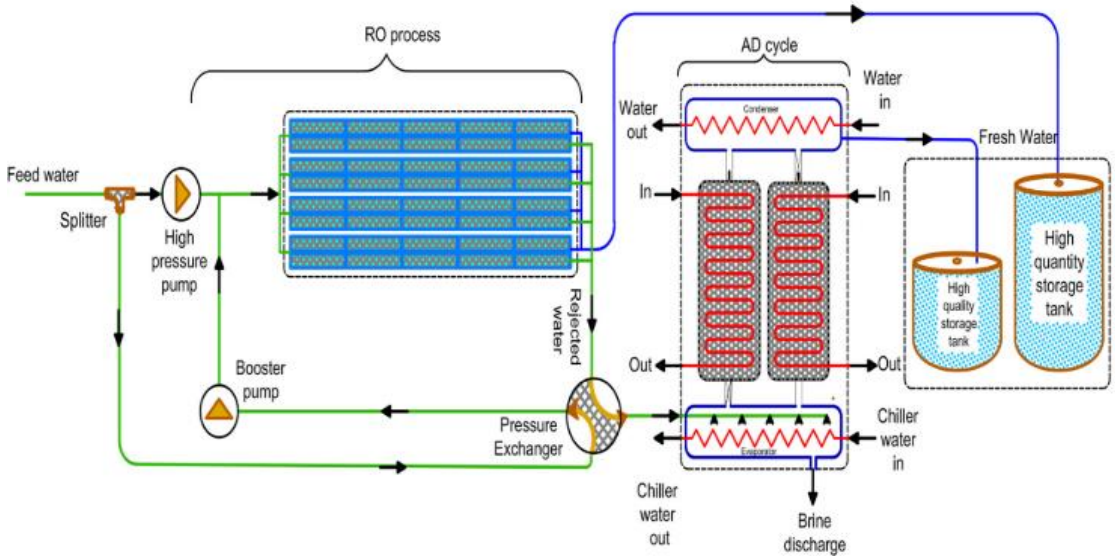



Figure 2-19. Integrating the adsorption system with RO [162]

Regarding the problem of high energy consumption, researchers have investigated new processes and systems for reducing the current level of energy consumption [170–172]. Batch reverse osmosis (BRO) is recently developed to minimise irreversible energy losses during the pressurisation process in the reverse osmosis (RO) system [173,174]. Because the applied pressure increases gradually with concentration in the BRO system, the irreversible energy loss is significantly reduced [175,176]. As a result of minimising the irreversibility, the energy consumption of the BRO is lower than the conventional continuous RO especially at high recovery rate [174]. Recently, design and modelling approaches in the BRO were developed for practical implementation in large-scale desalination systems with an 8-inch spiral wound module [177,178]. However, BRO and RO systems cannot easily increase the recovery to very high value for minimisation of brine disposal because the maximum durable pressure of RO membrane is still limited [179,180]. Although, BRO is an attractive solution for energy minimisation, there is still the environmental issue associated with brine disposal. Therefore, there is a need to investigate other methods for reducing brine disposal.

A new hybrid BRO-AD system could be a competitive solution to address the critical issues of energy minimisation and brine management. The hybrid configuration of BRO-AD has not been

investigated yet. However, BRO is a cyclic system, and the concentrated brine is periodically discharged. Because AD with two beds is a continuous system, the hybridisation of BRO and AD requires appropriate operating strategy and configuration to connect these systems effectively without needing a buffer tank. If the hybridisation of BRO and AD is successfully designed, the BRO-AD system would be a multifunctional and energy-efficient desalination process for minimal liquid discharge. Table 2-5 summarizes research work carried out regarding the effect of the water salinity on the performance of the adsorption desalinations system. Most of these studies showed that high water salinity has a slight impact on the SDWP of the adsorption system even with a salinity of up to 200,000 ppm.

Table 2-5. Literature review in effect of water salinity in the adsorption desalination systems.

| References | Adsorbent material | Adsorbent mass (kg) | Study type | Operating conditions | water salinity | SDWP | Effect of water salinity in product |
|---|---|---|---|---|---|---|---|
| [181] | zeolite 13X | - | Numerical and experimental | $T_{des}$: 85°C, $T_{evaporator}$: 14°C | 0 to 100,000 ppm | 18 L/kg/day | at water salinity of 70,000 ppm, 68.72% reduction in SDWP |
| [182] | silica gel | 29.17 kg | Experimental | $T_{des}$: 83°C, | TDS: 30,710 ppm | 4.69 L/kg/day | Meets the quality standard for drinking water in China |
| [183] | silica gel | 14 kg | Experimental | $T_{des}$: 65-85°C, $T_{evap}$: 12-30°C | 3.4 to 19.3 wt%. | 6.76 L/kg/day | Consistent performance at different salinity, can be used in zero-liquid discharge (ZLD) systems |
| [160] | silica gel | 36 kg | Numerical and experimental | $T_{des}$: 50-85°C, | TDS: 9.09 to 86,800 ppm | 6.7 L/kg/day | high purity (TDS<15 ppm) product at high water recovery (75%) |
| [162] | silica gel | - | Numerical | $T_{des}$: 60-85°C, $T_{evap}$: 30°C | 27,000 ppm | 6.3 L/kg/day | Drinking water product with water salinity < 10ppm |
| [163] | silica gel | 47 kg | Numerical | $T_{des}$: 55-95°C, | 0 to 220,000 ppm | 6.5 L/kg/day | A slight impact on the SDWP when the feeding salinity increased to 220,000 ppm |

## 2.9. Summary

From the above literature review, the following knowledge gaps can be highlighted:

- Designing an effective heat exchanger for the adsorber bed is requried to optimize the heat and mass transfer in the adsorbent material.
- Packing the adsorbent material has a limitation in the heat transfer since the thermal contact resistance with the heat exchanger surface is high. Furthermore, the effective thermal conductivity is also low since the voids between the granules has a negative impact on the thermal properties. Therefore, the SDWP and SCP have lower values compared to the coating method. However, packing has a potential of increasing the volumetric capacity of the adsorption system since more adsorbent material mass can be packed in the heat exchanger compared to the coating method. Coating the heat exchanger surface with adsorbent material by mixing it with binder agent eliminates the thermal contact resistance and increase the thermal conductivity of the material which ultimately increases the SDWP and SCP of the system. However, because of the limited coating thickness, more heat exchanger metal mass is required which resulted in lower COP of the adsorption system compared to the packing method. Therefore, further study needs to be considered to increase the coating thickness in the heat exchanger on the adsorber bed without significantly affecting the mass transfer of the vapour through the adsorbent material. Also, combining the packed and coated methods can overcome the drawbacks in both method, since packing has a good mass transfer through the voids between the granules, while the coating has a good heat transfer.
- Scaling up the adsorber bed by including more heat exchanger modules need to be investigated to optimize the gap (vapor passage) between the heat exchangers and their connection whether to be parallel or series.
- The numerical models for solving the partial differential equations of heat and mass transfer in adsorber beds with simple and complex geometries need to be investigated to obtain the best approach in terms of results accuracy and computational time.

- Despite the low heat transfer coefficient in the flooded evaporators compared to the falling film ones in low-pressure applications such as the adsorption system, it is simpler and requires less amount of energy compared to the falling film. Additionally, the tube design can improve the heat transfer coefficient in some cases to be higher than the falling film particularly by using the capillary-assisted tube surface. Additionally, the evaporator chamber dead volume is smaller than the falling film, since no region is required to spread the mist water over the tube surface. However, more investigation needs to be carried out to study the dead volume of the flooded evaporator to achieve a compact adsorption system design.
- The optimization of the adsorption system design should be based on using MOF adsorbent materials since higher water capacity, faster kinetics and lower energy consumption can be obtained compared to the conventional adsorbent materials.
- A newly developed MOF with better thermal properties should be investigated to overcome the poor thermal conductivity of the adsorbent material and to improve the cyclic performance of the adsorption system.
- There are promising hybrid systems for different applications (solar, ORC, and desalination systems) that can be integrated with the adsorption system need to be investigated using MOF material to produce higher energy conversion ratio and better performance compared to the existing hybrid systems that are based on the conventional adsorbent material like silica gel and zeolites.

# Chapter 3: Modelling of the wire-finned tube heat exchanger using the coupled solution approach

This chapter studies the modelling of the heat exchanger in the adsorber bed using the coupled solution approach. A 3D model of the wire-finned tube packed, coated and a combination of both with adsorbent material is developed.

The wire-finned tube heat exchanger is used in this chapter to investigate the ability to increase the metal surface area that is in contact with the adsorbent material compared to the conventional finned tube to increase the amount of the adsorbent material mass that can be coated/packed. A coupled solution approach is used to overcome the difficulty in solving the non-linear partial differential equations with such complex geometry.

This chapter is based on a published work presented in the following journal paper:
**I. Albaik,** R. Al-Dadah, S. Mahmoud, M. Ismail and M. Almesfer. Coated, packed and combined wire finned tube adsorption cooling and desalination system using metal-organic framework: Numerical study. Energy 2022;247:123506. https://doi.org/10.1016/j.energy.2022.123506.

### Credit Authors statament:

**I.Albaik:** Modelling methodology (developing the heat and mass transfer model) using Comsol Multiphysics, Conducting a case study by applying the coated wire-finned heat exchanger modules in adsorption desalination and cooling system, analysing the results, and writing the outcomes of the study. **R. Al-Dadah and S. Mahmoud:** Reviewing and supervision, **M. Ismail and M. Almesfer:** Project funding and administration

## 3.1. Abstract

The adsorber bed design and the method of integrating the adsorbent material in the bed have a major effect on the overall performance of the adsorption system. This study numerically investigates the performance of wire-finned tube adsorber bed with aluminum fumarate metal-organic framework material integrated either using coating, packing, or a combination of coating and packing. A 3D heat and mass transfer model using the coupled solution approach with a variable vapor pressure through the adsorbent voids between the particles is developed. Results showed that the coated wire finned heat exchanger outperforms the packed and the combined packed and coated heat exchanger in terms of the specific daily water production (SDWP) and specific cooling power (SCP). Also, a parametric study was carried out of the coated wire finned heat exchanger geometry including different tube diameters, fin height, and a number of fins to predict the best geometrical parameters that produce maximum output using different coating thicknesses. Results revealed that by applying the coated wire finned tube design in a case study with a capacity of 300L/day water production and 8.3kW of cooling power, the maximum adsorbent performance (SDWP = 21 L/kg/day, SCP = 585 W/kg ) was achieved using tube diameter of 10mm, fin height of 7mm, 20fin per loop and coating thickness of 0.3 mm.

## 3.2. Brief introduction

In the segregated solution approach, each partial differential equation will be solved sequentially and separately which will lead to having only one variable that needs to be solved in each equation, while the other variables are constant. Each equation has its iteration to get a convergence using a linear algebraic equation solver. This type of iteration is called inner iteration. After solving all the equations separately, an outer iteration should be used to get convergence of the results by using an iteration called Picard iteration. In the coupled solution approach, all the equations are solved in one go in a coupled manner, thus one outer iteration is only required if the equations are linear.

Modularity is one of the major advantages of the segregated solution approach which will ease extending the code in case of any additional equations are required to be added. On the other hand,

applying the same task to the code in the coupled solution approach is very complex. Very low computational cost (low memory usage) is another advantage of using the segregated solution approach. This can be clearly shown in the simulation of an adsorption system that has eleven variables and equations, if the model requires 2GB in computer memory to solve the equations using the segregated solution approach, it needs $2^{number\ of\ equation} = 2^{11} GB$ to solve it using the coupled solution approach. On the other hand, to model a complex heat exchanger geometry, the segregated solution approach cannot provide convergent results, which causes more iterations and computational time. Therefore, the coupled solution approach is considered in this study which can be used for the larger computational domain as well.

In this study, using various design and operational conditions, the performance of an adsorption system employing wire-finned tube in an adsorber bed with MOF material was numerically investigated for three different adsorber bed design scenarios: (i) tubes were coated with MOF material, (ii) tubes were packed with granular MOF material and, (iii) both techniques, coating and packing, were jointly employed on the finned tubes of the adsorber bed. For this purpose, the transient 3D local thermal equilibrium (LTE) models of the proposed systems with the non-uniform pressure approach were developed in COMSOL Multiphysics software to conduct the simulation. To the best of our knowledge, there is only one numerical study that investigated the combined effect of coating and packing techniques inside the adsorber bed and, this study was based on the lumped analytical model with uniform pressure assumption. Then, a parametric study using a coated wire-finned tube with aluminum fumarate MOF material was carried out to optimize the geometry of the wire-finned tube including tube diameter, fin height, and a number of fins.

## 3.3. Model description

In this section, the modelling of three methods of adsorbent material integration in adsorber bed heat exchanger is described using aluminum fumarate metal-organic framework material. The used heat exchangers are based on wire-finned tube geometry and the adsorbent material was integrated

either using coating, packing or a combination of both (see **Figure 3-1**). In the coated wire-finned tube, the aluminum fumarate powder with a particle size of less than 10 µm was mixed with a binder solution of 10% Hydroxyethyl Cellulose (HEC) [15]. This binder solution was obtained by dissolving the HEC in distilled water with a mass ratio of 1:50 through heating and mixing the solution. The maximum water uptake of the coated aluminum fumarate is 0.49 $kg.kg^{-1}$, which is slightly lower than the packed one with maximum water uptake of 0.55, due to the effect of mixing the material with the binder [184].

In a packed wire-finned tube, the adsorbent material is in the form of granular particles with a particle size of 0.12mm. The adsorbent material is packed between the fins and the voids in the gap of the fin width (see **Figure 3-1** (c)). While in the combined coated and packed wire finned tube, the coating layer is first applied onto the fins surface at a specific thickness followed by packing the adsorbent material granules (see **Figure 3-1** (d)).

In this study, a numerical 3D heat and mass transfer model with variable vapor pressure through the packed and coated fins is developed using the COMSOL Multiphysics software based on the Finite Element Method (FEM). The model consists of five domains; thermal fluid, metal tube, wire fins and coated/packed adsorbent material as shown in **Figure 3-1**. The wire fins are made of copper wires soldered to the metal tube using a soldering material made of Tin (40%) and Lead (60%) with effective thermal conductivity of 45 $W.m^{-1}.K^{-1}$. The wire fins have a thermal resistance with the metal tube of 0.001 $m^2.K.W^{-1}$ [28]. The model is studied by taking a quarter of the tube and applying symmetric conditions on two sides.

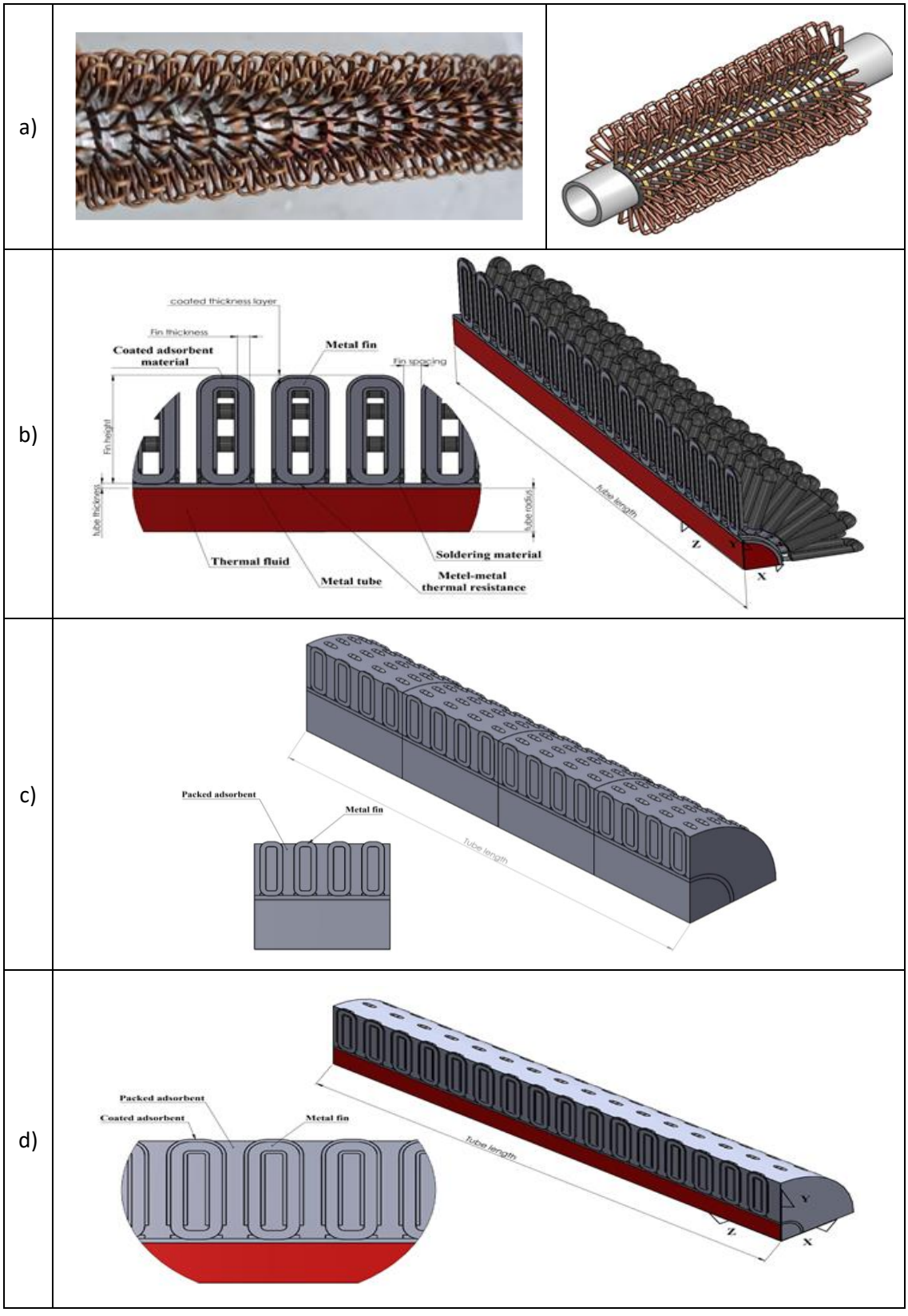



Figure 3-1. (a) Wire finned tube, (b) Coated wire finned tube, (c) packed wire finned tube, (d) 3D combined packed and coated wire finned tube model.

The main geometrical parameters of the wire finned tube are the tube diameter, tube thickness, number of fins, fin spacing, fin thickness and, fin height. The number of the fins is directly related to the tube diameter, where 22 fin loops can be fitted on a tube outer diameter of 10mm, while the number of the fins for the tube diameter of 15 and 22 mm is 32 and 44 fins as shown in **Figure 3-2.** The number of fins is also based on ensuring a maximum coating thickness of 0.5mm without overlapping.

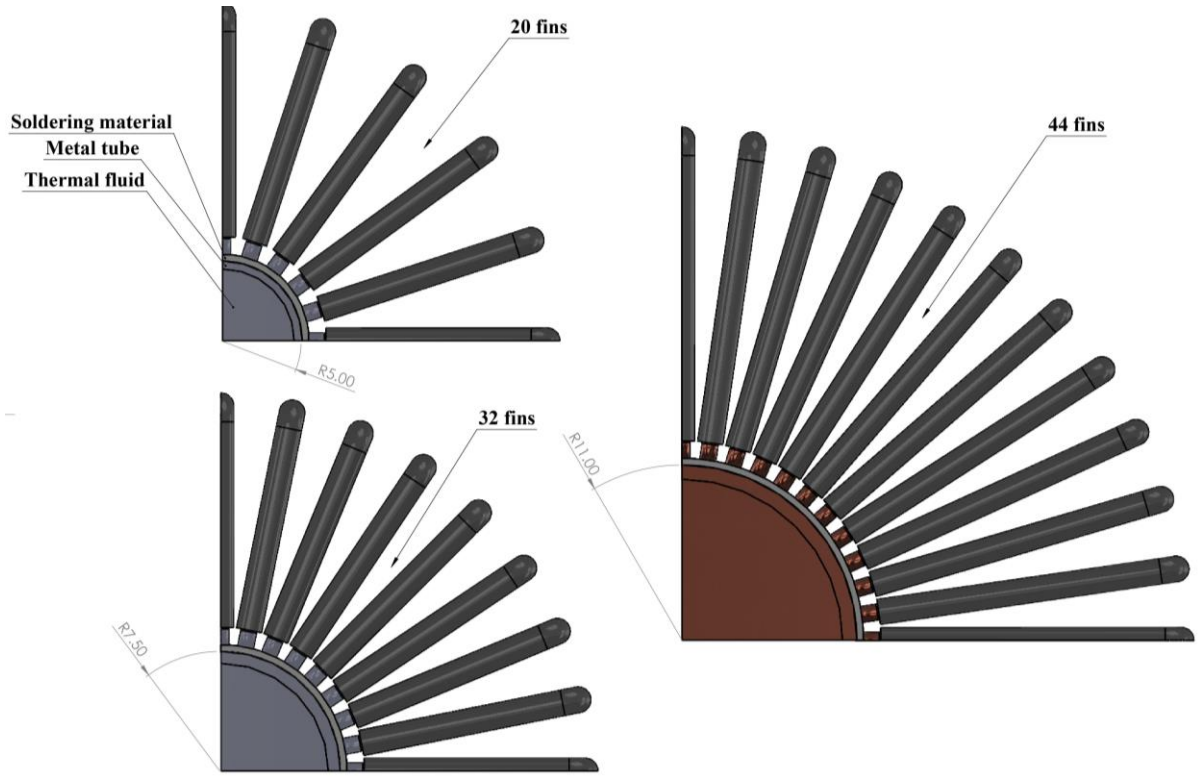



Figure 3-2. The number of fins at different tube diameters in the wire-finned tube.

The detailed dimensions of the coated wire finned tube are shown in **Table 3-1.**

Table 3-1. Coated wire finned tube dimensions.

| Outer tube diameter (mm) | Number of fins | Fin height (mm) | Coating thickness (mm) |
|---|---|---|---|
| 10 | 20 | 7,10,15 and 20 | 0.3,0.4 and 0.5 |
| 15 | 32 | | |
| 22 | 44 | | |

The flow of the thermal fluid used to heat up/cool down the coated adsorbent material is assumed to be turbulent and modelled using K-$\varepsilon$ RANS equations as follows:

$$\boldsymbol{\rho_{tf}\frac{\partial u}{\partial t}+\ \rho_{tf}(u\ .\nabla)u=\ \nabla\ .(-pI+K\ )} \tag{3.1}$$

where:

$$\boldsymbol{K=\ (\mu+\mu_t)\left(\nabla u+(\nabla u)^T\right)} \tag{3.2}$$

The mass conservation equation of the thermal fluid is written as follows:

$$\boldsymbol{\rho_{tf}\nabla.u=\ 0} \tag{3.3}$$

and the thermal fluid energy equation is defined as follows:

$$\boldsymbol{\rho_{tf}C_{p,tf}\frac{\partial T_{tf}}{\partial t}+\ \rho_{tf}C_{p,tf}u\ \nabla T\ +\ \nabla.\left(-\left(k_{tf}+k_t\right)\nabla T\right)=0} \tag{3.4}$$

where $k_{tf}$ is the thermal conductivity, while $k_t$ is the turbulent fluid thermal conductivity.

The energy equation for the second domain which is the metal tube is presented by the following equation:

$$\boldsymbol{\rho_{sf/mt}C_{p,sf/mt}\frac{\partial T_{sf/mt}}{\partial t}+\ \nabla.\left(-\ k_{sf/mt}\nabla T\right)=\ 0} \tag{3.5}$$

By taking into consideration the porosity ($\varepsilon_t$) of the adsorbent material, the mass balance equation of the adsorbent domain is written as follows:

$$\boldsymbol{\varepsilon_t\frac{\partial\rho_v}{\partial t}+\nabla.(\rho_v u_2)+(1-\varepsilon_t)\ \rho_s\frac{\partial X}{\partial t}=0} \tag{3.6}$$

where $X$ is the water uptake of the adsorbent material.

The energy equation of the adsorbent material assuming local thermal equilibrium can be defined as follows:

$$\boldsymbol{(\rho C_p\ )_{eff,ads}\frac{\partial T_{ads}}{\partial t}+\ \rho_v C_v\ u_2\ \nabla T+\nabla.(k_{eff,ads}\nabla T)\ =\ (1-\varepsilon_t)\ \rho_{ads}\frac{\partial X}{\partial t}\Delta H_{ads}} \tag{3.7}$$

$$\boldsymbol{(\rho C_p\ )_{eff,ads}=(1-\varepsilon_t)\rho_{ads}C_{p,ads}+\ \varepsilon_t\rho_v C_{p,v}+\ (1-\varepsilon_t)\rho_{ads}XC_{p,l}} \tag{3.8}$$

$$\boldsymbol{k_{eff,ads} = (1 - \varepsilon_t)k_{ads} + \varepsilon_t k_v} \quad (3.9)$$

where $\Delta H_{ads}$ is the isosteric heat of adsorption, $k_{ads}$ is the thermal conductivity of the adsorbent material and $k_v$ is the refrigerant vapor thermal conductivity.

The momentum equation of the refrigerant through the adsorbent material is based on Navier-Stokes equations, which is written as follows [185]:

$$\frac{\boldsymbol{1}}{\boldsymbol{\varepsilon_t}}\boldsymbol{\rho_v}\frac{\boldsymbol{\partial u_2}}{\boldsymbol{\partial t}} + \frac{\boldsymbol{1}}{\boldsymbol{\varepsilon_t}}\boldsymbol{\rho_v}\,(\boldsymbol{u_2}.\boldsymbol{\nabla})\boldsymbol{u_2}\frac{\boldsymbol{1}}{\boldsymbol{\varepsilon_t}} = \boldsymbol{\nabla}.(-\boldsymbol{p_2 I} + \boldsymbol{K}) - \left(\frac{\boldsymbol{\mu_v}}{\boldsymbol{K_d}} + \frac{\boldsymbol{Q_m}}{\boldsymbol{\varepsilon_t}^2}\right)\boldsymbol{u_2} \quad (3.10)$$

$p_2$ is the pressure of the vapor calculated using ideal gas as follows:

$$\boldsymbol{p_2 = \rho_v R_v T} \quad (3.11)$$

$Q_m$ is the mass source of the adsorbate through the adsorbent material which is calculated using the following equation:

$$\boldsymbol{Q_m = -(1 - \varepsilon_t)\rho_{ads}\frac{\partial w}{\partial t}} \quad (3.12)$$

The partial differential equations of the heat and mass transfer model are numerically solved using COMSOL Multiphysics software based on the Finite Element Method (FEM). To solve the mass, momentum, and energy equations, three physics modules were used namely; the turbulent flow physics of the thermal fluid, the heat transfer physics, and flow in porous media physics. The kinetic and isotherm equations of the adsorbent material were solved by the convection-diffusion equation. All physics were solved numerically using the coupled solution approach. This approach provides an accurate result with minimum iterations due to solving the non-linear partial differential equations simultaneously [7], in addition to considering the internal and external mass transfer resistances which are needed in the numerical simulation to compare between coating and packing methods [135]. The initial boundary condition is set by assuming that the adsorbent material is dry after heating the material to a temperature of 90°C, where the water uptake is only 0.05 $g.g^{-1}$. The boundary conditions are varied between the adsorption, desorption, and switching processes, in which the thermal fluid temperature

changes between 30ºC and 90ºC for the thermal fluid used in the cooling and heating processes respectively, while the vapor pressure is the saturation pressure corresponding to the saturation temperatures of 15ºC during the adsorption process and 30ºC during the desorption process. A symmetric boundary condition is applied at two sides of the 3D wire finned tube model since a quarter of the tube is used in this study. The boundary conditions can be summarized as shown in Figure 3-3

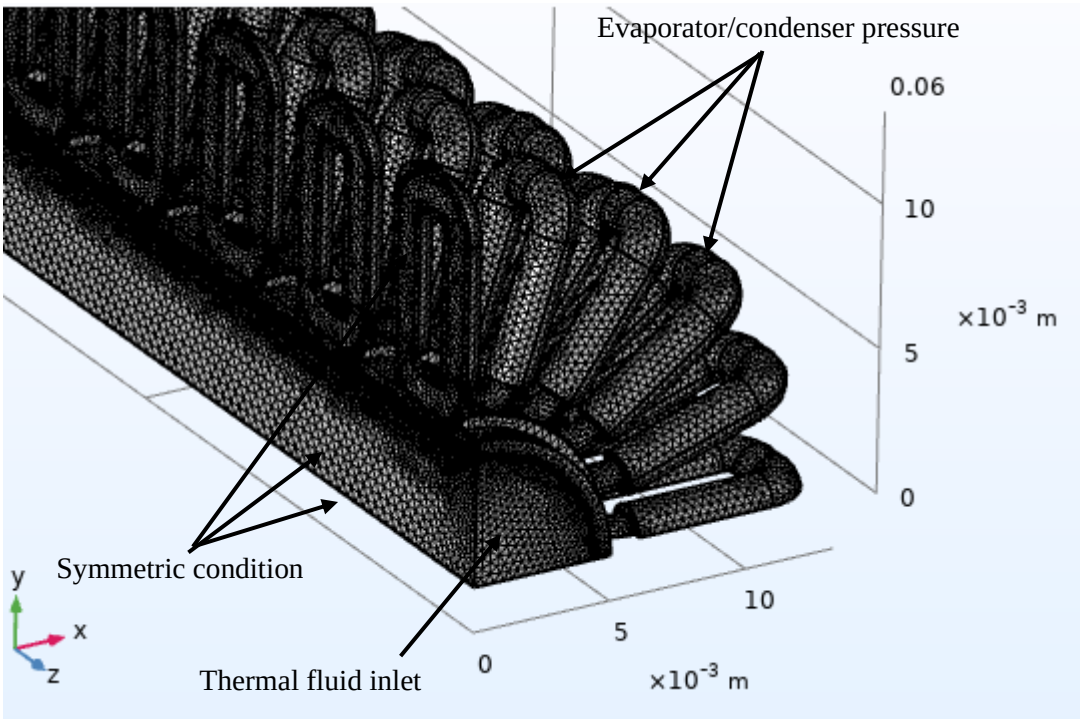



Figure 3-3. Boundary Condition of the wire-finned tube model

The governing equations of the wire-finned tube 3D model are based on the following assumptions:

a) The adsorbate (refrigerant) is considered an ideal gas.

b) The thermal contact between the coated adsorbent material and wire fins is negligible. While the thermal contact resistance in the packed one is calculated using the Rezk et al. model [28].

c) The particle size and porosity of the coated and packed adsorbent material are uniform and constant.

d) The pressure on the outer surface of the adsorbent material is the saturation evaporation and condensation pressures in the adsorption and desorption processes, respectively.

To reach a solution that is independent of the mesh size, physics-controlled mesh in COMSOL is used to study the element size effect on the adsorbent material temperature using tetrahedron mesh

shape at different element sizes (coarse (minimum size:0.904mm), normal (minimum size:0.581), fine (minimum size:0.323mm) and finer (minimum size:0.129mm)) as shown in Figure 3-4. It was found that using fine and finer mesh options, the results become convergent after taking into consideration applying the boundary layer mesh near the inner surface of the tube (interface between the thermal fluid and metal tube). The simulation to study the mesh size was carried out using 176 fins with a fin height of 20mm and a tube diameter of 22mm. In coarse, normal, fine, and finer sizes, the computational times needed to run four cycles were 20, 45,90 and 180 minutes using PC Intel core i7 processor, 7GB RAM, 1TB SSD Hard Drive. The step time was chosen based on the adaptive time stepping method, in which the timestep size is adjusted based on the required relative tolerance (which is the convergence criteria value in COMSOL Multiphysics and found to be equal to 0.01 for most heat and mass transfer models as recommended by the software). The initial step time size is 0.001 second, while the step time size is automatically increased until reaching a constant value of 1 second to maintain the required relative tolerance.

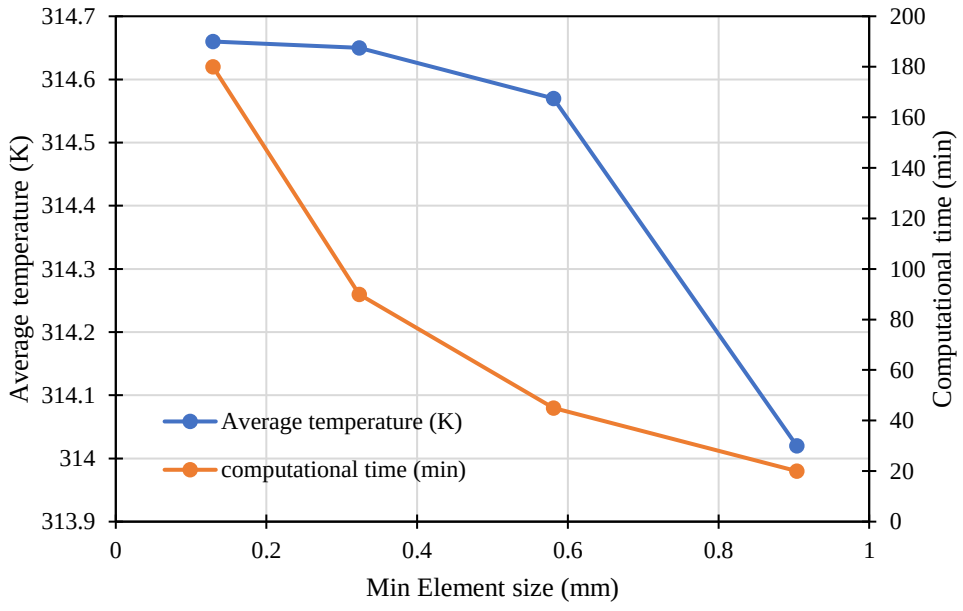



*Figure 3-4. Mesh sensitivity study*

The input parameters of the geometric and operating conditions studied in this chapter are shown in Table 3-2 and Table 3-3.

Table 3-2. Input geometry

| Parameter, unit | value |
|---|---|
| Tube diameter, mm | 10, 15 and 22 |
| Fin height, mm | 7, 10, 15 and 20 |
| Tube thickness, mm | 0.5 and 0.75 |
| Number of fins | 20, 32 and 44 |
| Fin spacing in axial direction, mm | 2 |

Table 3-3. Input operating conditions

| Parameter, unit | value |
|---|---|
| Adsorption temperature, $^{o}$C | 90 |
| Desorption temperature, $^{o}$C | 30 |
| Evaporation temperature, $^{o}$C | 15 |
| Condensation temperature, $^{o}$C | 30 |
| Half cycle time, sec | 250 |
| Switching time, sec | 40 |

The wire-finned tube is fitted inside a vacuum chamber. The adsorption system has a number of stages in each cycle; starting with heating and drying the adsorbent material. Then a switching time is carried out to feed the cooling water for 40 seconds. Then, the adsorption process is started for 250 seconds, followed by another switching time of 40 seconds to feed the heating water to start the desorption process for another 250 seconds. Four cycles are required to get a steady cyclic condition in the water uptake and temperature of the adsorbent material. During the cooling process, the adsorbent material's outer surface has the saturation pressure of the evaporator, while it has the saturation pressure of the condenser during the heating process.

## 3.4. Results and Discussions

To validate the coupled solution approach developed in this work using wire finned tube, the experimental results of Majdi et al. [186] with a coating thickness of 0.3mm are compared to the results predicted by the developed model as shown in Figure 3-5. The physics of the numerical model is validated through the variation of adsorbent temperature with time and the SCP of the adsorption system at the chilled water inlet temperatures of 15 and 20$^{o}$C. The model shows a good agreement with the experimental work with a maximum deviation of 6.36%.

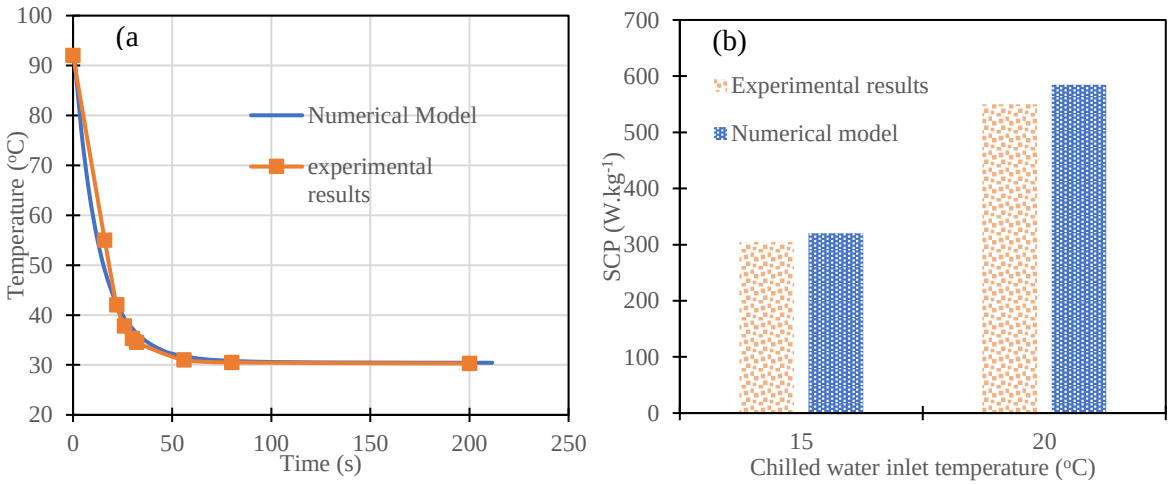



Figure 3-5. Validation of the current numerical model with published experimental works from literature [186] (a) adsorbent temperature with time and (b) the effect of chilled water inlet temperature on SCP-wire finned tube with 2mm fin spacing, fin thickness of 1mm, fin height of 7mm, tube diameter of 10mm.

This coupled modelling approach was used to model the heat and mass transfer in wire finned tube to investigate the effect of integrating the MOF adsorbent material to the tube metal structure including coating, packing and combined packing and coating using a tube diameter of 22mm and fin height of 20mm**.** Figure 3-6 shows the temperature, vapor pressure, and water uptake distributions in the packed wire finned tube in the adsorption process. As the granular particles have a thermal contact resistance [143] with the copper metal due to its porosity, heat transfer is negatively affected as can be seen through the temperature difference between the outer surface of the tube and the outer surface of the adsorbent material. On the other hand, the granular particles in the packed adsorber bed provide better mass transfer of the vapor through the voids between the particles. This is observed from the vapor pressure profile between the outer surface of the tube and the outer surface of the adsorbent material. By taking into consideration the temperature and pressure profiles, the maximum water uptake was found near the tube surface as shown in Figure 3-6.

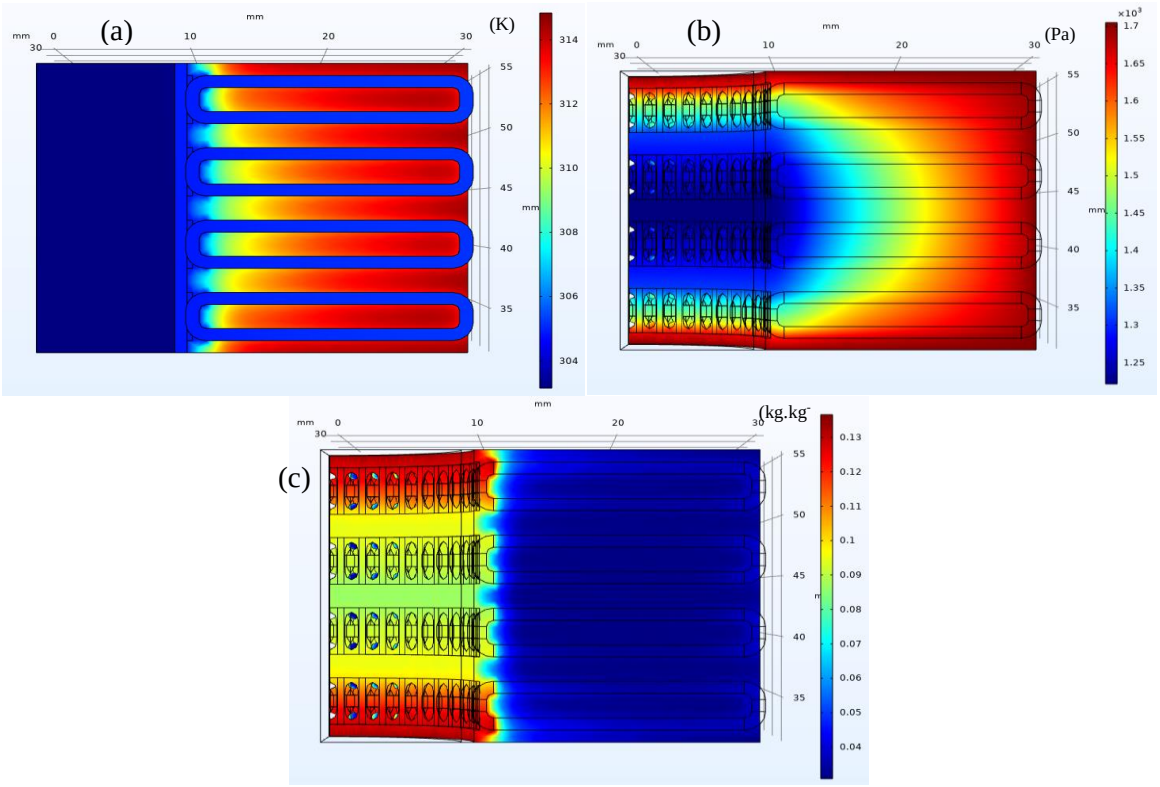



Figure 3-6. Packed wire finned tube with tube diameter of 22mm and fin height of 20mm - Adsorption process after 250 seconds at $T_{evap}$ = 15 ºC, $T_{cond}$ = 30 ºC, $T_{des}$ = 90 ºC and $T_{ads}$ = 30ºC (a) vapor pressure (Pa), (b) temperature (K) and (c) water uptake (kg.kg$^{-1}$).

To enhance the thermal conductivity and eliminate the thermal contact resistance between the metal surface and adsorbent material, the wire-finned tube is coated with adsorbent material (powder adsorbent and binder) with a coating thickness of 0.3mm. After 80 seconds of cooling the adsorbent material from 90 to 30ºC, the heat transfer becomes steady since the adsorbent material reaches the same temperature of the cooling water inside the tube. Therefore, the temperature profile is presented after only 50 seconds of the process to show the temperature variation along the fins height as shown in Figure 3-7. On the other hand, it was found that the pressure drop through the coated layer of 0.3mm is remarkable since the small particle diameter and binder effect increased the mass transfer resistance. However, it is insignificant due to the thin coating thickness. Thus, the water uptake is extremely increased in the adsorbent material compared to the packed type after 250 seconds of the adsorption process, which leads to obtaining higher material performance in terms of SCP and SDWP.

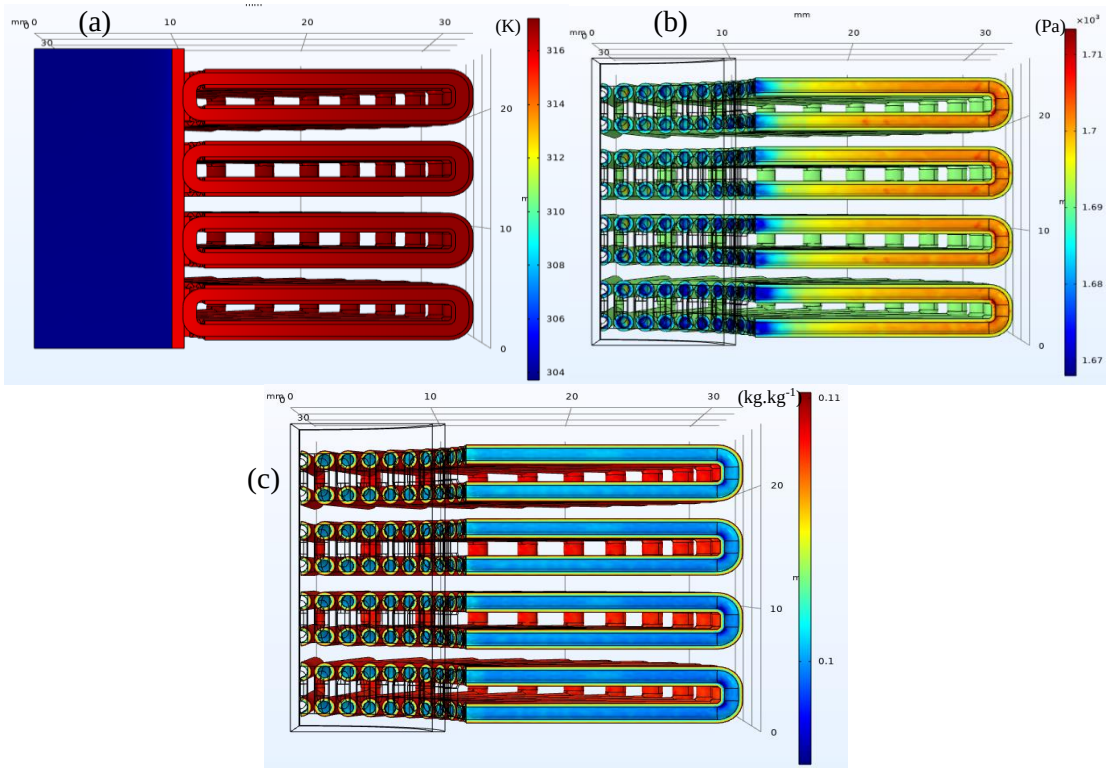



Figure 3-7. Coated wire finned tube with tube diameter of 22mm and fin height of 20mm - Adsorption process at $T_{evap}$ = 15°C, $T_{cond}$ = 30°C, $T_{des}$ = 90°C and $T_{ads}$ = 30°C (a) vapor pressure after 50 seconds (Pa), (b) temperature after 50 seconds (K) and (c) water uptake after 250 seconds ($kg.kg^{-1}$).

**Figure 3-8** shows the temperature, pressure and water uptake distributions of a coated wire finned tube using 0.3mm coating thickness combined with adsorbent packing in the remaining space for a tube with a diameter of 22mm and fin height of 20mm after cooling the adsorbent for 250 seconds at 30°C. The temperature profile through the adsorbent material predicts the enhancement of the heat transfer when the coating is used on the fins surfaces as shown in **Figure 3-9.** There is a temperature difference of 4°C between the packed and coated adsorbent material, while there is a significant vapor pressure drop in the coated material compared to the packed one in the X-direction as shown in **Figure 3-9.** A pressure drop ranging from 1700 to 1590 Pa was found in 0.3mm in the X-direction of the coated adsorbent, while there was only a pressure drop ranging from 1700 to 1683 Pa in the same direction and distance through the packed adsorbent material. This indicates that there is a significant enhancement in the mass transfer when adsorbent packing is used over the adsorbent coating since the packed adsorbent has a higher permeability as the particle and voids size are larger than the coated adsorbent which will decrease the mass transfer resistance. Moreover, the binder used in the coating process also increases the mass transfer resistance. The combination of the packed and coated

adsorbents could provide a good combination between heat and mass transfer. **Figure 3-10** predicts the effect of the combination of the coating and packing as it shows the water uptake in Y-direction at different locations inside the adsorbent. The coordination of the X and Y direction is shown in **Figure 3-8.** The water uptake is shown at X-direction of 2, 4, 10, 15, and 20mm from the outer surface of the fins. The variation in the Y-direction started from 0 to 1mm in the middle of the fin spacing as the fin spacing is selected to be 2mm. It is observed that the water uptake has its maximum value when the material is close to the outer surface (in X-direction) of the fins as the vapor pressure has its maximum value in this region. While moving in Y-direction will increase the water uptake as the adsorbent will be closer to the metal surface of the fins which has a higher heat transfer until reaching 0.7mm where the coated adsorbent layer starts.

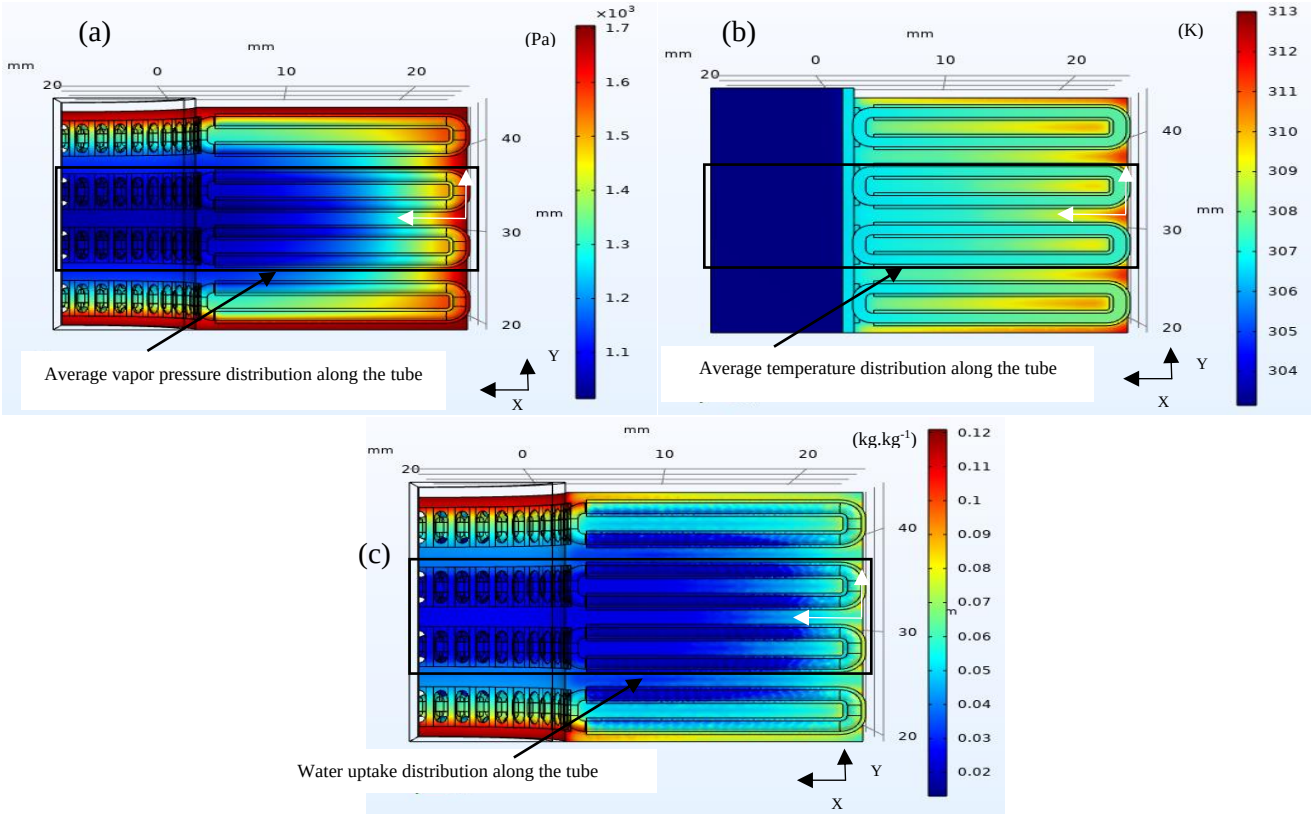



Figure 3-8. Wire finned tube with tube diameter of 22mm and fin height of 20mm - Adsorption process after 250 seconds at $T_{evap}$ = 15 ºC, $T_{cond}$ = 30 ºC , $T_{des}$ = 90 ºC and $T_{ads}$ = 30 ºC (a) Vapor pressure (Pa), (b) Temperature (K) and (c) Water uptake ($kg.kg^{-1}$).

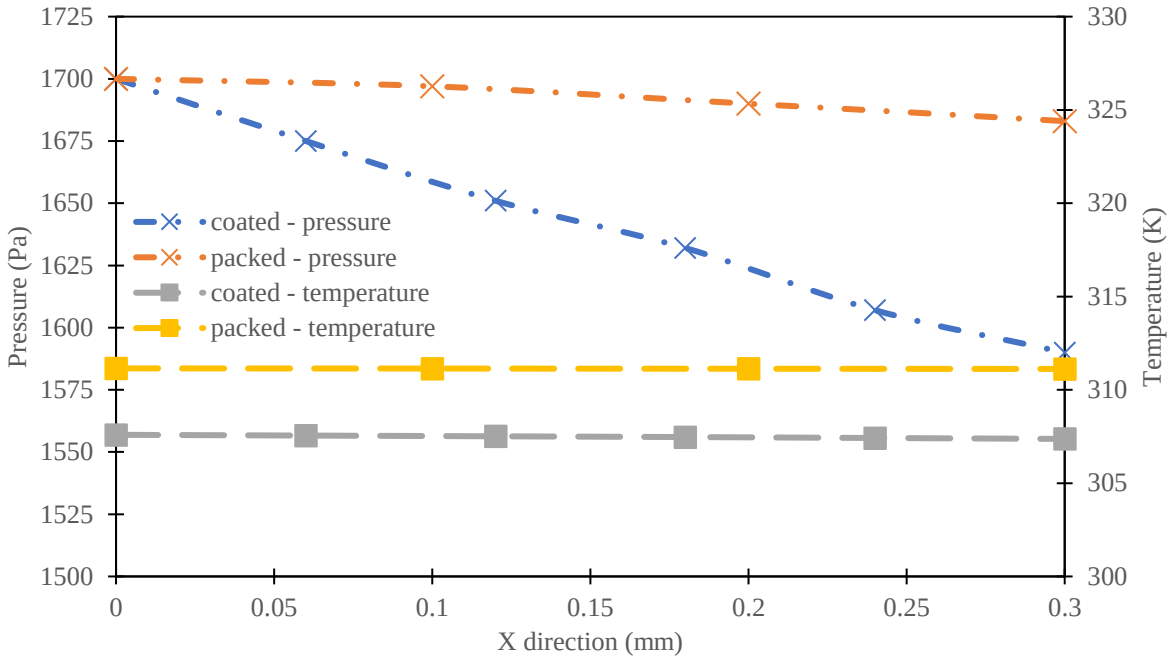



Figure 3-9. Pressure and temperature variation in combined packed and coated wire finned tube in the X-direction using tube diameter of 22mm and fin height of 20mm.

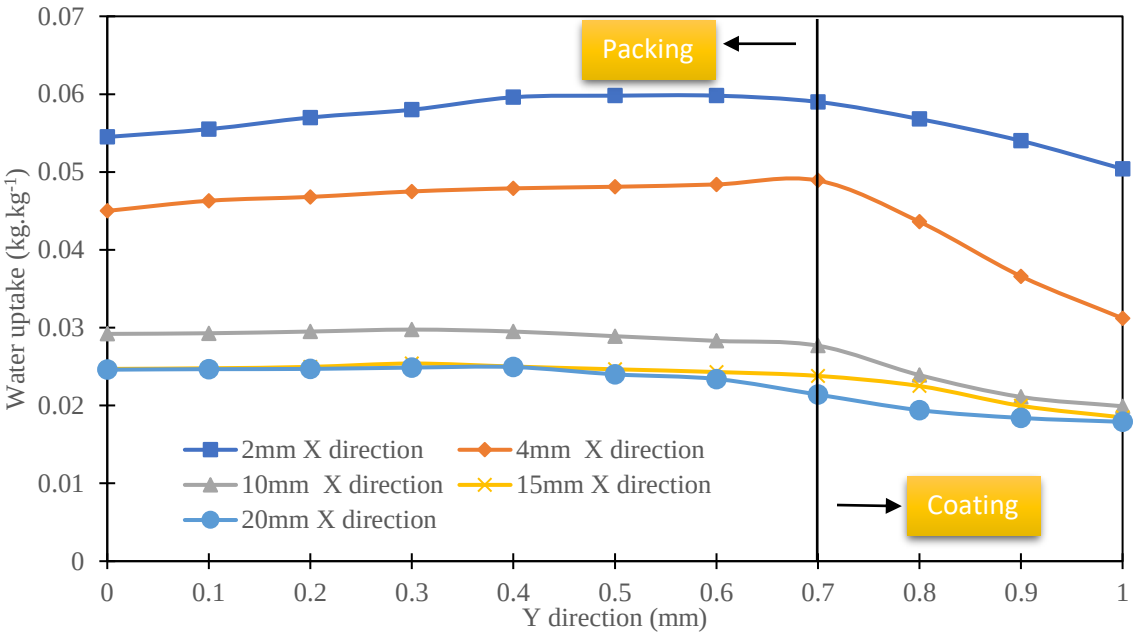



Figure 3-10. Water uptake variation in combined packed and coated wire finned tube in the Y-direction using tube diameter of 22mm and fin height of 20mm.

**Figure 3-11** compares the coated, packed and combined coated and packed wire finned tube at different tube geometry in terms of the SCP and SDWP. At tube diameter and fin height of 22 and 20mm respectively, at coated thickness of 0.3 and 0.5mm, the SCP and SDWP are 17.52 $L.kg^{-1}.day^{-1}$, 487

W.kg$^{-1}$ and 15.81 L.kg$^{-1}$.day$^{-1}$, 439 W.kg$^{-1}$, respectively. The combined packed and coated adsorbent has a drop in overall adsorbent performance as the SDWP is decreased to less than 4.7 L.kg$^{-1}$.day$^{-1}$. While the packed wire finned tube has the lowest SDWP (2.17 L.kg$^{-1}$.day$^{-1}$) and SCP (60.3 W.kg$^{-1}$). Therefore, the combination of the packed and coated adsorbent material has the advantage of enhancing heat transfer by eliminating the thermal contact resistance and increasing the thermal conductivity of the adsorbent material compared to the packed type. The same observation was found with different wire-finned tube geometry (tube diameter of 22mm and fin height of 10mm) as shown in Figure 3-12. However, higher SCP (532.5 W.kg$^{-1}$) and SDWP (19.17 L.kg$^{-1}$.day$^{-1}$) were found at smaller fin height coated wire finned tube with a coating thickness of 0.3mm.

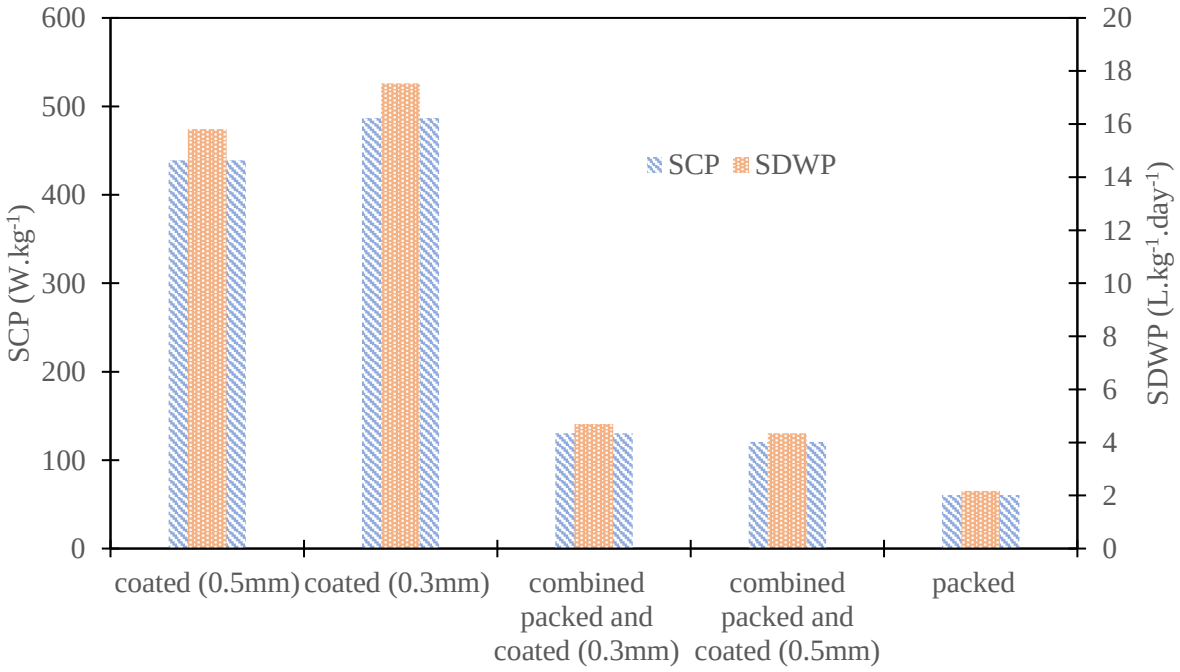



Figure 3-11. Effect of packed, coated and combined wire finned tube on SCP and SDWP using tube diameter of 22mm, fin height of 20mm.

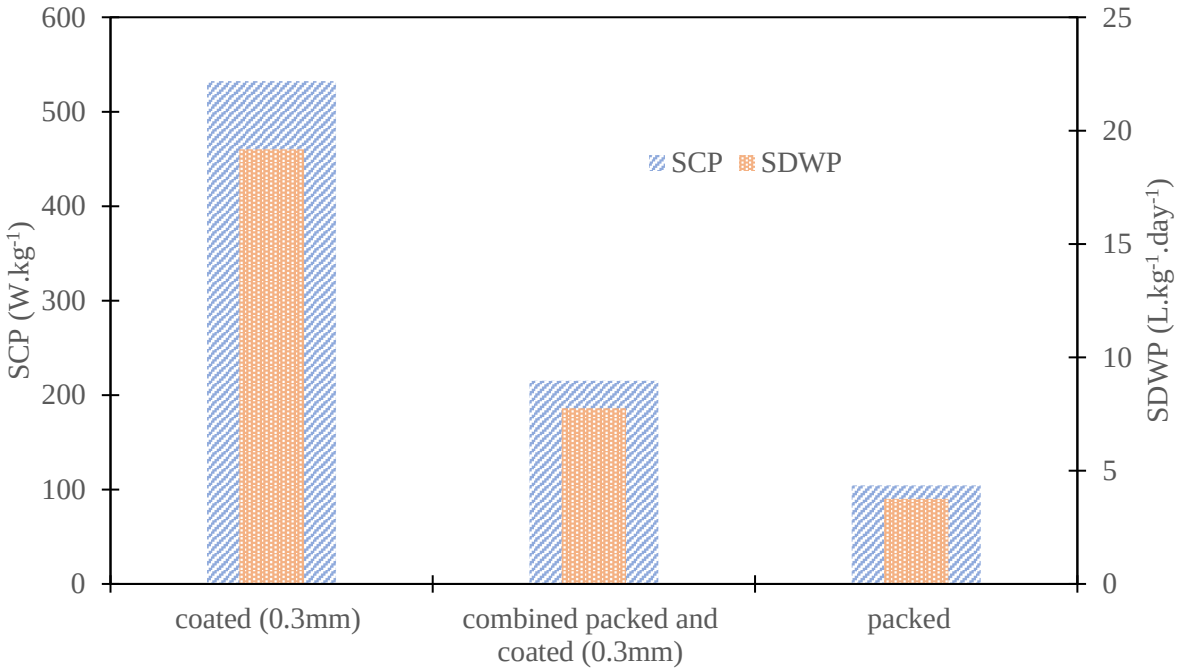



Figure 3-12. Effects of packed, coated, and combined wire finned tube on SCP and SDWP using tube diameter of 22mm, fin height of 10mm.

### 3.4.1. Optimisation of wire finned coated heat exchanger geometry

Based on the above results, it is clear that the coated wire finned tube heat exchangers outperform the packed and the combined coated and packed wire finned heat exchanger. Therefore, in this section, a detailed parametric study of the wire finned geometry namely tube diameter, fin height and number of fins with fixed fin spacing of 2mm using a coating thickness of 0.3mm was carried out at a constant water flow rate to establish the wire fin geometry that produces the highest performance in terms of SCP and SDWP. **Figure 3-13** shows the effect of the wire finned geometry on SCP and SDWP where increasing the fin height from 7 to 20mm has a negative impact on the SCP and SDWP at different tube diameters and a number of fins. For example, at tube diameter of 10mm and 20 fins, the SCP and SDWP decreased from 585 $W.kg^{-1}$ and 21 $L.kg^{-1}.day^{-1}$ to 539 $W.kg^{-1}$ and 19.4 $L.kg^{-1}.day^{-1}$ when the fin height increased from 7 to 20mm. This reduction is considered relatively small compared to the effect of increasing the tube diameter and number of fins. Decreasing the performance of the adsorbent material is due to the lower velocity in the tube when the tube diameter increased. Moreover, using a larger tube

diameter with higher number of fins results in having more adsorbent material that can be coated on the surfaces which requires more thermal energy compared to the smaller diameters.

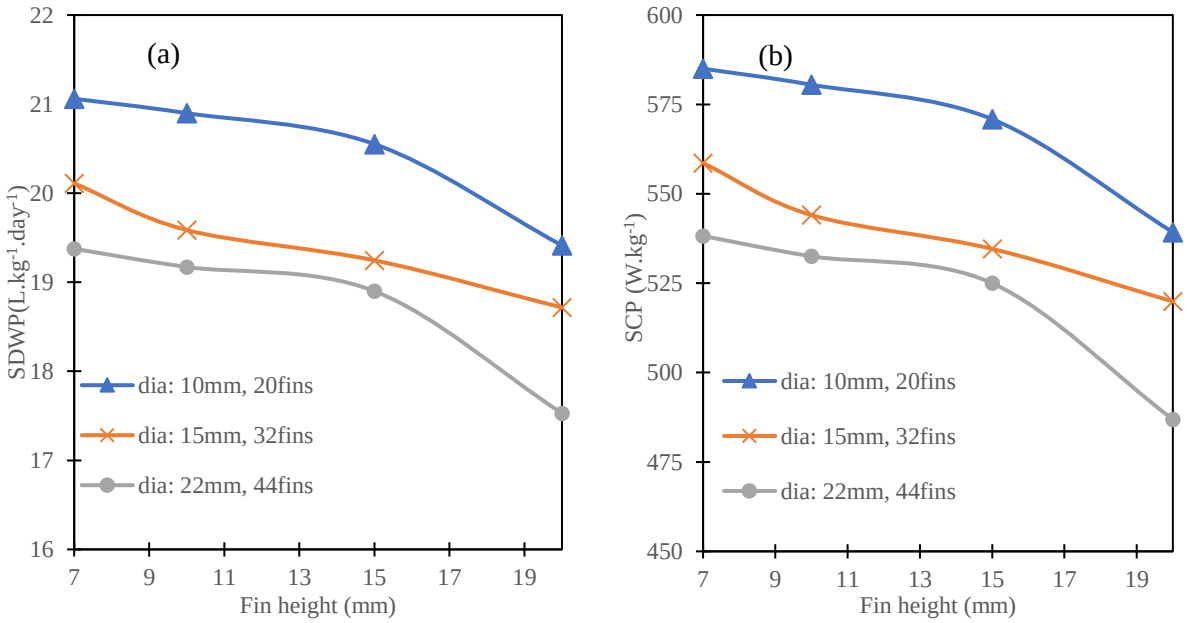



Figure 3-13. Effect of fin height on (a) SDWP and (b) SCP using different tube diameters and fin numbers.

Despite the lower performance of the larger tube diameter, it can be coated with more adsorbent material than the smaller tube diameter particularly, if a compact adsorber bed design with less amount of metal mass is required. Thus, a case study was investigated to design an adsorption cooling and desalination system that can produce 300L/day of fresh water and around 8kW of cooling power using two adsorber bed systems. The wire-finned tube heat exchanger module which is placed in the chamber is restricted in its length and width to 600 and 400 mm respectively, while its height depends on the required number of coated wire-finned tube heat exchanger modules. A number of single coated wire finned tubes are fitted in a heat exchanger module as shown in **Figure 3-14.**

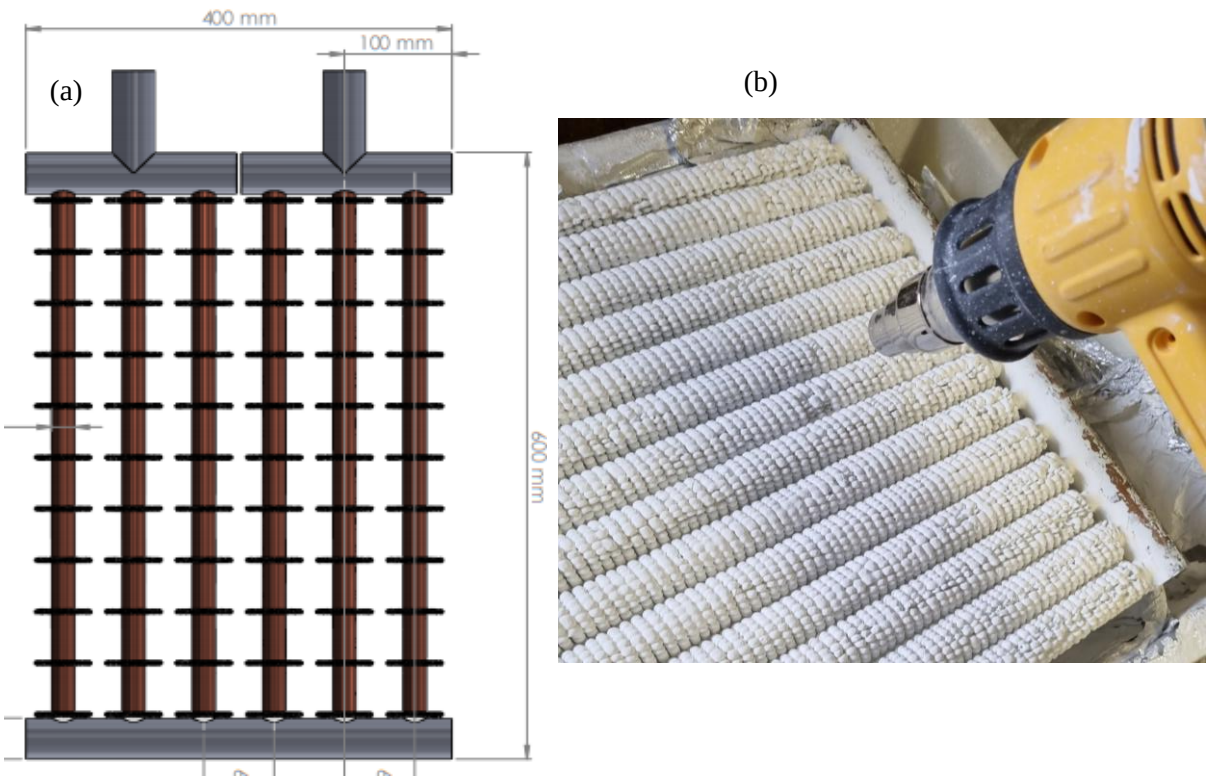



Figure 3-14. Coated wire finned heat exchanger module (a) module geometry, (b) module after coating.

The number of the single tubes in the module is varied with the tube diameter and fin height as shown in **Table 3-4.** The height of the adsorber bed depends on the required number of modules with a vapor gap of 4mm between the modules.

Table 3-4. Heat exchanger module dimensions (coating thickness = 0.3mm)

| Module length (mm) | Module width (mm) | Outer tube diameter (mm) | Number of fins | Fin spacing (mm) | Fin thickness (mm) | fin height (mm) | number of tubes in module | Adsorbent mass per module (g) | Metal mass per module (g) |
|---|---|---|---|---|---|---|---|---|---|
| 600 | 400 | 10 | 20 | 2 | 1 | 7 | 15 | 255 | 4864 |
| | | | | | | 10 | 12 | 292 | 4852 |
| | | | | | | 15 | 9 | 329 | 4861 |
| | | | | | | 20 | 7 | 341 | 4705 |
| | | 15 | 32 | | | 7 | 12 | 327 | 6358 |
| | | | | | | 10 | 10 | 390 | 6962 |
| | | | | | | 15 | 8 | 468. | 7290 |
| | | | | | | 20 | 7 | 547 | 7884 |
| | | 22 | 44 | | | 7 | 10 | 375 | 8589 |
| | | | | | | 10 | 9 | 482 | 9251 |
| | | | | | | 15 | 7 | 564 | 9265 |
| | | | | | | 20 | 6 | 644 | 9715 |

The daily water production (DWP) and cooling power (CP) are calculated as follows:

$$\boldsymbol{DWP = SDWP * M_{ads}} \quad (4.13)$$

$$\boldsymbol{CP = SCP * M_{ads}} \quad (4.14)$$

Where $M_{ads}$ is the adsorbent material mass.

While the required adsorbent material in each bed to produce 300L/day is calculated using the following equation:

$$\boldsymbol{M_{ads} = \frac{300}{SDWP}} \quad (4.15)$$

Then the metal mass can be obtained based on the required adsorbent material mass and the module dimensions as shown in **Table** 3-4**.**

Figure 3-15 shows the daily water production and cooling power per heat exchanger module that can be produced using different wire-finned configurations.

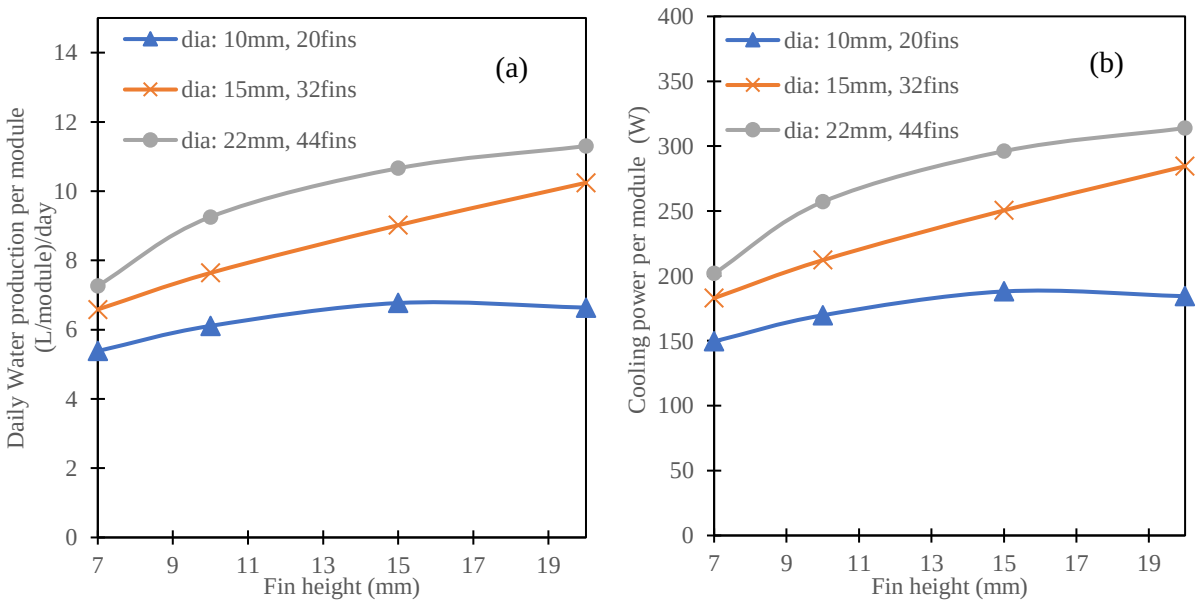



Figure 3-15. (a) Daily water production and (b) cooling power per module at different coated wire finned tube geometry.

The daily water production and cooling power increased from 5.38 L/day and 149.5 W to 11.3 L/day and 314 W, when the tube diameter and fin height increased from 10 and 7mm to 22 and 20mm, respectively. However, due to the lower SDWP and SCP of tube diameter and fin height of 22 and

20mm, it requires more adsorbent material and metal masses to produce 300L/day and around 8kW of cooling power compared to smaller tube sizes as shown in Figure 3-16

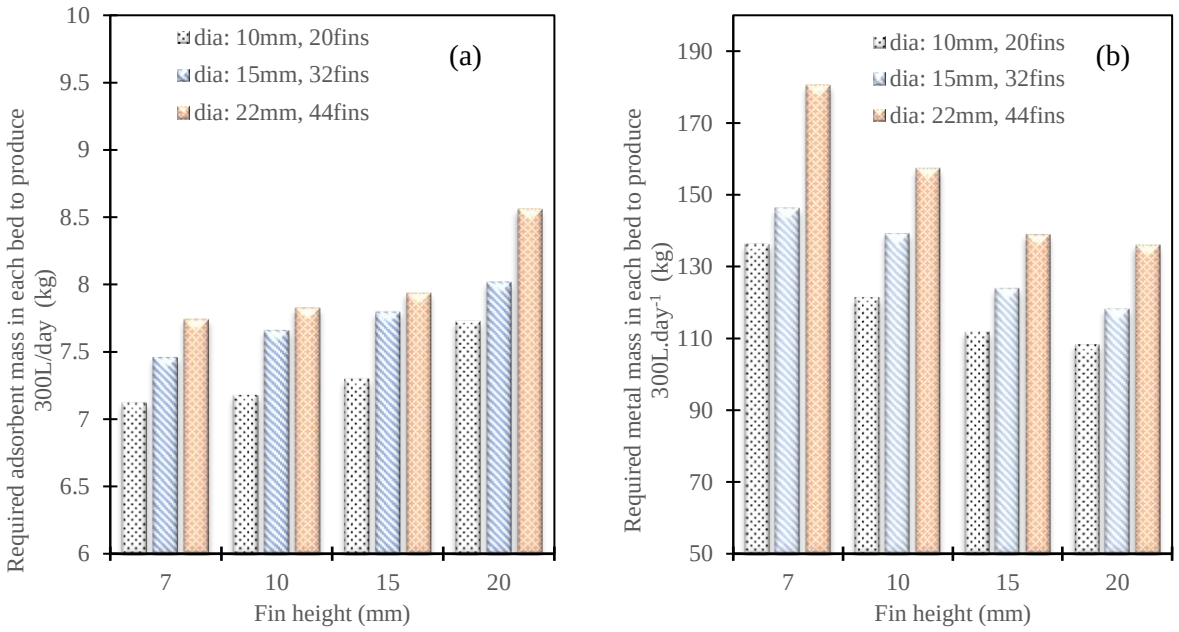



Figure 3-16. (a) Required adsorbent and (b) metal mass at different coated wire finned tube geometry.

At tube diameter of 10mm and fin height of 7mm, 7.12 kg of adsorbent material mass and 136.2 kg of metal mass in each adsorber bed are required with the metal-adsorbent mass ratio of 19.12. This ratio is considered a high ratio for the adsorption system as it requires high thermal energy to heat up and cool down the metal mass before reaching the adsorbent material mass. At tube diameter of 22mm and fin height of 20mm, the required adsorbent mass is increased to 8.55 kg, while the required metal mass is almost identical (136 kg) compared to tube diameter of 10mm and fin height of 7mm. Thus, the metal-adsorbent mass ratio decreased to 15.9. The lowest amount of metal mass (108.2 kg) can be achieved at tube diameter of 10mm and fin height of 20mm which requires an adsorbent mass of 7.72 kg. However, the metal-adsorbent mass ratio is high (23.3) at this configuration.

Figure 3-17 shows the required bed height to accommodate the required amount of adsorbent to produce 300L/day of fresh water. At a tube diameter of 10mm, the bed height varies from 812 to 1265mm at different fin heights, while at a tube diameter of 15mm, the bed height is between 782 and 900mm. The bed height ranges between 861 and 938mm at a tube diameter of 22mm. Therefore, the most compact design is obtained using a tube diameter of 15mm, followed by 22mm tube diameter.

Therefore, the selection of the best tube configuration should be specified according to the requirements which can be classified into; the highest adsorbent material performance, the required adsorbent and metal masses and the volume of the space that the heat exchanger occupies to produce the same amount of water and cooling capacity. In terms of the highest performance, this can be achieved by a tube diameter of 10mm, fin height of 7mm and 20 fins per loop. In terms of the volume space which represents the compactness of the adsorber bed, this can be achieved using a tube diameter of 15 or 22mm, especially at fin height between 15 and 20mm. In terms of the minimum amount of metal mass, this can be obtained using a tube diameter of 10mm and fin height of 20mm. In terms of the minimum amount of adsorbent mass, this can be found at a tube diameter of 10mm and fin height of 7mm. while the minimum metal-adsorbent mass ratio can be achieved using a tube diameter of 22mm and fin height of 20mm.

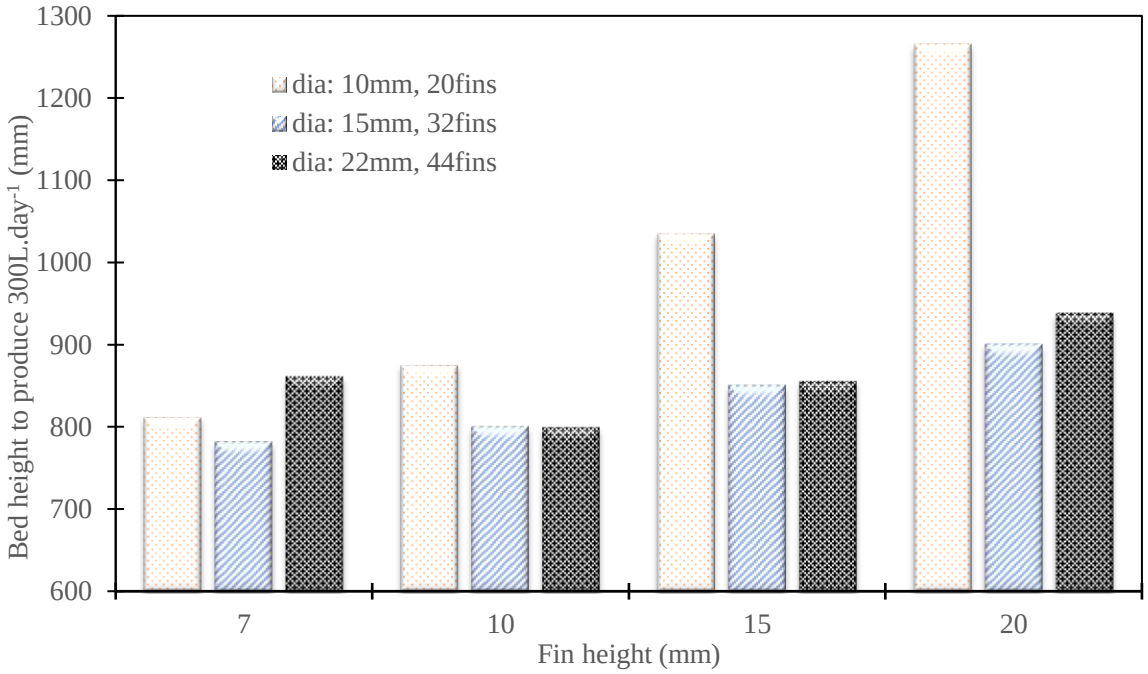



Figure 3-17. The bed height at different coated wire finned tube geometry.

The best four-wire finned tube configurations (tube diameter: 15 and 22mm and fin height: 15 and 20mm) that provide a compact adsorber bed design were selected to study the effect of the coating thickness on the adsorbent material performance as shown in **Figure 3-18.** It is observed that increasing the coating thickness from 0.3 to 0.5mm has a negative impact on the SCP and SDWP. At tube diameter

of 22mm and fin height of 20mm, the SCP and SDWP decreased from 487 $W.kg^{-1}$ and 17.52 $L.kg^{-1}.day^{-1}$ to 439.2 and 15.81 $L.kg^{-1}.day^{-1}$, respectively, when the coating thickness is increased from 0.3 to 0.5mm. The reduction in the performance is due to the increase in the mass transfer resistance of the vapor flow through the voids between the adsorbent material. The mass resistance increases the vapor pressure drop which will lead to a decrease in the water uptake of the adsorbent material. Despite the reduction of the material performance, it can still provide more water and cooling production per unit volume as a result of having more adsorbent material mass on the fins surfaces.

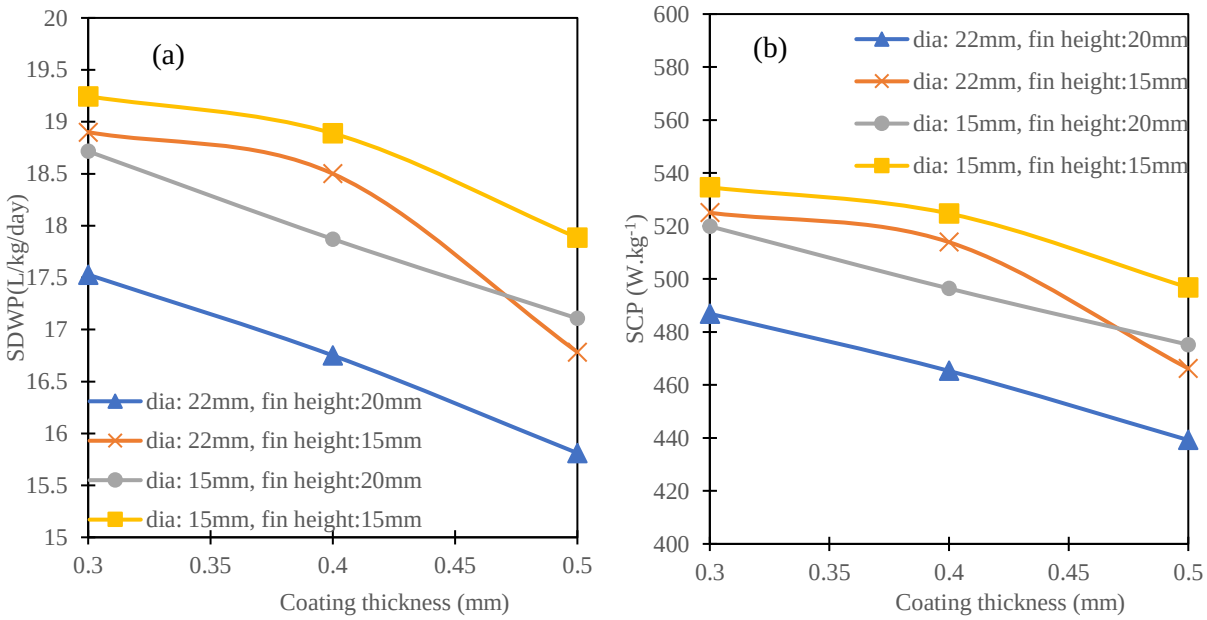



Figure 3-18. Effect of coating thickness on (a) SDWP and (b) SCP at different coated wire finned geometries.

**Figure 3-19** shows the required amount of adsorbent and metal masses in each bed to produce 300L/day of fresh water using different coating thicknesses and four-wire finned tube configurations. At tube diameter of 22mm and fin height of 20mm, it requires the maximum amount of the adsorbent material (9.48 kg) to deliver the required production using a coating thickness of 0.5mm. The amount of adsorbent material mass can be decreased when the tube diameter, fin height or coating thickness decreases, since the performance of the adsorbent material is higher at these conditions. A crucial advantage is observed when the coating thickness is increased, the required amount of metal mass is significantly decreased. This leads to gaining a low metal-adsorbent mass ratio in the coated wire finned tube since the ratio decreases to 9.2 when the coating thickness is increased to 0.5mm. On the other

hand, the coating thickness of 0.3mm needs a large metal mass to deliver the required amount of water and cooling production. At the same tube configuration, an increase in the metal mass of 55% is required when the coating thickness is decreased from 0.5 to 0.3mm, while only an increase of 9.8% of the adsorbent material mass is required. The minimum amount of the required metal mass was found using tube diameter of 15mm and fin height of 15 and 20mm at a coating thickness of 0.5mm, which requires only around 80kg of metal mass.

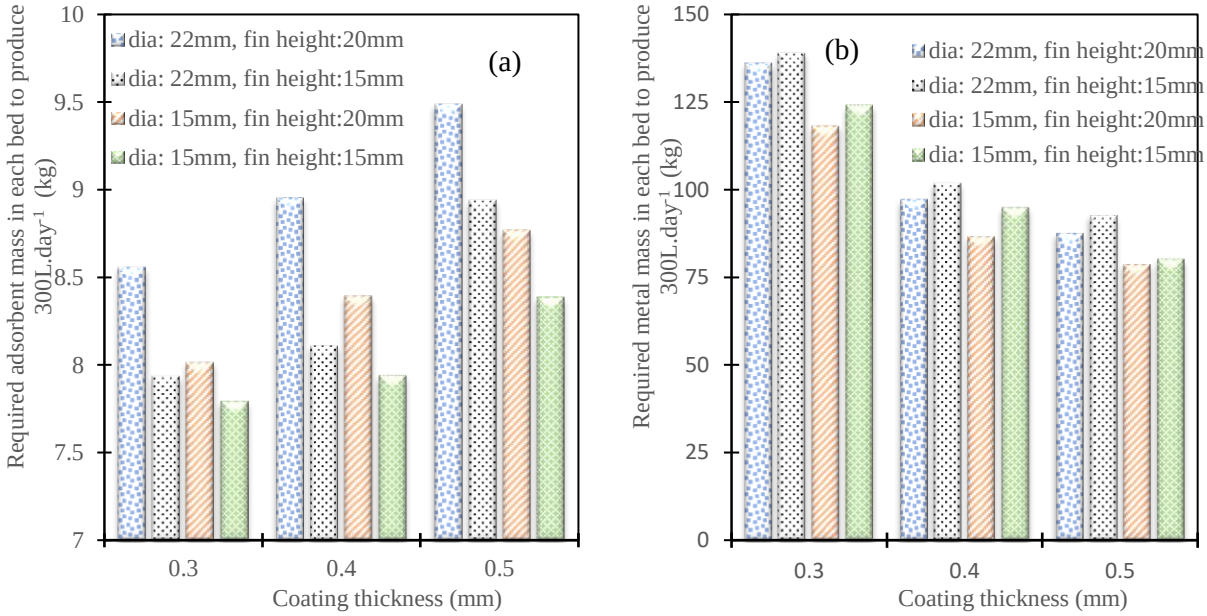



Figure 3-19. Required (a) adsorbent and (b) metal mass at different coating thickness.

**Figure 3-20** shows the effect of increasing the coating thickness on the height of the adsorber bed to produce the required amount of water and cooling power. As the metal mass and metal-adsorbent material mass ratio are significantly decreased when the coating thickness is increased from 0.3 to 0.5mm, the bed height will decrease. By using the same four-wire finned tube configurations, the bed height is larger than 850 mm at coating thickness of 0.3mm, while at coating thickness of 0.4mm, the bed height decreased to less than 670mm. The minimum bed height of less than 600mm was found at coating thickness of 0.5mm. Therefore, using a thicker coating layer has an advantage over thinner coating layers in terms of the compactness of the adsorber bed design.

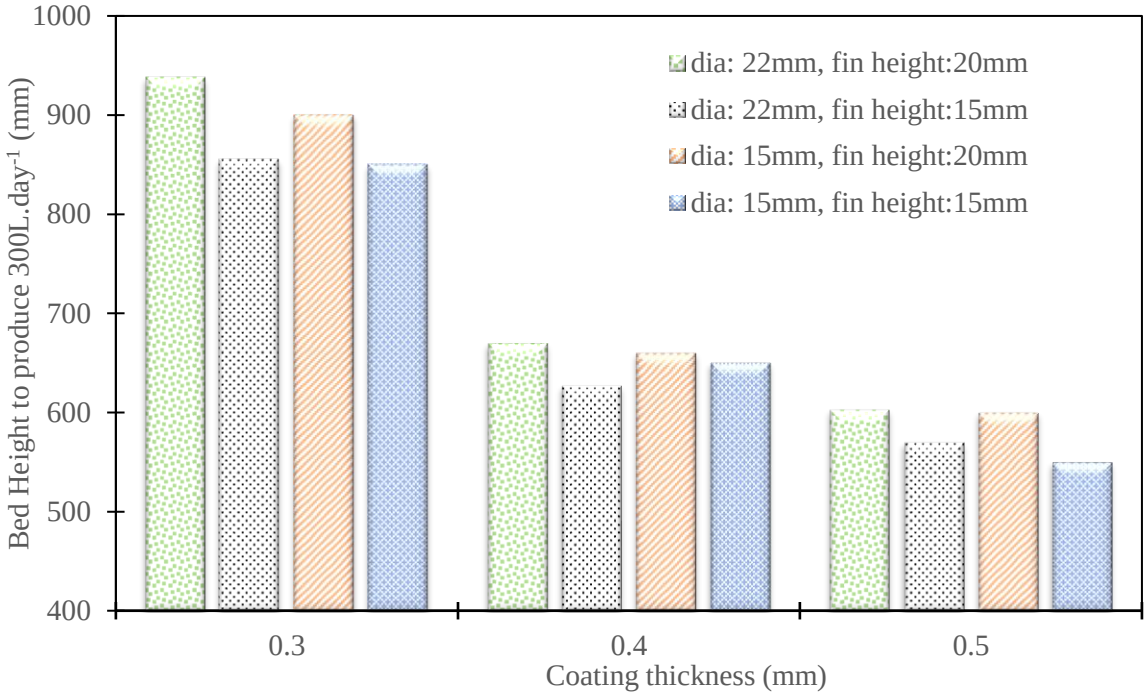



Figure 3-20. Bed height at different coating thickness.

### *3.4.2.* Effect of operating conditions

The evaporation temperature in the adsorption system is an important parameter that needs to be understood especially with aluminum fumarate MOF material. Due to the S shape of the isotherm of this material, increasing the evaporation temperature has a significant positive effect on the adsorbent material performance. The water heating temperature in the desorption process is another parameter that needs to be investigated in the coated wire finned tube. **Figure 3-21** shows the effect of the evaporation temperature and water heating temperature (desorption temperature) on the SCP and SDWP at condensation and adsorption temperatures of 30°C using tube diameter of 22mm and fin height of 20mm at coating thickness of 0.5mm. Increasing the evaporation temperature from 7 to 20°C, enhances the SCP and SDWP from 81.9 $W.kg^{-1}$ and 2.94 $L.kg^{-1}.day^{-1}$ to 537 $W.kg^{-1}$ and 19.35 $L.kg^{-1}.day^{-1}$. While increasing the desorption temperature from 60 to 90°C produced a slight improvement on the adsorbent performance of 22% (from 12.92 to 15.81 $L.kg^{-1}.day^{-1}$). This phenomenon provides an advantage of this material over the conventional adsorbent material as it can be operated by low-grade thermal energy that can be obtained from the waste heat or solar energy.

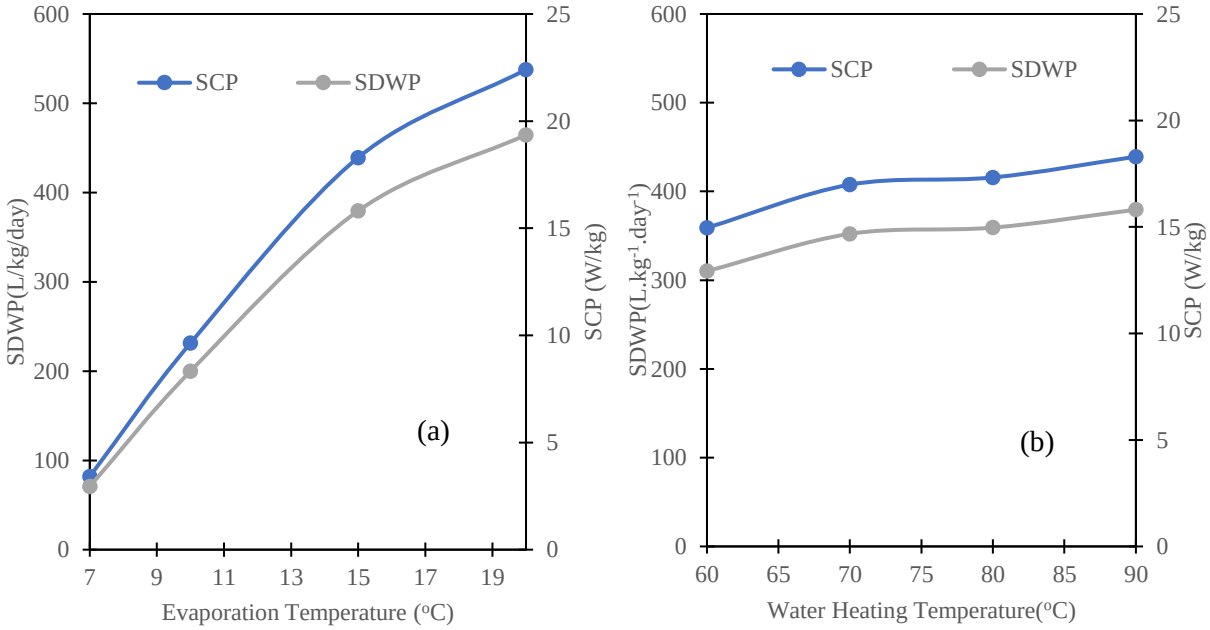



Figure 3-21. Effect of evaporation and water heating temperatures on the (a) SDWP and (b) SCP using tube diameter of 22mm and fin height of 20mm and coating thickness of 0.5mm.

## 3.5. Conclusions

A 3D heat and mass transfer model with a variable vapor pressure using a coupled solution approach is developed for packed/coated adsorber beds using aluminum fumarate MOF and the following have been concluded:

a. The coated wire finned tube has a better performance compared to the packed and the combined packed/coated adsorber beds in terms of specific cooling power and specific daily water production. Using a combined packed/coated wire finned tube with coating thickness ranging from 0.3 to 0.5mm has better performance than the packed wire finned tube, since this design combines the enhancement in the heat transfer in the coated adsorbent layer and the decrease in the mass transfer resistance in the packed adsorbent material.

b. Increasing the fin diameter, fin height and coating thickness at the same thermal fluid flow rate will decrease the SDWP and SCP of the adsorption system. However, increasing the fin height from 7 to 20mm has only a slight impact on the performance compared to tube diameter and coating thickness.

c. Using tube diameter of 10mm, fin height of 7mm, 20 fins, fin spacing of 2mm and coating thickness of 0.3mm has the highest SCP (585 $W.kg^{-1}$) and SDWP (21 $L.kg^{-1}.day^{-1}$) at evaporation temperature of 15°C, condensation and adsorption temperature of 30°C and desorption temperature of 90°C. When a case study of producing 300L/day of fresh water is investigated, it was found that the most compact design is achieved at tube diameters of 15 and 22mm and fin height of 15 and 20mm if coating thickness ranging from 0.3mm to 0.5mm is used. At a coating thickness of 0.3mm, the minimum amount of metal mass is achieved using a tube diameter and fin height of 10 and 20mm respectively. Since the amount of metal mass is the lowest at this configuration, it will require less amount of thermal energy to heat up the adsorbent material. Finally, the lowest metal-adsorbent mass ratio is obtained using a tube diameter of 22mm, fin height of 20mm and coating thickness of 0.5mm which has a ratio of 9.2.

d. The evaporation temperature has a significant impact on the aluminum fumarate MOF coated wire finned tube as increasing the temperature from 7 to 20°C, enhances the SDWP from 2.94 to 19.3 $L.kg^{-1}.day^{-1}$. While the desorption temperature has a slight impact on the SDWP (around 22% enhancement) when the temperature increases from 60 to 90°C.

# Chapter 4: Effect of adsorber bed heat exchanger modules connection method on a scaled-up adsorption system – Numerical and Experimental investigations

This chapter uses the numerical model developed in chapter 3 to study the effect of the method of connecting multiple heat exchanger modules on the performance of a scaled-up adsorption system. The developed coupled modelling approach is efficient when the computational domain is large. The modelling results are validated by experimental work using an adsorption system fitted with multiple rectangular finned tube modules packed with granular aluminum fumarate MOF material.

This chapter is based on a published work presented in the following journal paper:
**I. Albaik**, M. Badawy Elsheniti, R. Al-Dadah, S. Mahmoud, İ. Solmaz, Numerical and experimental investigation of multiple heat exchanger modules in cooling and desalination adsorption system using metal-organic framework, Energy Convers. Manag. 251 (2022) 114934.
https://doi.org/10.1016/j.enconman.2021.114934.

**Credit Authors statament:**

**I.Albaik:** Developing the numerical model using the coupled solution approach, building the adsorption system with the control system, conducting the experimental works, analyzing the numerical and experimental results, and writing the outcomes of the study. **M. Badawy Elsheniti:** Technical support in using the COMSOL multiphysics software. **R. Al-Dadah and S. Mahmoud:** Reviewing and supervision, **M. Ismail:** Project funding and administration

## 4.1. Abstract

The cooling and desalination adsorption system is a heat-activated system based on the solid sorption process. The main challenge in this system is to decrease the energy consumption of this system while maintaining good performance. A scaled-up adsorption system, using multiple heat exchanger modules, packed with commercially available metal-organic framework material that operates at low

desorption temperature (less than 90°C), was numerically and experimentally investigated in the present paper. Three-dimensional and two dimensional-axisymmetric numerical models were developed to simulate heat and mass transfer phenomena, considering the internal and external mass transfer in the adsorbent domains. Effects of the modules' connection methods and vapor gap between modules on the system performance were investigated. The highest coefficient of performance was achieved when connecting the modules in series, due to the considerable reduction in the heating power. However, the highest specific cooling power and water daily production are achieved using the parallel connection method due to the increased amount of adsorbate released. It is also found that the optimum vapor gap is variable with the length of the heat exchanger module in which the longer the module, the larger gap is required to minimize the pressure drop between the modules. Additionally, a scaled-up adsorption cooling/desalination system using 23.2 kg of Aluminium Fumarate packed in 16 modules connected in series, was constructed and evaluated experimentally. The system produced desalinated water of 201 L/day and a cooling capacity of 5.25 kW at the evaporator, condenser, and desorption water temperatures of 24°C, 25°C, and 85°C, respectively. The specific daily water production decreased by 16.3% when the water salinity increased from 90 to 100,000 ppm, while the lowest specific electrical energy consumption of the proposed system is 1.87 kWh/$m^3$. The theoretical and experimental results will enable further scaling up of an efficient MOF adsorption system for cooling and water desalination.

## 4.2. Brief introduction and purpose of the study

The heat and mass transfer models, including the internal and external mass transfer resistances in two and three-dimensional geometries, are the most advanced and powerful simulation methods since they can solve the high degree of non-linearity of the partial differential equations especially when the model requires a huge computational domain to solve. This study aims at investigating the performance of a scaled-up MOF adsorption desalination/cooling system in which multiple heat exchanger modules are used. Therefore, 2D axisymmetric and 3D numerical models, based on the transient distributed parameter fully coupled approach that considered the internal and external mass transfer in the adsorbent domain were used. In addition, the 2D model is also integrated with the energy, momentum,

and mass balance equations of two domains namely the heat transfer fluid and the vapor gap between the heat exchanger modules. The results of the 2D axisymmetric model are first verified with the 3D numerical model, then the validation is confirmed by using the experimental data from the scaled-up system. Using the developed numerical modelling, the effect of the gap between heat exchanger modules and the modules' connectivity (series or parallel) on the system performance is investigated. Finally, this study experimentally investigates the development of a scaled-up adsorption system using 23.2 kg of AF packed in 16 modules (8 in each bed connected in series) for cooling and desalination applications and results were compared to those predicted by numerical modelling showing a good agreement (maximum deviation of 6.67%). This study also investigates the effect of a wide range of water salinity on the adsorption system performance, when a flooded evaporator is used.

## 4.3. Method (Numerical Model):

3D and 2D-axisymmetric transient local equilibrium models are developed. The 3D model consists of four domains (thermal fluid, metal tube, solid fins, and adsorbent material), while the 2D-axisymmetric model has five domains as the vapor domain of the vacuum chamber is added with inlet/outlet refrigerant vapor (water) from/to evaporator/condenser as shown in Figure 4-1.

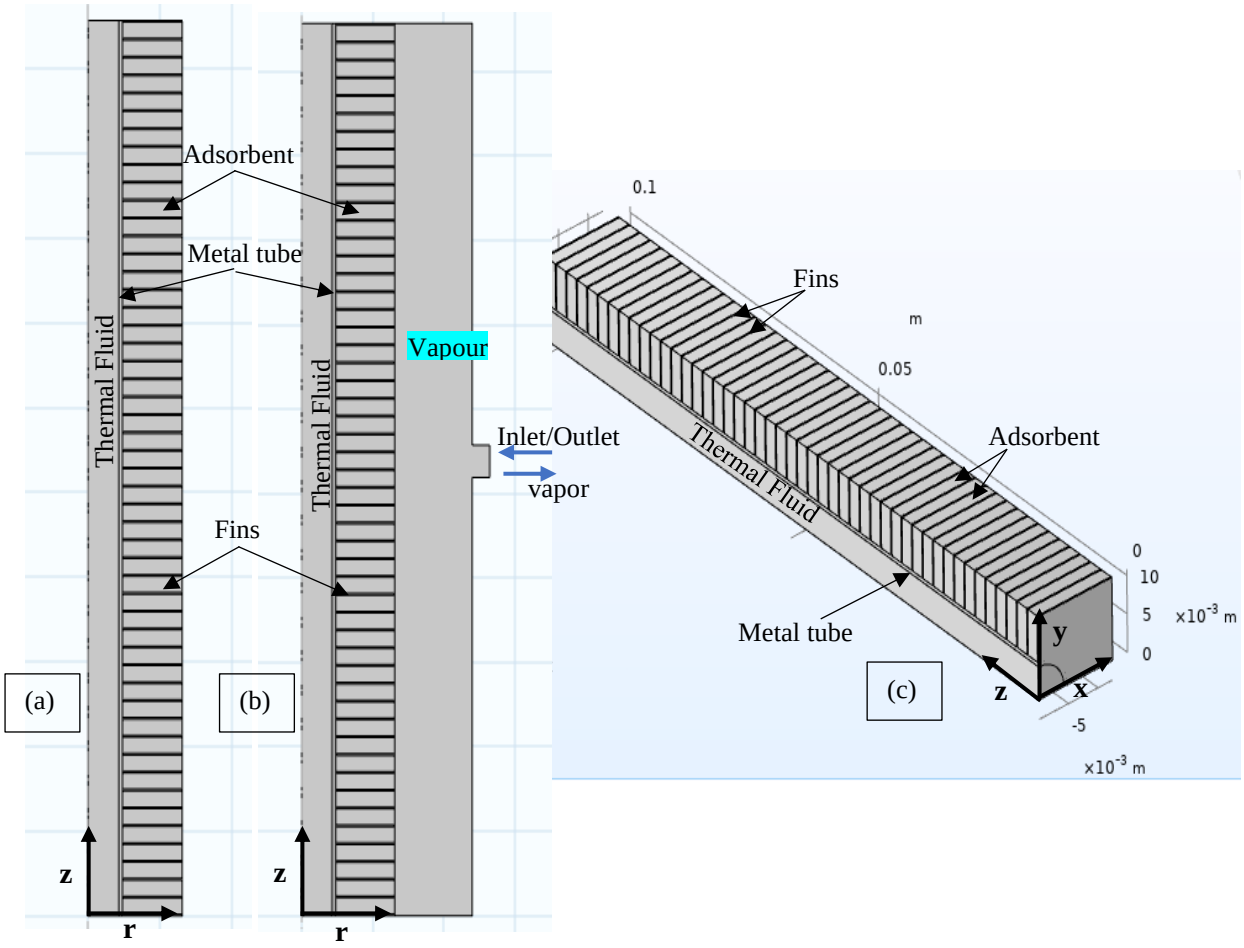



Figure 4-1. Computational domains of the packed finned tube heat exchanger (a) 2D *Axisymmetric* circular fins without vapor domain, (b)2D *Axisymmetric* circular fins with vapor domain and (c)3D rectangular fins

The effect of various geometric parameters of the rectangular fins in the packed heat exchanger modules can only be studied in 3D models. Thus, to simplify the modelling, it was converted to a 2D-axisymmetric model where the rectangular fins are converted to circular fins with an equivalent diameter to have the same adsorbent material between every two fins. This model can simulate the water uptake, temperature, velocity, and pressure distributions in the adsorbent material between the fins. The adsorption system performance can also be studied as the model is set up to include the cyclic operation (adsorption, desorption and switching) of the system. AF in granular particle form is used as the adsorbent material in this study with metal tubes and solid fins made of copper and aluminum, respectively. The input data of the thermophysical properties are illustrated in **Table 4-1,** while the fin and tube dimensions such as fins spacing, fin height, outer and inner tube diameter are 1.91mm, 8.5mm, 9.54mm and 8.54 mm, respectively.

*Table 4-1. Thermophysical properties of adsorbent material, tube and fins*

| Parameter | Value |
|---|---|
| Isosteric heat of adsorption (kJ/kg), $\Delta \boldsymbol{H_{ads}}$ | 2370 |
| Particle porosity (-), $\varepsilon_p$ | 0.67 |
| Particle diameter (mm), $d_p$ | 0.12 |
| Adsorbent bulk density (kg/m$^3$), $\rho_b$ | 520 |
| Specific heat of adsorbent (J/kg.K), $C_p$ | 970 |
| Thermal conductivity of metal tube (W/m.K), $k_t$ | 385 |
| Thermal conductivity of fins (W/m.K), $k_{fin}$ | 205 |
| Thermal conductivity of adsorbent material (W/m.K), $k_{ads}$ | 0.12 |
| Thermal conductivity of vapour (W/m.K), $k_g$ | 0.024 |
| Pre-exponential constant (1/s), $K_o$ | 1.29 |
| Activation Energy (J/mol), $E_a$ | 1.80E+04 |
| Ideal gas constant (J/mol.K), R | 8.314 |

The governing equations and assumptions are described in section 3.3.

The non-linear governing partial differential equations of the heat and mass transfer model are solved numerically using the finite element method of the COMSOL Multiphysics software. Four different physics are used to solve the mass, momentum and energy equations including the turbulent flow physics of the thermal fluid, the heat transfer physics that coupled the domains to calculate the temperature distributions, the porous and free media flow physics to calculate the vapor velocity and pressure in adsorbent and vapor domains and the Convection-Diffusion Equation to solve the kinetic equation coupled with the isotherm of the adsorbent. The heat transfer and turbulent flow physics are solved using the non-isothermal flow (Multiphysics). The turbulent flow physics of the thermal fluid is solved to obtain the variables of the thermal fluids such as the velocity and turbulent parameters. Then the coupled solution approach is used to solve three physics simultaneously. This approach is needed to solve the large computational domain to study the heat exchanger configurations (parallel or series) with a lower number of iterations, compared to the segregated solution approach, but it requires a large memory size to solve the non-linearity in the equations. By using the physics-controlled mesh with fine element size option in COMSOL Multiphysics (minimum element size of 0.006 mm and maximum size of 1.1mm), which is equivalent to 217,434 elements in tube length of 0.4m in the 2D axisymmetric model, the solution becomes independent of the mesh size as shown in Figure 4-2.

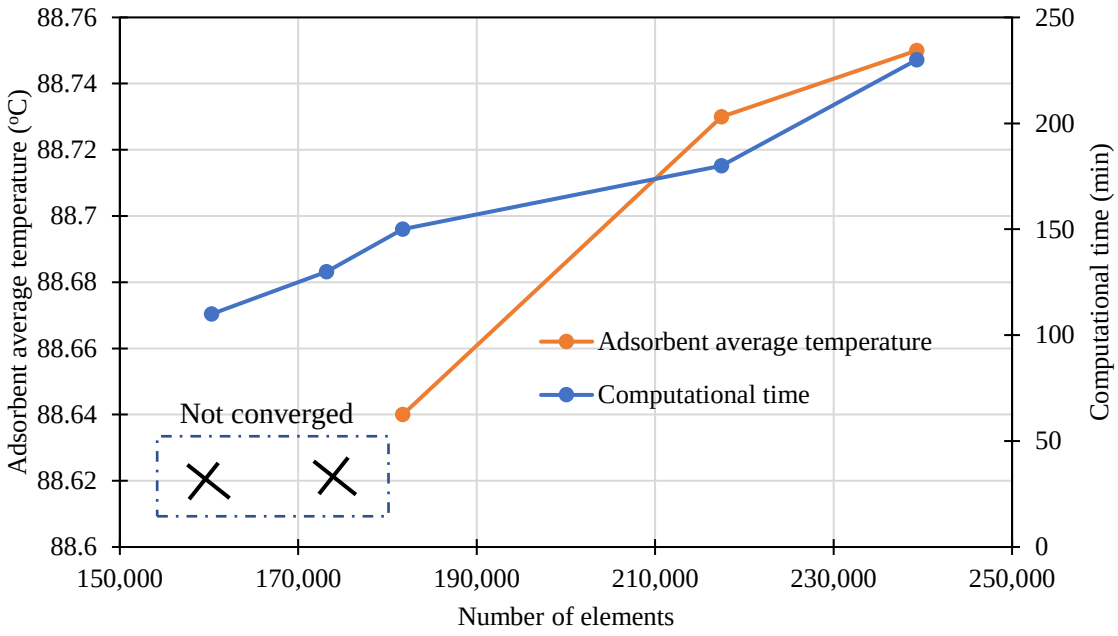



Figure 4-2. Mesh sensitivity analysis

The initial boundary conditions are set at the end of the desorption or preheating mode in order to dry the adsorbent material before starting the cycle. Thus, all the domains will be at the maximum thermal fluid temperature, while the initial vapour pressure is set to be the saturation pressure of the condenser. The boundary conditions of the model depend on whether the model has a vapor domain or not. If the model has a vapor domain, then the pressure of the inlet/outlet from/to the evaporator/condenser is set to be the saturation pressure of the adsorption/desorption process. If the model does not have a vapor domain, then the vapor pressure will be set at the outer surface of the adsorbent instead of the inlet/outlet vapor. The inlet thermal fluid temperature is the temperature of cooling/heating in adsorption/desorption process, while the outlet of the thermal fluid has a gauge pressure equal to zero. The boundary conditions can be summarized as shown in *Figure 4-3*.

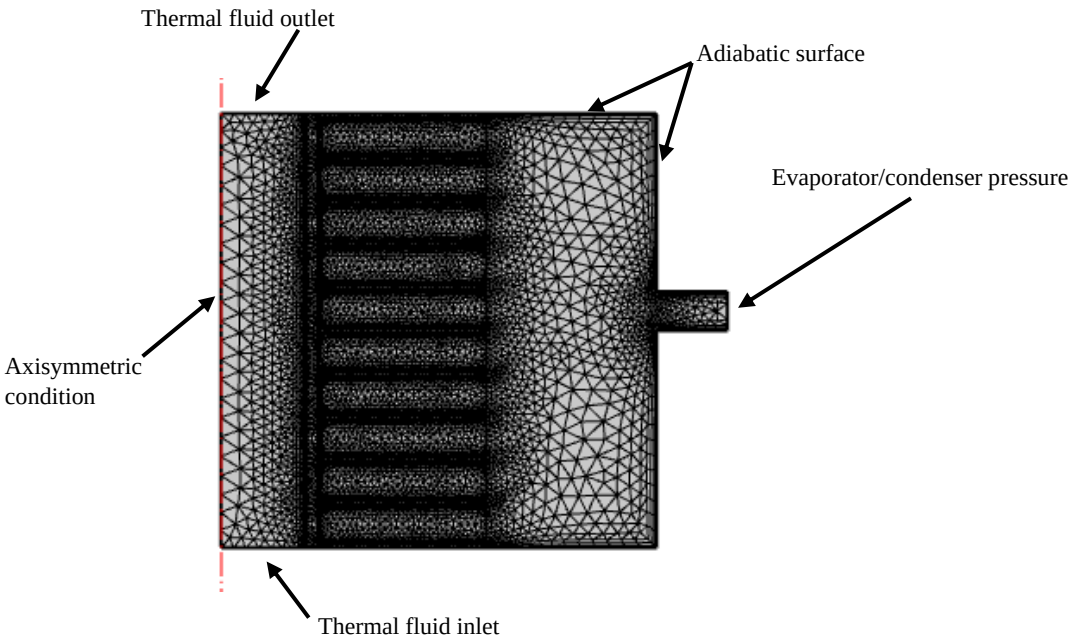



Figure 4-3. The boundary condition of the 2D axisymmetric model

In the 3D model, a symmetric boundary condition is applied to two side of the outer surface of the adsorbent as the domain of the finned tube is just a quarter of the tube. The overall performance indicators are evaluated after the system reaches the cyclic steady state condition.

## 4.4. Results and discussion (Numerical model):

Two models have been developed; three-dimensional and two-dimensional axisymmetric models. This simulation is carried out to prove that the three-dimensional model can be represented with an equivalent two-dimensional axisymmetric model by replacing the rectangular fins with a circular fin that can provide the same pressure, water uptake and temperature profile through the adsorbent material, means it can also provide the same performance as. **Figure 4-4** compares the predicted outer surface temperature of the adsorbent material of the 3D and 2D axisymmetric models, using the same amount of adsorbent material packed between the fins. It shows that the 2D axisymmetric model provides similar prediction to that of the 3D model. However, the 2D axisymmetric model requires 70% lower computational time compared to the 3D model, where only two hours were needed to model 0.4m tube length using 4 cycles of operation using PC core i7 (48GB RAM).

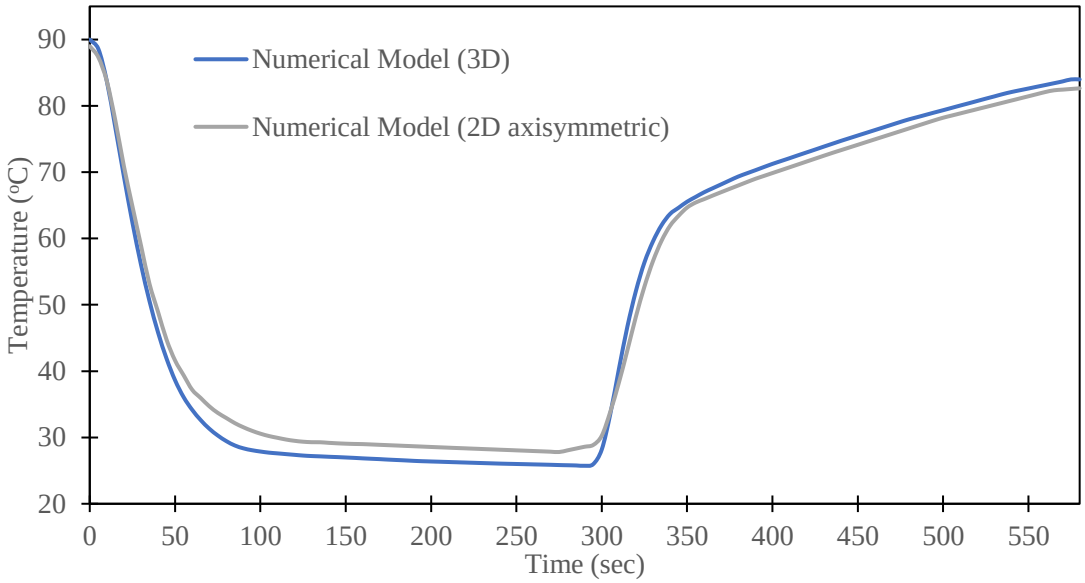



Figure 4-4. Outer surface temperature of the adsorbent material at pipe length of 20cm ($t_{cycle}$ = 250 sec, $t_{switching}$ = 40 sec, $T_{ad}$ = 25°C, $T_{des}$ = 85 °C at water flow rate of 27L/day, $T_{chilled}$ = 24°C and $T_{cond}$ = 25°C)

The vapor pressure, water uptake and temperature distributions of the 2D axisymmetric and 3D models are shown in **Figure 4-5.** At evaporator temperature of 15 °C and adsorption temperature of 30 °C, the pressure variations between the inner and outer surface of the adsorbent material ranges from 1 to 1.7 kPa in a 2D axisymmetric model, but between 0.9 and 1.7 kPa in the 3D model. This shows a very close pressure variation through the adsorbent material, indicating that the mass transfer resistance in both models are identical. The heat transfer resistances predicted by both models also indicates a good agreement where the temperature varies between 302 and 299 K and between 302 and 298 K in 2D axisymmetric and 3D models respectively. Based on the identical mass and heat transfer resistances, it is expected to obtain the same water uptake in both models **(see Figure** 4-5**(c)),** as the isotherm of the adsorbent is dependent mainly on the vapor pressure and adsorbent material temperature.

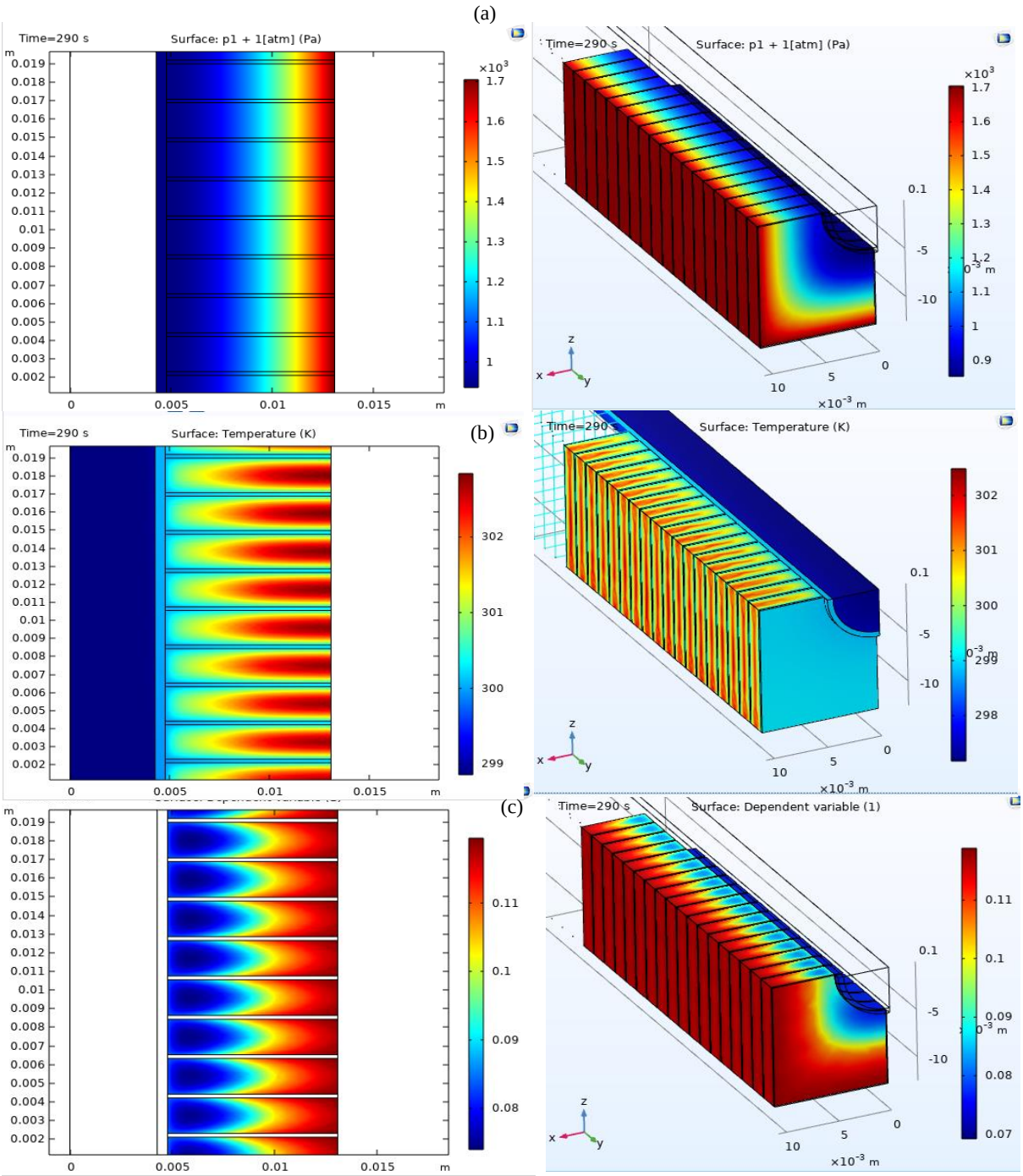



Figure 4-5. 2D axisymmetry and 3D models after 250 seconds of cooling (a) Vapor pressure distributions (Pa), (b) temperature distributions (K), and (c) water uptake (kg/kg). ($t_{cycle}$ = 250 sec, $t_{switching}$ = 40 sec, $T_{ad}$ = 25ºC, $T_{des}$ = 85 ºC at water flow rate of 27L/day, $T_{evaporator}$ = 24ºC and $T_{condenser}$ = 25ºC)

### 4.4.1. Effect of vapor gap between heat exchanger modules

When the adsorption system is scaled up, a number of heat exchanger modules should be used in the adsorber bed in order to deliver the required cooling and water production. The spacing between the heat exchanger modules in the adsorber bed affects the performance and size of the adsorber beds and the overall adsorption system. Therefore, the 2D axisymmetric model was used to investigate the effect of the gap between the heat exchanger modules in the adsorber bed. A heat exchanger module, with a length of 0.4m, and three vapor gaps (2, 4 and 5mm) have been investigated to predict the vapor pressure distribution along the vapor channel (vapor gap). The inlet/outlet vapor from/to evaporator/condenser is located at the middle of the module. Figure 4-6 shows the pressure variation for the adsorption process at a saturation temperature of 15$^{o}$C in the evaporator for the three gaps used. At a vapor gap of 2mm, there is a significant pressure drop between the inlet of the vapor and the last point of the vapor channel, which is varying from 1.7 to 1.28 kPa. This variation in pressure will adversely affect the performance of the module since the water uptake of the adsorbent is affected by the vapor pressure and adsorbent material temperature. Increasing the vapor gap to 4mm, resulted in pressure variation from 1.7 to 1.5 kPa, which increases the performance of the module as the last point of the vapor passage will have higher water uptake compared to a vapor gap of 2mm. Increasing the vapor gap further to 5mm, resulted in negligible vapor pressure variation in z-direction (direction of the water vapor flow). Thus, to have modules configuration that is independent of the vapor gap, the gap should be equal or higher than 5mm, and as the model is 2D axisymmetric, the vapor gap should be at least 10mm between each two heat exchanger modules.

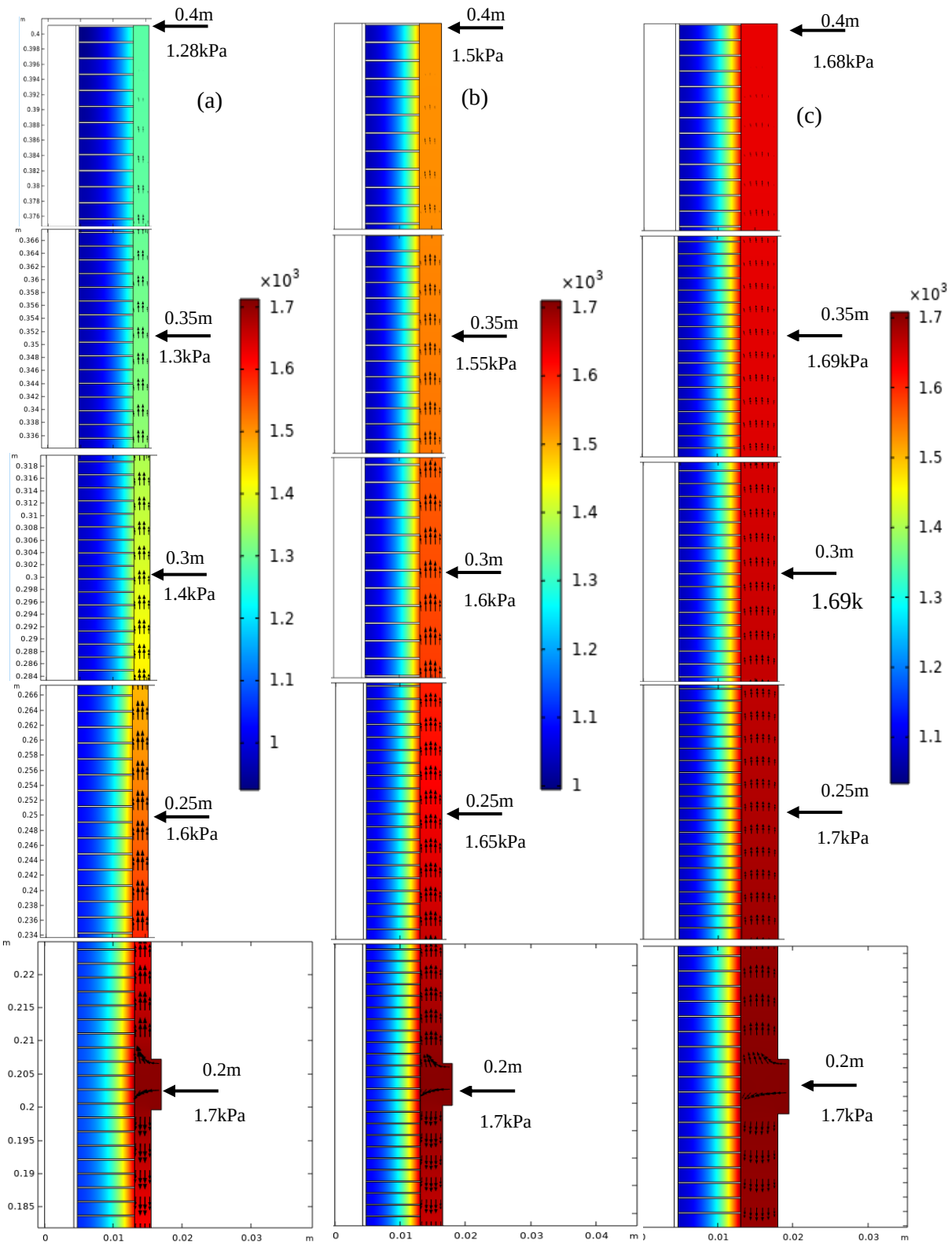



Figure 4-6. Effect of vapor gap between heat exchanger module on vapor pressure variation (a) 2mm vapor gap, (b) 4mm vapor gap and (c) 5mm vapor gap. ($T_{ad}$ =30 °C, $T_{des}$ = 90 °C, $T_{evaporator}$ = 15°C and $T_{condenser}$ = 30°C)

The vapor gap is a function of the module height, as increasing the module height will require a wider gap to reduce the variation of the pressure along the module. Figure 4-7 illustrates the effect of module height on the required vapor gap to maintain the maximum performance of the module. At a module height of 0.8m, the vapor gap that produced no variation in pressure along the module is found to be 7mm, while reducing the module height to 0.2m, the vapor gap is found to be 4mm.

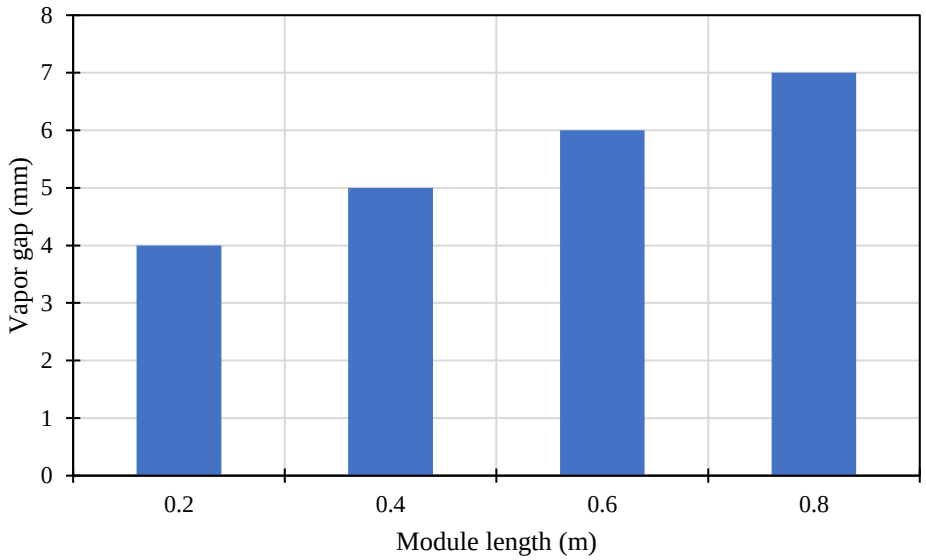



Figure 4-7. Effect of module length on the vapor gap distance between the modules

### *4.4.2.* Heat exchanger modules connection (series and parallel)

When multiple heat exchanger modules are required for scaling up adsorption systems, the connection of these heat exchanger modules need to be investigated. The 2D axisymmetric model was used to investigate the effect of connecting four heat exchanger modules with 0.4m height using these scenarios:

a. **Scenario-1:** All modules are connected in series, where the water enters from the first module and discharges from the fourth module as shown in **Figure** 4-8**(a).** The inlet water velocity is 0.6 m/s in every single tube to ensure turbulent flow in the pipe.

b. **Scenario-2:** Half the modules are connected in series and half connected in parallel, where the water enters from first and third modules and discharges from the second and fourth modules as shown in **Figure** 4-8**(b).** The inlet water velocity in each single tube is 0.6 m/s.

c. **Scenario-3:** All modules are connected in parallel, where the water enters from the first, second, third and fourth modules and discharges from the same modules as shown in **Figure** 4-8**(c).** The inlet water velocity in every single tube is 0.6 m/s.

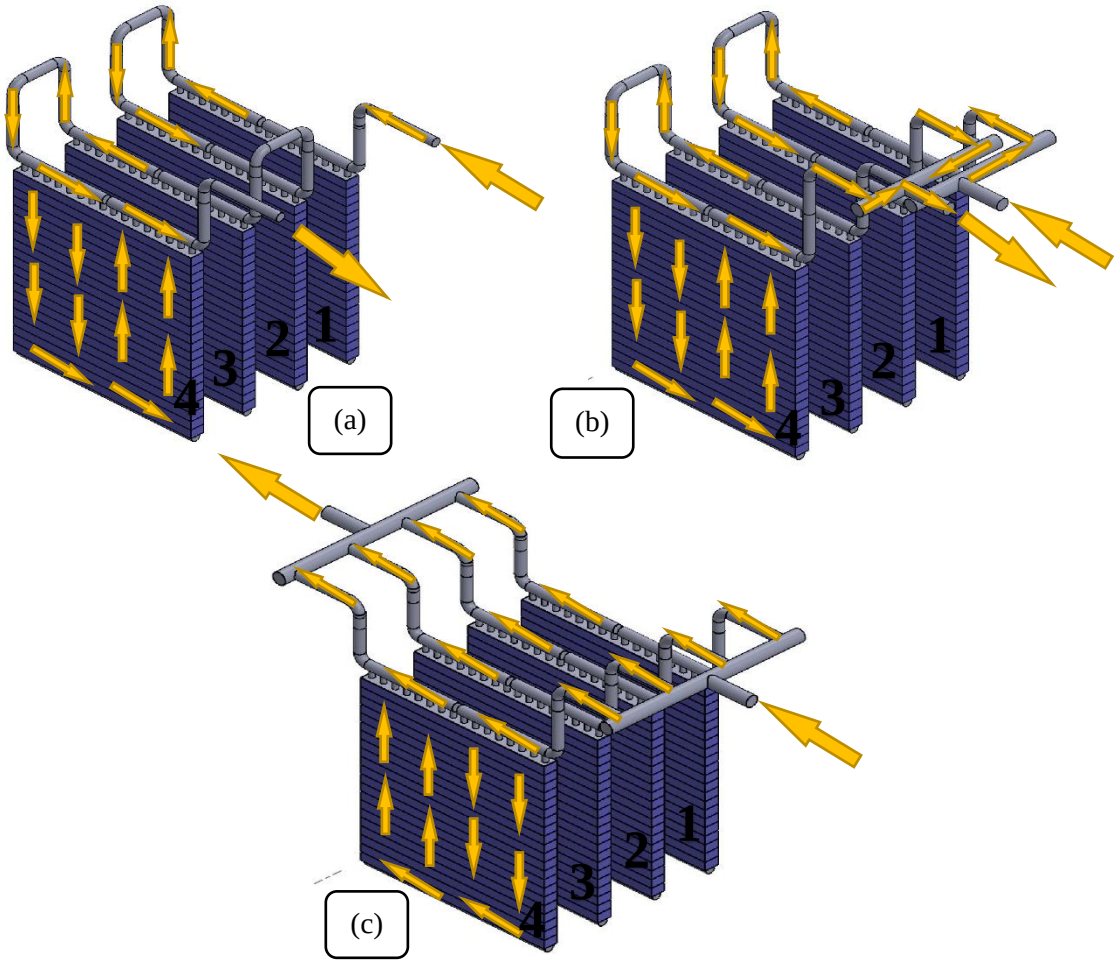



Figure 4-8. Packed heat exchanger modules configurations (a)Scenario 1, (b)Scenario 2 and (c)Scenario 3

The comparison between the three scenarios is based on the same water velocity in all the tubes, this means that each scenario will require a different amount of input water flow rate as this depends on the modules connections. Figure *4-9* shows the predicted heating power and input flow rate for the three investigated scenarios. Scenario 1 shows that the required heating power, to produce the same water and cooling outputs is only 5.32 kW, while it is 5.6 and 5.9 kW in scenario 2 and scenario 3 respectively. This shows the advantage of the series configuration over the other scenarios as the thermal fluid will pass through a longer path compared to the parallel connection. As the length of the module is 0.4 m and there are two-pass in the module, the thermal fluid will pass through 0.4X2 = 0.8m m in each

module, so in series connection, the thermal fluid will pass through 0.8X4 = 3.2m tube length. Passing through a longer tube will require less heating power as the heat conduction through the metal tube in the flow direction will enhance the heating process, so the modules will require less amount of energy to heat up the adsorbent material. While connecting the modules or half of the modules in parallel will lose the advantage of heat conduction along longer tube metal, so it needs more heating power to compensate for this loss. The series connection will also reduce the required water flow rate to 25L/min compared to the 50 and 100 L/min in scenario 2 and scenario 3 respectively.

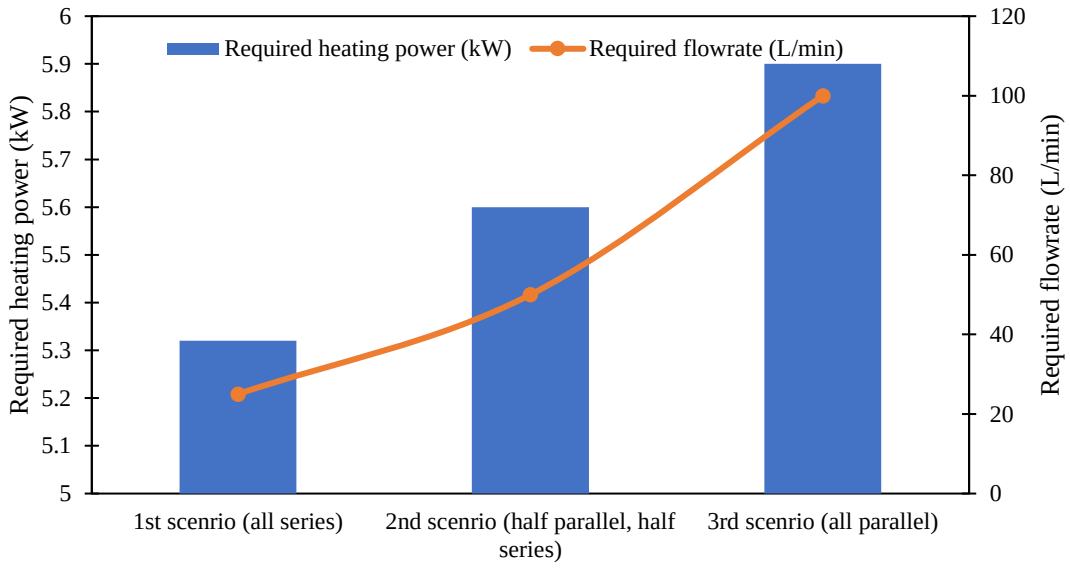



Figure 4-9. Packed heat exchanger modules scenarios effect on required heating power and water flow rate (Tad =30 ºC, Tdes = 90 ºC, Tevaporator = 15ºC and Tcondenser = 30ºC)

Figure 4-10 shows effect of the three scenarios on the performance of the adsorption system in terms of the SCP and COP. It can be seen that connecting the heat exchanger modules in series (scenario-1) showed higher COP values compared to the parallel connection (scenario-3) but with lower SCP values. Connecting the heat exchanger modules in series produced a COP of 0.34 compared to a COP of 0.329 for the parallel connection. On the other hand, scenario-1 produced SCP of 321.1 W/kg compared to SCP of 344.5 W/kg for scenario-3. The reduction in the SCP is caused by the reduction in the thermal fluid temperature along the tube length when the modules are connected in series, since the water temperature is decreased by 0.5 degrees for each 0.8m of tube length. This will reduce the water uptake in the adsorbent as it depends on the adsorbent temperature. Moreover, passing the water flow through the modules in series connection will delay the maximum water uptake in the adsorption cycle

in the last module compared to the first module. This also has a negative impact on the SCP of the adsorption system.

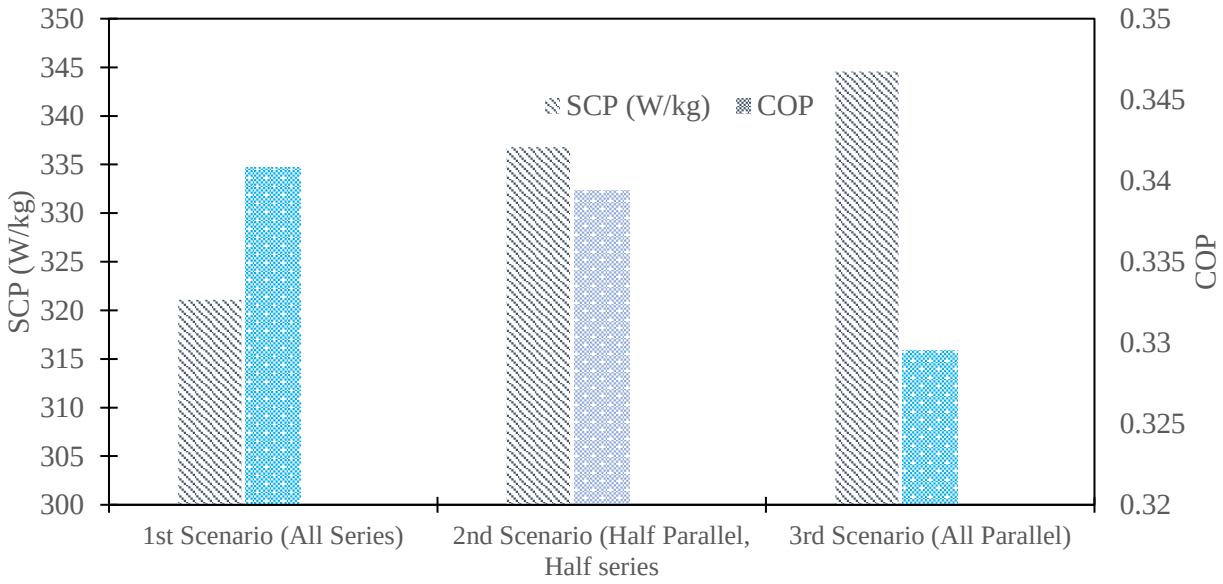



Figure 4-10. Packed heat exchanger modules scenarios effect on SCP and COP ($T_{ad}$ =30 ºC, $T_{des}$ = 90 ºC, $T_{evaporator}$ = 15ºC and $T_{condenser}$ = 30ºC)

Therefore, selecting the best configuration of the module's connections depends on the available thermal fluid source. For example, if the thermal fluid source is abundant from solar energy or waste heat from industry, the parallel configuration can be a good option to produce the high SCP from the adsorption system without considering the slight increase in the required heat power. However, the heat source should have a very high flow rate to maintain the flow in the tubes in the turbulent regime. On the other hand in cases where a limited flow rate from the heat source is available and if a high COP of the system is needed, then the series connection is recommended as it requires less amount of heating power.

Based on the studied scenarios, the experimental work presented in the next section is based on obtaining the highest COP. Thus, the series connection of the multiple heat exchanger modules is considered in the lab-scale design with a vapor gap of more than 10mm between the modules to avoid the pressure drop of the vapor flow between the modules.

## 4.5. Experimental testing of a scaled-up adsorption system

Figure 4-11 **and** Figure 4-12 **s**how a picture and schematic diagram of the developed adsorption system which consists of two adsorber beds, evaporator, condenser, vacuum pump, water pumps, and control system (details of connections are given in appendix A). All cylinders for adsorber beds, evaporator and condenser are made of stainless steel 316 L to avoid corrosion and the effect of the saline water on the evaporator.

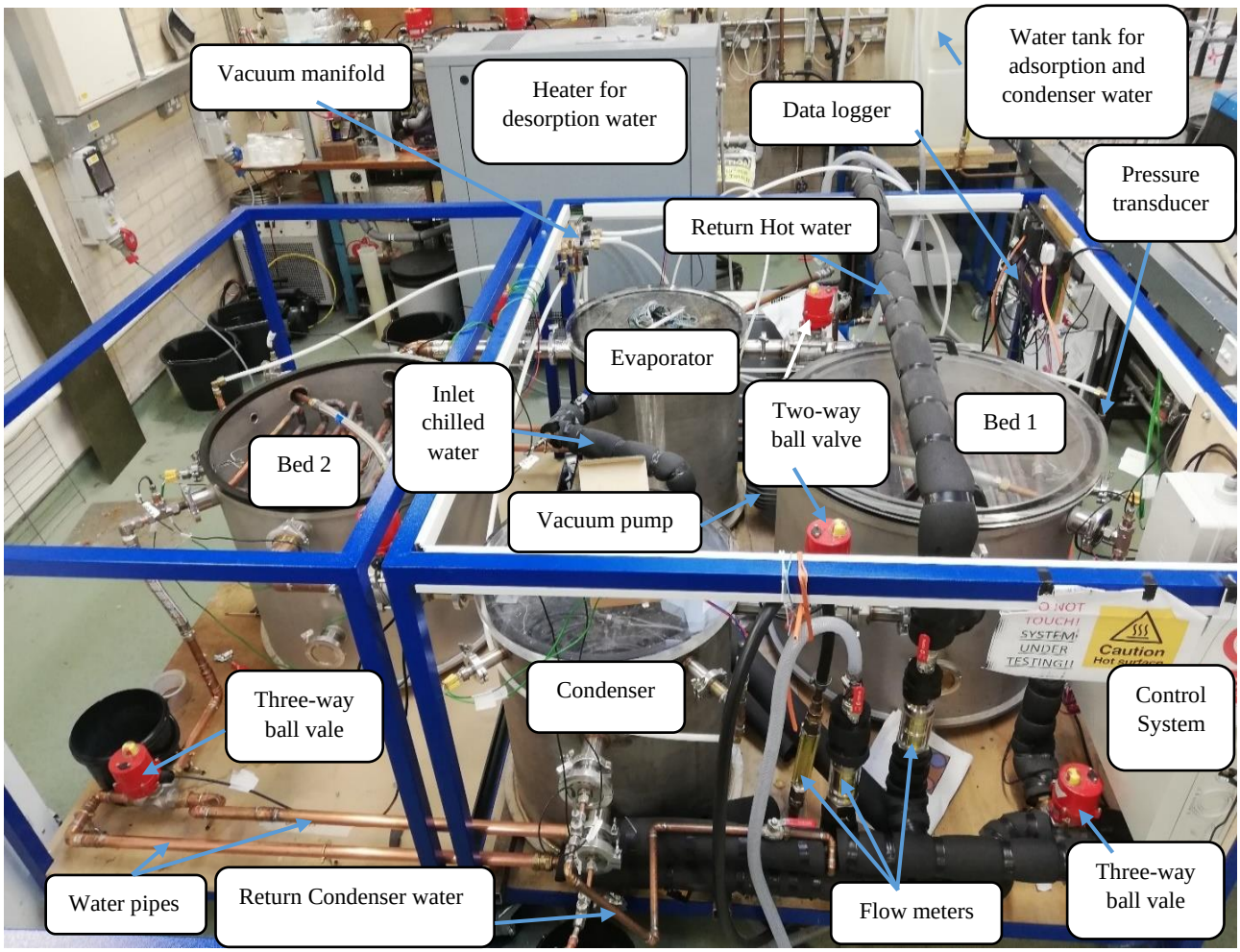



Figure 4-11. Scaled-up adsorption system components

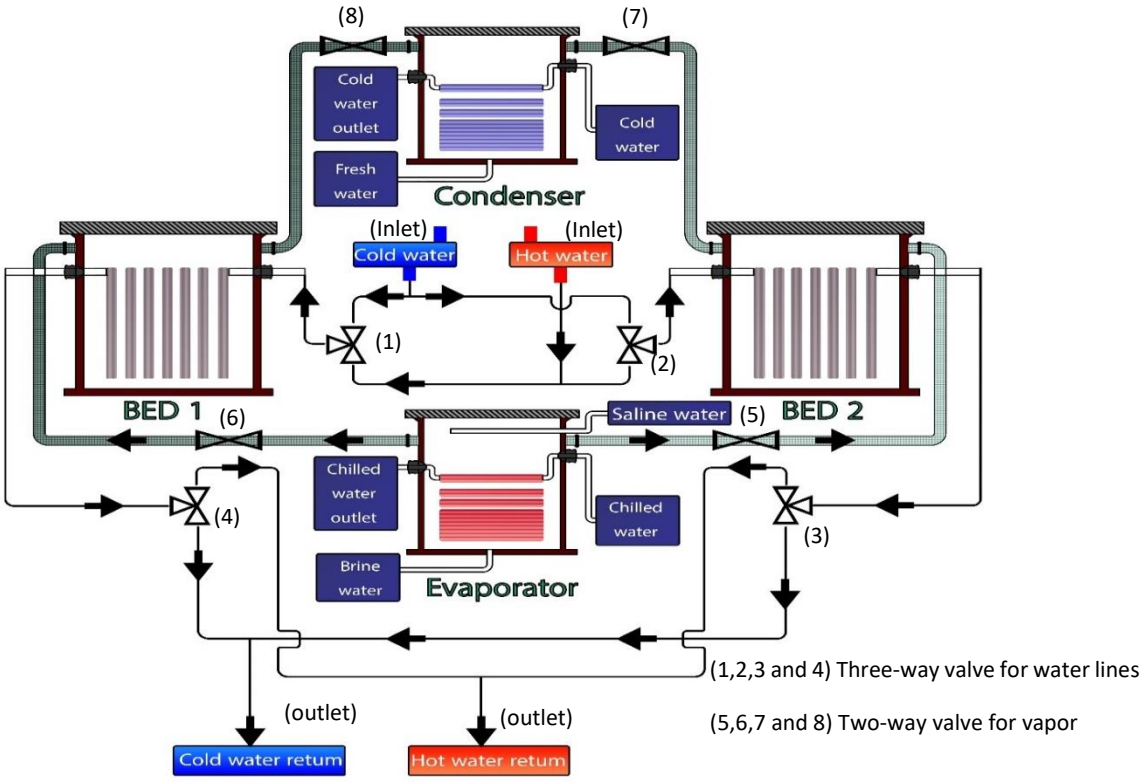



Figure 4-12. Schematic diagram of the adsorption system

*Figure 4-13* **(a, b, c)** shows the details of the cylindrical adsorber bed which contains eight rectangular finned tube heat exchanger modules packed with 11.6 kg of granular AF MOF adsorbent material. These modules are of three different sizes to fit in the cylindrical adsorber bed and they are connected in series to achieve a high coefficient of performance as predicted by the modelling results. The vapor gap between the modules are adjusted based on the numerical results at module height of 0.4 m. *Figure 4-13* **(a, b)** illustrates the packed heat exchanger modules configurations in the adsorber bed, while *Figure 4-13* **(c)** shows the adsorber bed assembly. Aluminum strips are placed in each module to glue a mesh sheet on one side of the module using silicon adhesive. Then the adsorbent material is packed from the other side of the module. Aluminum strips are placed on the other side of the module followed by gluing a mesh on this side using fixing silicon adhesive. The modules are then placed on a plastic carrier that has grooves to fix the spacing between the modules and each carrier has 4 modules in which each bed has two carriers as shown in *Figure 4-13* **(b).** The modules are then connected in series by soldering two 90-degree copper elbows between each module. The connection is then tested under 4 bar pressure to ensure no leakage. The modules are then lifted and placed in the beds, carrier by carrier. All chambers have an acrylic lid that sits on a rubber gasket providing an effective seal when

the chambers are under vacuum. Also, all chambers are insulated to minimize heat transfer to or from the surroundings.

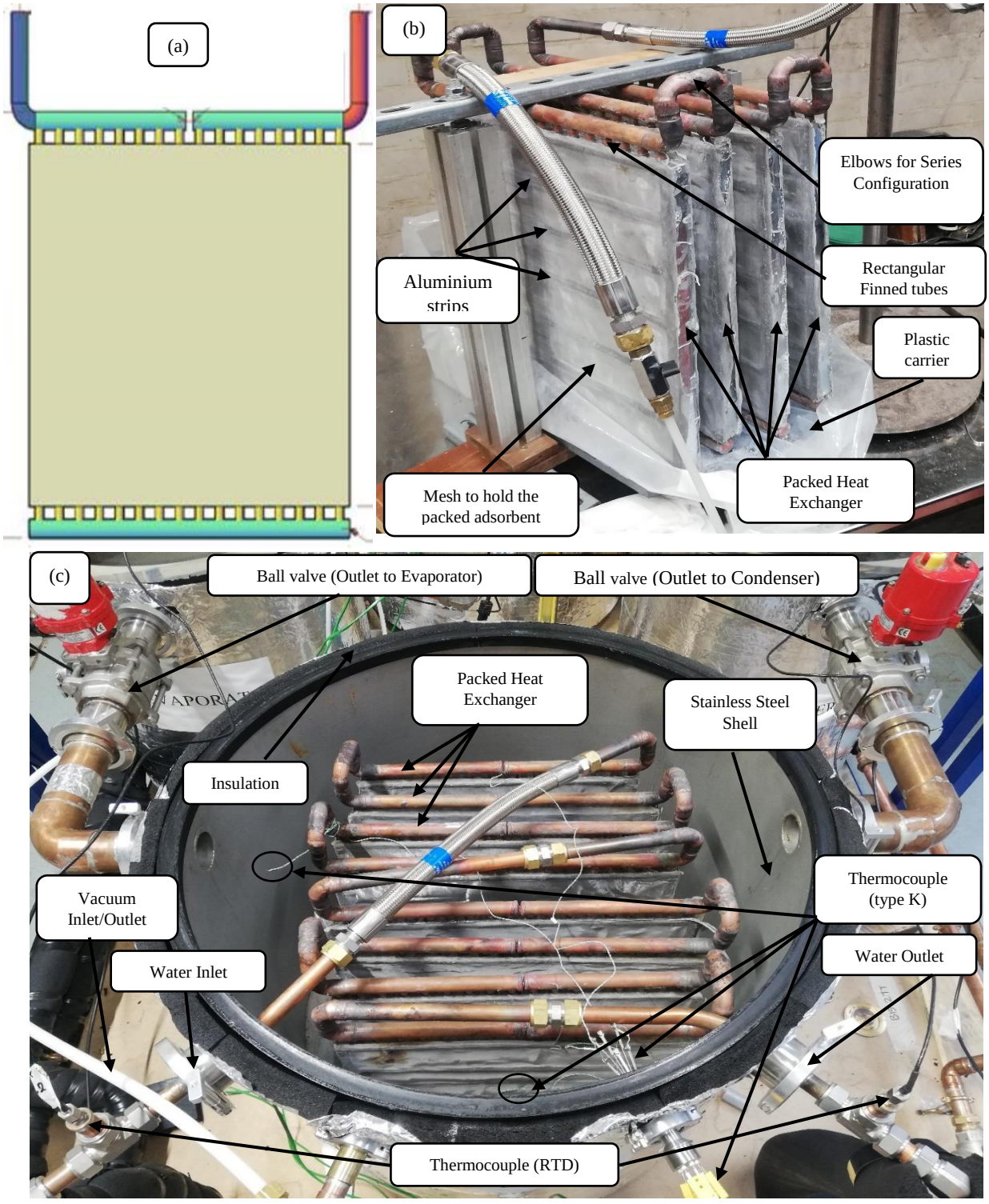



Figure 4-13. (a) single packed heat exchanger module, (b) the heat exchanger modules connection and (c) adsorber bed assembly

Figure 4-14 illustrates the stainless-steel coil which is placed in the evaporator with a total length of 60 meters where the chilled water flow splits into the two parts of the coil; the hexagonal flat shape which has 30 meters and the hexagonal double conical shape with 30 meters length. The condenser also has 60 meters of copper coils of 3/8" outer diameter.

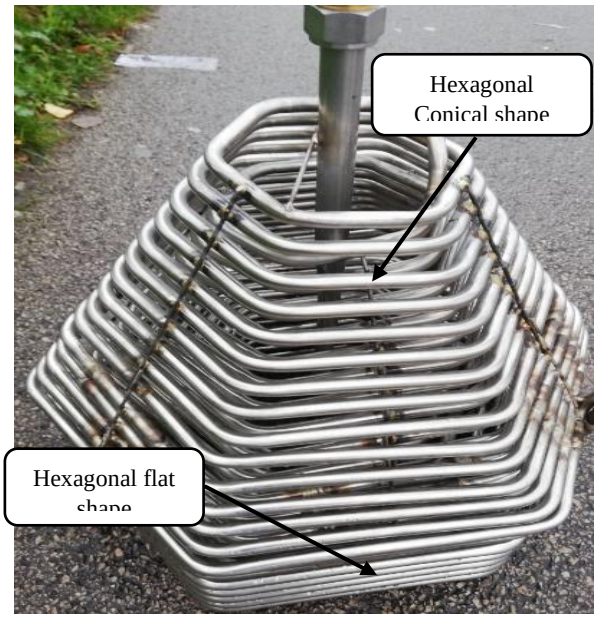



Figure 4-14. Stainless coil for the evaporator

Two types of thermocouples are used which are K-type and RTD type. The RTD is used to measure the water temperature in the copper pipes between the inlet and outlet for each chamber, while the K-type is used to measure the temperature of the adsorbent material and vapor temperature of each chamber which can operate in rugged environmental conditions and can be inserted through the adsorbent material to measure the temperature of the material without getting affected by the surrounding temperature. The RTD is manufactured by "RS Pro" and has a model number of "RS Pro 123-5602" and a temperature range between -50 to 250ºC, while K type has a model number of "RS Pro 621- 2158" with the same temperature range. The thermocouples are connected to data logger (DT 85 series 4 DataTaker) to measure the temperature in real-time and store the readings in a PC. A pressure transducer type PX M19-0.35AI with 0-350 mbar pressure range is fitted to each chamber to measure vacuum pressure in mbar scale, it is manufactured by "OMEGA" with an accuracy of ±0.8 mbar. Two-way and three-way solenoid electrical ball valves are connected between the chambers and the water pipes to control the drying, switching and adsorption /desorption processes in the cycle. The valves are

connected to a control panel using Relay Output Modules (National instruments NI-9482 C series). The system is controlled and monitored using LABVIEW. A vacuum pump is connected to a manifold that connects the vacuum pump to the various chambers. An electrical heater with a maximum temperature of 92 $^{o}$C is used to provide the heating water to the adsorber beds during the desorption process.

At the start of each experiment, all chambers are evacuated to reach a vacuum pressure of 30 mbar corresponding to the saturation pressure of the evaporator and condenser. During the drying process, all the two-way vapor ball valves (5,6,7 and 8) are switched off, since the adsorber beds need to be heated and dried to ensure that the adsorbent material is dry before starting the cycling process, while the three-way ball valves (1,2,3 and 4) are switched on to feed hot water into both beds. After the drying process, the switching between the adsorption and desorption processes is carried out by controlling the three-way ball valves to feed cold water to Bed 1 and hot water to Bed 2. Once the switching time is exceeded, the vapor valve between the Bed 1 and evaporator and the vapor valve between the Bed 2 and condenser will be switched on, so the adsorption and desorption processes will be performed at Bed 1 and 2 respectively.

The geometrical details of the adsorption system components are shown in **Table** 4-2**,** which illustrates the dimensions of the shells, packed heat exchanger modules and coils. While **Table** 4-3 shows the operating conditions of the system such as the temperatures and mass flow rates of the heating and cooling water.

Table 4-2. input parameter of adsorber bed, condenser and evaporator

| Adsorber bed (Shell dimensions) | | |
|---|---|---|
| **Shell diameter** | mm | 700 |
| **Shell height** | mm | 500 |
| **Module thickness** | | |
| **size 1** | mm | 28 |
| **size 2** | mm | 28 |
| **size 3** | mm | 28 |
| **number of finned pipes in module** | | |
| **size 1** | (-) | 18 |
| **size 2** | (-) | 17 |
| **size 3** | (-) | 16 |
| **module height** | | |
| **size 1** | mm | 400 |
| **size 2** | mm | 400 |
| **size 3** | mm | 400 |
| **Number of modules in each bed** | (-) | **8** |
| **pipe configuration** | | |
| **Fin height** | mm | 8.5 |
| **fin spacing** | mm | 1.91 |
| **fin thickness** | mm | 0.2 |
| **pipe inner diameter** | mm | 8.54 |
| **pipe outer diameter** | mm | 9.54 |

| Evaporator | | |
|---|---|---|
| **Shell diameter** | mm | 500 |
| **Shell height** | mm | 500 |
| **SS coils length** | m | 60 |
| **coil outer diameter** | mm | 10 |
| **coil inner diameter** | mm | 8.5 |
| **coil type** | (-) | Plain |
| Condenser | | |
| **Shell diameter** | mm | 500 |
| **Shell height** | mm | 500 |
| **copper coils length** | m | 60 |
| **coil outer diameter** | mm | 10 |
| **coil inner diameter** | mm | 9 |
| **coil type** | (-) | Plain |

Table 4-3. Operating conditions of the adsorption desalination system

| Parameter | Unit | Value |
|---|---|---|
| water adsorption flow rate | L/min | 25 |
| water desorption flow rate | L/min | 27 and 17 |
| chilled water flow rate | L/min | 12 |
| condenser water flow rate | L/min | 12 |
| adsorption water temperature | °C | 22, 25, 30 and 40 |
| desorption water temperature | °C | 60 and 85 |
| chilled water temperature | °C | 20, 24, 27.5, 30 and 35 |
| condenser water temperature | °C | 12, 20 and 25 |
| water content in evaporator | mL | 6000,9000,12000 and 15000 |
| half cycle time | sec | 150,200,250, 300 and 500 |
| switching time | sec | 40 |
| adsorbent material content in each bed | kg | 11.6 |

## 4.6. Experimental results and discussion:

To assess the adsorption system performance, experimental testings were carried out at different half-cycle times, chilled water inlet temperature, adsorption water inlet temperature, desorption water inlet temperature, and condenser inlet water temperature. The performance of the adsorption system was evaluated in terms of the specific daily water production (SDWP), specific cooling power (SCP) and the cooling coefficient of performance (COP). To calculate the daily water

production (DWP) of the system experimentally, the collected water ($L_{water}$) from the condenser in each cycle is multiplied with the number of the cycle in the day (which is the total time in the day ($t_{day}$) divided by the total time of the cycle ($t_{cycle}$) ) using the following equation:

$$\boldsymbol{DWP = \frac{L_{water}}{t_{cycle}}\left(t_{day}\right)} \tag{4.1}$$

To determine the cooling power (CP) of the system, the following equation is used:

$$\boldsymbol{CP = \frac{Q_{evaporator}}{t_{cycle}}} \tag{4.2}$$

Where $Q_{evaporator}$ is the cooling rate of the evaporator and can be calculated using the following equation:

$$\boldsymbol{Q_{evaporator} = \frac{\sum_{t_{adsorption}+\, t_{switching}}[\, \dot{m}_{chilled}\, C_p\, (T_{chilled,in} - T_{chilled,out}\,)\Delta t]}{t_{adsorption} + \, t_{switching}}} \tag{4.3}$$

Where $\dot{m}_{chilled}$ is the mass flow rate of the chilled water, $C_p$ is the specific heat capaciy, $T_{chilled,in}$ is the chilled water inlet temperature, $T_{chilled,out}$ is the chilled water outlet temperature, $\Delta t$ is the time step between each two temperature readings by the DataTaker which is 5 seconds and $\boldsymbol{t_{switching}}$ is the switching time between the two processes (adsorption and desorption). The required $\boldsymbol{t_{switching}}$ to heat up/cool down the adsorbent material was found at 40 seconds.

To calculate the SDWP and SCP of the adsorption system, DWP and CP are divided by the adsorbent mass ($M_{adsorbent}$) respectively.

The COP of the system can be calculated using the following equation:

$$\boldsymbol{COP = \frac{Q_{evaporator}}{Q_{desorption}}} \tag{4.4}$$

Where $Q_{desorption}$ is the total heating rate required during the switching and desorption process and can be calculated as follows:

$$Q_{desorption} = \frac{\sum_{t_{desorption}+\, t_{switching}} [\, \dot{m}_{des}\, C_p\, (T_{des,in} - T_{des,out}\,)\Delta t]}{t_{desorption} + \, t_{switching}} \qquad (4.5)$$

**Figure** 4-15 illustrates the profile of the water temperature based on running the experiment using one bed after running the system for four cycles. The system achieved a good cyclic operation as the temperature profiles in each cycle are identical. In this system, the inlet and outlet temperatures of the adsorption and desorption water have a difference of around 5°C, which is considered a relatively high temperature difference in the adsorption system compared to previous studies [187]. This difference occurs due to the heat exchanger modules configuration, as the eight modules are all connected in series. The cooling temperature difference of the chilled water varies between 4 to 7 °C while the temperature difference of the condenser water varies between 1 to 8 °C.

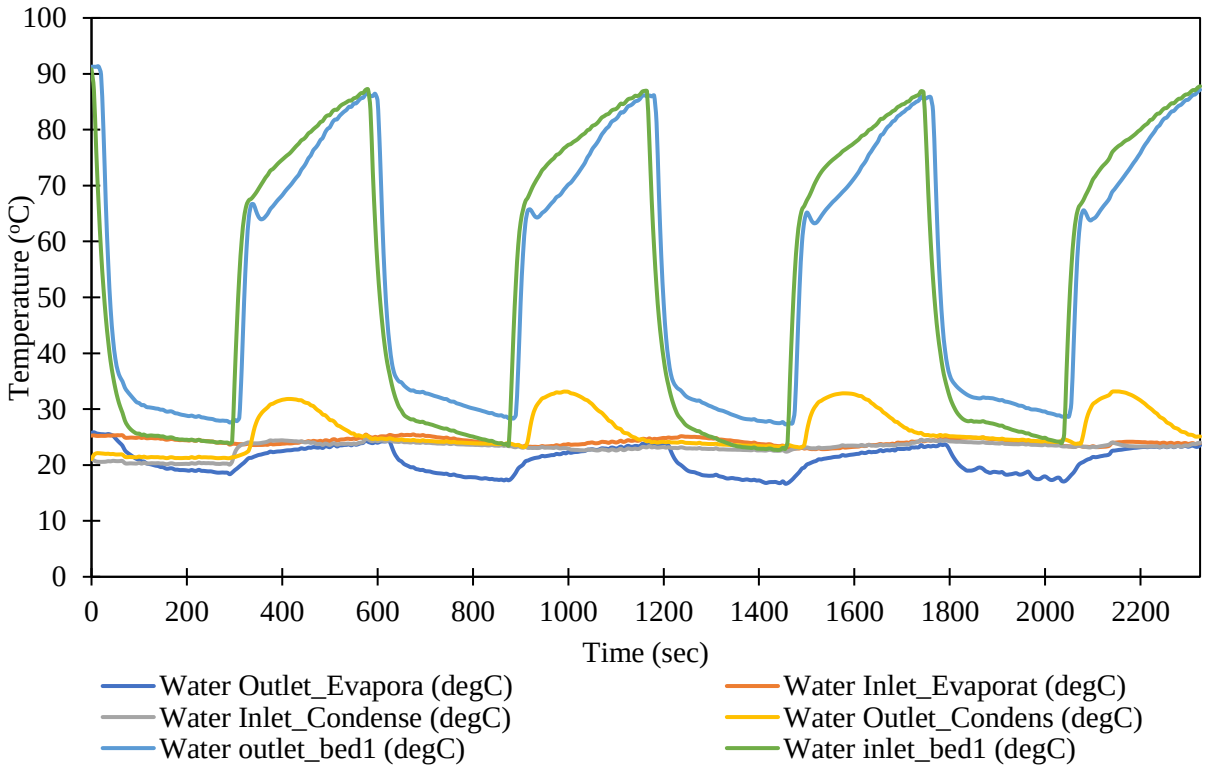



Figure 4-15. Experimental reading of the Water temperature profiles in each component in the adsorption system ($t_{half\ cycle}$ = 250 sec, $t_{switching}$ = 40 sec, $T_{ad}$ = 25°C, $T_{des}$ = 85 °C, $T_{chilled}$ = 24°C and $T_{cond}$ = 25°C)

The developed numerical 2D-axisymmetric model is compared with the experimental results in terms of the outer surface temperature of the adsorbent material with 20 cm of the tube length showing good agreement after 50 seconds as shown in **Figure** 4-16. While there is a deviation between the experiment

and numerical results in the first 50 seconds as a result of the heat losses in the chamber mass which is not considered in the model. The model is also validated using the SDWP at different operating conditions and showed a good agreement with a maximum deviation of 6.67% as shown in **Figure** 4-17**.**

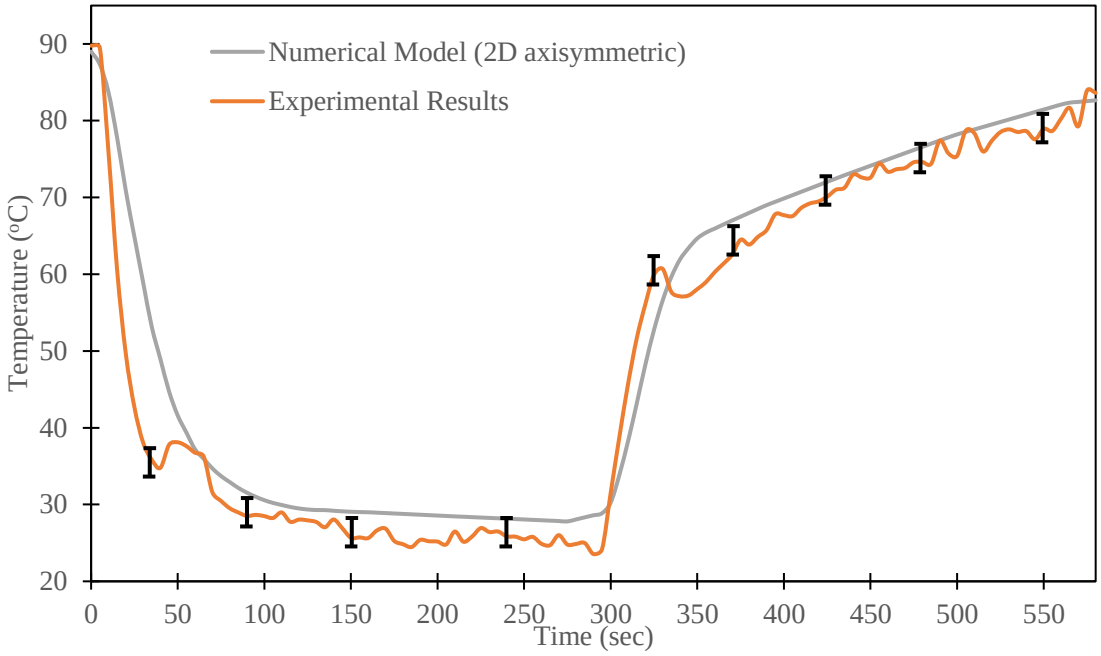



Figure 4-16. Model validation by using adsorbent temperature ($t_{cycle}$ = 250 sec, $t_{switching}$ = 40 sec, $T_{ad}$ = 25°C, $T_{des}$ = 85 °C at water flow rate of 27L/day, $T_{chilled}$ = 24°C and $T_{cond}$ = 25°C)

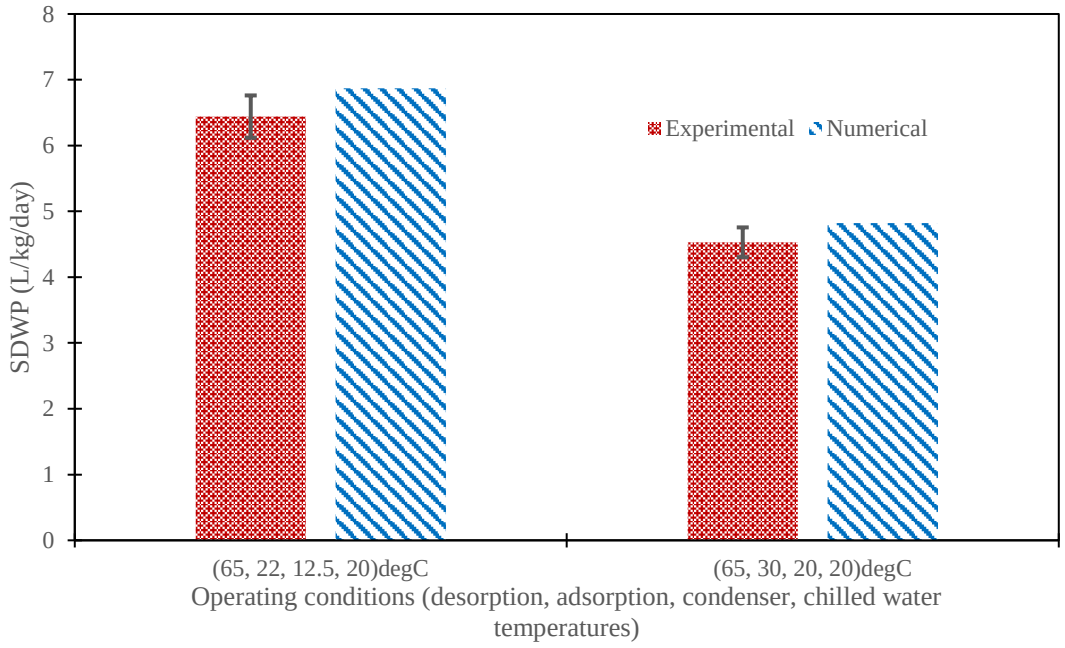



Figure 4-17. Model validation by using SDWP values at different operating conditions

Figure 4-18 shows the effect of the half cycle time on the DWP, SDWP, CP and SCP at chilled water, adsorption water, desorption water and condenser inlet temperatures of 24, 25, 85 and 25 °C respectively. The optimum half-cycle time is found to be 250 seconds where the system can produce 201 L/day and 5.25 kW of daily water production and cooling. Thus, the maximum achieved SDWP and SCP are 8.66 L/kg/day and 226 W/kg respectively.

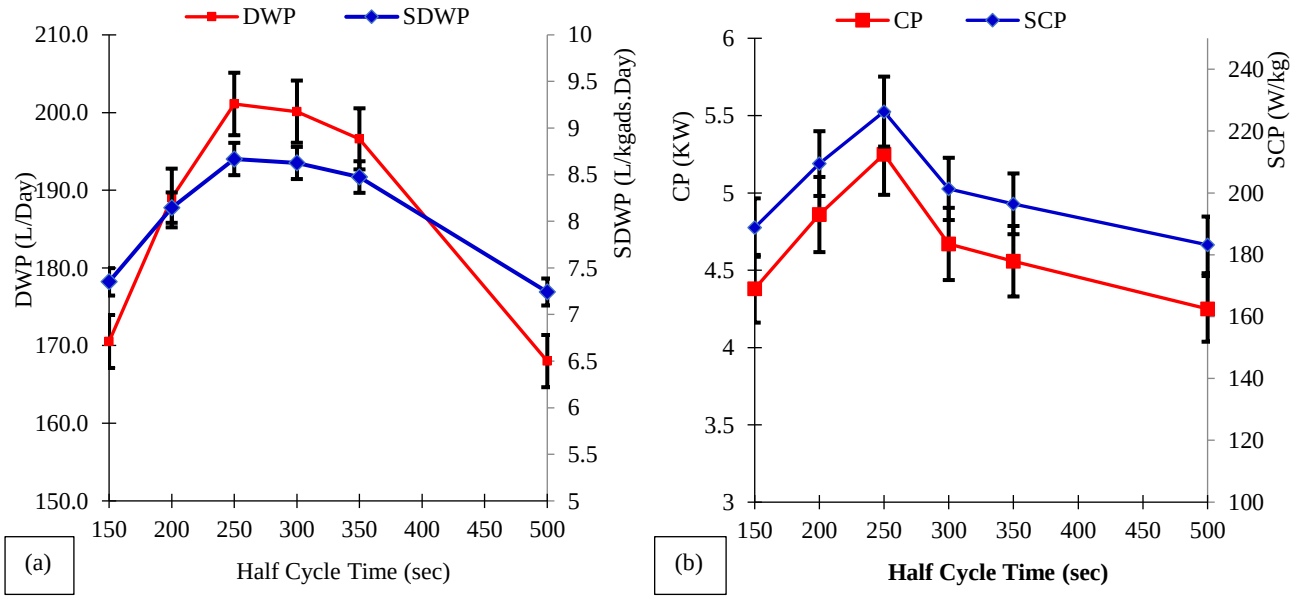



Figure 4-18. Effect of half-cycle time on DWP, SDWP, CP and SCP ($t_{switching}$ = 40 sec, $T_{ad}$ = 25°C, $T_{des}$ = 85 °C, $T_{chilled}$ = 24°C and $T_{cond}$ = 25°C at desorption water flow rate of 27 L/day)

The optimum half-cycle time increased when the water flow rate of the desorption water decreases from 27 to 17 L/day and temperature decreased from 85 to 60 °C as shown in **Figure** 4-19. The chilled water and condenser water inlet temperatures also decreased to 20 and 12.5 °C respectively, so the optimum half-cycle time increased from 250 to 350 seconds. Therefore, the optimum half-cycle time is not only affected by the heat exchanger geometry and modules configurations, it is also affected by the operating conditions such as the water flow rate and water temperatures [188]. The half-cycle time is also a function of the kinetic and isotherm equations of the adsorbent material and the thermophysical properties. The isotherm of the AF has a (S) shape relationship between the relative pressure and water uptake [67], so changing the operating conditions will change the isotherm region of the material, whether to be in the exponential part of the polynomial curve.

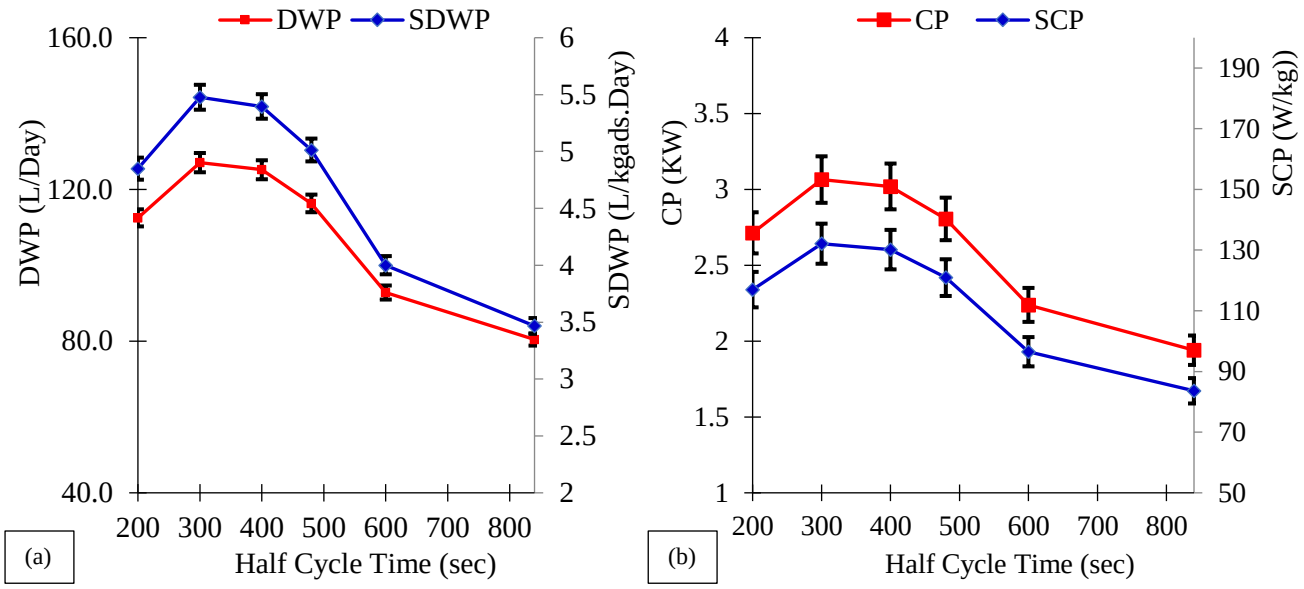



Figure 4-19. Effect of half-cycle time on DWP, SDWP, CP and SCP ($t_{switching}$ = 40 sec, $T_{ad}$ = 30°C, Tdes = 60°C, $T_{evap}$ = 20°C and $T_{cond}$ = 12.5°C at water desorption flow rate of 17L/day)

The COP of the system is one of the main parameters that describe the efficiency of cooling systems. To increase the COP of the system, the fin spacing in the heat exchanger is increased to 1.91 mm compared to the previous experimental works on the AF [187] which used a fin spacing of 1mm. Thus, the metal mass in the heat exchanger will be reduced to almost half which will lead to an increase in the COP value. Additionally, connecting the heat exchanger modules in a series configuration will also increase the COP value since heating the adsorbent material will require less energy to desorb the water content. Figure 4-20 shows that the maximum COP (0.50) of the system was obtained at half cycle time of 250 seconds, since the thermal energy in the desorption process is consumed efficiently to produce the highest cooling power at this time. The COP value of the scaled-up adsorption system using AF, shows a significant increase compared to studies where a limited scale with less than 1kg of adsorbent material was used [189].

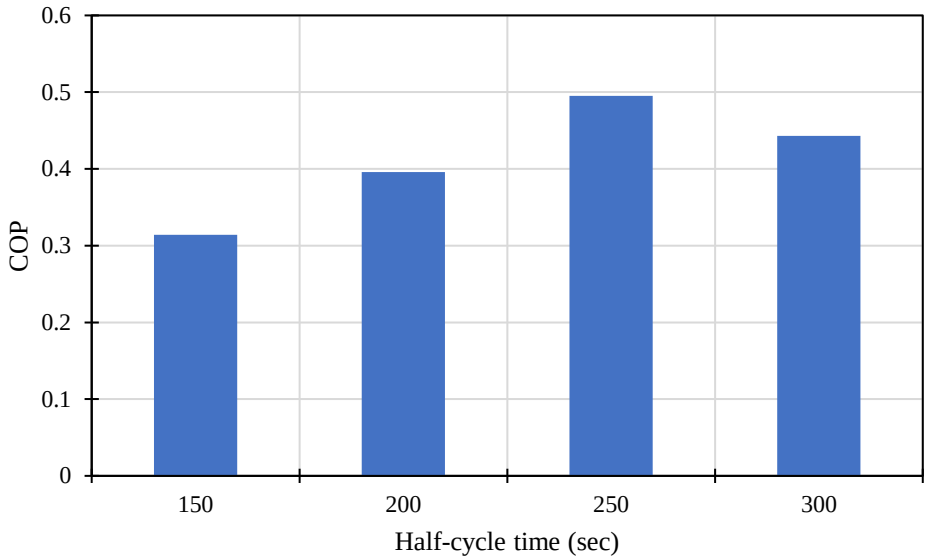



Figure 4-20. Effect of the half cycle time on the COP of the adsorption system (Tad = 25°C, $T_{des}$ = 85 °C at water flow rate of 27L/day, $T_{chilled}$ = 24°C and $T_{cond}$ = 25°C)

**Figure 4-21** shows the effect of adsorption cooling water inlet temperature on DWP, SDWP, CP and SCP of the adsorption system at evaporator water temperature of 20°C. Results showed significant reduction in the system performance as the adsorption water temperature increases. The significant variation in the performance between 22 and 40 °C adsorption water temperature is due to the significant variation of water uptake of the AF between these temperatures.

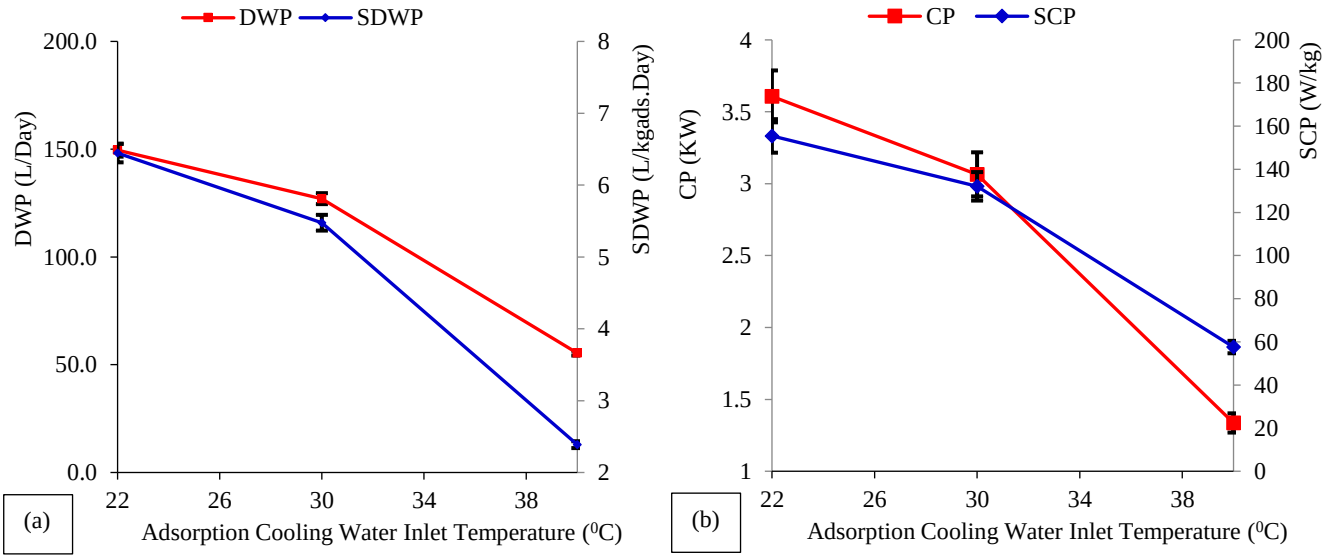



Figure 4-21. Effect of adsorption cooling water inlet temperature on DWP, SDWP, CP and SCP ($t_{half\ cycle}$ = 350 sec, $t_{switching}$ = 40 sec, $T_{des}$ = 60°C, $T_{evap}$= 20°C, $T_{cond}$ = 12.5°C at water desorption flow rate of 17L/day)

**Figure** 4-22 shows the effect of the evaporator chilled water inlet temperature on DWP, SDWP of the system at condenser cooling water inlet temperatures of 12.5 and 20°C. It can be seen that decreasing the evaporator chilled water inlet temperature decreased the SDWP and SCP of the system. On the other hand, decreasing the condenser cooling water temperature increases the SDWP and SCP of the system. At the evaporator chilled water inlet temperature of 27.5 °C, the daily water production is 169 L/day at a condenser water temperature of 20 °C, while it is 199 L/day at a condenser water temperature of 12.5 °C.. The maximum SDWP is 9.3 L/kg/day which is achieved using chilled water temperature of 30 °C and condenser water temperature of 12.5 °C.

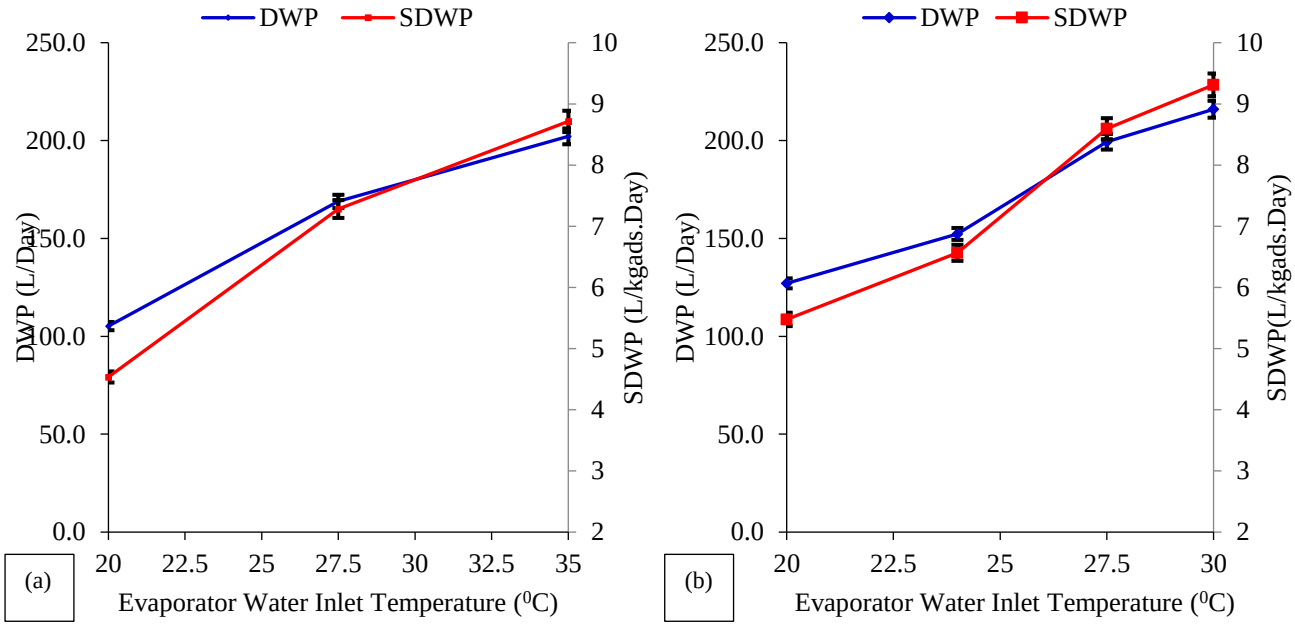



Figure 4-22. Effect of evaporator water inlet temperature on DWP and SDWP (thalf cycle = 350 sec, tswitching = 40 sec, $T_{ad}$ = 30°C, $T_{des}$ = 60°C at water desorption flow rate of 17L/day) (a) $T_{cond}$ = 20°C (b)$T_{cond}$ = 12.5°C

The advantage of the aluminum fumarate over the conventional adsorbent and MOF materials such as silica gel, zeolite (AQSQA-Z02) and CPO-27Ni is the high SDWP at low desorption temperature as shown in **Figure 4-23**. At a desorption temperature of 65°C, the SDWP of aluminum fumarate is 4.53 and 7.9 L/kg/day at a chilled water temperature of 20 and 30°C respectively, while AQSQA-Z02 and CPO-27Ni have very low SDWP (1 and 0.4 L/kg/day respectively) at both chilled

water temperatures [6]. Silica gel has higher SDWP compared to AQSQA-Z02 and CPO-27Ni, but aluminum fumarate still provides better performance under these operating conditions [6].

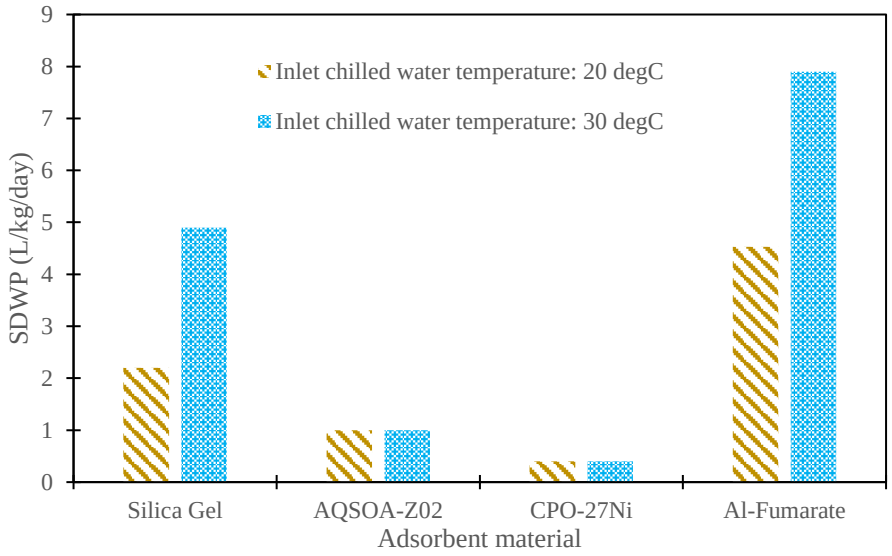



Figure 4-23. Comparison between conventional adsorbent and MOF materials and aluminum fumarate at a desorption temperature of 65°C using different chilled water temperature

The system performance is tested under a wide range of water salinity ranging from 90 to 100,000 ppm as shown in **Figure** 4-24**.** From 90 to 25,000 ppm the water is considered brackish water, while a salinity of 50,000 ppm can be considered as the salinity of the seawater [190]. At 75,000 and 100,000 ppm water salinities, the water is considered brine water which can be extracted from any other desalination technology such as the RO, in which 55% of the feeding water to the RO system will be disposed of as brine water with a very high-water salinity. The reduction in SDWP between 90 to 100,000 ppm water salinity is only 16% (from 8.6 to 7.2 L/kg/day). This reduction is due to the increase in the saturation temperature of the saline water and the salt sedimentation on the chilled tube surface of the evaporator. The adsorption system using AF can operate as a desalination system with wide range of water salinity with no significant loss in performance. The water salinity of the production has a value of less than 10 ppm regardless of the quality of the feeding water to the system, since the quality of the water is directly related to the evaporation and condensation processes.

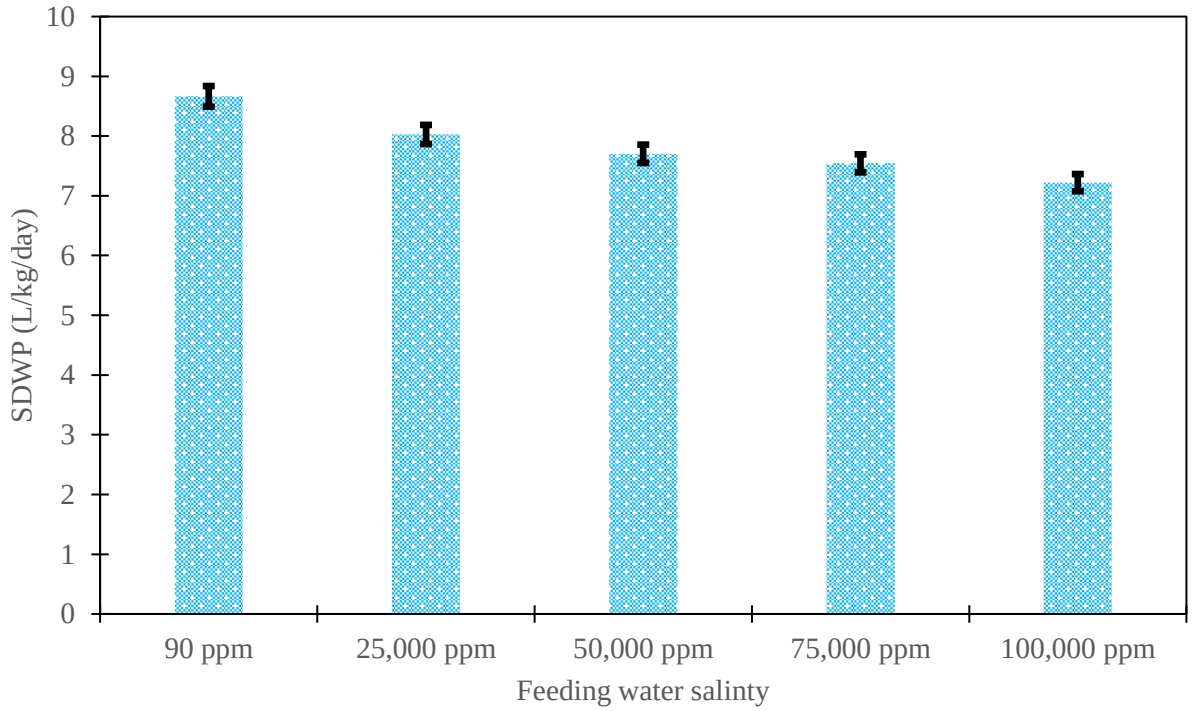



Figure 4-24. Effect of Feeding water salinity on the SDWP ($t_{cycle}$ = 250 sec, $t_{switching}$ = 40 sec, $T_{ad}$ = 25ºC, $T_{des}$ = 85ºC at water flow rate of 27L/day, $T_{chilled}$ = 24ºC and $T_{cond}$ = 25ºC)

**Figure** *4-25* shows the specific electrical energy consumption of the adsorption system at different water salinity which ranged between 1.87 to 2.24 kWh/$m^3$. The proposed scaled-up adsorption system in the present study shows better electrical consumption compared to the existing desalination technologies such as the reverse osmosis (RO) system [191]. Kim et al. [170] provided a comprehensive review of the electrical consumption of seawater RO desalination systems. The study showed that the energy consumption of various RO types is ranging between 3-6 kWh/$m^3$. Chaffour et al.[192] reviewed the other desalination technologies such as multistage flash distillation (MSF) which has an electrical consumption range of 2.5-4 kWh/$m^3$. Thus, the proposed system using the MOF material is a promising desalination system in terms of electrical energy consumption and ability to handle high feeding water salinity.

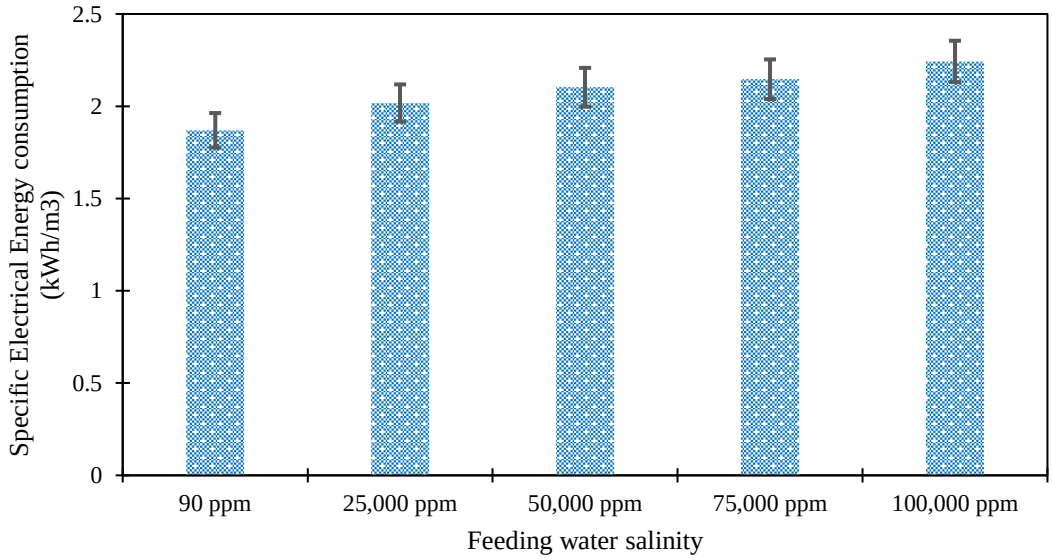



Figure 4-25. Effect of Feeding water salinity on the specific electrical energy consumption ($t_{cycle}$ = 250 sec, $t_{switching}$ = 40 sec, $T_{ad}$ = 25ºC, $T_{des}$ = 85 ºC at water flow rate of 27L/day, $T_{chilled}$ = 24ºC and $T_{cond}$ = 25ºC)

## 4.7. Conclusions:

Numerical and experimental investigations have been carried out to study a scaled-up adsorption system for water desalination and cooling applications using aluminum fumarate MOF material, and the following have been concluded:

a. Compared to other adsorption mathematical models, the fully coupled heat and mass transfer-based models allow for predicting the variable vapor pressure through the adsorbent material and the surrounding vacuum space. This offers an effective method to study large computational domains, including the thermal fluid and vapor gap domains for packed finned tube heat exchanger modules.

b. The numerical simulations showed that the pressure variation in a narrow vapor gap between the heat exchanger modules was considerable and can negatively affect the overall system performance. Thus, there is a minimum gap distance that should be used depending on the module length to eliminate the vapor pressure drop. For example, a vapor gap of 10mm would fit with the module length of 0.4 m, under the investigated conditions.

c. The heat exchanger modules can be connected all in series, in parallel, or half in series and half in parallel, where the selected connection will depend on the available heat source. Connecting the modules in series will take advantage of using a minimum thermal fluid flowrate and the effect of the heat conduction in the metal tube along the thermal fluid direction, so that the COP will be increased, while the SCP will be decreased by only 6.8%, under the investigated conditions. On the other hand, using the parallel connection will increase the SCP of the system, however, it requires 4 times the thermal fluid flow rate if 4 modules are used.

d. The best half-cycle time is dependent on the fins' configurations design and the operating water temperature of the adsorption system. The best half-cycle time was found ato be 250 seconds, when the evaporator, condenser, adsorption and desorption water temperatures are 24$^{o}$C, 25$^{o}$C, 25$^{o}$C and 85 $^{o}$C, respectively, providing SCP, SDWP and COP of 226 W/kg, 8.66 L/kg/day and 0.5, respectively. While reducing the desorption water flow rate from 27 to 17 L/min at a temperature of 60$^{o}$C, increased the best half cycle time to 350 seconds at a condenser water temperature of 12.5 $^{o}$C, an evaporator water temperature of 20$^{o}$C and adsorption water temperature of 20$^{o}$C. Additionally, the adsorption system performance using aluminum fumarate is significantly affected by the evaporator and cooling water temperature.

e. The aluminum fumarate is a good adsorbent for desalination applications for a wide range of water salinity between the brackish water to the brine water (from 90 to 100,000 ppm), in which the SDWP only decreased by 16.3% (from 8.66 to 7.22 L/kg/day). The specific electrical energy consumption of the proposed system is between 1.87 to 2.24 kWh/m$^3$, which provides better consumption compared to the reverse osmosis and multistage flash distillation systems.

# Chapter 5: Experimental study of multiple coated wire finned tube heat exchanger modules in a scaled-up adsorption system

## 5.1. Introduction

Following the outcomes from chapter 3, a wire finned tube with a diameter of 10mm, fin height of 7mm, fin thickness of 1mm, fin spacing of 2mm and 20 fins per loop that provides the highest SDWP and SCP is used in the experimental work described in this chapter to study the coating method in a scaled-up adsorption system using multiple heat exchanger modules. Additionally, the adsorption kinetic of thicker coating layers is investigated using the Dynamic vapor sorption (DVS) apparatus to apply a coating layer that is thicker than 0.5mm, which can enhance the COP of the adsorption system since less amount of metal mass is studied in this chapter. On the other hand, the other components of the adsorption system such as the evaporator and condenser are investigated for the first time to study the effect of the dead volume of the evaporator and condenser chambers on the SDWP, which consequently enhances the compactness of the adsorption system. This chapter ends with a comparative study between the experimental work using the packed rectangular finned tube from chapter 4 and the coated wire finned tube in this chapter.

This chapter is based on an accepted study for publication as presented in the following journal paper:

**Albaik**, K. Diab, M. Saleh, R. Al-Dadah, S. Mahmoud, M. F. El-Kady, İ. Solmaz and M. Elsheniti, ‘MOF based Water Desalination and cooling Coated Adsorption System Integrated with Pre-treatment unit’, Sustainable energy technologies and assessment journal. **(accepted with corrections)**

### Credit Authors statament:

**I.Albaik:** Coating the heat exchanger with the adsorbent material, building the adsorption system with the control system, testing the system and conducting the experimental works, analyzing the results, and writing the outcomes of the study. **K. Diab:** characterization of the MOF adsorbent material. **M. Saleh:** Coating the heat exchanger with the adsorbent material. **R. Al-Dadah and S. Mahmoud:**

Reviewing and supervision, **M. F. El-Kady:** Project funding and administration. **İ. Solmaz and M. Elsheniti:** reviewing the results.

## 5.2. Preparation of MOF adsorbent material coating for the adsorption heat pump desalination and cooling unit

Figure 5-1 shows the preparation of aluminum fumarate MOF adsorbent material (purchased from MOF Technology Co. in a powder form) for coating. 2000 ml of distilled water is heated and mixed with 40g of binder agent (hydroxyethyl cellulose) at a temperature of 90ºC for 30 minutes, followed by mixing 400g of aluminum fumarate powder with the solution for another 30 minutes under stirring.

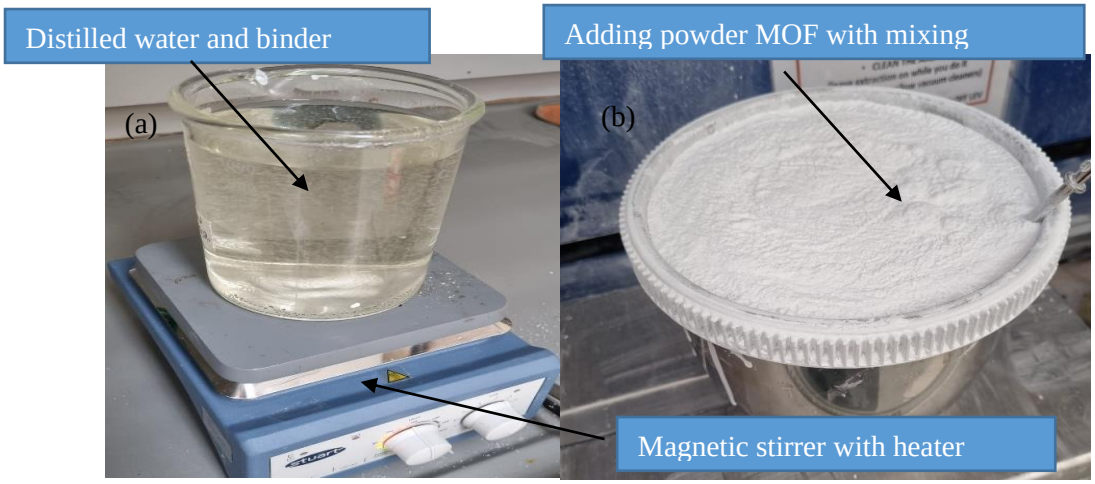



Figure 5-1. Aluminum fumarate preparation for coating (a) distilled water mixed with a binder (b) mixing distilled water and binder with adsorbent material powder

## 5.3. Characterization of MOF adsorbent material coating

To examine the effect of coating thickness on the performance in an adsorption heat pump for water desalination and cooling applications, five different coating thicknesses (0.3, 0.5, 0.75, 0.85 and 1.1mm) were prepared to be tested, using dynamic vapor sorption apparatus (DVS). A cyclic performance study was conducted, using an adsorption temperature of 25ºC and a desorption temperature of 90ºC at a relative pressure of 90% in the adsorption process as shown in Figure 5-2. The fastest adsorption kinetic was observed using the coating thickness of 0.3 and 0.5mm in which the cycle time was only 35 and 45

minutes respectively. This kinetic is much faster than using the conventional packing method of adsorbent granular which showed a cycle time of 85 minutes due to the higher thermal conductivity and the smaller particle size of powder MOF used for coating [193]. In terms of the gravimetric water uptake, the coating method, using 0.3mm can provide double the SCP and SDWP values compared to the packing one [65]. However, due to the thin coating thickness, the coating method requires more heat exchanger surfaces which ultimately increases the required heat exchanger mass thus more energy will be required to heat up the adsorbent material and metal mass during the regeneration process. Therefore, in this study, more investigations were performed, using thicker coating layers such as 0.75, 0.85 and 1.1mm. Figure 5-2 shows that the cycle time at a coating thickness of 0.75mm is 42 min which is slightly higher than the coating thickness of 0.5mm with a cycle time of 41 min. A remarkable increase in the cycle time was observed at a coating thickness of 0.85mm (47 min). As for the 1.1mm coating thickness, the cycle time exceeded that of the packing method due to the binder effect on blocking the pores of the adsorbent material. These results showed that there is an opportunity to decrease the heat exchanger mass by using a thicker coating layer compared to Elsayed et al. [15] who investigated thicknesses up to 0.5mm only, this ultimately can increase the COP of the adsorption system since less heating energy will be required in the regeneration process.

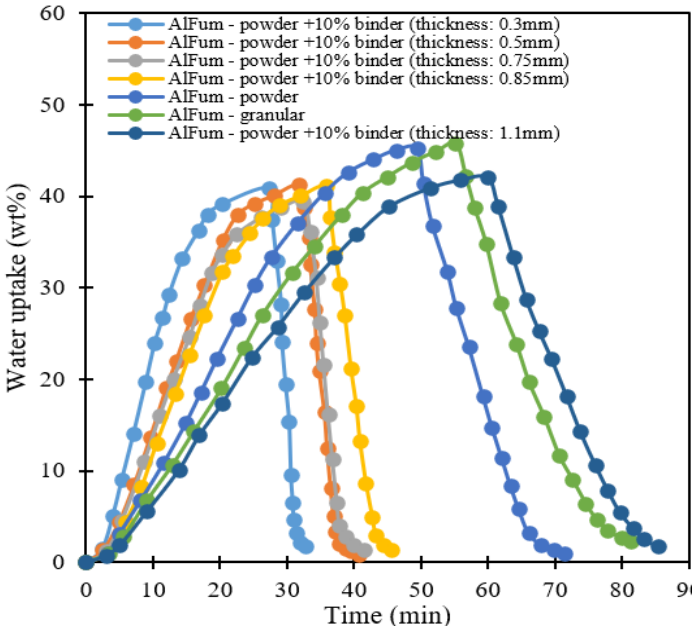



Figure 5-2. Water cyclic performance at different coating thicknesses

## 5.4. Coating the heat exchanger for adsorber beds

Figure 5-3 shows the wire-finned tube heat exchanger module coated with 0.75mm of adsorbent material thickness, where several layers of coating of the adsorbent material were applied to obtain this thickness as shown in Table 5-1.

Table 5-1. Coating layers procedure to obtain 0.75mm coating thickness

| Layer number | Pre-heating before oven | Drying in Oven Duration | The temperature in the oven |
|---|---|---|---|
| 1st layer | 5 min with electrical heater gun | 120 minutes | 90°C |
| 2nd layer | | 60 minutes | 90°C |
| 3rd layer | | | |
| 4th layer | | | |
| 5th layer | | | |
| 6th layer | | 24 hours | 70°C |

The first layer of adsorbent material is sprayed on the heat exchanger surface until achieving 0.1mm coating thickness with a coating tolerance of 0.02mm. It is found that using the spraying technique provides uniform thickness compared to the dipping one. Additionally, the material waste during the spraying is negligible compared to the dipping technique. Then an electrical heater gun is used to dry the adsorbent material for 5 minutes to avoid adsorbent material dripping when the module is placed inside the oven. Then, the module is placed in the oven at 90°C for 120 minutes to ensure a solid layer of coated material before starting the next coating layer. It was found that with this duration, the layer gets sufficient heating to become strong and rigid to start adding the next layer without damaging the earlier one. This duration can be reduced to 90 minutes or less by increasing the oven temperature to 120°C. The coating procedure is repeated until achieving the required thickness. The intermediate coating layers are placed in the oven for only 60 minutes as it is found that the intermediate layers can stick and bond stronger to a porous surface compared to the metal surface (in the first layer). After the last coating layer is applied, the coated heat exchanger module is kept in the oven overnight

at 70°C to ensure having a fully dried adsorbent material. This temperature is sufficient to regenerate aluminum fumarate MOF before placing the heat exchanger module in the adsorber bed. Finally, the coating thickness is measured using two methods. The first one is by using a digital caliper with a tolerance of 0.01mm, so that the coating thickness is equal to $(\frac{the\ measured\ overall\ metal\ wire\ with\ the\ coated\ layer\ thicknesses}{wire\ metal\ thickness\ (1mm)*2})$. The second one is by weighing the heat exchanger module before and after the coating and taking into account the bulk density of the coating layer.




Figure 5-3. (a) adsorbent material spraying and (b) initial drying before placing the heat exchanger in the oven

## 5.5. Assembly of the coated MOF adsorption system

Figure 5-4 illustrates the two-bed adsorption desalination and cooling system which consists of two adsorber beds, condenser and evaporator as the main components (CAD drawing is given in appendix C).

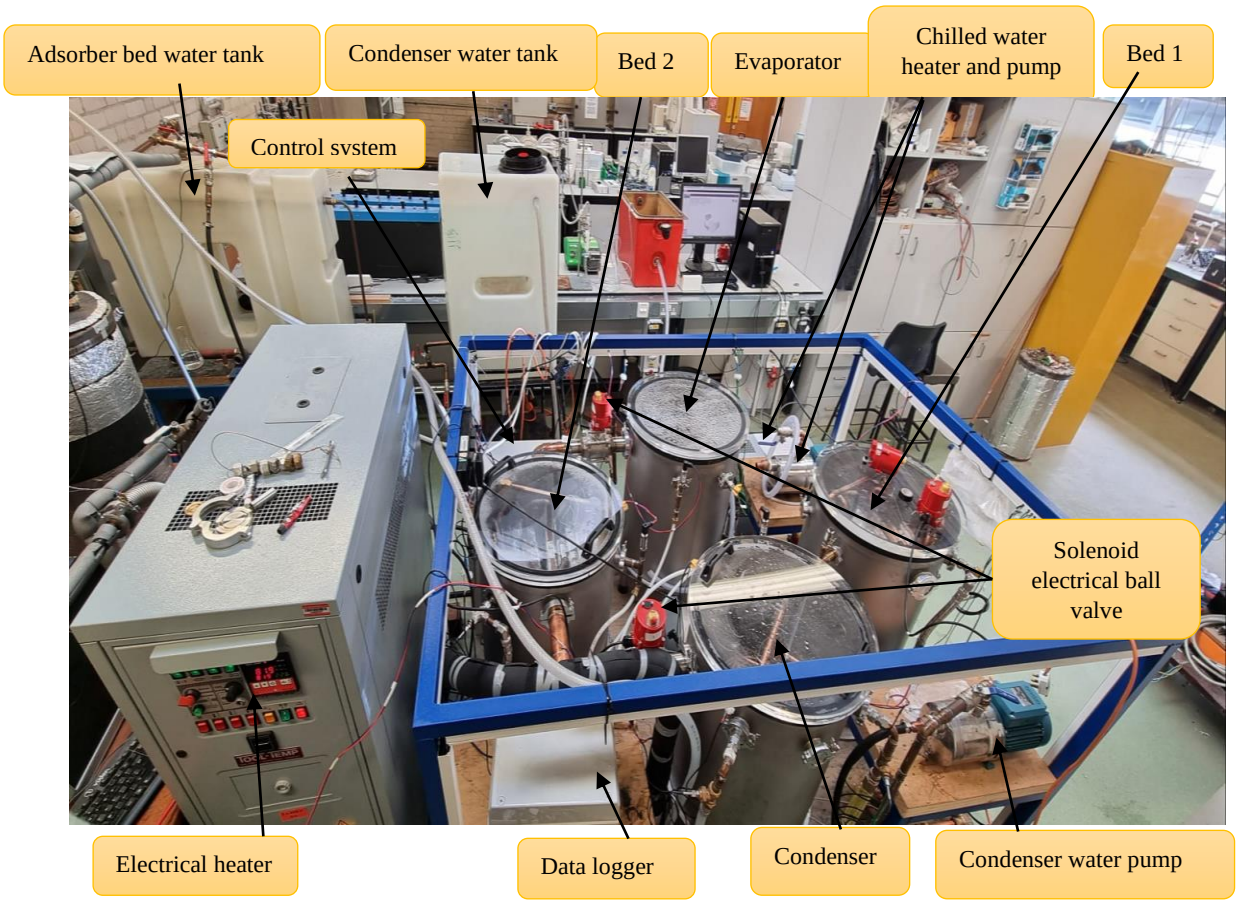



Figure 5-4. Two-bed adsorption heat pump system for desalination and cooling

These components are connected using 50mm copper pipe diameter as vapor lines. This diameter size allows the vapor to pass smoothly from the adsorber beds to avoid the vapor to be accumulated and condensing in the adsorber bed chamber during the desorption process. It also eases the vapor flow from the evaporator to the adsorber bed during the adsorption process. These lines are controlled using four electrical solenoid ball valves to alternate between the adsorption, desorption and switching processes. The two adsorber beds contain aluminum fumarate MOF adsorbent material coated on the surface of wire-finned heat exchanger modules. The adsorbent material is heated/cooled using another copper water line with a diameter of 28mm. This diameter size was selected to minimize the pressure drop by providing a water velocity of slower than 0.4m/s in the main water lines, while the tube diameter is reduced to ¾ inch when the water enters the adsorber bed chambers to increase the velocity and enhance the heat transfer coefficient by obtaining a turbulent flow. This line is also controlled using four three-way electrical solenoid ball valves. Thus, the system has eight electrical valves that are

controlled by LabView software using PC. This software is also used to input the preheating, switching, and half-cycle times as well as the number of cycles used in testing. Three K-type thermocouples (RS Pro 621–2158, with a temperature range between -50 to 250$^{o}$C) are fitted in each chamber to measure the vapor and adsorbent material temperature, while RTD temperature sensors (RS Pro 123–5602, with a temperature range between -50 to 250$^{o}$C) are used to measure the inlet and outlet water temperatures to the heat exchangers inside each chamber. All temperature sensors are calibrated as shown in appendix F. The electrical wirings of the adsorption system are shown in appendix D. The temperature readings of water, vapor and adsorbent material are stored using a data logger (DT 85 series 4 DataTaker) (more details of data logger connection are shown in appendix B). Feeding the water to the system is achieved using temperature controlled electric heater unit (ToolTemp – TT-138 , 24kW) to provide the thermal energy required for the desorption process, cooling water tank and pump to provide the cooling required by the adsorber beds during the adsorption process, cooling water tank and pump to provide cooling required by the condenser and another temperature controlled electric heater unit (ToolTemp – TT-188 , 9kW) to provide the heating load for the evaporator (more details about the hot and cold water sources are shown in appendix B). A vacuum pump (nXDS dry scroll pump from Edwards Co) is connected to the various chambers through a manifold. Each adsorber bed has 12 heat exchanger modules coated with around 9 kg of adsorbent material. A rigid plastic carrier with 12 grooves is machined to fix the modules such that a minimum gap of 3mm between the modules is achieved as shown in Figure 5-5. Note that the gap between the modules is narrow compared to the packed heat exchanger modules in chapter 4. The vapor flow is not restricted by the gap between the modules when the coated wire-finned heat exchanger module is used since the wire-finned tube provides sufficient vapor flow through the modules in all directions which is not the case with the packed one. All the modules are connected in series by soldering the outlet of the module with the inlet of the next module using two copper elbows. The plastic carrier is connected with an aluminum bar profile using steel threaded studs to be used for carrying the modules to be placed inside the chamber (more details on connecting the coated modules are shown in appendix B).

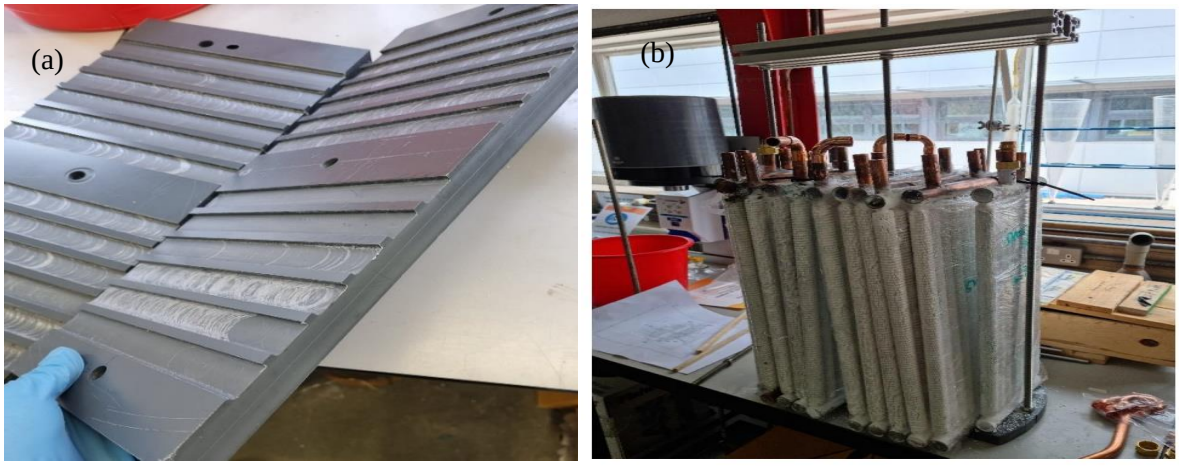



Figure 5-5. (a) Plastic carrier of the heat exchanger and (b) Connecting the coated wire finned tube heat exchanger modules by soldering

Figure 5-6 shows how the heat exchanger modules are placed inside the adsorber chamber with a diameter of 500mm and height of 800mm. The chamber dimensions are selected to minimize the dead volume inside the cylinders.

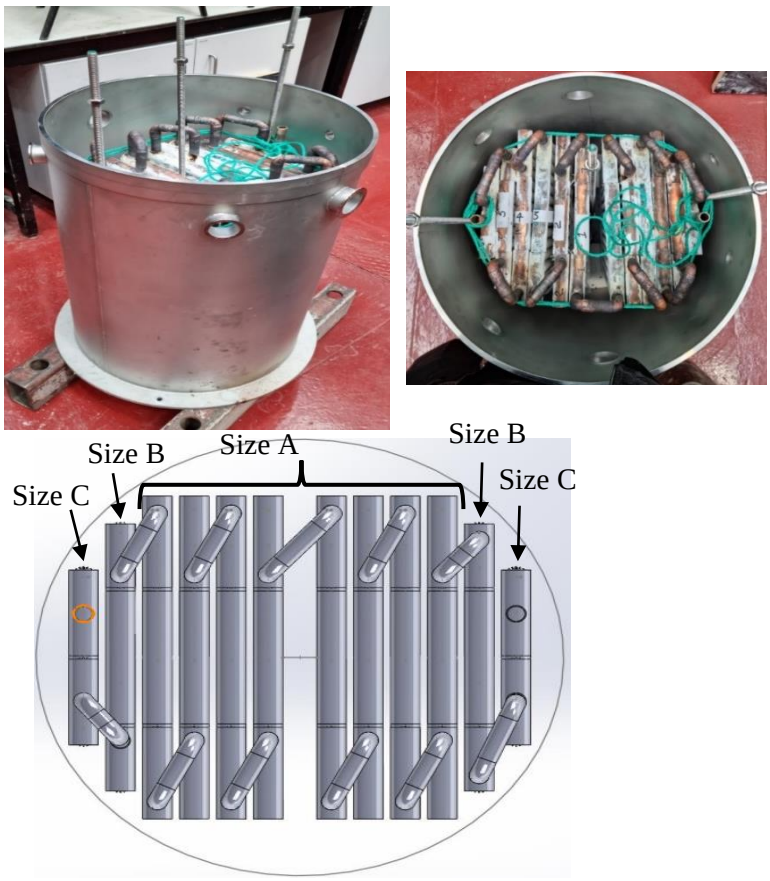



Figure 5-6. Placing the heat exchanger modules inside the adsorber bed

Three module sizes, as shown in Figure 5-6 and Table 5-2 were used to minimize the dead volume in the cylindrical chamber of the adsorber beds.

Table 5-2. Heat exchanger modules dimensions

| Parameters | value | Unit |
|---|---|---|
| Module size A | | |
| Number of modules in each bed | 8 | |
| Module width | 370 | mm |
| Module length | 600 | mm |
| Number of tubes | 14 | |
| Header diameter | 28 | mm |
| Module size B | | |
| Number of modules in each bed | 2 | |
| Module width | 300 | mm |
| Module length | 600 | mm |
| Number of tubes | 12 | - |
| Header diameter | 28 | mm |
| Module size C | | |
| Number of modules in each bed | 2 | - |
| Module width | 200 | mm |
| Module length | 600 | mm |
| Number of tubes | 8 | - |
| Header diameter | 28 | mm |
| Tube geometry | | |
| Tube diameter | 10 | mm |
| Fin height | 7 | mm |
| Fin spacing | 2 | mm |
| Number of fins | 21 | - |
| Fin thickness | 0.7 | mm |

Figure 5-7 shows the heat exchanger copper coils fixed inside the evaporator and condenser chambers (internal diameter of 450mm for each chamber). Each chamber has 60 meters length of copper coils with a diameter of 3/8 inch. This length is selected based on the cooling and heating load for this scale and an overall heat transfer coefficient of 1000 $W/m^2$-K [6]. The coils are connected in parallel by splitting the length of the coil into four portions, each one 15 meters in length. In the condenser, the coils are spread inside the chamber while they are kept flat inside the evaporator to minimize the water height required to cover the coils (heat exchanger coils connections in evaporator and condenser are shown in appendix B).

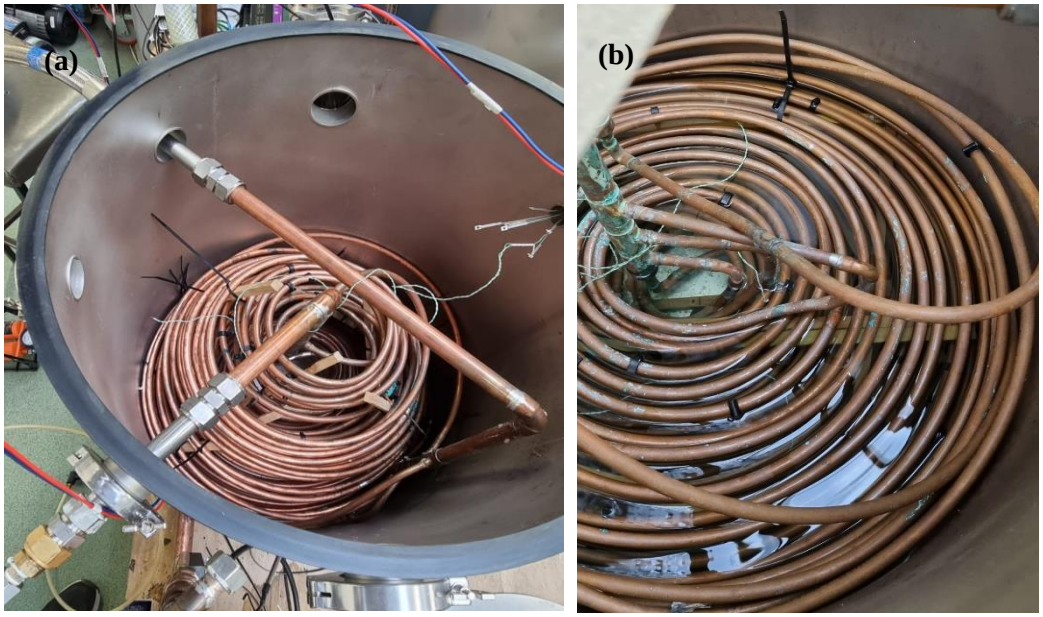



Figure 5-7. Copper coils placed inside the chambers (a) condenser and (b) flooded evaporator

## 5.6. The testing procedure of the coated MOF adsorption system

To prepare the adsorption system for testing, the evaporator is filled with 8 to 12 liters of water, then the lid is placed on top of the evaporator chamber while any water inside the condenser chamber is discharged through the bottom line underneath the condenser. Then, hot water is fed to the adsorber beds at a temperature of 90$^{o}$C and flow rate of 20 l/min for one hour to fully dry the adsorbent material before starting the experiment, followed by vacuuming all chambers by opening the manifold valves between the chambers and the vacuum pump. During or before the vacuuming process, the circulation water inside the condenser and evaporator are turned on. The vacuuming process is continued till the saturation pressure in the chambers reaches a value between 15 to 40 mbar based on the temperature of water flowing inside each chamber. Once the required pressure is achieved, all the vacuum valves in the vacuum manifold are closed as well as turning off the vacuum pump.

The operating temperatures, half-cycle time, switching time and a number of cycles are defined before starting the experiment using the LabView software. Then, the data logger is initialized to store the temperature readings and the experiment is started. During the first 50 to 70 seconds, the hot water line that changed to a cold-water line, has an amount of hot water which will flow to the cold-water

tank thus heating it up. Therefore, the temperature of the adsorber bed is controlled by a cold-water tank feeding mains water to the tank while draining some of the warmed water to offset the increase in the water temperature. This step needs to be repeated every switching time. The same thing happens to the heater unit since it has a hot water tank that experiences temperature reduction due to the cold water return during the switching time. Thus, all the temperatures and drain lines are controlled and monitored during the experiment to maintain a constant feeding temperature to the system. After finishing the experiment, all pumps and heaters are switched off, followed by uploading the temperature readings from the data logger.

## 5.7. Results and discussions

### 5.7.1. Performance of coated wire finned adsorption system

In this section, the performance of the coated wire finned adsorption system is experimentally investigated at various operating temperatures including various heating water inlet temperatures ranging from 50 to 90$^{o}$C, various adsorber bed cooling water inlet temperatures ranging from 25 to 45$^{o}$C and various chilled water inlet temperature ranging from 13 to 31$^{o}$C. The results are then compared to the experimental work presented in chapter 5 using the packed rectangular finned adsorption system.

The operating conditions used in the experiment are illustrated in Table 5-3. At an inlet heating temperature of 90$^{o}$C, cooling temperature of 25$^{o}$C, a chilled water temperature of 23$^{o}$C, and half cycle time of 200 seconds, the MOF adsorption desalination and cooling unit is set to be the reference case in this study.

Table 5-3. Operating conditions

| Parameters | value | Unit |
|---|---|---|
| Adsorption water flowrate (in each chamber) | 25 | L/min |
| Desorption water flowrate (in each chamber) | 20 | L/min |
| Chilled water flowrate | 25 | L/min |
| Condenser water flowrate | 30 | L/min |
| Inlet water adsorption temperature | 25,30,35,40 and 45 | $^{o}$C |
| Inlet heating temperature | 90,80,70, 60 and 50 | $^{o}$C |
| Inlet chilled water temperature | 13, 18, 23, 27 and 31 | $^{o}$C |
| Inlet condenser water temperature | 25 | $^{o}$C |
| Switching time | 70 | sec |

Before carrying out the experiment, a repeatability test was conducted to check that the temperature reading results can be reproduced with the same operating conditions as shown in appendix E. Uncertainty calculations are presented in appendix G. Figure 5-8 shows the water outlet temperature profile in each component of the adsorption system for four cycles. The system was started by drying the adsorbent material in the two beds to ensure having fully dried material before starting the system. An average outlet chilled water temperature of 18$^{o}$C is maintained during all cycles with an increase of 4 degrees observed during the switching time in which a significant reduction in cooling energy is detected during this interval (70 seconds). The switching time is adjusted to suit the energy required to heat up the heat exchangers (12 modules connected in series). Additionally, once the valve between the evaporator and adsorber bed is switched on, a significant amount of water vapor flow to the bed which causes a temperature increase in the bed due to the large amount of water vapor that suddenly enters the bed which is adsorbed releasing a significant amount of adsorption heat. At this operating condition, the SDWP is 14.9 L/kg-day and the SCP is 385 W/kg.

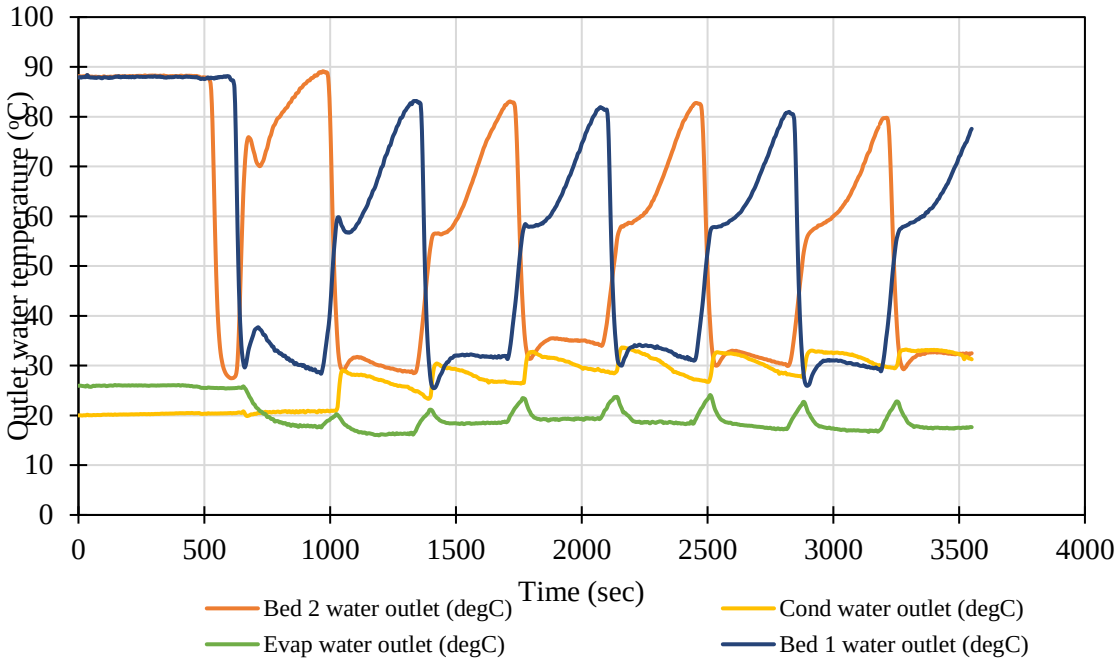



Figure 5-8. Temperature variation with time ($T_{cooling}$ = 25°C, $T_{heating}$ = 90°C, $T_{chilled}$ = 23°C and $t_{halfcycle}$ = 200 sec)

### *5.7.2.* Effect of half cycle time and operating temperatures

Before carrying on a parametric study to investigate the effect of various operating temperatures on the performance of the adsorption system, the optimum half-cycle time is investigated and the result are shown in Figure 5-9. It is observed that the optimum half-cycle time is between 200 and 400 seconds where the maximum daily water production (DWP) and cooling power are around 268 L/day and 6.9kW respectively, while the specific daily water production (SDWP) is 14.9 L/kg/day. A significant drop in water production is observed when the half-cycle time is lower than 200 seconds and higher than 400 seconds. The short half-cycle time indicates that the kinetics of the adsorbent material is significantly improved due to the coating technology which eliminates the thermal contact resistance and increases the effective thermal conductivity between the heating/cooling fluid and the adsorbent material.

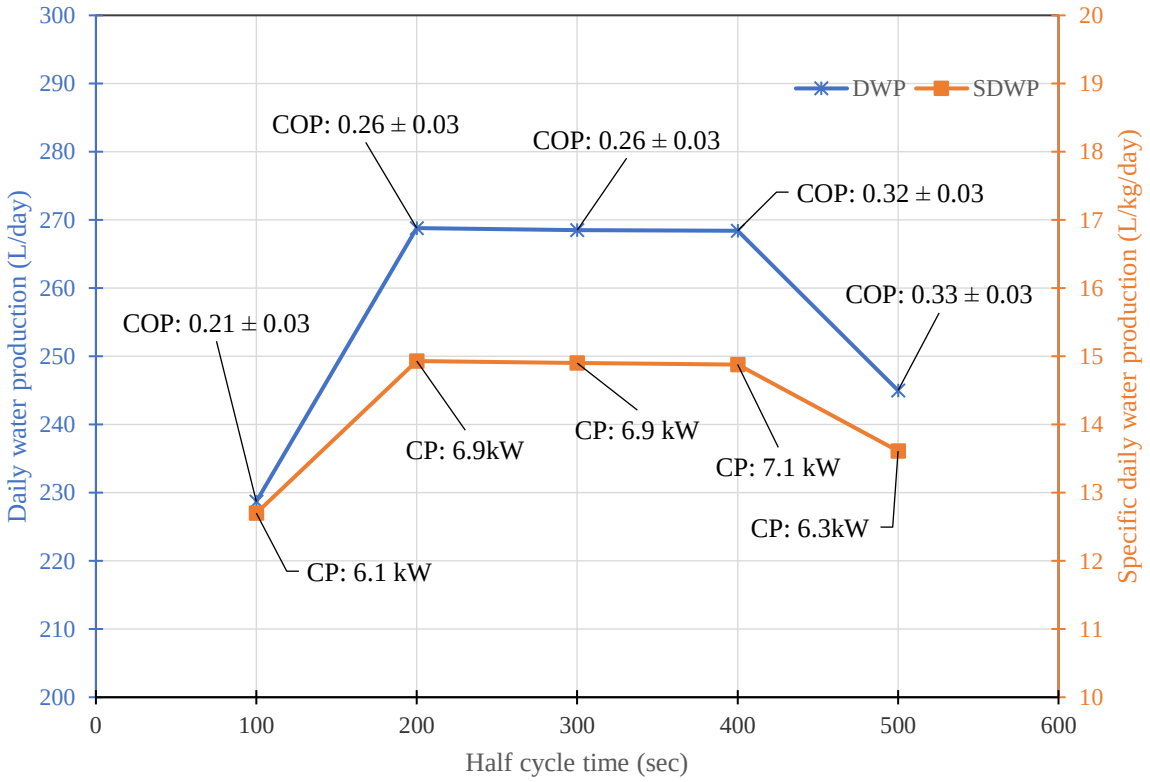



Figure 5-9. Effect of half cycle time on daily water production and specific daily water production. ($T_{des}$ =90°C, $T_{chilled}$ = 23°C, $T_{cond}$ = 25°C, $T_{ads}$ = 25°C)

The COP of the system is also studied at different half-cycle times which showed that increasing the half-cycle time will enhance the COP from 0.21 at half cycle time of 100 seconds and reached 0.33 at half cycle time of 500 seconds. This can be explained as: while the heating energy needed to heat up the adsorbent material is significantly decreased due to short cycle time, the cooling production showed a slight reduction leading to a significant reduction in COP. This is due to the significant amount of energy required at the beginning of the cycle to heat up 12 heat exchanger modules before heating the adsorbent material itself. After some time, this energy is only used to regenerate the material while almost no energy will be required for the metal masses.

Figure 5-10 shows the effect of heating water inlet temperature on the adsorption system performance. It can be seen that as the heating water inlet temperature decreases, the water production decreases. However, the rate of reduction in the water production is more significant as the heating water temperature decreases below 70°C. For example, the water production decreases from 261 to 234.5 L/day (10.1% reduction) when the heating water temperature decreases from 90 to 70°C. On the other hand, decreasing the hot water temperature from 70 to 50°C resulted in decreasing the daily water

production from 234.5 to 101 L/day (56.9% reduction). Thus, the results show that the system is still effective as long as the heating temperature does not drop below 70ºC.

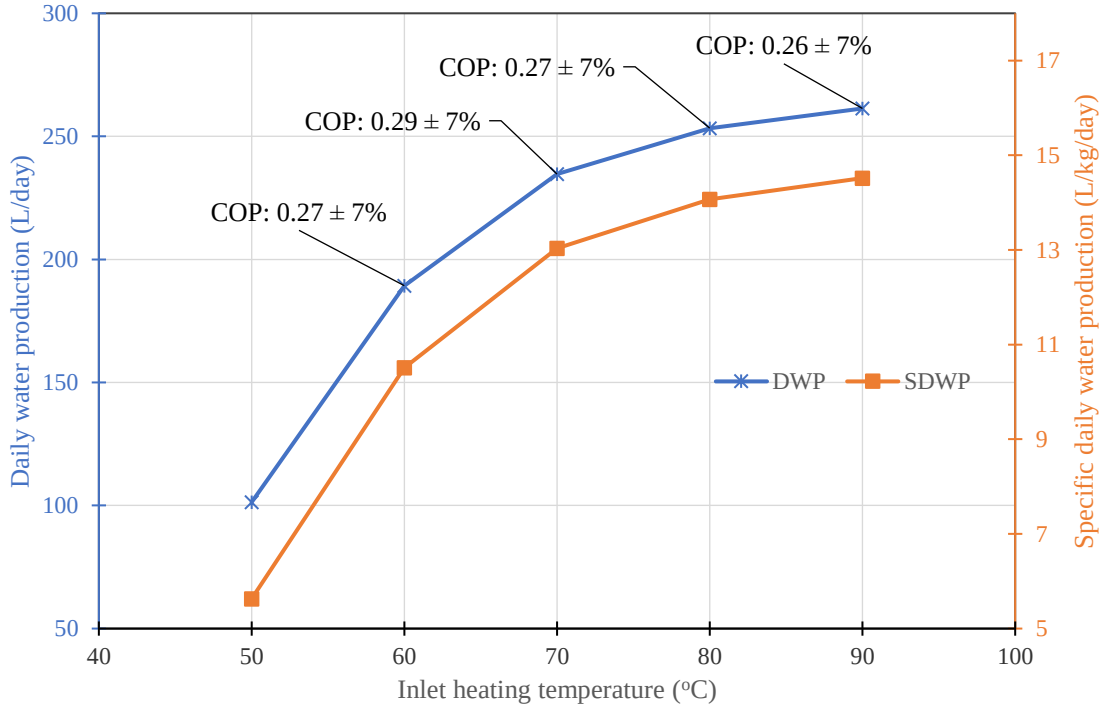



Figure 5-10. Effect of inlet heating temperature (desorption temperature) on daily water production and specific daily water production ($t_{half\ cycle}$ =200 sec, $T_{chilled}$ = 23ºC, $T_{cond}$ = 25ºC, $T_{ads}$ = 25ºC)

This result highlights the advantage of the aluminum fumarate adsorbent material as it requires a relatively low heating temperature to desorb the water vapor. Aluminum fumarate has a high reversible water adsorption with S shape isotherm, which is reflected by the moderate isosteric heat of adsorption (2370 kJ/kg) compared to other MOFs such as CPO-27 Ni (over 3000 kJ/kg) [6]. The maximum COP of the system was found at a heating temperature of 70ºC and any increase in the heating temperature will cause a reduction in the COP, which indicates that the heating energy at this temperature is sufficient to produce the same amount of water production/cooling power as those at higher heating temperature.

Figure 5-11 shows the effect of the evaporator chilled water inlet temperature on the system performance. The results show that this temperature has a significant impact on the system performance since the water production dramatically increased when the chilled water temperature increased from

13 to 23ºC where the daily water production is more than doubled (122.5 L/day to 261.5 L/day). Increasing the chilled water temperature from 23 to 31ºC resulted in increasing the daily water production at a lower rate from 261.5 to 341.5 L/day (30.5% increase). On the other hand, at low chilled inlet water temperature, the system is no longer effective as the performance dropped more than 50%. The effect of this temperature on the system performance can be explained using the adsorption isotherm of the aluminum fumarate with an S shape relation between the relative pressure and water uptake, where at a low relative pressure (lower than 0.2), the equilibrium uptake is very low. While a significant increase in the water uptake is observed at relative pressure between 0.2 and 0.3. Therefore, this adsorption system, using aluminum fumarate, is very effective at an evaporation temperature of 23ºC or above, which also can be indicated by the COP values.

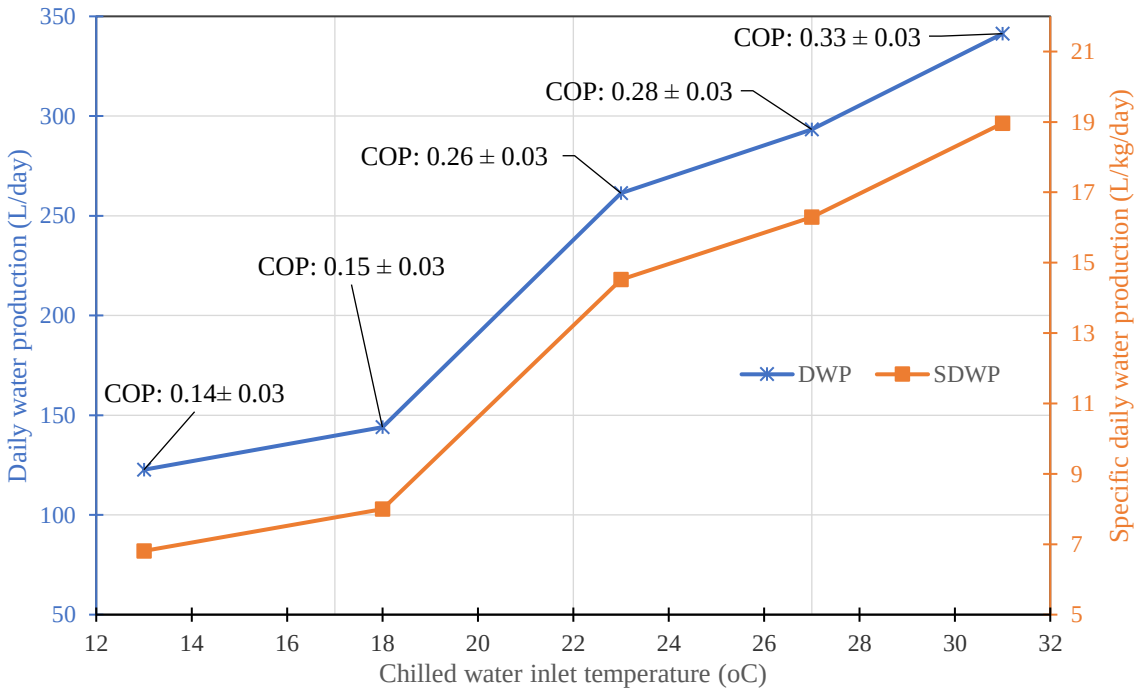



*Figure 5-11. Effect of chilled water inlet temperature (in evaporator) on daily water production and specific daily water production ($t_{half\ cycle}$ =200 sec, $T_{des}$ = 90ºC, $T_{cond}$ = 25ºC, $T_{ads}$ = 25ºC)*

Figure *5-12* investigates the effect of the adsorption of cooling water inlet temperature giving the same impact as the chilled water temperature on the system performance. It can be seen that decreasing the adsorption cooling water temperature resulted in a significant increase in daily water production. Decreasing the cooling water inlet temperature from 45 to 30ºC resulted in increasing the daily water

production from 122.5 to 250.5 L/day. However, a further decrease of the cooling water temperature from 30 to 25ºC resulted in increasing the water production at a lower rate (from 250.5 to 261.5 L/day). Therefore, it is concluded that the adsorber bed should have a cooling temperature of 30ºC or lower to maintain the system performance.

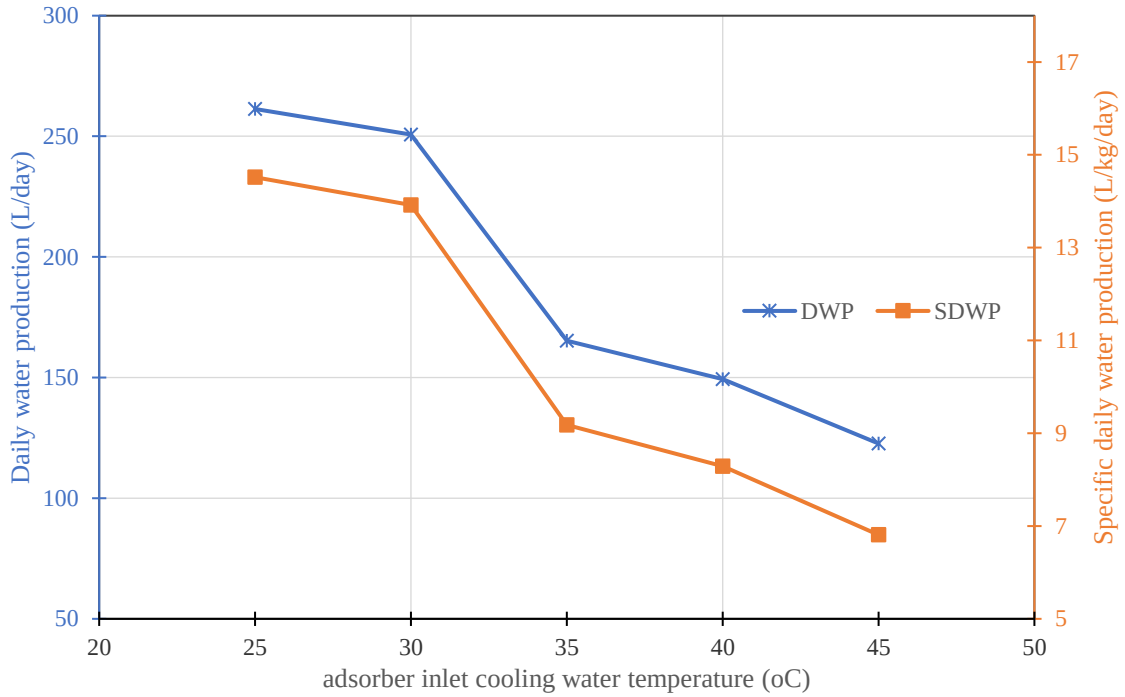



Figure 5-12. Effect of adsorber inlet cooling water temperature on daily water production and specific daily water production (half-cycle time=200 sec, Tdes = 90ºC, Tcond = 25ºC, Tchilled = 23ºC)

### *5.7.3.* Effect of Evaporator and condenser dead volume

One of the critical factors that have been overlooked in the literature, is the design of the evaporator and condenser in the adsorption system in terms of the available void volume above the heat exchanger. Many studies investigated the heat exchanger tube performance in terms of the overall heat transfer coefficient by introducing different tube designs such as plain and coated tubes as well as capillary-assisted tubes [108], while the volume of the chambers of the condenser and evaporator that represents about half of the adsorption system volume was not investigated. Therefore, an investigation on the effect of dead volume in the condenser and evaporator was carried out by occupying the dead volume with insulated wooden blocks (40mmX90mmX150mm). The wood material is selected to minimize the thermal mass impact on the heat transfer coefficient due to the very low thermal conductivity of this

material. Several blocks are placed in the condenser and evaporator to occupy 12.5%, 25%, 37.5% and 50% of the dead volume as shown in Figure 5-13.

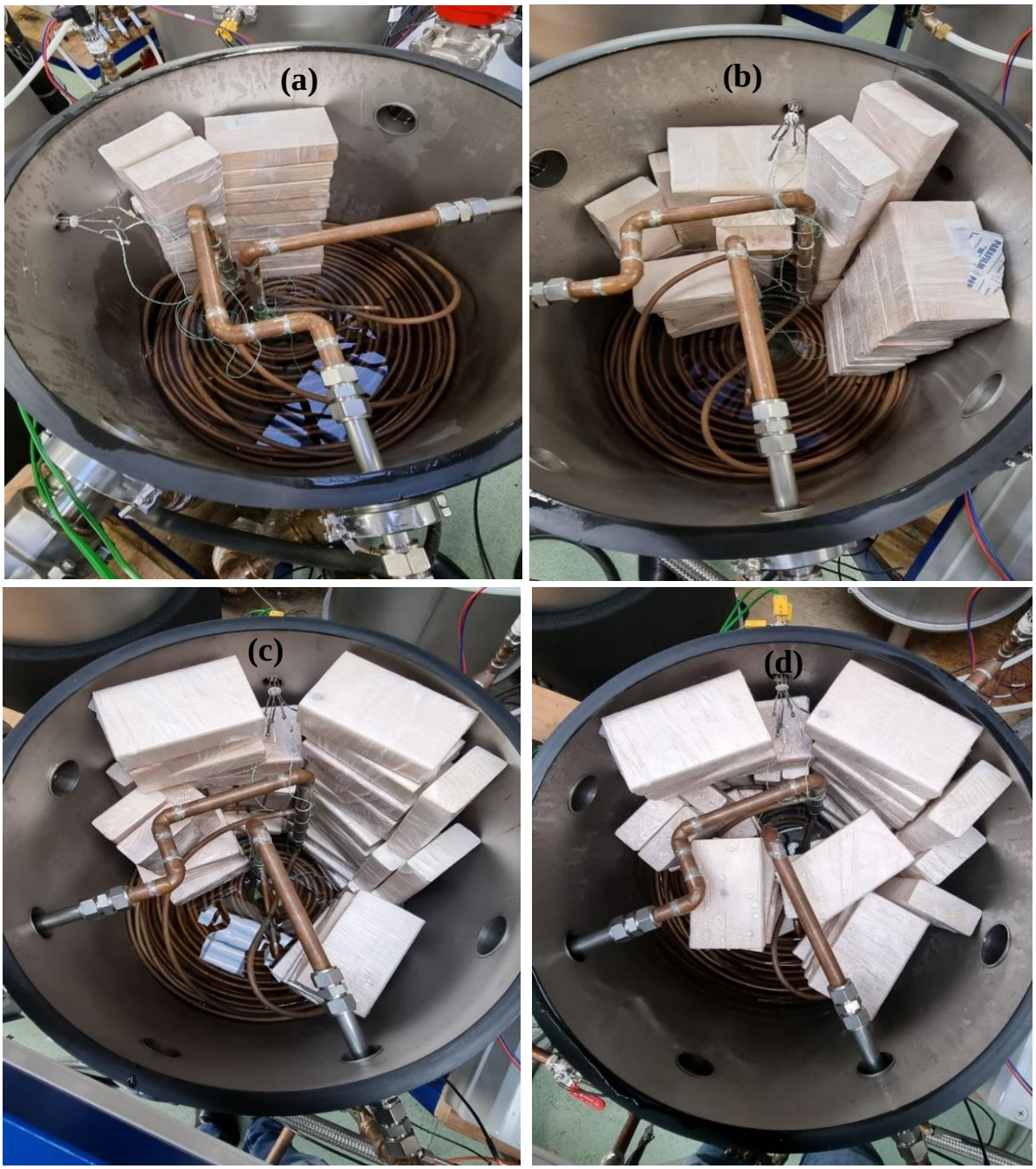



*Figure 5-13. Evaporator chamber (a) 12.5% occupied, (b) 25% occupied, (c) 37.5% occupied and (d) 50% occupied*

By taking into account the uncertainty in the results, it was found that by reducing 50% of the dead volume or less, the daily water production remained almost constant as shown in Figure 5-14. The wooden blocks also did not reduce the vapor flow from/ to the evaporator/condenser during the adsorption/desorption process. This indicates that 50% of the dead volume in the chamber can be

removed. The internal diameter of the chamber is 450mm while the height of the dead volume in the evaporator chamber is 400mm. Thus, the chamber height can be reduced by 200mm, so the overall height of the chamber will be 400mm (200mm the height of the water that fully submerge the coils plus 200mm dead volume).

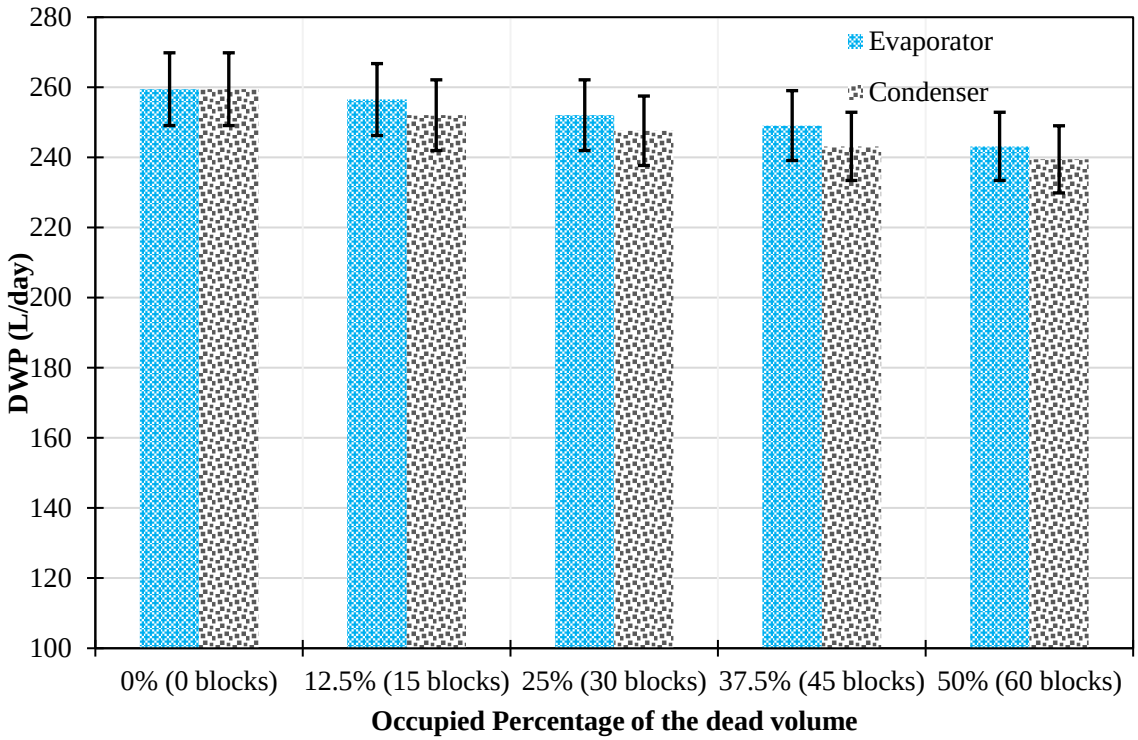



*Figure 5-14. Effect of the dead volume in the evaporator and condenser chambers on the water production*

### *5.7.4.* Comparative study between packed rectangular and coated wire finned tube heat exchanger

Figure 5-15 illustrates the difference between the inlet and outlet water temperatures in the adsorber bed using the packed heat exchanger from Albaik et al. [7] experiment (see section 4.6) and coated heat exchanger in this study. It is observed from the temperature differences that the energy consumed in the regeneration process using the coated method is higher than that of the packed one to produce the same amount of distilled water and cooling power, while the required coated adsorbent material is less than the required one using the packed method.

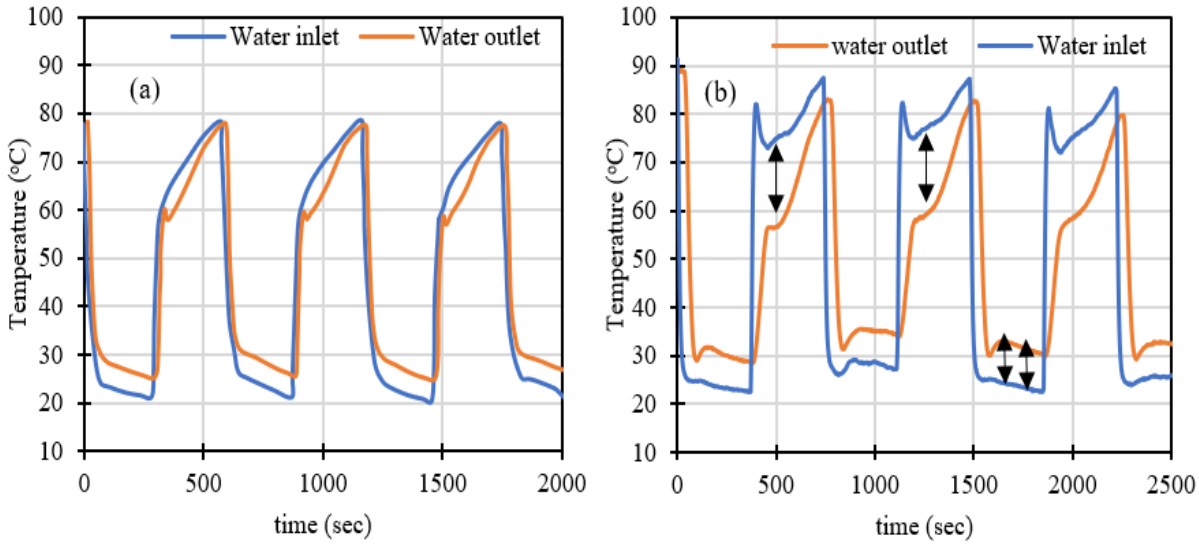



Figure 5-15. The temperature profile of inlet/outlet to/from the adsorber bed (a) packed heat exchanger and (b) coated heat exchanger

Figure 5-16 compares the performance of the packed and coated adsorption system investigated in chapters 4 and 5 in terms of COP, SDWP, and SCP. It can be seen that the COP of the packed adsorption system (0.396) is higher than the coated one (0.26) by 52% as a result of the higher metal mass used in the wire-finned adsorption system. On the other hand, the material performance (SDWP and SCP) shows a major advantage in the coated system over the packed one with an enhancement of around 82% due to the fast kinetics of the coated system. Thus, less amount of adsorbent material mass can be used with the coating method.

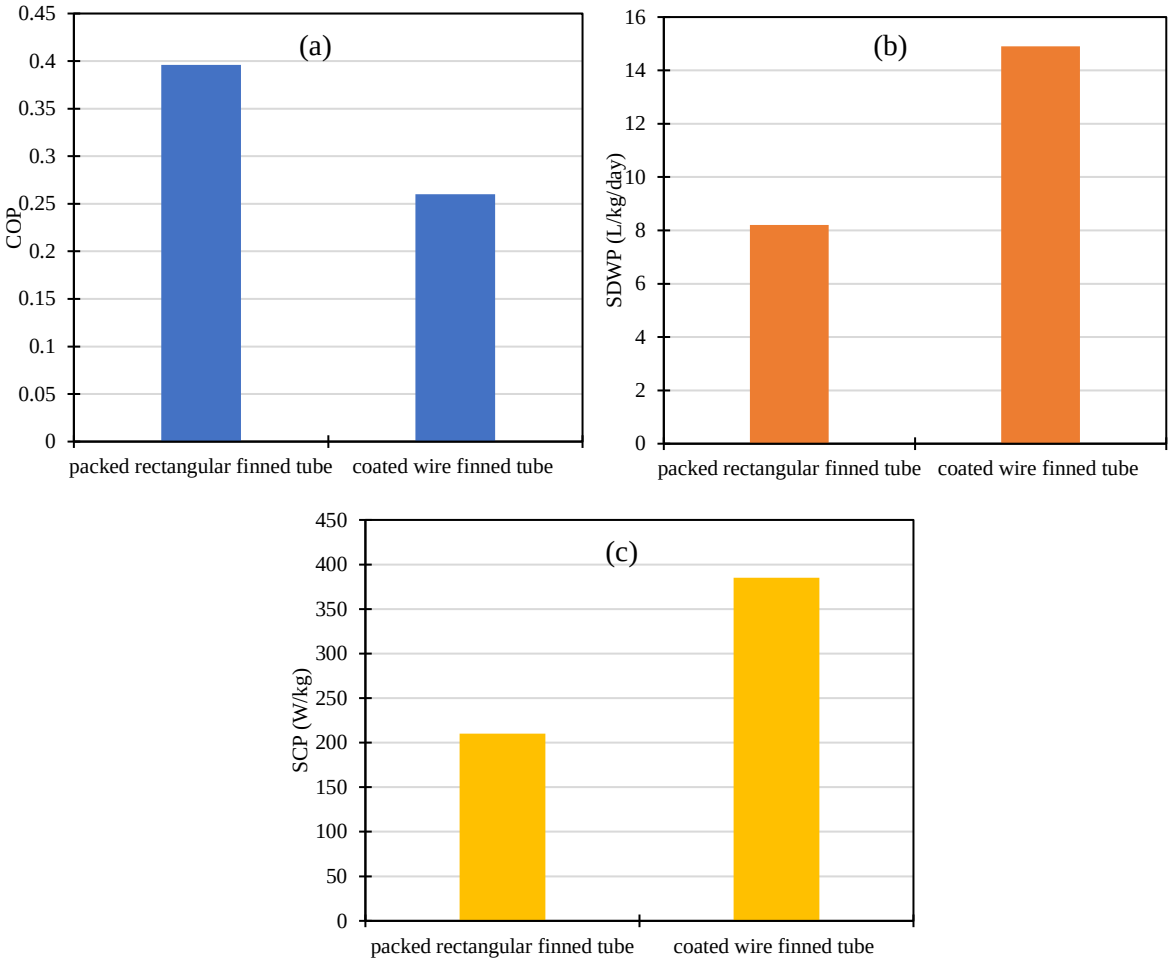



Figure 5-16. Comparative study between the packed rectangular finned heat exchanger and the coated wire finned one *(thalf cycle =200 sec, Tdes = 90°C, Tcond = 25°C, Tchilled = 23°C)* (a) COP, (b) SDWP and (c) SCP

Figure 5-17 shows the specific volume daily water production (SVDWP) of the packed bed compared to that of the coated bed adsorption system. SVDWP is obtained by dividing the daily water production by the volume of the adsorber beds. 8 packed rectangular heat exchanger modules in each bed are used in the adsorption system in chapter 4 to produce 200 L/day of water. Each bed is packed with 11.6 kg of adsorbent material. Each module has a height of 400mm, a width of 28mm and a length of 400mm with an average vapor gap of 10mm considered between the modules. Thus, the overall volume of the modules including the gaps is equal to (0.4m X 0.4m X (0.028m + 0.01m) X 8modules X 2bed = **0.0972 $m^3$ = 97.2L**). On the other hand, 12 coated wire finned tube heat exchanger modules in each bed are connected in the other adsorption system presented in this chapter to produce 261.5 L/day at the same operating conditions of those used in the packed adsorption system in chapter 4. Each module has a height of 600mm, a width of 25mm and a length of 400mm with an average vapor gap of 3mm between

the modules. So, the overall volume of the modules with the gaps is equal to (0.6m X 0.4m X (0.025m + 0.003m) X 12modules X 2bed = **0.1612 $m^3$ = 161.2L**). Therefore, to produce the same amount of water in the packed system (200 L/day), the volume of the coated system can be estimated as **123.3L** (200/261.5 X 161.2L). From this perspective, the packed rectangular finned heat exchanger has higher volumetric capacity compared to the coated finned tube one as the specific volumetric daily water production in the adsorber bed (SVDWP) is **2.057 $L_{water}$/day-$L_{AdsorberBed}$** in the packed one, while it is **1.622 $L_{water}$/day-$L_{AdsorberBed}$** in the coated one.

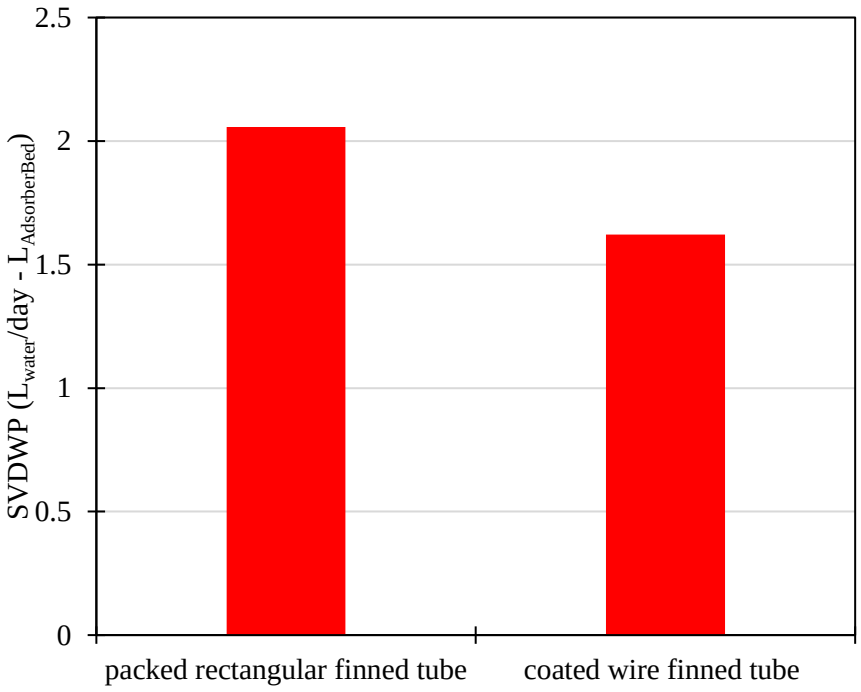



Figure 5-17. Specific volumetric daily water production in the adsorber bed between the packed and coated adsorption system

## 5.8. Conclusions:

Aluminum fumarate MOF material with different coating thicknesses was characterized and identified as potential Metal Organic framework material for water desalination and cooling system. A coating process was successfully developed for integrating the aluminum fumarate MOF material to the heat exchanger metal surfaces used in the adsorber beds. This coating process was shown to improve the adsorption system performance by reducing the thermal resistance between the heating and cooling fluids and the adsorbent material during desorption and adsorption. The adsorption system has a

production of more than 260 L/day of distilled water and 6.9kW of cooling. The system has the potential to be more compact after conducting an experiment on the effect of dead volume in the evaporator and condenser chambers on the system production and it was found that these component volumes can be significantly decreased by 50%.

This chapter ends with a comparative study between the packed rectangular heat exchanger and the coated wire finned one in the adsorber bed and it is concluded that the coated system provides higher adsorbent material performance (in terms of SDWP and SCP) compared to the packed one with an enhancement of 82%. On the other hand, the packed system provides an improvement in the COP by 52% compared to the coated one since less amount of metal mass is required. Additionally, in terms of the specific volumetric daily water production in the adsorber bed (SVDWP), the packed adsorption system has 2.057 $L_{water}$/day-$L_{AdsorberBed}$, which is higher than the coated one (1.622 $L_{water}$/day-$L_{AdsorberBed}$).

# Chapter 6: Hybrid Batch Reverse Osmose-Adsorption desalination system

## 6.1. introduction

The packed rectangular-finned tube is studied numerically and experimentally in chapter 4. In chapters 3 and 5, the coated, packed, and combined coated and packed wire-finned tube is investigated numerically and experimentally. From these chapters, it is concluded that both packed and coated heat exchangers with different geometries have some advantages over the others and some drawbacks. The packed rectangular-finned tube has low adsorbent material performance (such as SDWP and SCP) compared to the coated wire finned tube, while it has higher COP and volumetric capacity. Therefore, either of these designs can be used based on the availability of thermal energy, compactness of the system and applications. For example, when the low-grade energy source is available for free, lower attention is given to the value of the COP, thus the coated wire finned tube heat exchanger would be preferable which also requires less amount of adsorbent material. When the overall energy conversion ratio is important, a high COP is essential especially when the thermal energy source is limited. Additionally, with the packed design, the overall system volume will be smaller as well. In this chapter, the packed rectangular-finned tube heat exchanger is considered for integrating the adsorption cooling and water desalination with Batch Reverse Osmose (BRO) desalination system to have a hybrid BRO-AD system that has high water recovery with less electrical energy consumption and high water quality production.

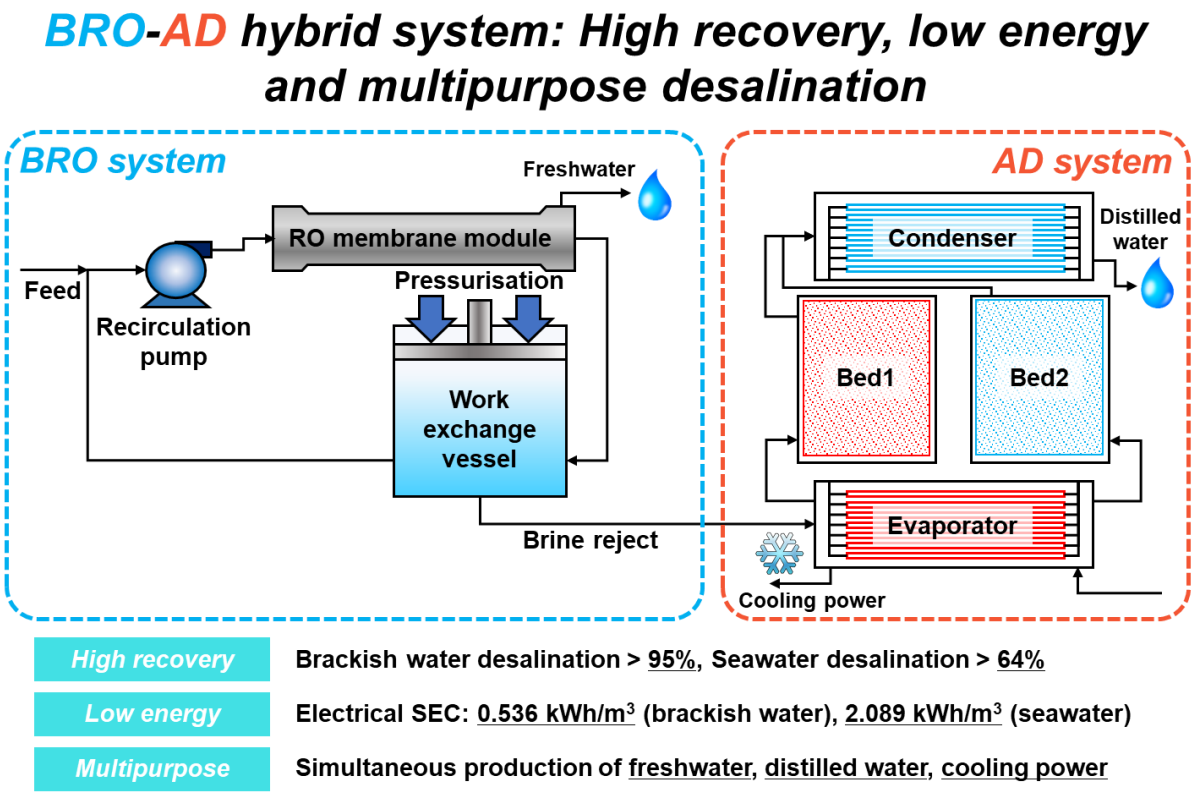
This chapter is based on a published work presented in the following journal paper:

K. Park, **I. Albaik**, P. A. Davies, R. Al-Dadah, S. Mahmoud, M. A. Ismail and M. K. Almesfer, Batch reverse osmosis (BRO)-adsorption desalination (AD) hybrid system for multipurpose desalination and minimal liquid discharge, **Desalination**, 2022 https://doi.org/10.1016/j.desal.2022.115945.

### Credit Authors statament:

**I.Albaik:** Developing a lumped parameter model for the adsorption system and integrating it with the batch reverse osmosis (BRO) model. **K. Park:** Developing the BRO model and integrating it with the

adsorption system. **P. A. Davies, R. Al-Dadah, and S. Mahmoud:** Reviewing and supervision, **M. A. Ismail and M. K. Almesfer:** Project funding and administration.




## 6.2. Abstract

Brine disposal and energy consumption are the two most important challenges for desalination. In this study, a new hybrid desalination process integrating batch reverse osmosis (BRO) and adsorption desalination (AD) is proposed for high recovery and energy efficiency. Hybrid BRO-AD produces distilled water and drinking water simultaneously. It also provides cooling. Simulation results reveal high recovery of 95.95% and 64.84%, the low specific electrical energy consumption of 0.536 and 2.089 kWh/m$^3$, the specific thermal energy consumption of 182.3 and 312.2 kWh/m$^3$, with cooling power generation of 302.5 and 139.5 kW achieved in brackish water and seawater desalination systems, respectively. Thermal energy consumption can be easily supplied by waste heat energy. The effects of feed concentrations in the ranges of 1–8 g/L (brackish water) and 30–44 g/L (seawater) and feed temperature of 25–35 °C are also investigated. The performance of the BRO-AD is compared against

conventional BRO and AD systems. The study showed that the BRO-AD hybrid system achieves higher recovery than BRO, while reducing the high requirements for adsorbent material in simple AD. With its versatile characteristics, the BRO-AD hybrid system can be considered as a breakthrough step toward the minimal/zero liquid discharge system.

## 6.3. Purpose of the study

In this study, we suggest a new design configuration of Batch reverse osmoses and Adsorption (BRO-AD) hybrid system for multipurpose desalination with minimal liquid discharge using MOF. Mathematical modelling for BRO-AD hybrid system was developed to estimate the performance of the BRO-AD hybrid system such as energy consumption, water production rate, permeate water quality, and cooling power generation. The applicability of the BRO-AD hybrid system for brackish water and seawater desalination was analysed. The effects of feed conditions such as concentration and temperature were investigated comprehensively to identify the appropriate operating conditions of the BRO-AD hybrid system. To reveal the competitiveness of the BRO-AD hybrid system, the conventional BRO and AD systems were compared in terms of energy consumption, permeate water quality, and cooling power generation. Finally, the potential of zero liquid discharge (ZLD) or minimal liquid discharge (MLD) was discussed.

## 6.4. Description of BRO-AD hybrid system

BRO-AD hybrid system consists of BRO and AD units, where these units are connected sequentially as shown in *Figure 6-1*. It is assumed that feed water is supplied after a pre-treatment system to avoid fouling or scaling in the BRO-AD system. The BRO unit in the BRO-AD hybrid system is operated by the same working principle of the conventional BRO. In a pressurisation phase, the feed water is fed into the left side of a work exchange vessel at a constant flow rate while increasing its pressure by a feed pump. The pressure in the feed water is transferred via a free piston to feed water in the right side of the work exchange vessel. During the pressurisation, the feed water on the right side of the work

exchange vessel flows to a RO module, and permeate water is produced by the applied pressure. At the end of the RO module, concentrated brine is recirculated by a recirculation pump and returns to the work exchange vessel. Because this is a batch-type operation, the concentration in the BRO unit increases continuously, and the applied pressure of the feed pump should be increased to maintain the constant permeate water production. When the free-piston reaches at the end of the work exchange vessel, the pressurisation phase is finished, and the purge-and-refill phase begins. In the purge-and-refill phase, the concentrated brine in the BRO unit is discharged, and new feed water is supplied by the feed pump to the BRO unit. At that time, the feed water on the left side of the work exchange vessel is moved by the recirculation pump to the right side for starting the next cycle. When the concentration of the discharged brine drops below a certain level, the purge-and-refill phase is finished, and the next pressurisation phase is started.

In the AD cooling and desalination system, two beds are used to ensure continuous water and cooling production to be integrated with the continuous brine discharge from the BRO system. During the first half cycle of the system, the first bed operates in adsorption mode by opening the valve between the evaporator and the first bed while feeding cold water to cool down the adsorbent material. During this process, the brine water in the evaporator starts to evaporate at a specific saturation temperature (less than 15 °C) while the adsorbent material adsorbs the evaporated water, and a cooling effect is generated in the evaporator. On the other hand, the second bed operates in desorption mode by opening the valve between the condenser and the second bed to allow the stored water in the adsorbent material to be desorbed and condensed in the condenser by feeding hot water to heat up the adsorbent material. A switching time of 40 seconds is required to switch the processes (adsorption and desorption processes) between the beds. During the switching time, more brine water will be accumulated in the evaporator until the adsorption process starts. The required adsorbent mass is determined based on the water recovery of the AD.

BRO is advantageous for water treatment with low-energy consumption. However, the required energy and pressure increase to a very high value as recovery increases. For example, feed water with a 3 g/L concentration is desalinated by BRO at 80% recovery, and the required specific energy consumption

(SEC) and peak pressure are 0.39 kWh/m3 and 16.9 bar. At the recovery of 90%, the peak pressure of the BRO is higher than 30 bar [173]. Because the RO membrane has maximum durable pressure, the recovery cannot be easily over a certain level for reaching ZLD or MLD without violating the pressure limitation. Therefore, any subsequent water treatment system which is not significantly affected by the increase of osmotic pressure should follow the BRO to further increase the recovery. AD system is a candidate for the subsequent system after the BRO because the AD system is energy-efficient thermal desalination technology that is less affected by the osmotic pressure. Therefore, the key aspect in this study is to design the hybridisation of BRO and AD systems for a very high recovery toward ZLD and MLD systems.

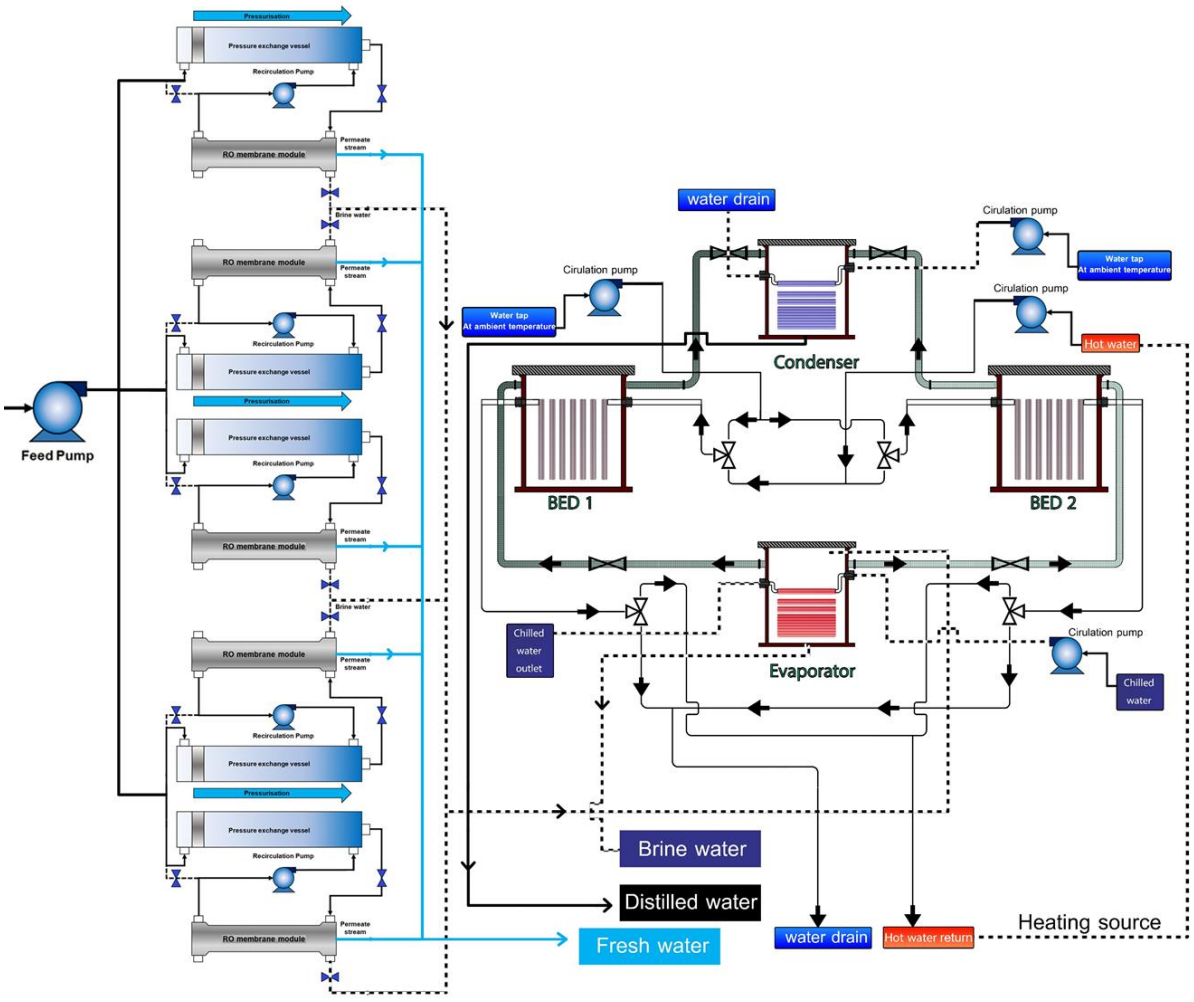



*Figure 6-1. Schematic illustrations of BRO-AD hybrid process.*

However, BRO is a cyclic system inherently. The concentrated brine from the BRO is discharged intermittently. Thus, a connecting strategy between the BRO and AD should be designed to make the BRO-AD hybrid system be operated continuously. To illustrate how the continuous operation in the BRO-AD hybrid system is obtained, five BRO units (80% recovery assumed) are connected in parallel in which the pressurization and purge phases are simultaneously operated to produce continuous brine flow from the BRO units. The two-bed adsorption unit also operates simultaneously in which the first bed is working under the adsorption process while the second bed is in the desorption process to ensure continuous water production as shown in Figure 6-2.

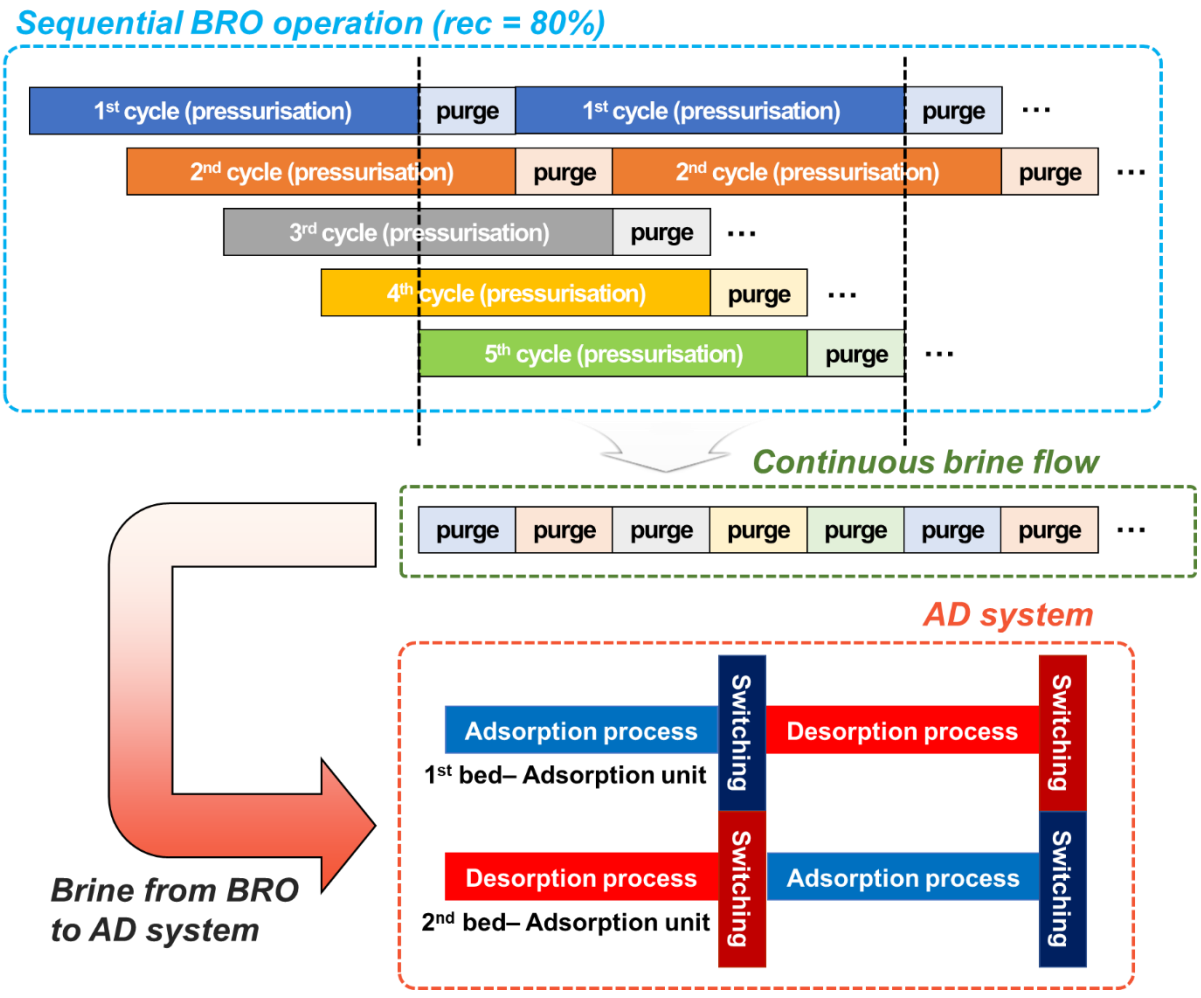



Figure 6-2. Operating strategy for continuous water production in BRO-AD hybrid system.

## 6.5. Mathematical modelling

To simulate the BRO-AD hybrid process, mathematical modelling equations of BRO and AD were used. Each model was solved individually, and the simulation results from the BRO were used as the feed conditions for the AD model as described in Figure 6-2. The BRO and AD models have been validated in previous papers [7,173,194]. The simulation program was developed using MATLAB R2020b.

To simulate the processes in the AD system, mass, energy, water adsorption isotherm and kinetics equations are modelled.

**(I)** Conservation of mass

The evaporator has one inlet (the brine from BRO) and two outlets: the brine discharge from the evaporator and the evaporated water are transferred to the active adsorber bed. During the switching time, the evaporation of water is paused. Therefore, to determine the rate of change of mass in the evaporator ($\frac{dm_{evap}}{dt}$), the mass balance equation is used as follows:

$$\frac{dm_{evap}}{dt} = \dot{m}_{BRO,b} - \dot{m}_{AD,b} - \emptyset\, m_{ads} \frac{dX}{dt} \tag{6.1}$$

where $m_{ads}$ is the adsorbent material mass, $\dot{m}_{BRO,b}$ is the brine mass flow rate from BRO system, $\dot{m}_{AD,b}$ is the brine mass flow rate of the AD system, $X$ is the instantaneous water uptake fraction by the active adsorber bed, and $\emptyset$ equals 1 during the adsorption process and 0 during the switching time.

Similarly, the salt balance equation in the evaporator gives:

$$m_w \frac{dS_{evap}}{dt} = \dot{m}_{BRO,b}.S_{BRO,b} - \dot{m}_{AD,b}.S_{AD,b} - \emptyset.S_{ads}\, m_{ads} \frac{dX}{dt} \tag{6.2}$$

where $S$ is the mass fraction of salt in each case, as indicated by the respective subscripts.

(2) Conservation of energy

Starting with the energy balance equation of the evaporator, based on the inlet and outlet streams of fluid, the energy equation can be written as follows:

$$(m_{HX}Cp_{HX} + m_w Cp_w)\frac{dT_{evap}}{dt} = h_f m_{BRO,b} - h_f \dot{m}_{AD,b} - \emptyset\, h_{fg}\, m_{ads}\frac{dX}{dt} + \dot{m}_{ch}Cp_{ch}\left(T_{ch,in} - T_{ch,out}\right) \quad (6.3)$$

where $m_{HX}$ and $Cp_{HX}$ are respectively the mass and specific heat of the heat exchanger in the evaporator, $h_f$ and $h_{fg}$ are respectively the enthalpy of liquid and the latent heat of evaporation, $\dot{m}_{ch}$ is the chilled water flow rate, $Cp_{ch}$ is the specific heat of the chilled water and $T_{ch,in}$ and $T_{ch,out}$ are the chilled water inlet and outlet temperatures respectively.

The left-hand side of eq 6.3 represents the rate of change of sensible heat stored in the evaporator (heat exchanger and water content). The right-hand side represents the heat added by the brine water from the BRO, the rate of heat removed by the discharged brine from the evaporator, the rate of heat extracted due to the evaporation, and the rate of heat extracted from the chilled water that passes through the heat exchanger coils respectively.

In each bed, the energy balance equation is based on the process (adsorption or desorption). Cold water inlet/outlet is used during the adsorption process, while hot water inlet/outlet is used during the desorption process. Therefore, the energy balance is calculated as follows:

$$(m_{HX}Cp_{HX} + m_w Cp_w + m_{ads}Cp_{ads})\frac{dT_{bed}}{dt} = \emptyset\, Q_{st}\, m_{ads}\frac{dX}{dt} + m_{cw/hw}Cp_{cw/hw}\left(T_{cw/hw,in} - T_{cw/hw,out}\right) \quad (6.4)$$

where $Q_{st}$ is the isosteric heat of adsorption and $\dot{m}_{cw/hw}$ is the mass flow rate of the cold/hot water.

The left side of the equation represents the extracted/added heat from/to the heat exchanger in the bed, adsorbent material and adsorbed water inside the pores of the adsorbent material. While the right side of the equation represents the generated/extracted during adsorption/desorption process and heat transfer to/from the thermal fluid during these processes.

In the condenser, there are one inlet from the desorber bed and one outlet to discharge the condensed distilled water during the desorption process. The energy balance equation is calculated as follows:

$$(m_{HX}Cp_{HX} + m_w Cp_w)\frac{dT_{cond}}{dt} = -h_f \dot{m}_{AD,dis} + \emptyset\, h_{fg} m_{ads}\frac{dX}{dt} + \dot{m}_{cond} Cp_{cond}\left(T_{cond,in} - T_{cond,out}\right) \quad (6.5)$$

where $\dot{m}_{AD,distilled}$ is the mass flow rate of the discharge of distilled water from the condenser.

The left side of Eq. (6.5) represents the rate of the extracted heat from the heat exchanger and distilled water of the condenser respectively, while the right-hand side represents the extracted heat from the outlet distilled water, added heat due to the condensation, and the rate of heat transfer to the cooling water of the condenser.

(1) Heat transfer

The overall heat transfer coefficients (*U*) in each heat exchanger of the AD system (evaporator, condenser and adsorber bed) and the surface area of the heat exchanger are used to calculate the outlet water temperature based on the following equation:

$$T_{out} = \frac{\mathrm{UA}_s\ \mathrm{LMTD}}{\dot{M}Cp} + T_{in} \quad (6.6)$$

where $\mathrm{A}_s$ is the surface area of the heat exchanger and LMTD is the logarithmic mean temperature between the heat exchanger, inlet and outlet thermal fluid temperatures.

The overall heat transfer coefficient in the evaporator, condenser and adsorber bed heat exchangers consists of three thermal resistances which occur in series and are represented by the following equation:

$$\mathrm{UA}_s = \frac{1}{R_i + R_{tube} + R_o} \tag{6.7}$$

$R_{tube}$ is the metal tube thermal resistance, $R_o$ is the outer thermal resistance and $R_i$ is the internal thermal resistance of the heat exchangers which is related to the thermal fluid and can be calculated using the following equations:

$$R_i = \frac{1}{h_i A_s} \tag{6.8}$$

$$h_i = \frac{\mathrm{Nu\ k}}{D_{tube}} \tag{6.9}$$

$$\mathrm{Nu} = \frac{\frac{f}{8}(\mathrm{Re} - 1000)\mathrm{Pr}}{1 + 12.7\sqrt{\frac{f}{8}}\left(Pr^{\frac{2}{3}} - 1\right)} \quad when\ 3000 < \mathrm{Re} < 5(10)^6\ and\ Nu = 4.36\ \text{when Re} < 3000 \tag{6.10}$$

$$\mathrm{f} = \frac{1}{\left(1.8 log_{10}\left(\frac{6.9}{Re} + \left(\frac{\frac{\varepsilon}{d}}{3.7}\right)^{1.11}\right)\right)^2} \tag{6.11}$$

where $h_i$ is the internal heat transfer coefficient, Nu is the Nusselt number, Pr is the Prandtl number, f is the friction factor and $\varepsilon$ is the surface roughness.

As the heat exchanger in the beds is a finned tube type and packed with granular adsorbent material that has a thermal contact resistance, the outer heat transfer coefficient in the adsorber

bed is calculated using the Rezk et al. model [28]. While the outer heat transfer coefficient in the evaporator is based on the nucleate pool boiling in the flooded evaporator and is based on laminar falling film condensation over horizontal tubes in the condenser.

The thermophysical properties of the AD system can be summarized as shown in Table 6-1.

*Table 6-1. Thermophysical properties of the AD system*

| Parameter | Value |
|---|---|
| Adsorbent bulk density ($kg/m^3$) | 520 |
| Isosteric heat of adsorption (kJ/kg) | 2370 |
| Thermal conductivity of metal tube in condenser/adsorber bed (W/m-K) | 385 (copper) |
| Thermal conductivity of metal tube in evaporator (W/m-K) | 15 (stainless steel) |
| Thermal conductivity of fins in adsorber bed (W/m-K) | 205 (Aluminium) |
| Thermal conductivity of adsorbent material (W/m-K) | 0.12 |
| Specific heat of adsorbent (J/kg-K) | 970 |
| Activation Energy (J/mol) | $1.80 \times 10^4$ |
| Pre-exponential constant (1/s) | 1.29 |

To combine the AD unit with the BRO, the operating temperatures and cycle time (see Table 6-2) of the AD unit are adjusted to ensure continuous distilled water production as well as cooling power at low temperatures (less than 20 °C).

Table 6-2. Operating conditions of AD unit.

| Parameter | Unit | Value |
|---|---|---|
| Inlet brine water temperature from BRO | °C | 25, 30 and 35 |
| Inlet adsorption water temperature | | |
| Inlet condenser water temperature | | |
| Inlet chilled water temperature | °C | 24 |
| Inlet desorption water temperature | °C | 90 |
| Half cycle time | s | 300 |
| Switching time | s | 40 |

(5) AD cycle performance

To indicate the performance of the AD system, SDWP, SCP and COP are calculated using the following equations:

$$\text{SDWP} = \int_0^{tcycle} \frac{Q_{cond}}{h_{fg} M_{ads}} dt \tag{6.12}$$

$$\text{SCP} = \int_0^{tcycle} \frac{Q_{evap}}{M_{ads}} dt \tag{6.13}$$

$$\text{COP} = \int_0^{tcycle} \frac{Q_{evap}}{Q_{des}} dt \tag{6.14}$$

where $Q_{cond}$ , $Q_{evap}$ and $Q_{des}$ are the extracted/added energy in the condenser, evaporator and desorber bed, respectively.

(6) Specific electrical and thermal energy consumptions

The electrical energy consumption in the AD system is mainly the water pumping energy to the heat exchanger coils in the evaporator and condenser and the packed finned tube in the adsorber bed. The electrical pumping power is calculated using the following equation:

$$PW_{elec} = \eta \frac{q\,\rho\,g\,h}{3.6\,(10^6)} \tag{6.15}$$

where $PW_{elec}$ is the electrical pumping power (kW), q is the flow rate ($m^3/h$), g is the acceleration due to gravity ($m/s^2$), $\rho$ is the density and $h$ is the differential head (m).

The differential head consists of the minor losses ($h_{minor}$) (due to components in the system such as elbows and valves) and major losses ($h_{major}$) (due to friction in the pipe). The ($h_{major}$) is calculated as follows:

$$h_{major} = \lambda \frac{l\,V^2}{2g\,d_h} \tag{6.16}$$

where λ is the friction coefficient of the copper pipes in the condenser/adsorber bed and stainless pipes in evaporator [195], $l$ is the pipe length and $d_h$ is the hydraulic diameter.

The pipe length is calculated based on the surface area of the pipes in the evaporator and condenser (outer diameter of 15mm) determined using the overall heat transfer coefficients. While the pipe length in the adsorber bed is calculated based on the required amount of adsorbent material in which each packed heat exchanger module consists of 8 parallel finned tubes with an outer diameter of 9.54 mm, length of 800 mm, fin spacing of 2 mm and fin height of 8.5 mm. The velocity in all pipes is 0.5 m/s.

The ($h_{minor}$) is calculated as follows:

$$h_{minor} = \xi \frac{V^2}{2g} \tag{6.17}$$

where ξ is the minor loss coefficient (0.05 for the ball valve, 7 for the flowmeter, 1.5 for 180 ° elbow and 1 for the inlet and outlet) [195]

Thus, the $SEC_{elec,AD}$ is calculated as follows:

$$\mathrm{SEC_{elec,AD}} = \frac{(24).PW_{elec}}{\mathrm{SDWP}.M_{ads}} \tag{6.18}$$

Regarding the thermal consumption in the AD system, which is calculated from the required heating energy during the desorption process, the following equation is used:

$$\mathrm{SEC_{heat,AD}} = \left(\frac{\mathrm{SCP}.M_{ads}}{\mathrm{COP}}\right).\frac{(24)}{\mathrm{SDWP}.M_{ads}} \tag{6.19}$$

where $\left(\frac{\mathrm{SCP}.M_{ads}}{\mathrm{COP}}\right)$ is the heating power (kW).

The overall electrical and thermal SEC in the BRO-AD hybrid system are expressed as follows:

$$\mathrm{SEC_{elec}} = \frac{\mathrm{SEC_{elec,BRO}} \cdot \dot{\mathrm{V}}_{\mathrm{feed}} + \mathrm{SEC_{elec,AD}} \cdot \dot{\mathrm{V}}_{\mathrm{cond}}}{\dot{\mathrm{V}}_{\mathrm{feed}} + \dot{\mathrm{V}}_{\mathrm{cond}}} \tag{6.20}$$

$$\mathrm{SEC_{heat}} = \frac{\mathrm{SEC_{heat,AD}} \cdot \dot{\mathrm{V}}_{\mathrm{cond}}}{\dot{\mathrm{V}}_{\mathrm{feed}} + \dot{\mathrm{V}}_{\mathrm{cond}}} \tag{6.21}$$

$\dot{\mathrm{V}}_{\mathrm{cond}}$ is the distilled volumetric flow rate output from the condenser ($m^3$/hr) which can be calculated using the following equation:

$$\dot{\mathrm{V}}_{\mathrm{cond}} = \frac{\mathrm{SDWP\ M_{ads}}}{24(1000)} \tag{6.22}$$

To study the salinity effect on the water production of the AD, a linear equation is considered based on the experimental study that was carried out in chapter 4 for a salinity concentration of up to 100,000 ppm (100 g/L). The results showed that the SDWP is decreased by only 16.3% when the salinity

concentration increased from 90 to 100,000 ppm (0.09 to 100 g/L). The reduction percentage on the water production is calculated as follows:

$$SE = (0.001382626\, BC) + 0.010087 \quad (6.23)$$

where SE is the salinity effect and BC is the brine concentration from the BRO system.

The adsorbent mass is calculated to study the effect of water salinity and temperature based on ensuring that the water salinity of the brine water that is discharged from the AD system does not exceed 130,000 ppm (130 g/L) in which the heat transfer coefficient in the evaporator is not affected significantly by the water salinity. To apply the SE in the model, the rate of the water uptake $\frac{\mathrm{dX}}{dt}$ in the LDF equation (Eq. (27)) is multiplied by (1-SE).

## 6.6. Results and discussion

### 6.6.1. Base case analysis for BRO-AD hybrid system

Because we are considering the implementation of a BRO-AD hybrid system for brackish water and seawater desalination, two base cases are needed for the analysis. In brackish water desalination, the base case was selected as 3 g/L of feed concentration, 3,000 L/h of feed flow rate, and 25 °C of feed temperature. In seawater desalination, the base case condition was 35 g/L, 1,200 L/h, and 25 °C.

The operating temperatures of the adsorption system for the two base cases were set to be 25 °C, 90 °C, 20 °C and 25 °C for the inlet of the cooling, heating, chilled and condenser water, respectively. Table 6-3 and

*Table 6-4* showed the simulation results for the base case of the BRO-AD hybrid system in brackish water desalination with XLE-440 membrane for high-flux (from Dupont) and with BW440R membrane for high-rejection (from LG Chem.), respectively. The results showed that the BRO-AD hybrid system can be operated at very high recovery of over 95%. The BRO unit in the BRO-AD hybrid system is

operated at 80% recovery, and the subsequent AD unit desalinates the brine after the BRO unit to reach a very high recovery. This is a very remarkable feature because the importance of ZLD or MLD has been emphasized recently [179]. The energy consumptions of the BRO-AD hybrid system with XLE-440 (high-flux) membrane are 0.536 kWh/m3 (electricity) and 182.3 kWh/m3 (thermal energy). The SECelec is relatively small compared to the energy consumption of brackish water reverse osmosis (BWRO) processes (0.6–1.7 kWh/m3) [196–198]. Note that the BWRO processes are assumed to be operated at 70–80% recovery, which is much lower than the recovery (over 95%) achieved in this study. Thus, SECelec in the BRO-AD hybrid system is very low when considering its very high recovery. Although BRO-AD hybrid system requires substantial thermal energy, it is not a significant issue if the required thermal energy can be obtained from low-grade thermal resources. The operating temperature of the AD unit in the BRO-AD hybrid system is 90 °C, which can be achieved by low-grade thermal energy. In addition, SECheat in the BRO-AD hybrid system is relatively lower than other thermal desalination systems such as membrane distillation [199].

Besides the low energy consumption, BRO-AD hybrid system can be utilized as a multipurpose desalination process. The freshwater produced by BRO unit has a sufficient quality for use as drinking water (0.238 g/L at the case with high-flux membrane and 0.065 g/L at the case with a high-rejection membrane). The drinking water concentration recommended by environmental protection agency (EPA) in United States is less than 500 ppm (0.5 g/L) [200]. However, many countries require less than 200 ppm (0.2 g/L) for satisfying high-quality drinking water [201]. BRO-AD hybrid system produces high quality drinking water at the case with high-rejection membrane, and relatively good quality water at the case with high-flux membrane. In addition, distilled water that has much lower concentration approximately 0.01 g/L is produced from the AD system. Thus, two different types of permeate can be produced by the BRO-AD hybrid system. Furthermore, the temperature of chilled water is cooled down across the AD unit due to the water evaporation (from 24 °C to around 14–18 °C). The generated cooling power is around 301.6–302.5 kW and COP in the AD unit is around 0.575–0.58. The versatility of the BRO-AD hybrid system (fresh water, distilled water, and cooling power production) is noteworthy as well as the possibility of achieving low-energy consumption and high recovery.

The main reason why conventional BWRO does not easily reach very high recovery over 95% is the pressure limitation in the RO membrane. If the feed concentration is 3 g/L, the osmotic pressure of concentrated brine at 95% recovery would be 46.5 bar. This exceeds the working pressure of spiral-wound type BWRO membranes (41 bar). By considering that the actual applied pressure should be higher than the osmotic pressure, the current BWRO membranes cannot be used for reaching very high recovery. Although SWRO membranes which have higher working pressure (82.7 bar) might be used in the high recovery system, the utilisation of SWRO membranes is detrimental to energy and economic feasibilities due to its low water permeability and high capital cost. Therefore, if it is viable to reach very high recovery without changing BWRO membranes to SWRO membranes, it is energetically and economically beneficial. As shown in Tables 4 and 5, the peak pressure in the BRO-AD hybrid system is only 15.63 bar (with high-flux membrane) and 17.90 bar (with high-rejection membrane) even at very high recovery over 95%.

The choice of membranes in BRO affects the overall performances such as permeate water quality, energy consumption, and cooling power generation. High-flux membrane (XLE-440 from Dupont in this study) can produce permeate water by low energy consumption due to its high water permeability. However, the high flux membrane also has high salt permeability which increases the passage of salt ions into the permeate. Thus, the permeate quality, brine concentration, and energy consumption are low when using the high-flux membrane. The utilisation of high-rejection membrane makes opposite results, and the permeate quality, brine concentration, and energy consumption are high as shown in Table *6-3* and Table *6-4*. Due to the difference in brine concentration in the cases of high-flux and high-rejection membranes, the vapor pressure in the AD unit is different, and the cooling power generation is affected by the brine concentration. However, the difference in brine concentration is not significant. Thus, the performance of AD units (cooling power and COP) is almost the same.

*Table 6-3. Simulation results at the base case of BRO-AD hybrid system (brackish water desalination, RO membrane: XLE-440 (high-flux membrane) from Dupont)*

| | BRO unit in BRO-AD system | AD unit in BRO-AD system | Overall process (BRO-AD) |
|---|---|---|---|
| $SEC_{elec}$ (kWh/m$^3$) | 0.348 | 1.476 | 0.536 |
| $SEC_{heat}$ (kWh/m$^3$) | N/A | 1096 | 182.3 |
| Peak pressure (kPa) | 1563 | N/A | 1563 |
| Freshwater production rate (L/h) | 2,400 | N/A | 2,400 |
| Freshwater concentration (g/L) | 0.238 | N/A | 0.238 |
| Distilled water production rate (L/h) | 0 | 478.6 | 478.6 |
| Distilled water concentration (g/L) | N/A | 0.01 | 0.01 |
| Recovery (%) | 80 | 79.76 | 95.95 |
| Brine concentration (g/L) | 14.05 | 59.83 | 59.83 |
| Cooling power (kW) | N/A | 302.5 | 302.5 |
| COP (-) | N/A | 0.58 | 0.58 |

*Table 6-4. Simulation results at the base case of BRO-AD hybrid system (brackish water desalination, RO membrane: LG-BW440R (high-rejection membrane) from LG Chem.)*

| | BRO unit in BRO-AD system | AD unit in BRO-AD system | Overall process (BRO-AD) |
|---|---|---|---|
| $SEC_{elec}$ (kWh/$m^3$) | 0.439 | 1.481 | 0.611 |
| $SEC_{heat}$ (kWh/$m^3$) | N/A | 1100 | 182.4 |
| Peak pressure (kPa) | 1790 | N/A | 1790 |
| Freshwater production rate (L/h) | 2,400 | N/A | 2,400 |
| Freshwater concentration (g/L) | 0.065 | N/A | 0.065 |
| Distilled water production rate (L/h) | 0 | 476.7 | 476.7 |
| Distilled water concentration (g/L) | N/A | 0.01 | 0.01 |
| Recovery (%) | 80 | 79.44 | 95.89 |
| Brine concentration (g/L) | 14.74 | 62.18 | 62.18 |
| Cooling power (kW) | N/A | 301.6 | 301.6 |
| COP (-) | N/A | 0.575 | 0.575 |

*Table 6-5* showed the simulation results of the BRO-AD hybrid system for seawater desalination. Unlike the results for brackish water desalination, only high-rejection SWRO membrane was used for seawater desalination, because the permeate concentration using the high-flux SWRO membrane is higher than the drinking water regulation. The recovery of BRO unit was fixed at 50%, resulting in an overall recovery 69.8 % for the BRO-AD system. $SEC_{elec}$ and $SEC_{heat}$ in the BRO-AD system were 2.098 kWh/$m^3$ and 312.2 kWh/$m^3$, respectively. By considering that SEC of a single-stage conventional SWRO system at the same feed condition (35 g/L concentration and 25 °C) is around 3.16 kWh/$m^3$ at 70% recovery [202]. $SEC_{elec}$ of BRO-AD is much lower than that of conventional SWRO. Compared to SEC of two-stage SWRO (2.6 kWh/$m^3$) [203] and cascading osmotically mediated RO (COMRO) (2.1–2.2 kWh/$m^3$) [202] BRO-AD hybrid system has lower $SEC_{elec}$. In practical, single-stage and two-stage SWRO cannot reach the high recovery (70%) due to the current pressure limitation and concentration polarisation, pressure losses, and device inefficiencies were not considered in the energy calculation of COMRO [179]. The peak pressure of the BRO-AD hybrid system for seawater desalination is 71.51 bar, within the upper limit of SWRO membranes. By considering all these limitations, the BRO-AD hybrid system is more practical for high-recovery seawater desalination. Besides the low SEC and low-pressure operation, versatile desalination to produce fresh water, distilled water, and cooling power is another advantage of the BRO-AD hybrid system, which applies to seawater desalination as well as brackish water desalination.

*Table 6-5. Simulation results at the base case of BRO-AD hybrid system (seawater desalination, RO membrane: LG-SW440R (high-rejection membrane) from LG Chem.)*

| | BRO unit in BRO-AD system | AD unit in BRO-AD system | Overall process (BRO-AD) |
|---|---|---|---|
| $SEC_{elec}$ (kWh/m$^3$) | 2.213 | 1.850 | 2.089 |
| $SEC_{heat}$ (kWh/m$^3$) | N/A | 1364 | 312.2 |
| Peak pressure (kPa) | 7151 | N/A | 7151 |
| Freshwater production rate (L/h) | 600 | N/A | 600 |
| Freshwater concentration (g/L) | 0.197 | N/A | 0.197 |
| Distilled water production rate (L/h) | 0 | 178.1 | 178.1 |
| Distilled water concentration (g/L) | N/A | 0.01 | 0.01 |
| Recovery (%) | 50 | 29.68 | 64.84 |
| Brine concentration (g/L) | 69.80 | 108.4 | 108.4 |
| Cooling power (kW) | N/A | 139.5 | 139.5 |
| COP (-) | N/A | 0.574 | 0.574 |

### *6.6.2.* Effects of feed salinity and temperature

The feed salinity and temperature have significant effects on the performance of the BRO-AD hybrid system due to the change in corresponding osmotic pressure. In this chapter, the effects of feed salinity

and temperature on the BRO-AD hybrid system were analysed quantitatively in two difference cases (i.e. brackish water and seawater desalination).

Figure 6-3 showed the results of the BRO-AD hybrid system for brackish water desalination with high-rejection RO membrane. As the feed salinity increases from 1 g/L to 8 g/L, $SEC_{elec}$ of the BRO-AD system increases (Figure 6-3a). Because the osmotic pressure of the feed solution is directly correlated with the feed salinity, $SEC_{elec}$ in the BRO unit increases as increasing the feed salinity. $SEC_{elec}$ in AD unit is maintained almost constant, regardless of the change in feed salinity. This is because the electrical energy consumption in the AD unit is mainly required to operate pumps and valves and the energy is not affected by the osmotic pressure of the feed solution. On the other hand, the increased brine concentration after the BRO unit due to high feed salinity decreases its vapor pressure. Thus, higher $SEC_{heat}$ is required in the AD unit for the treatment of brine after the BRO unit. Because the same amount of adsorbent is used in the simulation of the change in the feed concentration, the decreased vapor pressure at higher brine concentration reduces the recovery in the AD unit as shown in Fig. 4b. In this simulation, the recovery in the BRO unit is fixed at 80% for a fair comparison. In other words, the amount of freshwater production rate in the BRO unit is the same (2,400 L/h) for all ranges of feed concentration. On the other hand, the distilled water production rate is decreased as the feed concentration increases. Thus, total recovery is reduced at higher feed concentrations. Nevertheless, it should be noted that the total recovery in the BRO-AD hybrid system is very high (> 94%) regardless of the feed concentration. Even at high feed concentration (8 g/L), the advantage of a very high recovery in the BRO-AD hybrid system can be maintained.

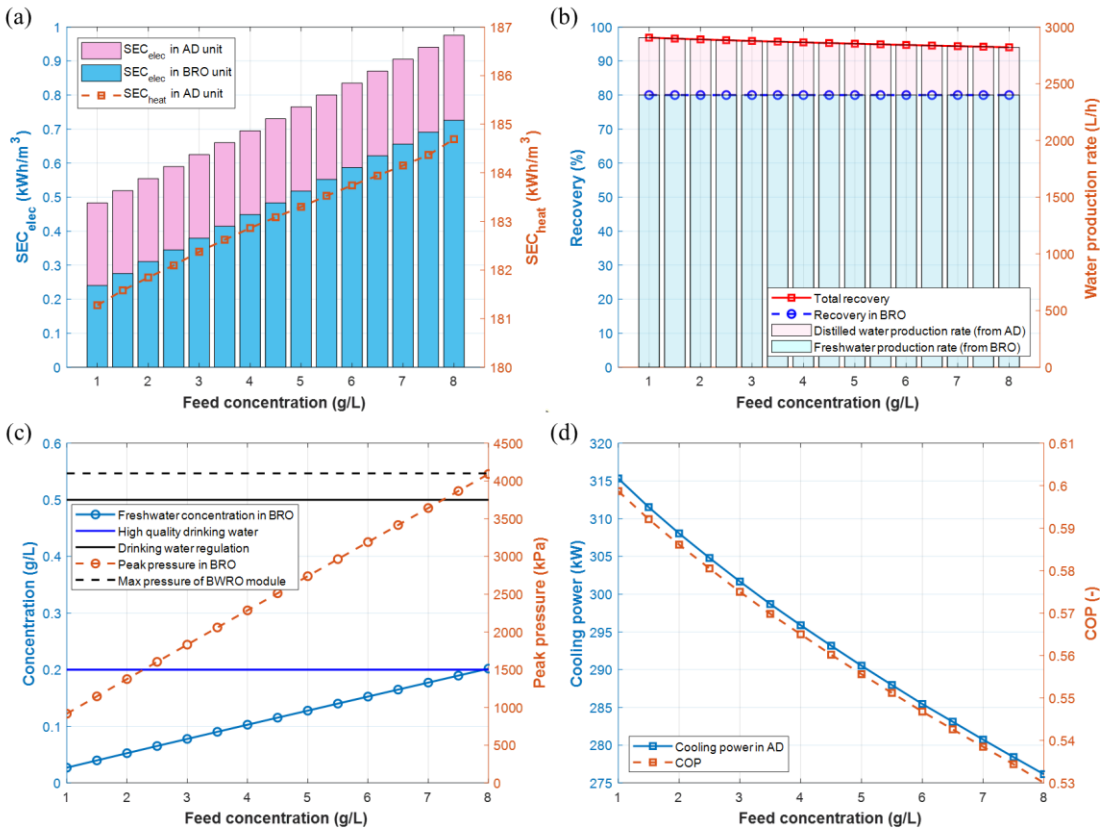



Figure 6-3. Effects of feed concentration on the performances of BRO-AD hybrid system for brackish water desalination. RO membrane: LG-BW440R (high-rejection membrane) from LG Chem. (a) SECelec and SECheat, (b) recovery and water production rate in each unit, (c) permeate quality and peak pressure at RO unit, and (d) cooling power and COP.

Regarding the quality of freshwater produced from the BRO unit, the freshwater concentration meets the standard of high-quality drinking water (<0.2 g/L) for all the ranges of feed concentration except 8 g/L. In addition, the peak pressure in the BRO unit is lower than the maximum pressure of spiral-wound type BWRO membrane modules. Considering that the recovery of the BRO-AD hybrid system is higher than 94% even at high brackish water feed concentration (>5 g/L), the remarkable advantage of the BRO-AD hybrid system is that it can employ the current BWRO membranes for brackish water desalination of high salinity feed at high recovery. Cooling power generation and COP in the AD unit depending on the feed concentration are around 275–315 W and 0.53–0.6, respectively. As the feed concentration increases, the cooling power and COP is reduced due to the reduced vapor pressure at higher feed concentration.

The analysis of feed concentration in brackish water desalination using high-flux BWRO membrane was conducted and the results are shown in Figure 6-4. At the feed concentration of 8 g/L, the overall $SEC_{elec}$ of the BRO-AD hybrid system with a high-flux membrane is 0.884 kWh/m$^3$ (Fig. 5a). Compared to the case with a high-rejection membrane (0.976 kWh/m$^3$), the high-flux BWRO membrane is advantageous for low-energy consumption though at the cost of poorer permeate quality. If the feed concentration is higher than 2.5 g/L, the freshwater produced in the BRO unit showed a higher concentration than the standard of high-quality drinking water. Although the freshwater does not violate the drinking water regulation (0.5 g/L) for all feed concentrations, the relatively lower quality of water might be inappropriate depending on preferred specifications. For example, according to Bruvold and Ongerth, an excellent taste is achieved at less than 0.3g/L. Thus, there is a trade-off between energy consumption and water quality.

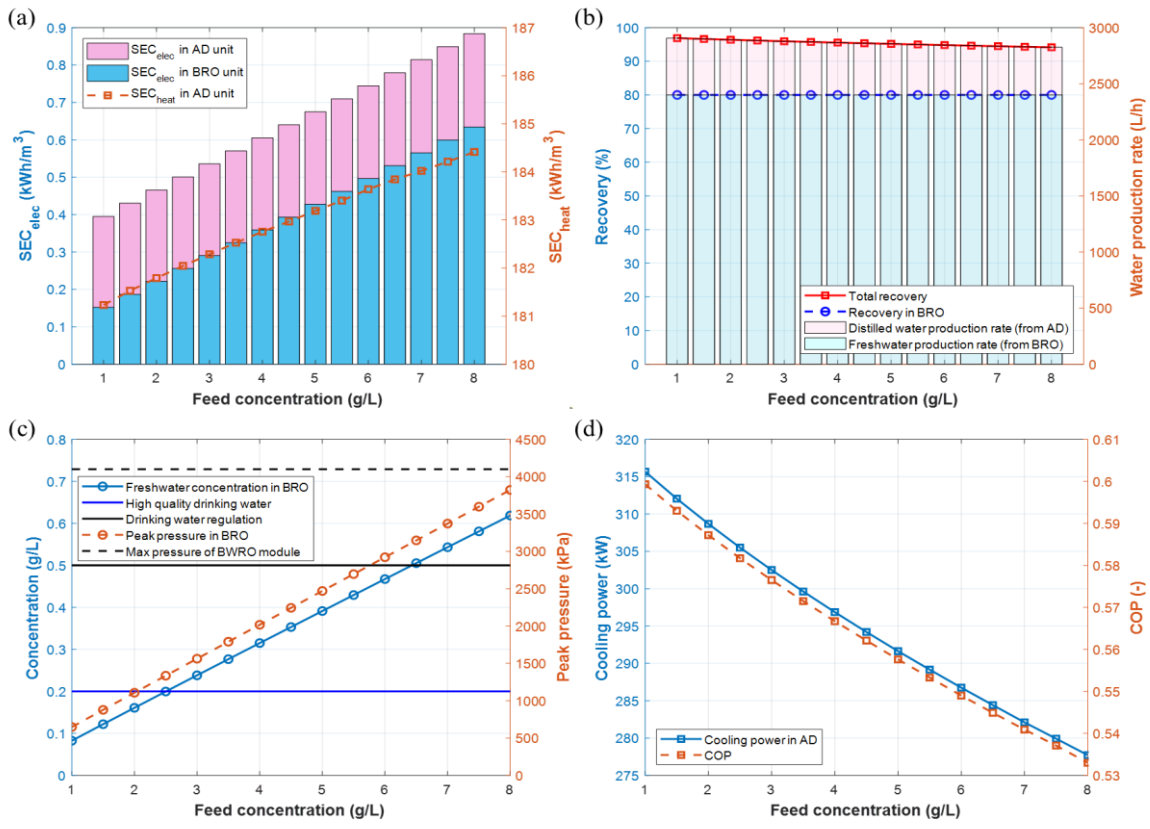



Figure 6-4. Effects of feed concentration on the performances of BRO-AD hybrid system for brackish water desalination. RO membrane: XLE-440 (high-flux membrane) from Dupont. (a) $SEC_{elec}$ and $SEC_{heat}$, (b) recovery and water production rate in each unit, (c) permeate quality and peak pressure at RO unit, and (d) cooling power and COP.

To analyse the effects of feed concentration on the BRO-AD hybrid system for seawater desalination, the feed concentration was changed from 30 g/L to 44 g/L, and the results are displayed in Figure 6-5. As mentioned above, only a high-rejection membrane was used for seawater desalination because the results with high-flux membrane showed poor freshwater quality higher than the regulation (0.5 g/L). $SEC_{elec}$ increases from 1.923 kWh/$m^3$ to 2.503 kWh/$m^3$ depending on the feed concentration. Regardless of the feed concentration, the proportion of $SEC_{elec}$ consumed in the BRO and AD units is approximately 78% and 22%, respectively. The required $SEC_{heat}$ for seawater desalination is around 310.4–315.1 kWh/$m^3$. $SEC_{heat}$ for seawater desalination is much larger than that for brackish water desalination due to its high feed concentration as discussed in the paragraphs above. In terms of $SEC_{elec}$, the energy consumption in a two-stage SWRO system with internal stage design (ISD) at the 50 g/L feed concentration and 40% recovery is 3.03 kWh/$m^3$ [201]. Although the feed concentration of the two-stage SWRO (50 g/L) is higher than the current study (44 g/L), the recovery in this study (64.01%) is much higher than 40%. In addition, the pump efficiency in this study (70%) is lower than the case of two-stage SWRO 80% [201]. Considering all factors, $SEC_{elec}$ of BRO-AD hybrid system is much lower than the other configurations like two-stage SWRO. If thermal energy could be supplied freely or cheaply, the competitiveness of the BRO-AD hybrid system can be highlighted.

The major barrier to the application of SWRO at high recovery and high salinity seawater desalination is the maximum working pressure of SWRO membranes [179]. If the feed concentration is lower than 42 g/L, the peak pressure in the BRO unit is lower than the maximum pressure limitation. At the feed concentration of 43–44 g/L, the peak pressure is slightly higher than the maximum limit. In this range of feed concentration, the BRO-AD hybrid system can be operated by lowering the recovery of BRO unit. About the freshwater quality, the freshwater produced by the BRO-AD hybrid system for seawater desalination is in the range of 0.169–0.247 g/L, which can be regarded as the high-quality drinking water. Cooling power generation is around 134.2–142.6 W, which is much lower than the case for brackish water desalination. This is because the reduced vapor pressure, and the high feed concentration reduce the cooling power generation and COP.

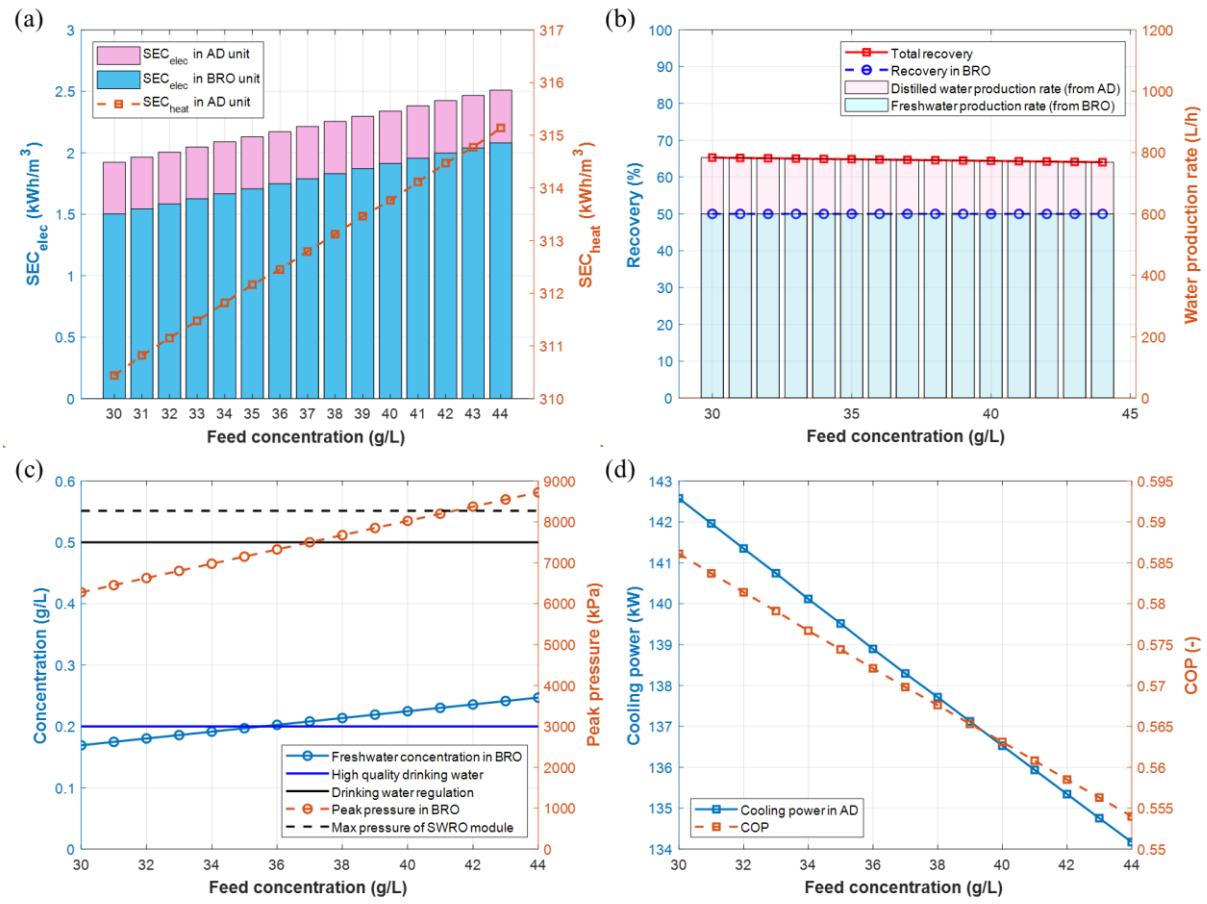



Figure 6-5. Effects of feed concentration on the performances of BRO-AD hybrid system for seawater desalination. RO membrane: LG-SW440R (high-rejection membrane) from LG Chem. (a) $SEC_{elec}$ and $SEC_{heat}$, (b) recovery and water production rate in each unit, (c) permeate quality and peak pressure at RO unit, and (d) cooling power and COP.

To investigate the effects of feed temperature, the temperature range was determined from 25 to 35 °C. The higher the feed temperature, the higher the osmotic pressure, which increases the SEC. Meanwhile, the higher feed temperature increases the water permeability of the RO membrane, which influences the reduction of SEC [201]. The trade-off effects should be considered simultaneously. In addition, the effect of high feed temperature on the AD unit should be analysed. The results are shown in Figure 6-6 (brackish water desalination) and 8 (seawater desalination).

The effect of feed temperature on energy consumption is analysed in Figure 6-6a. As the feed temperature increases, $SEC_{elec}$ in the BRO unit decreases. Although the osmotic pressure of the feed solution increases with temperature, the increased water permeability more than offsets the osmotic pressure rises, giving a net benefit in reducing $SEC_{elec}$ in the BRO unit. About the AD unit, $SEC_{elec}$ is

increased and $SEC_{heat}$ is reduced at high feed temperature. Because the high temperature of the feed solution reduces the maximum loading in the AD unit, the recovery in the AD unit decreases from 95.89% (at 25 °C) to 91.94% (at 35 °C) as shown in Figure 6-6b. The reduced recovery affects $SEC_{elec}$ in the AD unit, because the denominator of $SEC_{elec}$ is decreased. The reduced maximum loading in the AD unit decreases $SEC_{heat}$ from 182.4 kWh/m$^3$ (at 25 °C) to 152.3 kWh/m$^3$ (at 25 °C). The increased $SEC_{elec}$ in the AD unit is much lower than the reduced $SEC_{elec}$ in the BRO unit. Overall, $SEC_{elec}$ and $SEC_{heat}$ in the BRO-AD hybrid system decrease as increasing the feed temperature, however, the overall recovery deteriorates at the high feed temperature.

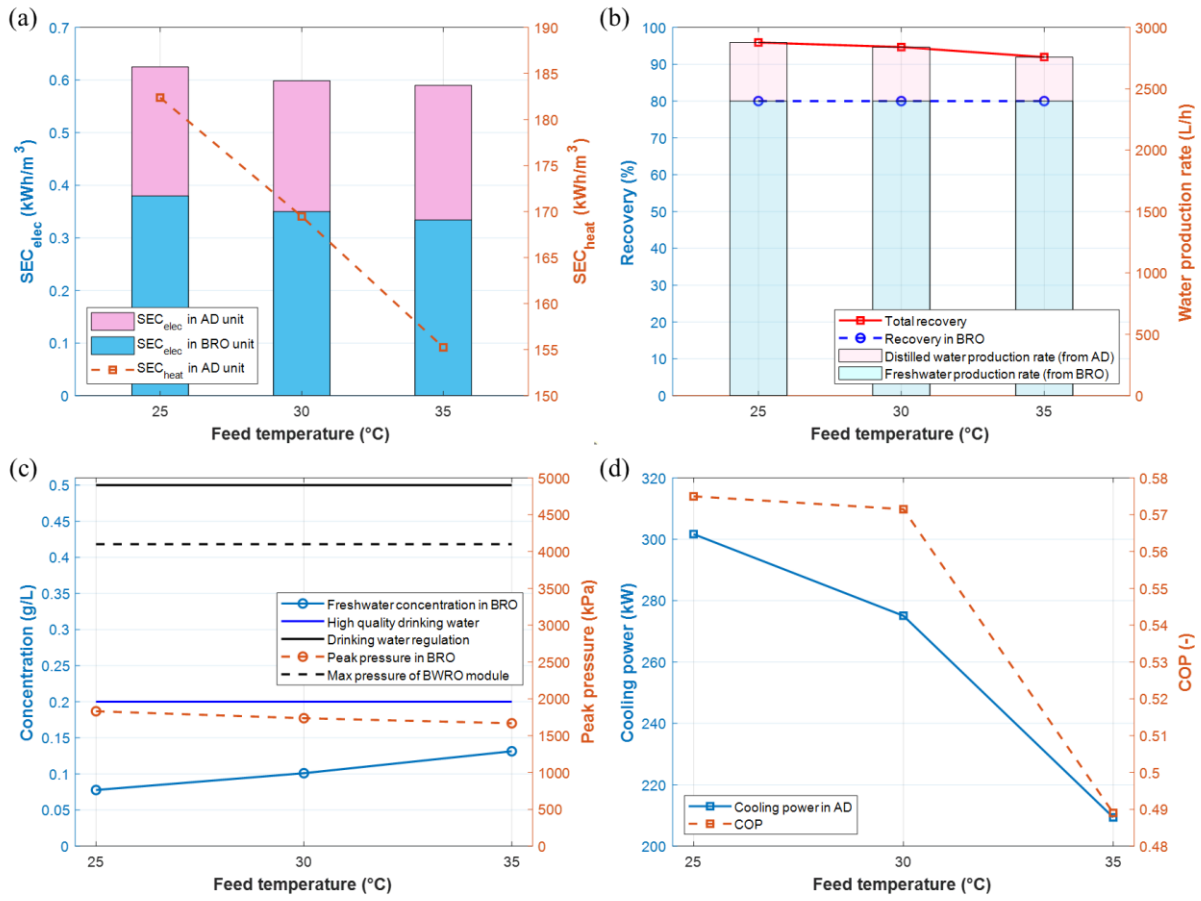



Figure 6-6. Effects of feed temperature on the performances of BRO-AD hybrid system for brackish water desalination. RO membrane: LG-BW440R (high-rejection membrane) from LG Chem. (a) $SEC_{elec}$ and $SEC_{heat}$, (b) recovery and water production rate in each unit, (c) permeate quality and peak pressure at RO unit, and (d) cooling power and COP.

In addition, the high temperature of the feed solution lowers the permeate water quality and cooling power generation as shown in Figure 6-6 (c and d). The permeate water concentration is increased from

0.078 g/L to 0.131 g/L, and the cooling power is reduced from 301.7 W to 209.4 W, when the feed temperature increases from 25 °C to 35 °C. The peak pressure of the BRO unit is slightly reduced from 18.31 bar (at 25 °C) to 16.52 bar (at 35 °C) by the increased water permeability. Thus, although the high temperature operation has lower energy consumption, the decreased quality of permeate water, recovery, and cooling power generation may favour feed water temperature below 25 °C.

The same study was conducted in seawater desalination, and the results are shown in Figure 6-7. In seawater desalination, the overall trend by the effect of feed temperature is similar to the results of brackish water desalination. The only difference is in the $SEC_{elec}$ of the BRO-AD hybrid system. Unlike brackish water desalination, the overall $SEC_{elec}$ increases slightly from 2.13 kWh/$m^3$ to 2.17 kWh/$m^3$ as the feed temperature increases from 25 to 35 °C (Figure 6-7a). The main reason is the difference in the portion of desalinated water in the BRO and AD units. Compared to brackish water desalination, the relative amount of water produced by the AD unit in seawater desalination is much larger. Distilled water from the AD makes up 16.5% of the total output in brackish water desalination, increasing to 22.8% in seawater desalination. Thus, the increased $SEC_{elec}$ in the AD unit has a larger effect on the overall $SEC_{elec}$ than the case in brackish water desalination. At 35 °C, the overall $SEC_{elec}$ and $SEC_{heat}$ are 2.17 kWh/$m^3$ and 273.9 kWh/$m^3$, respectively. Compared to the results at 25 °C (2.13 kWh/$m^3$ of $SEC_{elec}$ and 312.2 kWh/$m^3$ of $SEC_{heat}$), slightly higher (almost similar) $SEC_{elec}$ and lower $SEC_{heat}$ can be found.

When the feed temperature is changed from 25 to 35 °C, overall recovery is reduced from 64.88% to 60.77%, and the permeate water concentration is increased from 0.20 g/L to 0.33 g/L, and the cooling power generation is decreased from 139.5 W to 99.21 W, as shown in Figure 6-7 (b,c and d). Although the permeate water quality still meets drinking water regulations, most aspects of performance deteriorate. This kind of temperature change can be found in the seasonal variation of seawater temperature [204]. Therefore, the results imply that the seasonal variation of seawater temperature should be taken into consideration in the operation of the BRO-AD hybrid system.

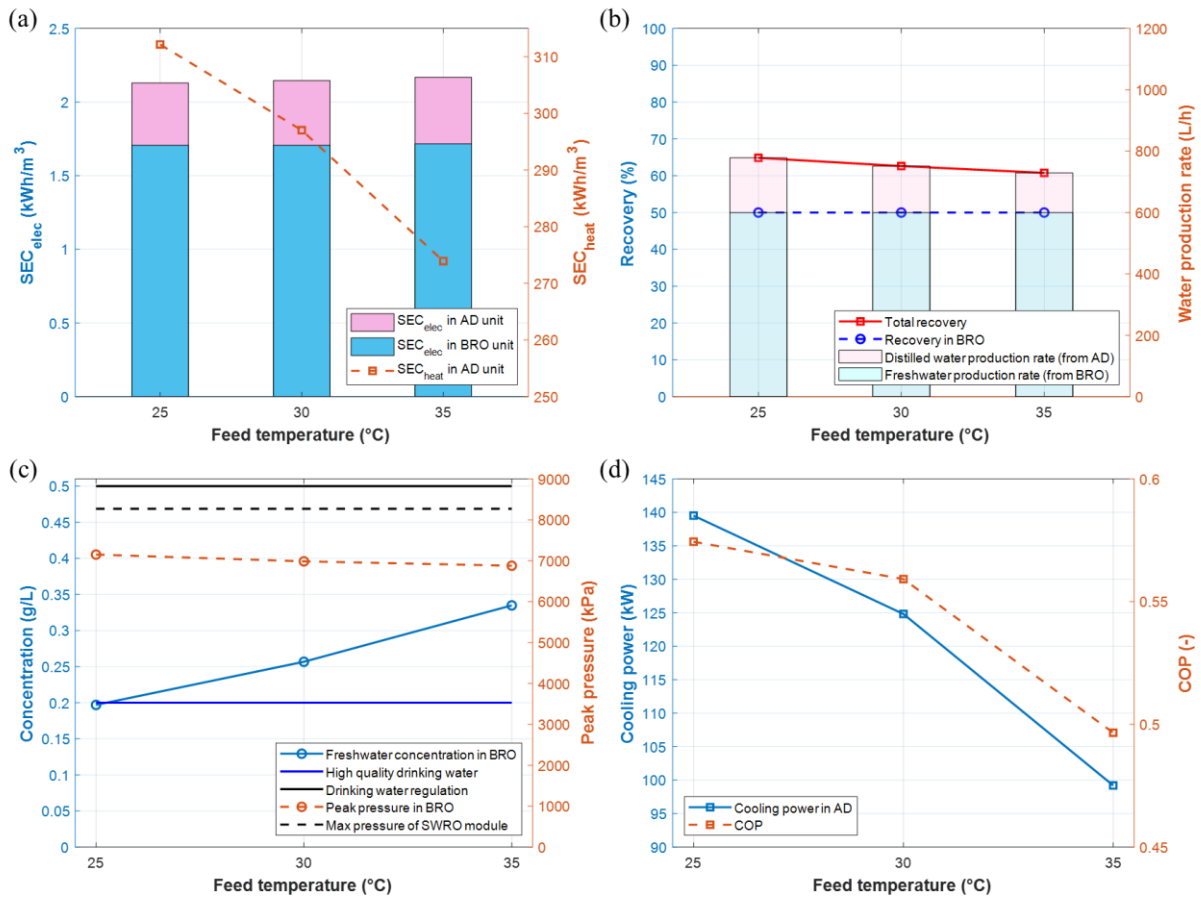



Figure 6-7. Effects of feed temperature on the performances of BRO-AD hybrid system for seawater desalination. RO membrane: LG-SW440R (high-rejection membrane) from LG Chem. (a) $SEC_{elec}$ and $SEC_{heat}$, (b) recovery and water production rate in each unit, (c) permeate quality and peak pressure at RO unit, and (d) cooling power and COP.

### *6.6.3.* Comparative analysis of energy consumption, water production rate, and cooling power generation in conventional BRO, conventional AD, and BRO-AD hybrid systems

To analyse the importance of the BRO-AD hybrid system over the conventional BRO and conventional AD systems, a study was carried out to compare brackish water and seawater desalination using the feeding concentration similar to the base cases (3 g/L for brackish water desalination and 35 g/L for seawater desalination) while maintaining water recovery (95.89% for brackish water desalination and 64.84% for seawater desalination) in all systems as shown in Figure 6-8. Only high-rejection membranes were considered in this section.

In brackish water desalination, the $SEC_{elec}$ and $SEC_{heat}$ of the conventional AD system show higher values compared to the BRO-AD hybrid system (Figure 6-8), as a result of the lower heat transfer coefficient in the evaporator required in the conventional AD system to produce the same water recovery as the BRO-AD hybrid system (95.89%). The lower heat transfer coefficient is caused due to the increase in the brine water salinity in the flooded evaporator as a result of higher water recovery, which increases the saturation temperature. While the conventional BRO system does not require any thermal energy, $SEC_{elec}$ of the conventional BRO (0.637 kWh/m$^3$) is slightly higher than that of the BRO-AD hybrid system (0.625 kWh/m$^3$). When considering $SEC_{heat}$ in the BRO-AD hybrid system (182.4 kWh/m$^3$), the energy-feasibility of the conventional BRO looks better than the BRO-AD hybrid system. However, as shown in Figure 6-8c, a crucial limitation can be found in the conventional BRO system. To reach the same recovery of the BRO-AD hybrid system, the applied pressure in the conventional BRO should be 71.3 bar, which is much higher than the maximum working pressure in a spiral-wound type BWRO membrane module (41 bar). In other words, the conventional BRO operation at the high recovery is impractical using standard membranes. It might be feasible if the membrane is changed to SWRO type. However, this would increase $SEC_{elec}$ because of lowered permeability [205]. In addition, the economic feasibility may be worsened by the increased capital cost of the SWRO membranes and the auxiliary units for sustaining high pressure. Therefore, the BRO-AD hybrid system is competitive compared to the conventional AD and BRO systems for very high recovery brackish water desalination in terms of energy feasibility and practical realizability.

Among the three systems, the water quality produced in the conventional AD system is the highest because all the produced water in the AD system is distilled water. In the conventional BRO and BRO-AD hybrid systems, the average permeates water quality of the BRO-AD hybrid system (which is defined as the average concentration of the freshwater from the BRO unit and distilled water from the AD unit) is superior to that of the conventional BRO as shown in Figure 6-8c. Although all options satisfy drinking water regulations, high-quality freshwater is economically beneficial. In terms of the cooling power (Figure 6-8e), as a result of the huge amount of the adsorbent mass required in the conventional AD system, it produces almost six times the cooling power of the BRO-AD hybrid system;

whereas the conventional BRO has no cooling production. However, cooling power generation is a by-product rather than the main purpose of these desalination systems. In addition, the required mass of adsorbent for operating the conventional AD system is 8348 kg, which is much larger than that for the BRO-AD hybrid system (1400 kg). Because the price of adsorbent is quite expensive, the huge mass of adsorbent is undesirable. Considering these results with the energy consumption simultaneously, the feasibility of the BRO-AD hybrid system is confirmed compared to the typical AD and BRO systems for brackish water desalination at very high recovery.

In seawater desalination, the energy consumptions in all three systems are comparable. $SEC_{elec}$ of the conventional AD system is the lowest (1.721 kWh/$m^3$), while $SEC_{heat}$ is the highest (1270 kWh/$m^3$) as shown in Figure 6-8b. In the BRO-AD hybrid system, 2.130 kWh/$m^3$ and 312.2 kWh/$m^3$ are required for $SEC_{elec}$ and $SEC_{heat}$, respectively. Although the conventional BRO requires only $SEC_{elec}$ (2.427 kWh/$m^3$), the applied pressure (96.22 bar) is much higher than the maximum pressure limitation of the SWRO membrane (82.7 bar) as shown in Fig. 9d. Thus, the BRO for seawater desalination at the high recovery (64.84%) is not applicable as discussed in the previous paragraphs. About the conventional AD system, although it has many advantages such as the highest permeate water quality and the largest cooling power among these systems as shown in Figure 6-8 (d and e), the successful implementation of the conventional AD system as a large-scale seawater desalination system is still questionable due to high capital cost and low adsorption rate. On the other hand, the BRO-AD hybrid system can be operated at 71.51 bar (less than the maximum durable pressure), and the average permeate concentration is 0.152 g/L (lower than the high-quality drinking water concentration) in the condition of seawater desalination. Thus, the BRO-AD hybrid system stands out in achieving a very high water recovery, compared to either AD and BRO alone.

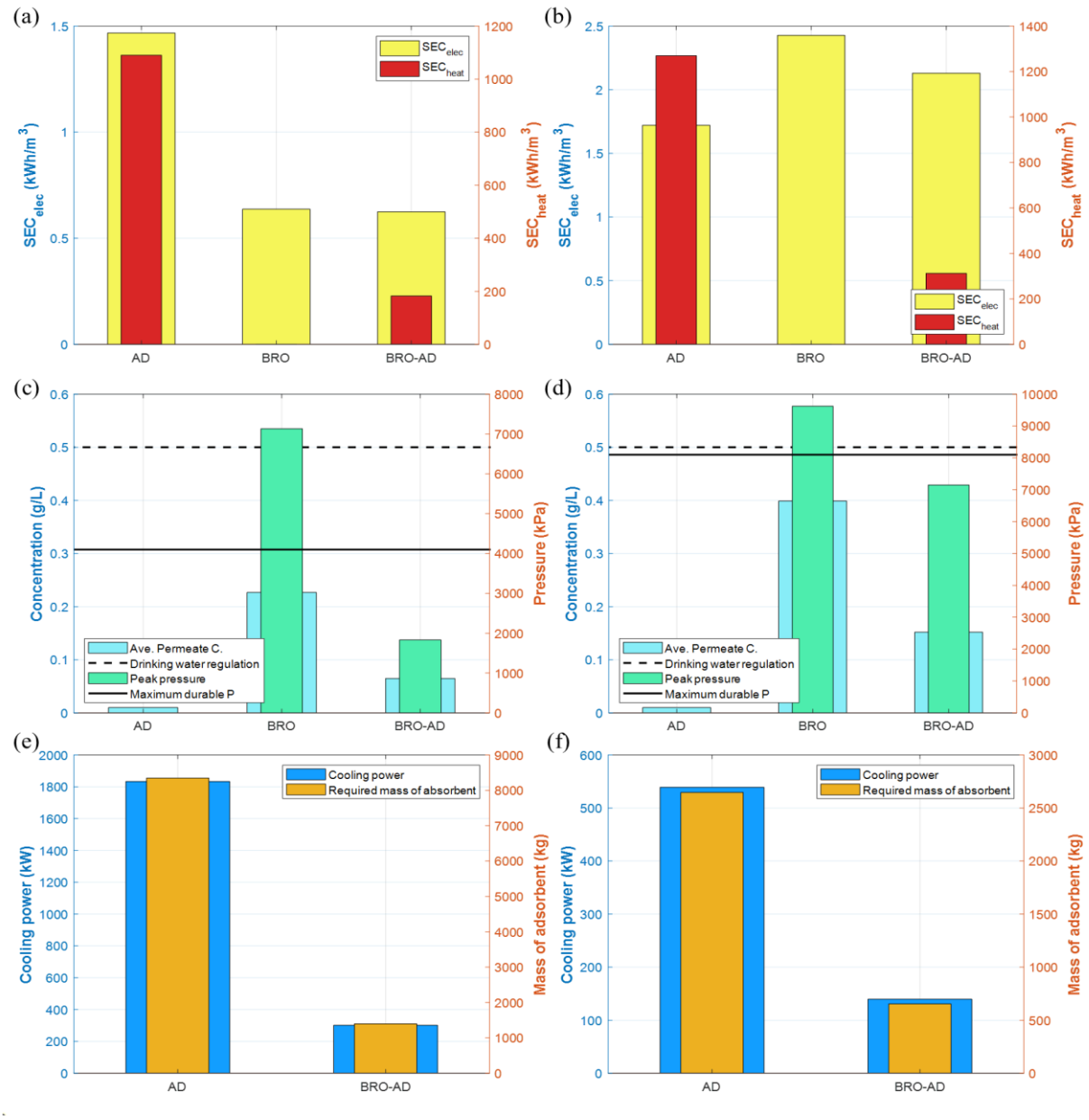



Figure 6-8. Comparative analysis results in conventional AD, BRO, and BRO-AD hybrid systems. Two cases (3 g/L and 35 g/L) are selected as representative cases for brackish water and seawater desalination, respectively. (a) $SEC_{elec}$ and $SEC_{heat}$ for brackish water desalination, (b) $SEC_{elec}$ and $SEC_{heat}$ for seawater desalination, (c) permeate water quality and peak pressure at RO system for brackish water desalination, (d) permeate water quality and peak pressure at RO system for seawater desalination, I cooling power and required mass of absorbent for brackish water desalination, and (f) cooling power and required mass of absorbent for seawater desalination.

To confirm the competitiveness of the BRO-AD hybrid system, a variable feed concentration from 1.5 to 8 g/L (brackish water desalination) and from 30 to 44 g/L (seawater desalination) were tested,

respectively. All the overall recovery in these systems is fixed at the same value for a fair comparison. The fixed recovery in each feed concentration can be found in Figure 6-4b and Figure 6-5b. The comparison results of the conventional AD, conventional BRO, and BRO-AD hybrid systems are shown in Figure 6-9 and *Figure 6-10*. In brackish water desalination, the BRO-AD system shows the lowest $SEC_{elec}$ compared to the conventional AD and BRO systems when the feed concentration of brackish water exceeds 2 g/L as shown in Figure 6-9a. The energy benefit of the BRO-AD hybrid system compared to the conventional BRO enlarges as the feed solution increases. Compared to the conventional AD system, the BRO-AD hybrid system has lower $SEC_{elec}$ and $SEC_{heat}$ in all ranges of brackish water feed concentration. As discussed in the previous paragraphs, the conventional BRO may require excessive pressure at recovery. As shown in Figure 6-9b, the peak pressure of the conventional BRO is higher than the maximum durable pressure of the BWRO membrane for all brackish water feed concentrations. On the other hand, the BRO-AD hybrid system can be operated by a feed concentration of less than 8 g/L. The permeate water concentration of these systems is shown in Figure 6-9c, and the cooling power and the mass of adsorbent required in these systems are shown in Figure 6-9d. As the feed concentration increases, the permeate contains more salt concentration by the large concentration gradient across the RO membrane. The results revealed that the conventional BRO system cannot meet the concentration of the drinking water regulation when the feed concentration of brackish water is higher than 7 g/L. The effects of concentration on the cooling power generation and the required mass of absorbent are not significant (Fig. 10d). Despite the significant increase in the cooling production when the conventional AD system is used, the conventional AD system is ineffective in terms of the adsorbent material cost to achieve the very high recovery like the BRO-AD hybrid system. In summary, the BRO-AD hybrid system is an energy-efficient, practical, and multipurpose brackish water desalination system, especially at high recovery.

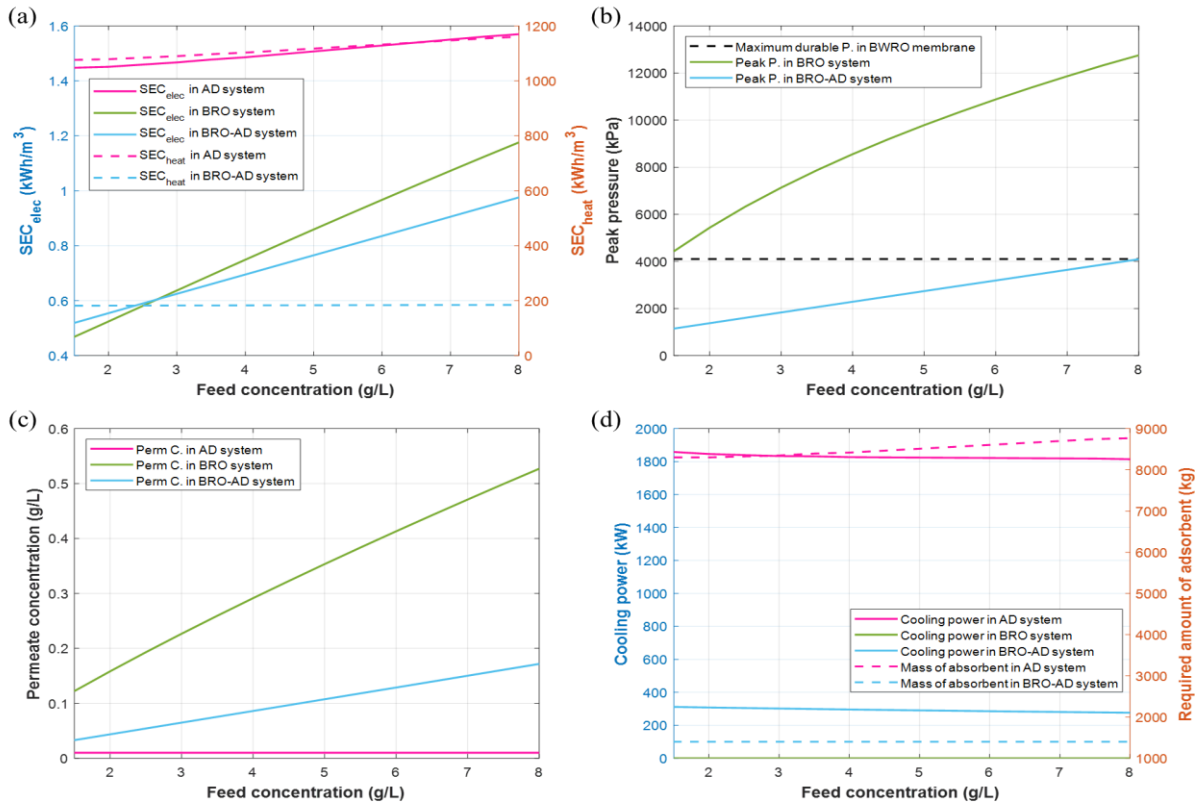



Figure 6-9. Comparative analysis results in conventional AD, BRO, and BRO-AD hybrid systems depending on feed concentration at brackish water desalination. (a) SECelec (solid line) and SECheat (dotted line), (b) peak pressure in RO system (maximum durable pressure of BWRO membrane is denoted as dotted black line), (c) permeate water quality, and (d) cooling power (solid line) and required mass of absorbent (dotted line).

Similar conclusions were obtained for seawater desalination as shown in *Figure 6-10*, which indicates a similar trend as Figure 6-8 for all seawater feed concentrations from 30 to 44 g/L. The energy effectiveness in these systems is comparable when considering $SEC_{elec}$ and $SEC_{heat}$ for all feed concentrations (see *Figure 6-10*a). However, as shown in *Figure 6-10*b, conventional BRO cannot operate over 30 g/L feed concentration at this recovery (66%) under the current pressure limitation, whereas BRO-AD hybrid system can be operated at feed concentration up to 40 g/L. The permeate water quality of the BRO-AD hybrid system is lower than 0.2 g/L in all the range of feed concentration as shown in *Figure 6-10*c. Thus, the BRO-AD hybrid system has wider applicability to the high feed concentration than the conventional BRO. The conventional AD system can be considered for high recovery seawater desalination with 30–44 g/L feed concentration, if the large $SEC_{heat}$ and huge mass of adsorbent would not be a serious issue. Thus, the BRO-AD hybrid system represents an effective

solution to increase the water recovery for the seawater application with a feed concentration up to 40 g/L even compared with the conventional BRO and AD systems.

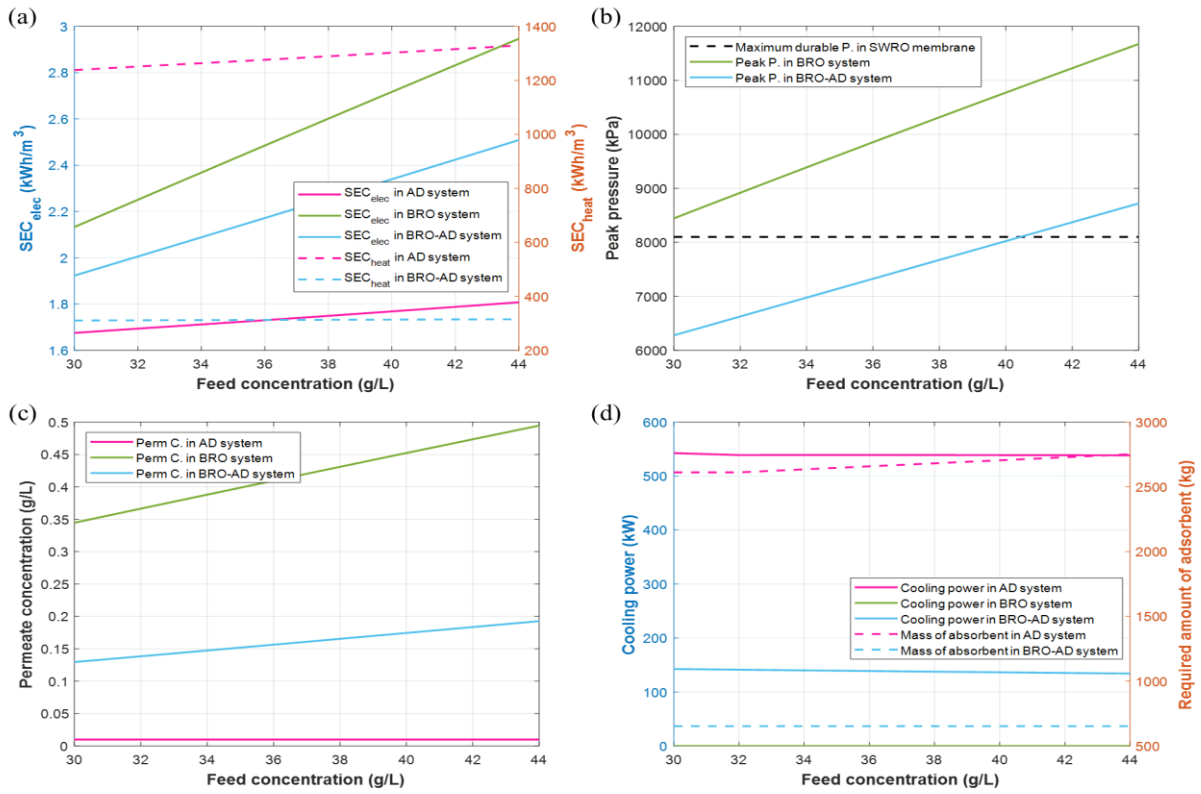



*Figure 6-10. Comparative analysis results in conventional AD, BRO, and BRO-AD hybrid systems depending on feed concentration at seawater desalination. (a) SECelec (solid line) and SECheat (dotted line), (b) peak pressure in RO system (maximum durable pressure of SWRO membrane is denoted as dotted black line), (c) permeate water quality, and (d) cooling power (solid line) and required mass of absorbent (dotted line).*

### *6.6.4.* Implementation for ZLD or MLD system

As discussed earlier, the BRO-AD hybrid system is feasible for both brackish water and seawater desalination. The main advantage of the BRO-AD hybrid system is the achievability of high recovery, applicability for high feed concentration, and availability of multipurpose desalination. Among the advantages, the high recovery achievability is the most significant feature because the current research trend in desalination is towards ZLD or MLD systems. In this section, the actual potential of the BRO-AD hybrid system for ZLD or MLD is discussed.

Even though the conventional BRO is regarded as one of the energy-efficient desalination at high recovery, there are limitations of maximum durable pressure and permeate water quality at the very high recovery over 95% of brackish water desalination. In addition, the conventional AD consumes large amounts of $SEC_{elec}$ and $SEC_{heat}$ and requires huge mass of adsorbent materials to reach at the very high recovery. On the other hand, the energy consumption and the applicability of conventional AD is not significantly affected by the feed concentration. The BRO-AD hybrid system utilises these characteristics to make an effective pathway for the high recovery desalination. At the start of desalination, BRO system is used because the BRO is effective in terms of energy consumption to reach a certain level of recovery. After reaching the certain recovery, the BRO cannot be effectively used to increase the recovery further due to the high osmotic pressure of the brine. From the certain recovery, the AD is used for further desalination. The utilisation of AD makes the BRO-AD system be free from the regulations caused by the high osmotic pressure. Therefore, the BRO-AD hybrid system can reach the very high recovery effectively and without any violations of practical limitations.

The advantage of the BRO-AD hybrid system is appropriate for ZLD or MLD systems. The main barrier of ZLD or MLD using membrane-based systems is the maximum durable pressure of the utilised membrane. The current ZLD or MLD systems have been approached by thermal-based systems [206]. However, the large amount of energy consumption should be overcome. Thus, the utilisation of BRO-AD hybrid system can suggest an effective solution for ZLD or MLD systems. The results in this study revealed the potential of the BRO-AD hybrid system for MLD system. Through future research, the actual applicability of the BRO-AD hybrid system will be investigated more extensively.

## 6.7. Conclusions

This study investigated the comprehensive feasibility of batch reverse osmose (BRO)-adsorption desalination (AD) hybrid system in terms of energy consumption, achievable recovery, cooling power generation, and applicability for brackish water and seawater desalination. The results showed a high potential for a minimal/zero liquid discharge system with low-energy consumption as a result of the high recovery that cannot be easily achieved by the conventional BRO and AD systems. The key findings in this study are summarised as follows:

a) To connect the BRO unit (batch system) and AD unit (continuous system) for continuous operation, multiple BRO units should be connected in parallel and operated sequentially to provide a continuous brine flow to the AD system and eliminate the buffer tank between the system.

b) Very high recovery rates of 94.1–96.9% (brackish water) and 64.0–65.3% (seawater) are obtained in the BRO-AD hybrid with the feed concentrations of 1-8 g/L and 30-44 g/L, respectively (at 25°C). The energy consumptions are in the range of 0.395–0.884 kWh/$m^3$ ($SEC_{elec}$) and 181.2–184.4 kWh/$m^3$ ($SEC_{heat}$) for brackish water desalination, and 1.923–2.509 kWh/$m^3$ ($SEC_{elec}$) and 310.4–315.1 kWh/$m^3$ ($SEC_{heat}$) for seawater desalination. Two water qualities (distilled water and fresh water) can be produced simultaneously. Additionally, cooling production (277.7–315.7 kW from brackish water desalination and 168.5–183.6 kW from seawater desalination) is also extracted from the evaporator of the AD system beside the distilled water production.

c) The BRO-AD hybrid system withstands severe conditions such as high concentration and high temperature feed solution. Under the current rising demand of hypersaline water desalination, it offers a competitive solution for the treatment of hypersaline water with low-energy, high recovery, and multi-objective desalination.

d) The BRO-AD hybrid system showed better performances in terms of permeate quality and energy consumption than the conventional BRO and AD systems. The pressure limit of the membrane, and the required mass of absorbent, are the main barriers preventing high recovery using the conventional BRO and AD system, respectively. The recovery in the BRO-AD hybrid system is not limited by a membrane, enabling recoveries of >90% to be readily achieved using brackish water and >60% using seawater. If using conventional AD, such higher recoveries would require very large mass of adsorbent. Thus, the BRO-AD hybrid system has a higher potential to be implemented for minimal/zero liquid discharge system.

# Chapter 7: Newly developed zirconium-based MOF

## 7.1. Introduction:

From chapter 3 to chapter 6, the adsorption cooling and water desalination system has been investigated numerically and experimentally to optimize:

a. The heat exchanger in the adsorber bed,
b. The method of applying the adsorbent material on the heat exchanger surface (packing, coating or combination between both),
c. The connection methods of the heat exchanger modules in the adsorber bed (series, parallel and vapour gap between the modules) in a scaled-up system,
d. The evaporator and condenser chamber volumes and
e. Integrating the adsorption system with different systems for various applications.

It is necessary to end these chapters by conducting a study of newly developed MOF materials that can be used for cooling and desalination applications. Additionally, porous materials including MOFs generally suffer from low thermal conductivity, which is another area that is investigated to optimize the cyclic performance of the adsorption system as well as the adsorption kinetics. This chapter, studies MOF-801 which is a zirconium-based MOF as mentioned in chapter 2 (section 2.3) is selected to be investigated since it has low regeneration temperature (similar to aluminum fumarate), thus, it can be used for cooling and desalination application. It also has a high-water uptake at low relative pressure.

**I.** This chapter is based on a submitted paper for publication in the following journal paper**I. Albaik**, K. E. Diab, R. Al-Dadah, S. Mahmoud, M. A. Ismail, M. K. Almesfer, M. F. El-Kady, Zirconium Metal Organic Framework / Graphene Nanoplatelets Composite for More Efficient Cooling and Desalination Adsorption System **(submitted).**

### Credit Authors statament:

**I.Albaik:** Developing a lumped parameters model to study the adsorption system using the neat and composite MOF, analysing the results, and writing the outcomes of the study. **K. Diab:** preparing the

composite material structure and characterizations. **R. Al-Dadah and S. Mahmoud:** Reviewing and supervision, **M. A. Ismail, M. K. Almesfer, and M. F. El-Kady:** Project funding and administration.

## 7.2. Abstract

Metal-Organic Frameworks (MOFs) are promising candidates for water sorption applications due to their high surface area, water uptake and stability. A novel approach for enhancing the efficiency of MOF-801in adsorption cooling and desalination system through its composite with graphene nanoplatelets is presented. The resulting thermally conductive composite demonstrated tremendous potential for cooling and desalination applications. The MOF-801 composite material with 10% of graphene showed an improvement in the SCP and SDWP by more than 40% compared to the neat MOF (SDWP increased from 9.23 to 12.88 L/kg/day) at a chilled water temperature of 20$^{o}$C and heating and cooling water temperatures of 90 and 25$^{o}$C respectively. The MOF composite also reduced the optimum half-cycle time of the adsorption system from 400 to 200 seconds as a result of the enhanced kinetics. Finally, MOF-801 and its composites showed better performance compared to silica gel, aluminum fumarate and CPO-27Ni at low chilled water and heating water temperatures.

## 7.3. Purpose of the study

One of the most promising MOFs in water sorption applications is MOF-801, which was firstly investigated by Yaghi et al. [56] for its efficiency in harvesting water from arid environments at very low relative pressure. Due to its chemical stability and high water uptake at low relative pressure and ease of regeneration, this makes it a good candidate for application in water adsorption systems. Moreover, porous materials including MOFs suffer from low thermal conductivity which represents a major barrier to their scale-up application. Many strategies have been studied to increase the thermal conductivity of MOFs such as mixing MOFs with high thermally conductive additives such as carbon nanotubes and expanded natural graphite as discussed in section 2.3.1. The effect of the MOF-801/graphene composites on the performance of MOF-801 in adsorption heat pumps for cooling and water desalination applications is studied. Since improvements in the thermal conductivity of porous

adsorbents have been restricted to high additive fractions (10 wt%), only the effect of adding 10 wt% of graphene on MOFs during the synthesis is considered here.

## 7.4. Materials

Zirconium Chloride (Sigma Aldrich, 99.99%), Ethanol, dimethylformamide (Sigma Aldrich, <0.0005% water, fumaric acid (Sigma Aldrich, ReagentPlus®, 99%), Triethylamine (Sigma Aldrich), acetic acid (Sigma Aldrich, 99.99%), formic acid (Sigma Aldrich, analytical standard) and graphene nanoplatelet have been used without any further purification.

**Synthesis of MOF-801**

In a typical synthesis, a mixture of $ZrCl_4$ (1.16 g) and fumaric acid (.55 g) was completely dissolved in DMF (150 mL). 10.5 ml Acetic acid, Triethylamine .460 ml. Subsequently, the solution was transferred into a 100 mL capped bottle (383 K) for 24 h. After cooling down to room temperature, the resulting precipitate was isolated by filtration and washed with EtOH. After that, the precipitate was immersed in EtOH (80 mL) for 36 h, during which EtOH was refreshed every 12 h. Finally, the white powder was collected by filtration and dried in a vacuum oven at 50 °C for 24 h.

**Synthesis of MOF-801/graphene nanoplatelets composite**

MOF-801 was prepared following the reported procedures with some modifications. In a typical synthesis, a mixture of ZrCl4 (1.16 g) and fumaric acid (.55 g) was completely dissolved in DMF (150 mL) dispersed with .1 g of graphene nanoplatelets. 10.5 ml Acetic acid, Triethylamine .460 were subsequently added. The solution was transferred into a 100 mL round-bottom flask and reflux-heated (383 K) under stirring for 24 h. After cooling down to room temperature, the resulting precipitate was isolated by centrifugation and washed with EtOH. After that, the precipitate was immersed in EtOH (80 mL) for 10 h, during which EtOH was refreshed every 12 h. Finally, the grey powder was collected

by centrifugation and dried in a vacuum oven at room temperature for 24 h. The MOF 801 with its composite during and after the synthesis is shown in **Figure** 7-1**.**

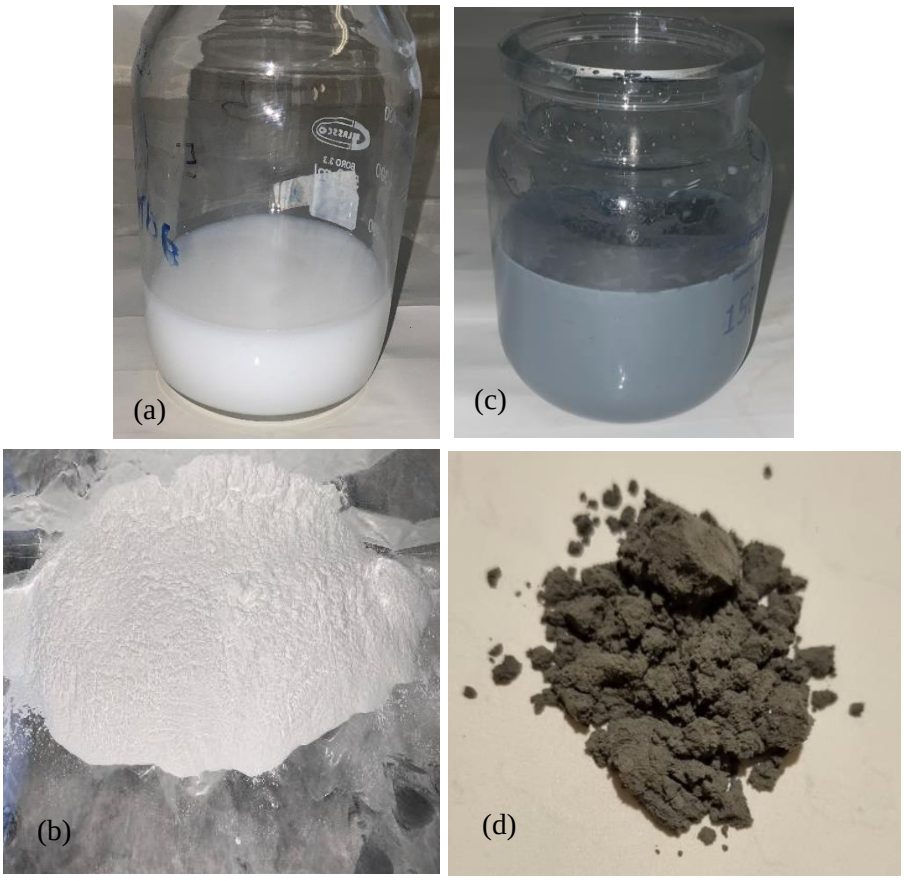



Figure 7-1.Optical pictures for (a) MOF 801 soaked in ethanol, (b) MOF 801 after drying (c) MOF 801-G10% soaked in ethanol and (d) MOF 801-G10% after drying

## 7.5. Methodology

### 7.5.1. Nitrogen isotherms

The apparent surface areas were determined from nitrogen adsorption-desorption isotherms measured at 77K using a Micromeritics Tristar II 3020. To verify the porosity of MOF-801 powder and its graphene composite, Brunauer, Emmett and Teller (BET) Nitrogen isotherms study is conducted to evaluate the surface area by BET analysis (**Figure** 7-2). Before surface area analysis, the samples were activated to remove solvent from the pores of the MOF powder. The BET surface area of pristine MOF-801 is 790 m2/g while the BET surface area of MOF-801/graphene is 772 $m^2$/g.

From the BET analysis, MOF-801/graphene composite showed a very slight decrease in surface area compared to the pristine MOF-801.

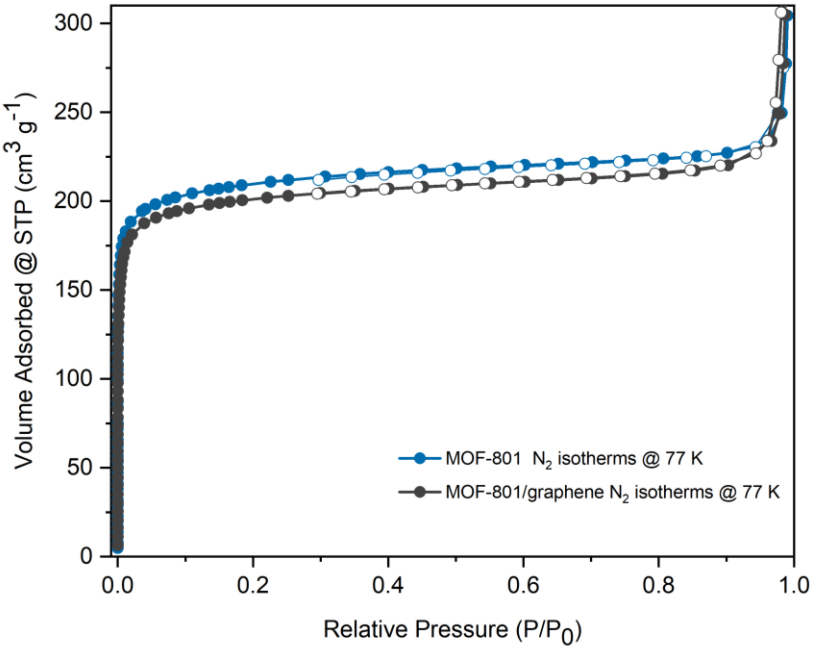



Figure 7-2. BET Nitrogen isotherms of MOF-801 particles and MOF-801/graphene composite

### *7.5.2.* water isotherms, kinetics and heat of adsorption

A dynamic vapor sorption (DVS) analyser is used to measure the gravimetric water uptake in the adsorbent material, which can be used to obtain the adsorption characteristics (isotherms, kinetics and isosteric heat of adsorption). Samples of 15-20mg of MOF-801 and MOF-801-G10% have been placed in the reaction chamber of the DVS and dried at 90°C for 120 minutes to ensure no mass change in the samples. Figure 7-3 shows the DVS water uptake measurement of MOF-801 taken with time at various relative pressure to determine the adsorption isotherms and kinetics at different adsorption temperatures. Therefore, the sample water uptake (isotherms) at each relative pressure is obtained at a point of no mass change where a mass change of less than 0.02 mg/min is maintained.

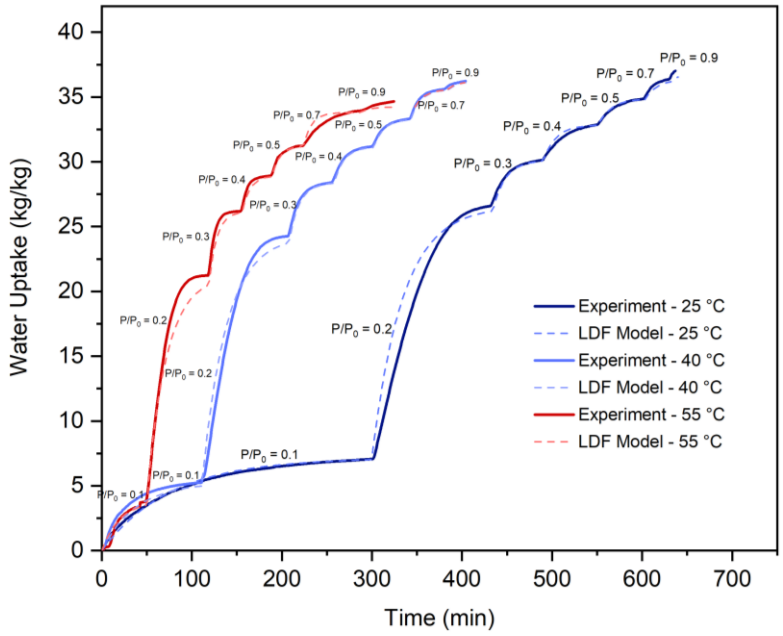



*Figure 7-3. Water kinetics at different adsorption temperatures and relative pressures using MOF-801*

In **Figure** 7-4**,** the same procedures are repeated with MOF-801-G10%. The composite structure shows a significant improvement in the required time to obtain the maximum water uptake, since the graphene reduced the equilibrium time at different relative pressures.

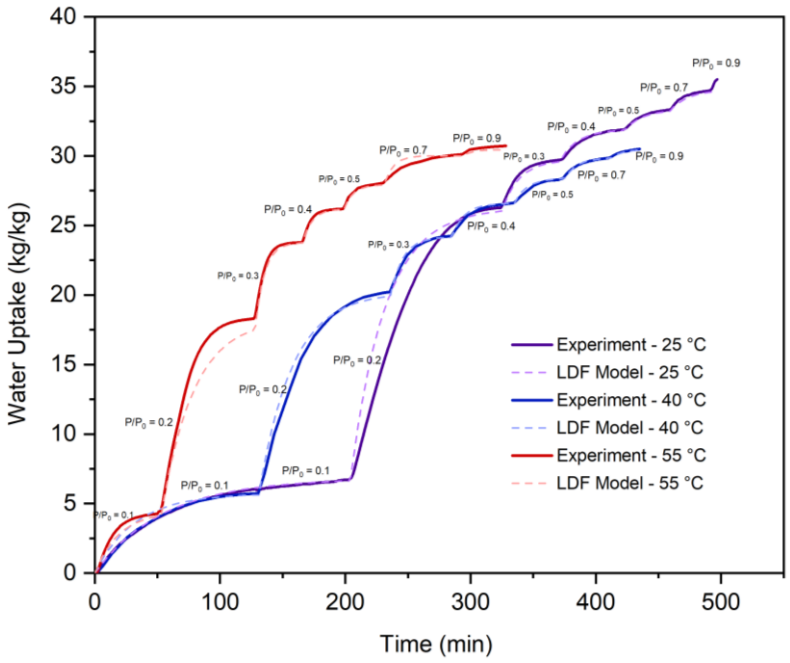



*Figure 7-4. Water kinetics at different adsorption temperatures and relative pressures using MOF-801-G10%*

The linear driving force (LDF) equation by Glueckauf [207] is used to describe the kinetics of the MOF-801 and MOF-801-G10% adsorbent materials as follows:

$$\frac{\mathrm{dX}}{dt} = \mathrm{k}_o \exp\left(\frac{-\mathrm{Ea}}{\mathrm{RT}}\right)\left(X_{inf} - X\right) \tag{7.1}$$

$$\mathrm{k}_o = \frac{FD_{So}}{{R_p}^2} \tag{7.2}$$

$$D_S = D_{So}\exp\left(\frac{-\mathrm{Ea}}{\mathrm{RT}}\right) \tag{7.3}$$

Where F is a constant that depends on the adsorbent particle shape and is equal to 15 for a spherical particle, Ea is the activation energy and $R_p$ is the particle radius.

The simulated MOF-801 and MOF-801-G10% constants using the LDF model are shown in Table 7-1.

Table 7-1. Simulated LDF constants

| **Adsorbent material** | $\boldsymbol{R_p}$**(m)** | **$E_a$ (J/mol)** | **$D_{so}$ (m2/s)** | **P $_{ratio} = \frac{P}{Po}$** |
|---|---|---|---|---|
| **MOF-801** | 25 E-9 | 36202.48 | 2.00E-14 | P $_{ratio}$< 0.1 |
| | | 11956.36 | 2.20E-18 | 0.1< P $_{ratio}$< 0.2 |
| | | 19723.3 | 1.10E-16 | P $_{ratio}$ > 0.2 |
| **MOF-801-G10%** | | 27708.06 | 9.00E-16 | P $_{ratio}$ < 0.1 |
| | | 1749.93 | 4.00E-20 | 0.1< P $_{ratio}$< 0.2 |
| | | 16639.63 | 8.00E-17 | P $_{ratio}$ > 0.2 |

Figure 7-3 and Figure 7-4 show that the LDF model predicted the experimental results well. Figure 7-5 shows the water isotherms for MOF-801 and MOF-801-G10% at different adsorption temperatures.

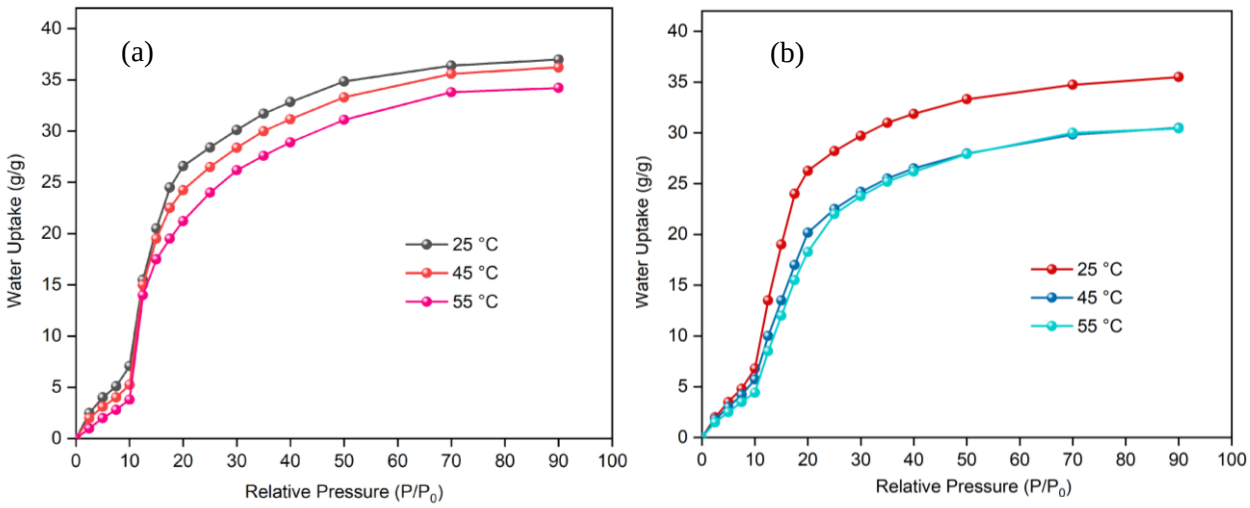



Figure 7-5. Water uptake at different relative pressures and adsorption temperatures (a) MOF-801 and (b) MOF-801-G10%

The modified Dubinin– Astakhov isotherm (D-A) is an empirical model that can be used to represent the water adsorption through microporous adsorbents. MOF-801 and MOF-801-G10% are modelled using this model at different adsorption temperatures. The following equations are developed to calculate the equilibrium water uptake ($X_{inf}$ ) using MOF-801:

$$X_{inf} = 7.1384274056 * \exp(-0.00081599 * A) \qquad A > 3987 \tag{7.4}$$

$$X_{inf} = 1.9(10)^{-12}A^3 - 1.67674(10)^{-8}A^2 + 0.00001116018122\,A + 0.36749145 \qquad A < 3987 \tag{7.5}$$

While the following equations are developed using MOF-801-G10%:

$$X_{inf} = 6.88496 * \exp(-0.00081359 * A) \qquad A > 3987 \tag{7.6}$$

$$X_{inf} = 3.9(10)^{-13}A^3 - 6.48676(10)^{-9}A^2 + 0.0000037696835\,A + 0.356179 \qquad A < 3987 \tag{7.7}$$

Where A is the adsorption potential that is calculated using the following equation:

$$A = -RT\ln\left(\frac{P}{Po}\right) \tag{7.8}$$

Where $\left(\frac{P}{Po}\right)$ is the relative pressure ratio between the saturation pressure in the condenser/ evaporator to the saturation pressure at adsorbent material temperature, R is the gas constant and T is the adsorption temperature.

The isosteric analysis is one of the critical characteristics of adsorbent materials that needs to be investigated [208] after obtaining the water uptake at different vapor pressures as shown in Figure 7-6 .

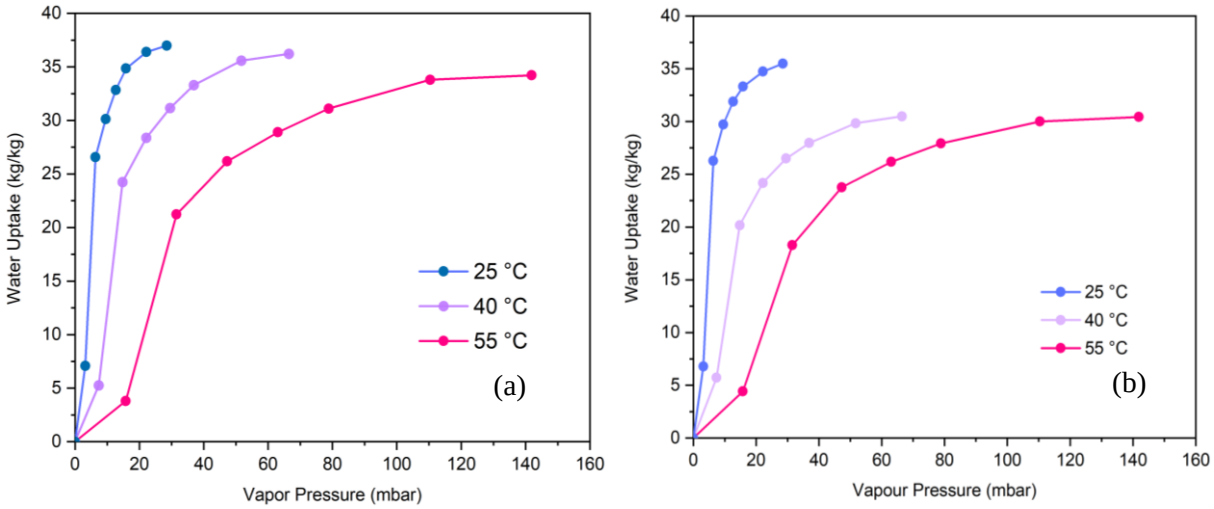



Figure 7-6. Water uptake at different vapor pressures (a) MOF-801 and (b) MOF-801-G10%

Based on the experimental data from DVS, a straight line between $\frac{1}{T}$ and ln $(P_{vapour})$ at different water uptake is calculated as shown in **Figure** 7-7. Three temperatures are used from 25 to 55°C since the maximum operating temperature of the DVS is 60°C. Four different water uptake have been selected which have the values at the given pressure and temperatures, so that the linear relationship can be obtained as shown in **Figure** 7-7**.**

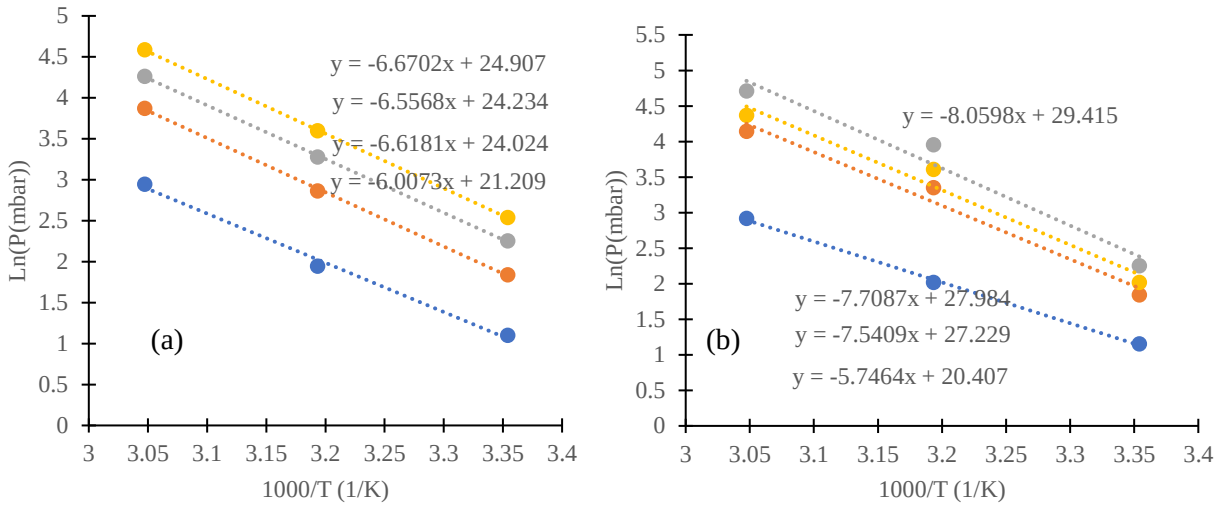



Figure 7-7. The relation between $\frac{1}{T}$ and $ln\ (P_{vapour})$ at different water uptake (a) MOF-801 and (b) MOF-801-G10%

The slopes of these lines represent the ratio between the isosteric heat of adsorption and gas constant $(Q_{st}/R)$ at different water uptake. Thus, $Q_{st}$ at different units are calculated as shown in **Table** 7-2**.**

Table 7-2. Isosteric heat of adsorption

| | **Water uptake (w %)** | **$Q_{st}$ (kJ/kg)** | **$Q_{st}$ (kJ/mol)** |
|---|---|---|---|
| **MOF-801** | 7.1 | 2772.2 | 49.94 |
| | 26.58 | 3054.2 | 55.02 |
| | 30.12 | 3025.9 | 54.51 |
| | 32.84 | 3078.3 | 55.45 |
| **MOF-801-G10%** | 6.79 | 2651.9 | 47.77 |
| | 26.27 | 3479.7 | 62.68 |
| | 27.92 | 3557.2 | 64.08 |
| | 29.71 | 3719.6 | 67.01 |

## 7.6. Results and discussion

The adsorption cooling and desalination system was modelled for three cycles until reaching a steady cyclic condition by using the developed lumped adsorption model from chapter 6 (section 6.5). To study MOF 801 and MOF 801-G10%, the temperature variation with time at each component in the system is investigated as shown in **Figure** 7-8**.** It is shown that the adsorbent material is cooled and heated faster using the composite MOF with graphene compared to the neat MOF. On the other hand,

due to the higher heat of adsorption in the composite MOF compared to the neat one, a significant increase in the temperature during the adsorption process is observed after the switching process. Additionally, using the composite MOF showed lower outlet chilled water temperature in the evaporator and higher outlet condenser water temperature compared to the neat MOF.

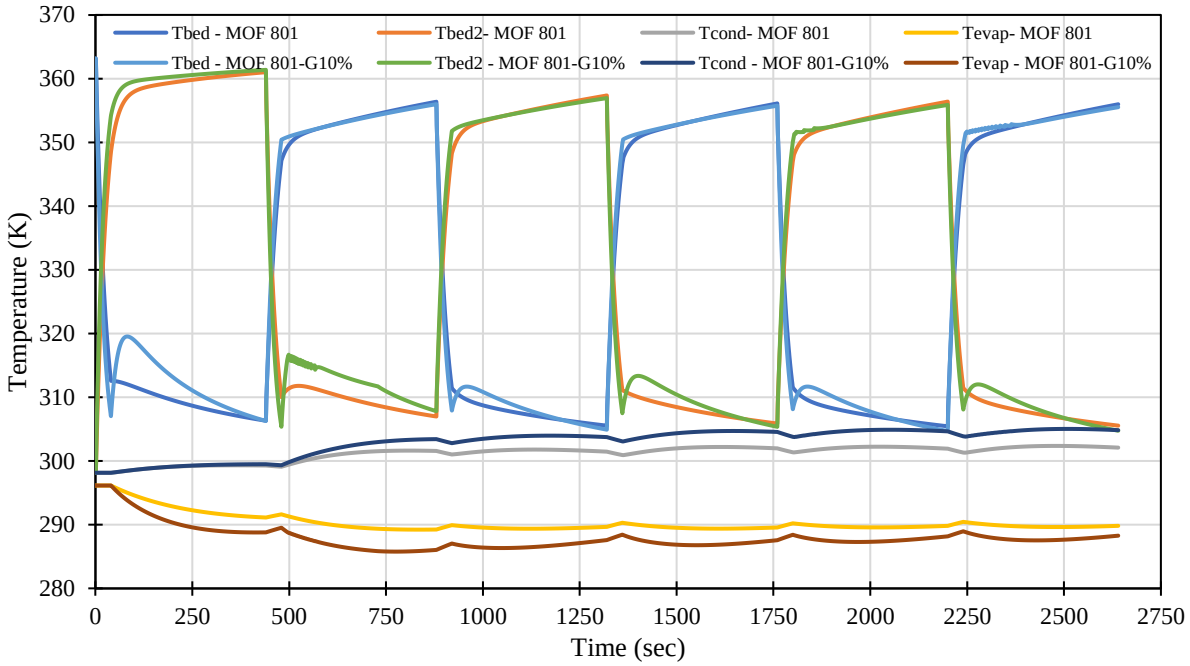



Figure 7-8. Temperature variation with time in each component in the adsorption system with time using different adsorbent materials ($t_{halfcycle}$ = 400 sec, $t_{switch}$ = 40 sec, $T_{chilled}$ = 23°C, $T_{heating}$ = 90°C, and $T_{cooling}$ = 25°C)

**Figure** 7-9 shows the added/rejected heat to/from the adsorption system components. The added heat to the component has a positive value which can be seen in the desorption and evaporation processes, while the rejected heat has a negative value as shown in the adsorption and condensation processes. The area under the curve represents the added/rejected energy to/from the system. The results show that increasing the half-cycle time will increase the area under the curve. At the beginning of the cycle, using composite MOF has a lower area compared to the neat MOF in the adsorption and desorption processes, which indicates that the COP in composite MOF is higher than the neat one at a short half-cycle time, while it is lower when the half cycle time is increased.

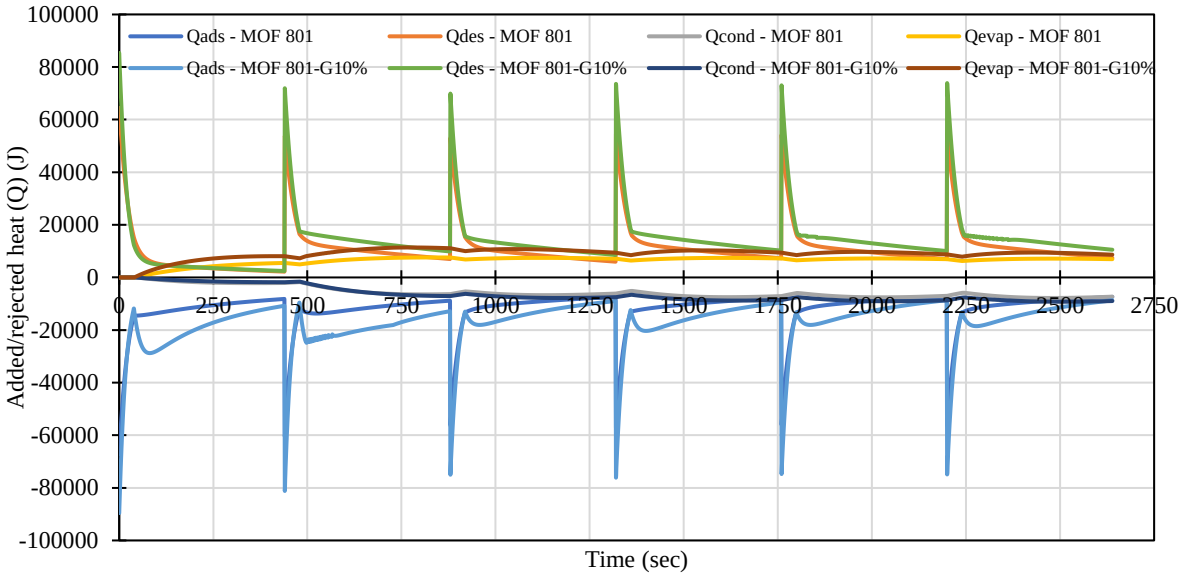



Figure 7-9. Heat variation with time in each component in the adsorption system with time using different adsorbent materials ($t_{halfcycle}$ = 400 sec, $t_{switch}$ = 40 sec, $T_{chilled}$ = 23°C, $T_{heating}$ = 90°C, and $T_{cooling}$ = 25°C)

The effect of adding 10% of graphene on the SCP and COP is shown in **Figure** 7-10**.** By using MOF 801, the optimum half cycle is obtained at 400 seconds which shows that the SCP and COP have values of 255 W/kg and 0.58 respectively. While, the composite MOF reduces the optimum half-cycle time to 200 seconds, when the SCP and COP are equal to 358 W/kg and 0.565 respectively. Due to the higher heat of adsorption in the composite MOF compared to the neat one, the COP of the composite is lower than the neat MOF when the half-cycle time exceeds 400 seconds.

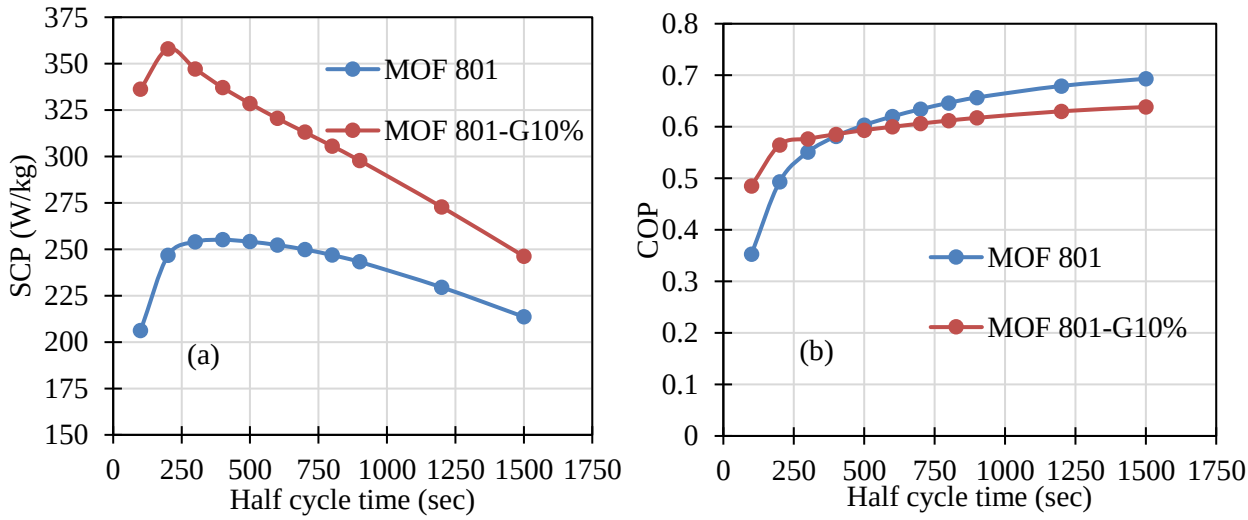



Figure 7-10. The Effect of half cycle time on (a)SCP and (b) COP using MOF 801 and MOF 801-G10%

The inlet chilled water temperature is a critical parameter that affects the performance of the adsorption system as shown in **Figure** 7-11**.** The effect of this temperature on the composite MOF is started to appear when the temperature exceeds 10ºC at a water adsorption temperature of 25ºC. This can be justified due to the effect of graphene on the water kinetics, since it has a significant enhancement at high relative pressure compared to the lower one. When the temperature of the water adsorption increases, the advantage of using the composite MOF over the neat one occurs at higher chilled water temperatures. It is observed that the SDWP is increased from 9.23 to 12.88 L/kg/day when the neat MOF is replaced with the composite one at an adsorption temperature of 25ºC. Increasing the adsorption temperature from 25 to 40ºC, has only a slight impact on the SDWP as shown in **Figure** 7-11.

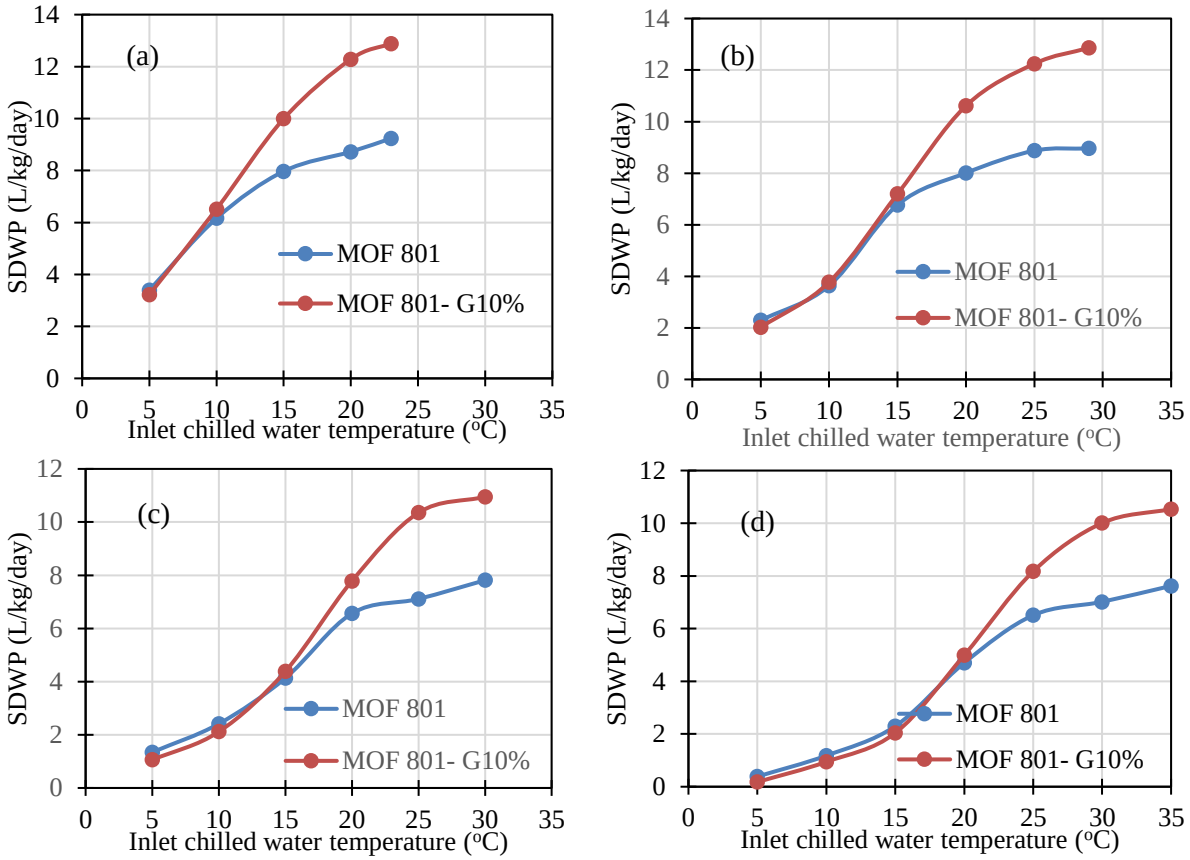



Figure 7-11. Effect of inlet chilled water temperature in the evaporator on the SDWP at inlet adsorption water temperature of (a) 25ºC, (b) 30ºC, (c) 35ºC and (d) 40ºC

The heating water temperature in the desorption process is an important factor that needs to be studied particularly when low-grade energy sources such as waste heat or solar energy is used. An inlet heating temperature is investigated with a range between 60 to 110ºC as shown in **Figure** 7-12. It is

observed that the adsorption system can still have a good performance at a heating temperature of 80°C when MOF 801 is used, while a slight decrease in the SDWP and SCP is observed when the heating temperature is decreased to 60°C. Due to the increase in the thermal conductivity when the composite MOF is used, the SCP and SDWP have the same values at a heating temperature of 60°C, when they are compared with the neat MOF at a heating temperature of 90°C. It is also shown that the adsorption system performance is tripled when the chilled water temperature is increased from 5 to 20°C.

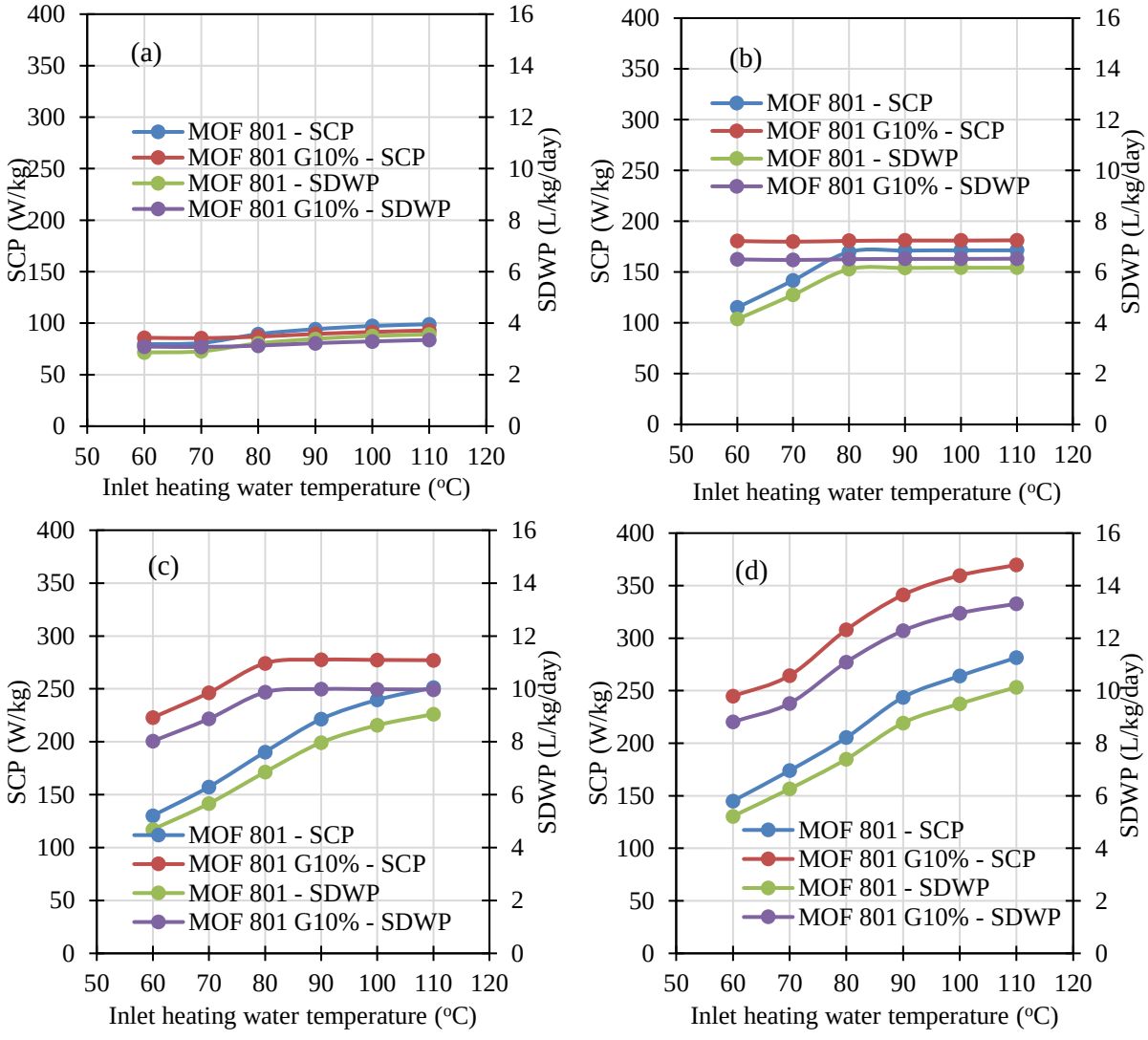



Figure 7-12. Effect of inlet heating water temperature (desorption) in the bed on the SDWP at inlet chilled water temperature of (a) 5°C, (b) 10°C, (c) 15°C and (d) 20°C

To present the advantages of MOF 801 with its graphene composite at low heating and chilled water temperatures compared to the other MOFs that were studied in the literature, Figure 7-13

compares the SDWP predicted by this study and silica gel, aluminum fumarate and CPO-27 Ni at a chilled water temperature of 10°C [6]. It is observed that the SDWP of MOF-801 and MOF-801-G10% is significantly higher than those of other MOFs at a heating temperature ranging from 65 to 110°C.

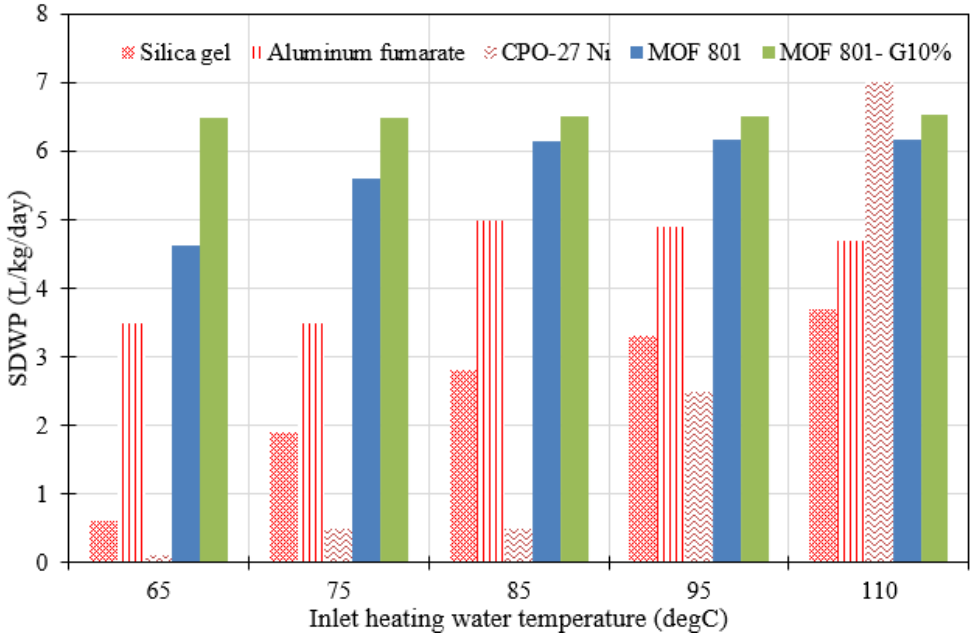



Figure 7-13. Comparison between the presented MOFs and other MOFs in the literature ($T_{chilled}$ = 10°C and $T_{cooling}$ = 30°C)

## 7.7. Conclusions

In summary, a novel MOF-801/graphene composite was developed and investigated in an adsorption cooling and desalination system. The effect of graphene addition to MOF-801 on the coefficient of performance (COP), specific cooling power (SCP) and specific daily water production (SDWP) is explored. The SCP and SDWP of the composite MOF are 40% higher than those of the pristine one, while the COP is enhanced only when the half-cycle time is less than 400 seconds due to the higher heat of adsorption of the composite MOF. Additionally, at a heating temperature of less than 110°C and chilled water temperature of 10°C, MOF-801 with its composite has higher SDWP compared to silica gel, aluminum fumarate and CPO-27Ni. The findings from this work are a crucial step toward the implementation of graphene with MOFs for better cooling and desalination system performance.

# Chapter 8: Conclusions and future work

## 8.1. Introduction

Adsorption technology for water desalination and cooling using MOFs is considered a promising sustainable solution to replace the conventional compression refrigeration system for cooling applications and pressure, thermal, and chemical-driven systems for desalination applications. This thesis summarizes the development of the MOF adsorption system for these applications through the following:

a. Development of numerical model using heat and mass transfer model with coupled solution approach (chapters 3 and 4) and using lumped parameter model (chapters 6 and 7) to study different heat exchanger geometries (rectangular finned tube and wire finned tube), scale (single tube and multiple heat exchanger modules) and MOF material for water desalination and cooling applications in the adsorber bed of the adsorption system.
b. Optimization of the heat exchanger in the adsorber bed using different methods of applying the adsorbent material (packing, coating and combination between both) (Chapters 3, 4 and 5).
c. Optimization of the method of connections between the heat exchanger modules in the adsorber bed of a scaled-up adsorption system that has multiple modules in terms of SDWP, SCP, thermal fluid flow rate and COP. Then optimization of the vapor gap between the modules to minimize the pressure losses and ensure good mass transfer throughout the adsorber bed (chapter 4).
d. Conduction of two experimental studies of a scaled-up adsorption system using a packed rectangular finned tube in one and coated wire finned tube in the other (chapters 4 and 5).
e. Study of the effect of the chamber volumes of the condenser and evaporator on the daily water production to obtain a compact adsorption water desalination and cooling system (chapter 5).
f. Investigation into the potential of integrating adsorption systems using aluminum fumarate MOF with low regeneration temperature with different adsorption systems to get a hybrid system freshwater, distilled water and cooling (chapter 6).

g. Investigation of the performance of new MOF material with enhanced thermal conductivity for application in adsorption heat pumps for water desalination and cooling using different coating thicknesses (chapter 7).

## 8.2. Conclusions

As the aim of this Ph.D. thesis is to numerically and experimentally optimize the performance of the adsorption system for cooling and water applications. The findings of the thesis can be summarized as follows:

a. The literature review shows the following:
   - Developing a high-performance heat exchanger for use in the adsorber bed requires optimizing the heat and mass transfer through the adsorbent material. Packing granular/beads/pellets adsorbent material has a limitation in terms of heat transfer, while coating the adsorbent material after mixing the powder with a binder agent can enhance the specific daily water production (SDWP) and specific cooling power (SCP) at a specific coating thickness. However, blocking the pores may lead to a significant mass transfer resistance. Thus, a comprehensive study is needed to find the best method of integration that provides good heat and mass transfer as well as a good coefficient of performance (COP) and volumetric capacity.
   - There are limited studies on the effect of scaling-up the adsorber bed by employing multiple heat exchanger modules on the overall system performance such as SDWP, SCP and COP. Further study should be carried out to obtain the best connection methods and vapor gap between modules. This requires development of heat and mass transfer model and further experimental work to investigate the temperature, pressure and water uptake distributions through the adsorbent material to obtain the best geometrical design.
   - Metal-organic framework (MOF) adsorbent materials can provide higher water uptake, faster adsorption kinetics and lower energy consumption compared to conventional adsorbent material. Thus, it is important to apply these materials in adsorption systems to obtain the best performance. However, further studies need to be carried out to enhance their

thermal conductivity to optimize the heat transfer and the cyclic performance of the adsorption system. However, using MOFs in water desalination and cooling systems can lead its integration with other systems to create hybrid systems for various applications such as water desalination. The studied integrated adsorption systems in the literature were based on using conventional adsorbent materials.

b. The coated wire-finned tube has better SDWP and SCP values compared to the packed and the combination of the packed and coated tube. However, the wire-finned tube heat exchanger with MOF integrated using 0.3 to 0.5 mm coating thickness and packing the remaining space between the wires with granular adsorbent material can have the advantage of the packed and coated methods of good heat and mass transfer performance.

c. In the wire-finned tube, it is found that using a fin height of 7mm, fin spacing of 2mm, tube diameter of 10mm, fin thickness of 1mm, 20 fins per loop, and coating thickness of 0.3mm has the highest SDWP value (21 $L.kg^{-1}.day^{-1}$) at evaporator chilled water inlet temperature of 15$^{o}$C, a heating water inlet temperature of 90$^{o}$C and cooling water inlet temperature for condenser and adsorber bed of 30$^{o}$C. However, to get a compact design while maintaining a slight reduction in SDWP, a tube diameter of 15 and 22mm and fin height of 15 and 20mm with a coating thickness ranging from 0.3mm to 0.5mm can be used. On the other hand, the lowest metal-adsorbent mass ratio (9.2) can be obtained by using a tube diameter of 22mm, fin height of 20mm and coating thickness of 0.5mm which is important to reduce thermal energy consumption.

f. When multiple rectangular packed heat exchanger modules in the adsorber bed are used in a scaled-up adsorption system, the vapor gap between them should be adjusted to minimize the vapor pressure drop and it was found that this gap depends on the module length, in which increases in the module length increases the required gap. For the experimental work, which has a module length of 400mm, the best vapor gap should be at least 10mm. Additionally, it was found that connecting the heat exchanger modules in series provides the highest COP since the effect of the heat conduction along the modules can reduce the thermal energy consumption, while the SCP will be reduced by 6.8% compared to connecting the modules in parallel.

g. Experimental testing of a scaled-up adsorption system using 8 modules of rectangular packed finned tube heat exchanger in each adsorber bed connected in series to produce more than 200L/day of fresh water, the maximum SDWP, SCP and COP are 8.66 L/kg/day, 226 W/kg and 0.5 respectively at a heating water inlet temperature of 85$^{o}$C, evaporator chilled water inlet temperature of 24$^{o}$C and cooling water inlet temperature of 25$^{o}$C for condenser and adsorber bed.

h. Experimental testing of a scaled-up adsorption system using 12 modules of wire finned tube heat exchanger coated with 0.75mm coating thickness in each adsorber bed connected also in series to produce more than 260 L/day, the SDWP and SCP were enhanced by 82% compared to the packed rectangular finned tube due to the fast kinetics of coating layer, while the COP is reduced by 52%. On the other hand, in terms of the specific volumetric daily water production in the adsorber bed (SVDWP), the coated one has SVDWP of (1.622 $L_{water}$/day-$L_{AdsorberBed}$), while the packed one has SVDWP of 2.057 $L_{water}$/day-$L_{AdsorberBed}$. Therefore, the selection between each method (packing or coating) should be based on the availability of the thermal energy source, compactness of the system and applications.

i. In the areas where an abundant amount of low-grade energy sources such as waste heat or solar energy is available, then low COP values are not of concern, thus the coated wire-finned tube in the adsorber bed can be used which also requires less amount of adsorbent material. On the other hand, in some applications where the overall energy conversion ratio is important, a high COP is important. Moreover, the packed rectangular finned tube has better volumetric capacity compared to the coated wire finned tube.

j. With evaporator and condenser chambers internal diameter of 450mm and height of 500mm, to produce/reject 6.9 kW of heat, the dead volume can be reduced by 50% with only a slight impact on the water production of the adsorption system.

k. A hybrid system is developed by integrating the adsorption system (AD) with Batch Reverse Osmosis (BRO) for desalination application. To have continuous production, multiple BRO units are connected in parallel and operated sequentially to provide a continuous brine flow that can be fed to the AD system to eliminate using the buffer tank between AD and BRO systems.

High-water recoveries of 94.1–96.9% and 64.0–65.3% for brackish water and seawater respectively using feed concentrations of 1-8 g/L and 30-44 g/L, respectively are obtained in the BRO-AD hybrid at feeding temperature of 25°C. The energy consumption is ranging between 0.395 to 0.884 kWh/$m^3$ ($SEC_{elec}$) and between 181.2 to 184.4 kWh/$m^3$ ($SEC_{heat}$) for brackish water desalination, while it is between 1.923 to 2.509 kWh/$m^3$ ($SEC_{elec}$) and between 310.4 to 315.1 kWh/$m^3$ ($SEC_{heat}$) for seawater desalination. Cooling production can also be obtained from the hybrid system ranging between 277.7 to 315.7 kW and between 168.5 to 183.6 kW for brackish water and seawater desalinations respectively. The hybrid system showed better performances in terms of energy consumption and permeate quality compared to the conventional BRO and AD systems.

l. MOF-801 (zirconium-based) and aluminum fumarate are investigated for coating using different thicknesses. It was concluded that the coated adsorbent material has better performance and faster kinetics compared to the packed one if the coating thickness does not exceed 0.85 and 1.1mm in aluminum fumarate and MOF-801 respectively.

m. By using 10% graphene nanoplatelet in a composite MOF-801 structure, the SCP and SDWP of the adsorption system increased by 40% compared to the neat pristine MOF-801, while the COP has a slight increase when the half-cycle time is less than 400 seconds. It is also concluded that at low evaporator chilled water inlet temperature of 10°C, and heating temperature of 110°C, both MOF-801 and its composite with graphene have higher SDWP compared to the silica gel, CPO-27 Ni and aluminum fumarate.

## 8.3. Future work and recommendations

In this research, significant progress was made to improve the performance of the MOF adsorption system for water desalination and cooling through (i) developing highly efficient wire-finned tube heat exchanger coated with MOF material that can produce up to 14.9 L/kg/day using a coating thickness of 0.75 mm (ii) reduce the size of the evaporator and condenser by up to 50% and (iii) investigating new MOF material that enhances the cooling production at low temperatures (less than 10°C), while these are possible optimizations that can be considered and recommended for future study as the following:

a. Study the composite MOF-801 and aluminum fumarate with graphene experimentally in an adsorption system for water desalination and cooling applications by applying the packing or coating method on the wire-finned tube or rectangular-finned tube.
b. Conduct more studies in optimizing the volumetric capacity of the adsorption system while maintaining a high adsorbent material performance.
c. More control for the temperature sources needs to be considered to maintain constant inlet water temperatures to the adsorber beds, condenser and evaporator in a scaled-up adsorption system.
d. Investigate different heat exchanger geometries such as the metal foam by either packing the adsorbent material inside the foam or coating the outer surface of the foam to enhance the heat and mass transfer.

# References


[1] T. Distefano, S. Kelly, Are we in deep water? Water scarcity and its limits to economic growth, Ecological Economics. 142 (2017) 130–147. https://doi.org/10.1016/j.ecolecon.2017.06.019.

[2] A. Al-Radif, Review of various combinations of a multiple effect desalination plant (MED) and a thermal vapour compression unit, Desalination. 93 (1993) 119–125. https://doi.org/10.1016/0011-9164(93)80099-9.

[3] P.G. Youssef, R.K. Al-Dadah, S.M. Mahmoud, Comparative analysis of desalination technologies, Energy Procedia. 61 (2014) 2604–2607. https://doi.org/10.1016/j.egypro.2014.12.258.

[4] K.C. Ng, X. WANG, L. Gao, A. Chakraborty, B.B. Saha, S. Koyama, A. Akisawa, T. Kashiwagi, Apparatus and method for desalination, WO2006121414A1, 2006.

[5] B.A. Sexton, A.E. Hughes, A comparison of weak molecular adsorption of organic molecules on clean copper and platinum surfaces, Surface Science. 140 (1984) 227–248. https://doi.org/10.1016/0039-6028(84)90394-7.

[6] P.G. Youssef, Experimental and numerical investigation of a new mof based adsorption water desalination system. Ph.D Dissertation [Online], University of Birmingham, April 2021, (2017) 6. https://etheses.bham.ac.uk/id/eprint/8376/.

[7] I. Albaik, M. Badawy Elsheniti, R. Al-Dadah, S. Mahmoud, İ. Solmaz, Numerical and experimental investigation of multiple heat exchanger modules in cooling and desalination adsorption system using metal organic framework, Energy Conversion and Management. 251 (2022) 114934. https://doi.org/10.1016/j.enconman.2021.114934.

[8] Y. Zhao, T.S. Ge, Y.J. Dai, R.Z. Wang, Experimental investigation on a desiccant dehumidification unit using fin-tube heat exchanger with silica gel coating, Applied Thermal Engineering. 63 (2014) 52–58. https://doi.org/10.1016/j.applthermaleng.2013.10.018.

[9] A. Frazzica, G. Füldner, A. Sapienza, A. Freni, L. Schnabel, Experimental and theoretical analysis of the kinetic performance of an adsorbent coating composition for use in adsorption chillers and heat pumps, Applied Thermal Engineering. 73 (2014) 1022–1031. https://doi.org/10.1016/j.applthermaleng.2014.09.004.

[10] A. Çağlar, The effect of fin design parameters on the heat transfer enhancement in the adsorbent bed of a thermal wave cycle, Applied Thermal Engineering. 104 (2016) 386–393. https://doi.org/10.1016/j.applthermaleng.2016.05.092.

[11] H. Niazmand, I. Dabzadeh, Numerical simulation of heat and mass transfer in adsorbent beds with annular fins, International Journal of Refrigeration. 35 (2012) 581–593. https://doi.org/10.1016/j.ijrefrig.2011.05.013.

[12] G. Ribatski, A.M. Jacobi, Falling-film evaporation on horizontal tubes - A critical review, International Journal of Refrigeration. 28 (2005) 635–653. https://doi.org/10.1016/j.ijrefrig.2004.12.002.

[13] F. Jeremias, D. Fröhlich, C. Janiak, S.K. Henninger, Water and methanol adsorption on MOFs for cycling heat transformation processes, New Journal of Chemistry. 38 (2014) 1846–1852. https://doi.org/10.1039/c3nj01556d.

[14] F. Jeremias, V. Lozan, S.K. Henninger, C. Janiak, Programming MOFs for water sorption: Amino-functionalized MIL-125 and UiO-66 for heat transformation and heat storage applications, Dalton Transactions. 42 (2013) 15967–15973. https://doi.org/10.1039/c3dt51471d.

[15] E. Elsayed, M.M. Saleh, R. AL-Dadah, S. Mahmoud, A. Elsayed, Aluminium fumarate metal-organic framework coating for adsorption cooling application: Experimental study, International Journal of Refrigeration. 130 (2021) 288–304. https://doi.org/10.1016/j.ijrefrig.2021.05.015.

[16] R. AL-Dadah, S. Mahmoud, E. Elsayed, P. Youssef, F. Al-Mousawi, Metal-organic framework materials for adsorption heat pumps, Energy. 190 (2020) 116356. https://doi.org/10.1016/j.energy.2019.116356.

[17] J. Wang, X. Guo, Adsorption isotherm models: Classification, physical meaning, application and solving method, Chemosphere. 258 (2020) 127279. https://doi.org/10.1016/j.chemosphere.2020.127279.

[18] R. Sips, On the structure of a catalyst surface, The Journal of Chemical Physics. 16 (1948) 490–495. https://doi.org/10.1063/1.1746922.

[19] J. Tóth, State Equation of the Solid-Gas Interface Layers, 69 (1971) 311–317.

[20] Freundlich H M F, Uber die Adsorption in Losungen, Zeitschrift Für Physikalische Chemie. 57 (1906) 385–470.

[21] I. Langmuir, the constitution and fundamental properties of solids and liquids., Journal of the American Chemical Society. 38 (1916) 2221–2295.

[22] B.P. Bering, V.A. Gordeeva, M.M. Dubinin, L.I. Efimova, V. V. Serpinskii, Development of concepts of the volume filling of micropores in the adsorption of gases and vapors by microporous adsorbents - Communication 4. Differential heats and entropies of adsorption, Bulletin of the Academy of Sciences of the USSR Division of Chemical Science. 20 (1971) 17–22. https://doi.org/10.1007/BF00849310.

[23] L.. Dubinin, M.M. and Radushkevich, The Equation of the Characteristic Curve of Activated Charcoal, Proceedings of the Academy of Sciences, Physical Chemistry Section. 55 (1947).

[24] B.B. SAHA;, E.C. BOELMAN;, T. KASHIWAGI, Computational analysis of an advanced adsorption-refrigeration cycle, Energy. 20 (1995) 983–994.

[25] E. Elsayed, R. Al-Dadah, S. Mahmoud, P. Anderson, A. Hassan, P. Youssef, Numerical investigation of MIL-101(Cr)/GrO composite performance in adsorption cooling systems, Energy Procedia. 142 (2017) 4131–4137. https://doi.org/10.1016/j.egypro.2017.12.336.

[26] P.G. Youssef, H. Dakkama, S.M. Mahmoud, R.K. AL-Dadah, Experimental investigation of adsorption water desalination/cooling system using CPO-27Ni MOF, Desalination. 404 (2017) 192–199. https://doi.org/10.1016/j.desal.2016.11.008.

[27] M.M. DUBININ, Physical Adsorption of Gases and Vapors in Micropores, Progress in Surface and Membrane Science. 9 (1975) 1–70. https://doi.org/https://doi.org/10.1016/B978-0-12-571809-7.50006-1.

[28] A. Rezk, Theoretical and experimental investigation of silica gel/water adsorption refrigeration systems, 2012.

[29] T.S. Ge, Y.J. Dai, R.Z. Wang, Z.Z. Peng, Experimental comparison and analysis on silica gel and polymer coated fin-tube heat exchangers, Energy. 35 (2010) 2893–2900. https://doi.org/10.1016/j.energy.2010.03.020.

[30] H. Niazmand, H. Talebian, M. Mahdavikhah, Effects of particle diameter on performance improvement of adsorption systems, Applied Thermal Engineering. 59 (2013) 243–252. https://doi.org/10.1016/j.applthermaleng.2013.05.043.

[31] K.C. Leong, Y. Liu, Numerical modeling of combined heat and mass transfer in the adsorbent bed of a zeolite/water cooling system, Applied Thermal Engineering. 24 (2004) 2359–2374. https://doi.org/10.1016/j.applthermaleng.2004.02.014.

[32] H. Demir, M. Mobedi, S. Ülkü, Effects of porosity on heat and mass transfer in a granular adsorbent bed, International Communications in Heat and Mass Transfer. 36 (2009) 372–377. https://doi.org/10.1016/j.icheatmasstransfer.2009.01.008.

[33] R. Haghpanah, A. Majumder, R. Nilam, A. Rajendran, S. Farooq, I.A. Karimi, M. Amanullah, Multiobjective optimization of a four-step adsorption process for postcombustion CO2 capture via finite volume simulation, Industrial and Engineering Chemistry Research. 52 (2013) 4249–4265. https://doi.org/10.1021/ie302658y.

[34] H. Qiu, L. Lv, B.C. Pan, Q.J. Zhang, W.M. Zhang, Q.X. Zhang, Critical review in adsorption kinetic models, Journal of Zhejiang University: Science A. 10 (2009) 716–724. https://doi.org/10.1631/jzus.A0820524.

[35] G. Shah, S. Sahota, V.K. Vijay, K.K. Pant, P. Ghosh, Recent developments in pressure swing adsorption for biomethane production, INC, 2021. https://doi.org/10.1016/b978-0-12-822808-1.00005-2.

[36] D. Lefebvre, P. Amyot, B. Ugur, F.H. Tezel, Adsorption Prediction and Modeling of Thermal Energy Storage Systems: A Parametric Study, Industrial and Engineering Chemistry Research. 55 (2016) 4760–4772. https://doi.org/10.1021/acs.iecr.5b04767.

[37] S. Sircar, J.R. Hufton, Why does the linear driving force model for adsorption kinetics work?, Adsorption. 6 (2000) 137–147. https://doi.org/10.1023/A:1008965317983.

[38] E. Alpay, D.M. Scott, The linear driving force model for fast-cycle adsorption and desorption in a spherical particle, Chemical Engineering Science. 47 (1992) 499–502. https://doi.org/10.1016/0009-2509(92)80041-A.

[39] T.S.Y. Choong, D.M. Scott, The linear driving force model for cyclic adsorption and desorption: The effect of external fluid-film mass transfer, Chemical Engineering Science. 53 (1998) 847–851. https://doi.org/10.1016/S0009-2509(97)00345-X.

[40] J.Y. Wang, R.Z. Wang, L.W. Wang, Water vapor sorption performance of ACF-CaCl2 and silica

gel-CaCl2 composite adsorbents, Applied Thermal Engineering. 100 (2016) 893–901. https://doi.org/10.1016/j.applthermaleng.2016.02.100.

[41] S. Narayanan, S. Yang, H. Kim, E.N. Wang, Optimization of adsorption processes for climate control and thermal energy storage, International Journal of Heat and Mass Transfer. 77 (2014) 288–300. https://doi.org/10.1016/j.ijheatmasstransfer.2014.05.022.

[42] L. Yong, K. Sumathy, Comparison between heat transfer and heat mass transfer models for transportation process in an adsorbent bed, International Journal of Heat and Mass Transfer. 47 (2004) 1587–1598. https://doi.org/10.1016/j.ijheatmasstransfer.2003.10.025.

[43] B.B. Saha, I.I. El-Sharkawy, T. Miyazaki, S. Koyama, S.K. Henninger, A. Herbst, C. Janiak, Ethanol adsorption onto metal organic framework: Theory and experiments, Energy. 79 (2015) 363–370. https://doi.org/10.1016/j.energy.2014.11.022.

[44] J. Ehrenmann, S.K. Henninger, C. Janiak, Water adsorption characteristics of MIL-101 for heat-transformation applications of MOFs, European Journal of Inorganic Chemistry. (2011) 471–474. https://doi.org/10.1002/ejic.201001156.

[45] S. Builes, S.I. Sandler, R. Xiong, Isosteric heats of gas and liquid adsorption, Langmuir. 29 (2013) 10416–10422. https://doi.org/10.1021/la401035p.

[46] S. Sircar, R. Mohr, C. Ristic, M.B. Rao, Isosteric Heat of Adsorption: Theory and Experiment, Journal of Physical Chemistry B. 103 (1999) 6539–6546. https://doi.org/10.1021/jp9903817.

[47] E.E. Anyanwu, Review of solid adsorption solar refrigeration II:: An overview of the principles and theory, Energy Conversion and Management. 45 (2004) 1279–1295. https://doi.org/10.1016/j.enconman.2003.08.003.

[48] L. Giraldo, P. Rodriguez-Estupiñán, J.C. Moreno-Piraján, Isosteric heat: Comparative study between Clausius-Clapeyron, CSK and adsorption calorimetry methods, Processes. 7 (2019). https://doi.org/10.3390/pr7040203.

[49] R.H. Mohammed, O. Mesalhy, M.L. Elsayed, L.C. Chow, Performance evaluation of a new modular packed bed for adsorption cooling systems, Applied Thermal Engineering. 136 (2018) 293–300. https://doi.org/10.1016/j.applthermaleng.2018.02.103.

[50] I.I. El-Sharkawy, K. Uddin, T. Miyazaki, B. Baran Saha, S. Koyama, H.S. Kil, S.H. Yoon, J. Miyawaki, Adsorption of ethanol onto phenol resin based adsorbents for developing next generation cooling systems, International Journal of Heat and Mass Transfer. 81 (2015) 171–178. https://doi.org/10.1016/j.ijheatmasstransfer.2014.10.012.

[51] H.W.B. Teo, A. Chakraborty, B. Han, Water adsorption on CHA and AFI types zeolites: Modelling and investigation of adsorption chiller under static and dynamic conditions, Applied Thermal Engineering. 127 (2017) 35–45. https://doi.org/10.1016/j.applthermaleng.2017.08.014.

[52] H.T. Chua, K.C. Ng, A. Chakraborty, N.M. Oo, M.A. Othman, Adsorption characteristics of silica gel + water systems, Journal of Chemical and Engineering Data. 47 (2002) 1177–1181. https://doi.org/10.1021/je0255067.

[53] B. Sun, A. Chakraborty, Thermodynamic formalism of water uptakes on solid porous adsorbents for adsorption cooling applications, Applied Physics Letters. 104 (2014). https://doi.org/10.1063/1.4876922.

[54] O.M. Yaghi, G. Li, Li Hailian, Selective binding and removal of guests in a imcroporous metal-organic framework, Nature. 378 (1995) 703–706.

[55] D. Lenzen, J. Zhao, S.J. Ernst, M. Wahiduzzaman, A. Ken Inge, D. Fröhlich, H. Xu, H.J. Bart, C. Janiak, S. Henninger, G. Maurin, X. Zou, N. Stock, A metal–organic framework for efficient water-based ultra-low-temperature-driven cooling, Nature Communications. 10 (2019) 1–9.

https://doi.org/10.1038/s41467-019-10960-0.

[56] H. Furukawa, F. Gándara, Y.B. Zhang, J. Jiang, W.L. Queen, M.R. Hudson, O.M. Yaghi, Water adsorption in porous metal-organic frameworks and related materials, Journal of the American Chemical Society. 136 (2014) 4369–4381. https://doi.org/10.1021/ja500330a.

[57] T. Qiu, Z. Liang, W. Guo, H. Tabassum, S. Gao, R. Zou, Metal–Organic Framework-Based Materials for Energy Conversion and Storage, ACS Energy Letters. 5 (2020) 520–532. https://doi.org/10.1021/acsenergylett.9b02625.

[58] Y.K. Seo, J.W. Yoon, J.S. Lee, Y.K. Hwang, C.H. Jun, J.S. Chang, S. Wuttke, P. Bazin, A. Vimont, M. Daturi, S. Bourrelly, P.L. Llewellyn, P. Horcajada, C. Serre, G. Férey, Energy-efficient dehumidification over hierachically porous metal-organic frameworks as advanced water adsorbents, Advanced Materials. 24 (2012) 806–810. https://doi.org/10.1002/adma.201104084.

[59] H. Kim, S.R. Rao, E.A. Kapustin, L. Zhao, S. Yang, O.M. Yaghi, E.N. Wang, Adsorption-based atmospheric water harvesting device for arid climates, Nature Communications. 9 (2018) 1–8. https://doi.org/10.1038/s41467-018-03162-7.

[60] R.H. Mohammed, A. Rezk, A. Askalany, E.S. Ali, A.E. Zohir, M. Sultan, M. Ghazy, M.A. Abdelkareem, A.G. Olabi, Metal-organic frameworks in cooling and water desalination: Synthesis and application, Renewable and Sustainable Energy Reviews. 149 (2021) 111362. https://doi.org/10.1016/j.rser.2021.111362.

[61] M. Wöllner, N. Klein, S. Kaskel, Measuring water adsorption processes of metal-organic frameworks for heat pump applications via optical calorimetry, Microporous and Mesoporous Materials. 278 (2019) 206–211. https://doi.org/10.1016/j.micromeso.2018.11.024.

[62] A. Rezk, R. Al-Dadah, S. Mahmoud, A. Elsayed, Characterisation of metal organic frameworks for adsorption cooling, International Journal of Heat and Mass Transfer. 55 (2012) 7366–7374. https://doi.org/10.1016/j.ijheatmasstransfer.2012.07.068.

[63] K.S.W. Sing, D.H. Everett, R.A.W. Haul, L. Moscou, R.A. Pierotti, J. Rouquerol, T. Siemieniewska, Reporting Physisorption Data for Gas/Solid Systems with Special Reference to the Determination of Surface Area and Porosity, Pure and Applied Chemistry. 57 (1985) 603–619. https://doi.org/10.1351/pac198557040603.

[64] P.D.C. Dietzel, R.E. Johnsen, R. Blom, H. Fjellvåg, Structural changes and coordinatively unsaturated metal atoms on dehydration of honeycomb analogous microporous metal-organic frameworks, Chemistry - A European Journal. 14 (2008) 2389–2397. https://doi.org/10.1002/chem.200701370.

[65] I. Albaik, R. Al-Dadah, S. Mahmoud, M.K. Almesfer, M.A. Ismail, E. Elsayed, M. Saleh, A comparison between the packed and coated finned tube for adsorption system using aluminium fumarate: Numerical study, Thermal Science and Engineering Progress. 22 (2021) 100859. https://doi.org/10.1016/j.tsep.2021.100859.

[66] N.C. Burtch, H. Jasuja, K.S. Walton, Water stability and adsorption in metal-organic frameworks, Chemical Reviews. 114 (2014) 10575–10612. https://doi.org/10.1021/cr5002589.

[67] E. Elsayed, R. Al-Dadah, S. Mahmoud, A. Elsayed, P.A. Anderson, Aluminium fumarate and CPO-27(Ni) MOFs: Characterization and thermodynamic analysis for adsorption heat pump applications, Applied Thermal Engineering. 99 (2016) 802–812. https://doi.org/10.1016/j.applthermaleng.2016.01.129.

[68] P. Youssef, S. Mahmoud, R. Al-Dadah, E. Elsayed, O. El-Samni, Numerical Investigation of Aluminum Fumarate MOF adsorbent material for adsorption desalination/cooling application, Energy Procedia. 142 (2017) 1693–1698. https://doi.org/10.1016/j.egypro.2017.12.551.

[69] X. Xia, M. Cao, Z. Liu, W. Li, S. Li, Elucidation of adsorption cooling characteristics of Zr-MOFs: Effects of structure property and working fluids, Chemical Engineering Science. 204 (2019) 48–58. https://doi.org/10.1016/j.ces.2019.04.006.

[70] S. Wang, J.S. Lee, M. Wahiduzzaman, J. Park, M. Muschi, C. Martineau-Corcos, A. Tissot, K.H. Cho, J. Marrot, W. Shepard, G. Maurin, J.S. Chang, C. Serre, A robust large-pore zirconium carboxylate metal–organic framework for energy-efficient water-sorption-driven refrigeration, Nature Energy. 3 (2018) 985–993. https://doi.org/10.1038/s41560-018-0261-6.

[71] W. Xu, O.M. Yaghi, Metal-Organic Frameworks for Water Harvesting from Air, Anywhere, Anytime, ACS Central Science. 6 (2020) 1348–1354. https://doi.org/10.1021/acscentsci.0c00678.

[72] N. Hanikel, M.S. Prévot, O.M. Yaghi, MOF water harvesters, Nature Nanotechnology. 15 (2020) 348–355. https://doi.org/10.1038/s41565-020-0673-x.

[73] E. Elsayed, H. Wang, P.A. Anderson, R. Al-Dadah, S. Mahmoud, H. Navarro, Y. Ding, J. Bowen, Development of MIL-101(Cr)/GrO composites for adsorption heat pump applications, Microporous and Mesoporous Materials. 244 (2017) 180–191. https://doi.org/10.1016/j.micromeso.2017.02.020.

[74] S. Yang, H. Kim, S. Narayanan, I.S. McKay, E.N. Wang, Dimensionality effects of carbon-based thermal additives for microporous adsorbents, Materials and Design. 85 (2015) 520–526. https://doi.org/10.1016/j.matdes.2015.06.166.

[75] Y. Yin, J. Shao, L. Zhang, Q. Cui, H. Wang, Study on heat conduction and adsorption/desorption characteristic of MIL-101/few layer graphene composite, Journal of Porous Materials. 28 (2021) 1197–1213. https://doi.org/10.1007/s10934-021-01074-4.

[76] A.A.E.-M. Mohammed Gamil, Osamu Tabata, Koichi Nakamura, Ahmed M.R. Fath El-Bab, Investigation of a New High Sensitive Micro-Electromechanical Strain Gauge Sensor Based on Graphene Piezoresistivity, Key Engineering Materials. 605 (2014) 207–210. https://doi.org/https://doi.org/10.4028/www.scientific.net/KEM.605.207.

[77] A.E. Rashed, A.A. El-Moneim, Two steps synthesis approach of MnO2/graphene nanoplates/graphite composite electrode for supercapacitor application, Materials Today Energy. 3 (2017) 24–31. https://doi.org/10.1016/j.mtener.2017.02.004.

[78] A. Rezk, R.K. Al-Dadah, S. Mahmoud, A. Elsayed, Effects of contact resistance and metal additives in finned-tube adsorbent beds on the performance of silica gel/water adsorption chiller, Applied Thermal Engineering. 53 (2013) 278–284. https://doi.org/10.1016/j.applthermaleng.2012.04.008.

[79] Y. Ming, H. Chi, R. Blaser, C. Xu, J. Yang, M. Veenstra, M. Gaab, U. Müller, C. Uher, D.J. Siegel, Anisotropic thermal transport in MOF-5 composites, International Journal of Heat and Mass Transfer. 82 (2015) 250–258. https://doi.org/10.1016/j.ijheatmasstransfer.2014.11.053.

[80] M. Li, Y. Zhao, R. Long, Z. Liu, W. Liu, Gradient porosity distribution of adsorbent bed for efficient adsorption cooling, International Journal of Refrigeration. 128 (2021) 153–162. https://doi.org/10.1016/j.ijrefrig.2021.03.013.

[81] G. Gediz Ilis, H. Demir, M. Mobedi, B. Baran Saha, A new adsorbent bed design: Optimization of geometric parameters and metal additive for the performance improvement, Applied Thermal Engineering. 162 (2019) 114270. https://doi.org/10.1016/j.applthermaleng.2019.114270.

[82] A. Caprì, A. Frazzica, L. Calabrese, Recent developments in coating technologies for adsorption heat pumps: A review, Coatings. 10 (2020) 1–24. https://doi.org/10.3390/coatings10090855.

[83] L. Calabrese, Anticorrosion behavior of zeolite coatings obtained by in situ crystallization: A critical review, Materials. 12 (2018). https://doi.org/10.3390/ma12010059.

[84] L. Calabrese, L. Bonaccorsi, D. Di Pietro, E. Proverbio, Effect of process parameters on behaviour of zeolite coatings obtained by hydrothermal direct synthesis on aluminium support, Ceramics International. 40 (2014) 12837–12845. https://doi.org/10.1016/j.ceramint.2014.04.138.

[85] L. Schnabel, M. Tatlier, F. Schmidt, A. Erdem-Şenatalar, Adsorption kinetics of zeolite coatings directly crystallized on metal supports for heat pump applications (adsorption kinetics of zeolite coatings), Applied Thermal Engineering. 30 (2010) 1409–1416. https://doi.org/10.1016/j.applthermaleng.2010.02.030.

[86] L. Bonaccorsi, L. Calabrese, E. Proverbio, A. Frazzica, A. Freni, G. Restuccia, E. Piperopoulos, C. Milone, Synthesis of SAPO-34/graphite composites for low temperature heat adsorption pumps, Journal of Energy Chemistry. 22 (2013) 245–250. https://doi.org/10.1016/S2095-4956(13)60030-3.

[87] F. Jeremias, D. Fröhlich, C. Janiak, S.K. Henninger, Advancement of sorption-based heat transformation by a metal coating of highly-stable, hydrophilic aluminium fumarate MOF, RSC Advances. 4 (2014) 24073–24082. https://doi.org/10.1039/c4ra03794d.

[88] A. Freni, L. Bonaccorsi, L. Calabrese, A. Caprì, A. Frazzica, A. Sapienza, SAPO-34 coated adsorbent heat exchanger for adsorption chillers, Applied Thermal Engineering. 82 (2015) 1–7. https://doi.org/10.1016/j.applthermaleng.2015.02.052.

[89] J. Ammann, B. Michel, P.W. Ruch, Characterization of transport limitations in SAPO-34 adsorbent coatings for adsorption heat pumps, International Journal of Heat and Mass Transfer. 129 (2019) 18–27. https://doi.org/10.1016/j.ijheatmasstransfer.2018.09.053.

[90] H. Kummer, G. Füldner, S.K. Henninger, Versatile siloxane based adsorbent coatings for fast water adsorption processes in thermally driven chillers and heat pumps, Applied Thermal Engineering. 85 (2015) 1–8. https://doi.org/10.1016/j.applthermaleng.2015.03.042.

[91] A. Sharafian, K. Fayazmanesh, C. McCague, M. Bahrami, Thermal conductivity and contact resistance of mesoporous silica gel adsorbents bound with polyvinylpyrrolidone in contact with a metallic substrate for adsorption cooling system applications, International Journal of Heat and Mass Transfer. 79 (2014) 64–71. https://doi.org/10.1016/j.ijheatmasstransfer.2014.07.086.

[92] W. Zheng, W.M. Worek, G. Nowakowski, Performance optimization of two-bed closed-cycle solid-sorption heat pump systems, Heat and Mass Transfer. 31 (1995) 1–9.

[93] K.C.A. Alam, B.B. Saha, Y.T. Kang, A. Akisawa, T. Kashiwagi, Heat exchanger design effect on the system performance of silica gel adsorption refrigeration systems, International Journal of Heat and Mass Transfer. 43 (2000) 4419–4431. https://doi.org/10.1016/S0017-9310(00)00072-7.

[94] K.C.A. Alam, Y.T. Kang, B.B. Saha, A. Akisawa, T. Kashiwagi, A novel approach to determine optimum switching frequency of a conventional adsorption chiller, Energy. 28 (2003) 1021–1037. https://doi.org/10.1016/S0360-5442(03)00064-1.

[95] R.Z. Wang, Adsorption refrigeration research in Shanghai Jiao Tong University, Renewable & Sustainable Energy Reviews. 5 (2001) 1–37. https://doi.org/10.1016/S1364-0321(00)00009-5.

[96] Y.B. Gui, R.Z. Wang, W. Wang, J.Y. Wu, Y.X. Xu, Performance modeling and testing on a heat-regenerative adsorptive reversible heat pump, Applied Thermal Engineering. 22 (2002) 309–320. https://doi.org/10.1016/S1359-4311(01)00082-5.

[97] R.E. Critoph, Z. Tamainot-Telto, G.N.L. Davies, A prototype of a fast cycle adsorption refrigerator utilizing a novel carbon-aluminium laminate, Proceedings of the Institution of Mechanical Engineers, Part A: Journal of Power and Energy. 214 (2000) 439–448. https://doi.org/10.1243/0957650001537994.

[98] Y.L. Liu, R.Z. Wang, Z.Z. Xia, Experimental performance of a silica gel-water adsorption chiller, Applied Thermal Engineering. 25 (2005) 359–375. https://doi.org/10.1016/j.applthermaleng.2004.06.012.

[99] R.H. Mohammed, O. Mesalhy, M.L. Elsayed, L.C. Chow, Novel compact bed design for adsorption cooling systems: Parametric numerical study, International Journal of Refrigeration. 80 (2017) 238–251. https://doi.org/10.1016/j.ijrefrig.2017.04.028.

[100] J.J. Guilleminot, A. Choisier, J.B. Chalfen, S. Nicolas, J.L. Reymoney, Heat transfer intensification in fixed bed adsorbers, Heat Recovery Systems and CHP. 13 (1993) 297–300. https://doi.org/10.1016/0890-4332(93)90052-W.

[101] G. Cacciola, G. Restuccia, G.H.W. Van Benthem, Influence of the adsorber heat exchanger design on the performance of the heat pump system, Applied Thermal Engineering. 19 (1999) 255–269. https://doi.org/10.1016/s1359-4311(98)00057-x.

[102] R.H. Mohammed, E. Rashad, R. Huo, M. Su, L.C. Chow, Pore-size engineered nanoporous silica for efficient adsorption cooling and desalination cycle, Npj Clean Water. 4 (2021) 1–10. https://doi.org/10.1038/s41545-021-00129-y.

[103] M.W. Shahzad, M. Burhan, K.C. Ng, Development of Falling Film Heat Transfer Coefficient for Industrial Chemical Processes Evaporator Design, in: Statistical Approaches With Emphasis on Design of Experiments Applied to Chemical Processes, IntechOpen, 2018: p. 13. http://dx.doi.org/10.1039/C7RA00172J%0Ahttps://www.intechopen.com/books/advanced-biometric-technologies/liveness-detection-in-biometrics%0Ahttp://dx.doi.org/10.1016/j.colsurfa.2011.12.014.

[104] Z.Z. Xia, G.Z. Yang, R.Z. Wang, Experimental investigation of capillary-assisted evaporation on the outside surface of horizontal tubes, International Journal of Heat and Mass Transfer. 51 (2008) 4047–4054. https://doi.org/10.1016/j.ijheatmasstransfer.2007.11.042.

[105] J. Castro, A. Oliva, C.D. Perez-Segarra, C. Oliet, Modelling of the heat exchangers of a small capacity, hot water driven, air-cooled H2O-LiBr absorption cooling machine, International Journal of Refrigeration. 31 (2008) 75–86. https://doi.org/10.1016/j.ijrefrig.2007.05.019.

[106] W. Li, X.Y. Wu, Z. Luo, R.L. Webb, Falling water film evaporation on newly-designed enhanced tube bundles, International Journal of Heat and Mass Transfer. 54 (2011) 2990–2997. https://doi.org/10.1016/j.ijheatmasstransfer.2011.02.052.

[107] P. Cheppudira Thimmaiah, A. Sharafian, W. Huttema, C. McCague, M. Bahrami, Effects of capillary-assisted tubes with different fin geometries on the performance of a low-operating pressure evaporator for adsorption cooling system applications, Applied Energy. 171 (2016) 256–265. https://doi.org/10.1016/j.apenergy.2016.03.070.

[108] F. Lanzerath, J. Seiler, M. Erdogan, H. Schreiber, M. Steinhilber, A. Bardow, The impact of filling level resolved: Capillary-assisted evaporation of water for adsorption heat pumps, Applied Thermal Engineering. 102 (2016) 513–519. https://doi.org/10.1016/j.applthermaleng.2016.03.052.

[109] L. Yong, K. Sumathy, Review of mathematical investigation on theclosed adsorption heat pump and coolingsystems, Renewable and Sustainable Energy Reviews. 6 (2002) 305–337.

[110] W.S. Teng, K.C. Leong, A. Chakraborty, Revisiting adsorption cooling cycle from mathematical modelling to system development, Renewable and Sustainable Energy Reviews. 63 (2016) 315–332. https://doi.org/10.1016/j.rser.2016.05.059.

[111] M Pons; F Meunier; G Cacciola; R E Critoph; M Groll; L Puigjaner; B Spinner; F Ziegler;, Thermodynamic based comparison of sorption systems for cooling and heat pumping, international Journal of refrigeration-revue internationale du froid. 22 (1999) 5–17.

[112] T. Núñez, H.-M. Henning, W. Mittelbach, Adsorption cycle modeling: characterization and comparison of materials, International Sorption Heat Pump Conference. (1999) 209–217.

[113] M. Pons, F. Poyelle, Adsorptive machines with advanced cycles for heat pumping or cooling applications, International Journal of Refrigeration. 22 (1999) 27–37. https://doi.org/10.1016/S0140-7007(97)00042-X.

[114] L.M. Sun, Y. Feng, M. Pons, Numerical investigation of adsorptive heat pump systems with thermal wave heat regeneration under uniform-pressure conditions, International Journal of Heat and Mass Transfer. 40 (1997) 281–293. https://doi.org/10.1016/0017-9310(96)00113-5.

[115] Y.B. Gui, R.Z. Wang, Practical three-heat-reservoir model on heat-regenerative adsorption air-conditioning system, 21 (2001) 1643–1656.

[116] K. Thu, Y.D. Kim, A. Myat, W.G. Chun, K.C. Ng, Entropy generation analysis of an adsorption cooling cycle, International Journal of Heat and Mass Transfer. 60 (2013) 143–155. https://doi.org/10.1016/J.IJHEATMASSTRANSFER.2012.12.055.

[117] R.E. Critoph, Performance limitations of adsorption cycles for solar cooling, Solar Energy. 41 (1988) 21–31. https://doi.org/10.1016/0038-092X(88)90111-9.

[118] A. Sakoda, M. Suzuki, Fundamental study on solar powered adsorption cooling system, Journal of Chemical Engineering of Japan. 17 (1984) 52–57. https://doi.org/10.1252/jcej.17.52.

[119] S. Cho, J. Kim, Modeling of a Silica Gel / Water Cooling System Adsorption-, Energy. 17 (1992) 829–839.

[120] G. Cacciola, A. Hajji, G. Maggio, G. Restuccia, Dynamic simulation of a recuperative adsorption heat pump, Energy. 18 (1993) 1125–1137. https://doi.org/10.1016/0360-5442(93)90085-R.

[121] S.M. Sami, C. Tribes, An improved model for predicting the dynamic behaviour of adsorption systems, Applied Thermal Engineering. 16 (1996) 149–161. https://doi.org/10.1016/1359-4311(95)00054-H.

[122] A.R.M. Rezk, R.K. Al-Dadah, Physical and operating conditions effects on silica gel/water adsorption chiller performance, Applied Energy. 89 (2012) 142–149. https://doi.org/10.1016/j.apenergy.2010.11.021.

[123] T. Basdanis, A. Tsimpoukis, D. Valougeorgis, Performance optimization of a solar adsorption chiller by dynamically adjusting the half-cycle time, Renewable Energy. 164 (2021) 362–374. https://doi.org/10.1016/j.renene.2020.09.072.

[124] I.P. Koronaki, E.G. Papoutsis, V.D. Papaefthimiou, Thermodynamic modeling and exergy analysis of a solar adsorption cooling system with cooling tower in Mediterranean conditions, Applied Thermal Engineering. 99 (2016) 1027–1038. https://doi.org/10.1016/j.applthermaleng.2016.01.151.

[125] H.T. Chua, K.C. Ng, A. Malek, T. Kashiwagi, A. Akisawa, B.B. Saha, Modeling the performance of two-bed, silica gel-water adsorption chillers, International Journal of Refrigeration. 22 (1999) 194–204. https://doi.org/10.1016/S0140-7007(98)00063-2.

[126] F. Duval, F. Fichot, M. Quintard, A local thermal non-equilibrium model for two-phase flows with phase-change in porous media, International Journal of Heat and Mass Transfer. 47 (2004) 613–639. https://doi.org/10.1016/j.ijheatmasstransfer.2003.07.005.

[127] M.H. Chahbani, J. Labidi, J. Paris, Effect of mass transfer kinetics on the performance of adsorptive heat pump systems, Applied Thermal Engineering. 22 (2002) 23–40. https://doi.org/10.1016/S1359-4311(01)00067-9.

[128] I. Solmuş, C. Yamali, C. Yildirim, K. Bilen, Transient behavior of a cylindrical adsorbent bed during the adsorption process, Applied Energy. 142 (2015) 115–124. https://doi.org/10.1016/j.apenergy.2014.12.080.

[129] M.M. Saleh, R. Al-Dadah, S. Mahmoud, E. Elsayed, O. El-Samni, Wire fin heat exchanger using aluminium fumarate for adsorption heat pumps, Applied Thermal Engineering. 164 (2020) 114426. https://doi.org/10.1016/j.applthermaleng.2019.114426.

[130] I. Albaik, R. Al-Dadah, S. Mahmoud, İ. Solmaz, Non-equilibrium numerical modelling of finned tube heat exchanger for adsorption desalination/cooling system using segregated solution approach, Applied Thermal Engineering. 183 (2021). https://doi.org/10.1016/j.applthermaleng.2020.116171.

[131] I. Solmuş, D. Andrew, C. Yamali, D. Baker, A two-energy equation model for dynamic heat and mass transfer in an adsorbent bed using silica gel/water pair, International Journal of Heat and Mass Transfer. 55 (2012) 5275–5288. https://doi.org/10.1016/j.ijheatmasstransfer.2012.05.036.

[132] M. Mahdavikhah, H. Niazmand, Effects of plate finned heat exchanger parameters on the adsorption chiller performance, Applied Thermal Engineering. 50 (2013) 939–949. https://doi.org/10.1016/j.applthermaleng.2012.08.033.

[133] Z. Rogala, Adsorption chiller using flat-tube adsorbers – Performance assessment and optimization, Applied Thermal Engineering. 121 (2017) 431–442. https://doi.org/10.1016/j.applthermaleng.2017.04.059.

[134] L.Z. Zhang, L. Wang, Effects of coupled heat and mass transfers in adsorbent on the performance of a waste heat adsorption cooling unit, Applied Thermal Engineering. 19 (1999) 195–215. https://doi.org/10.1016/S1359-4311(98)00023-4.

[135] M.B. Elsheniti, M.A. Hassab, A.E. Attia, Examination of effects of operating and geometric parameters on the performance of a two-bed adsorption chiller, Applied Thermal Engineering. 146 (2019) 674–687. https://doi.org/10.1016/j.applthermaleng.2018.10.043.

[136] J.J. Guilleminot, F. Meunier, J. Pakleza, Heat and mass transfer in a non-isothermal fixed bed solid adsorbent reactor: a uniform pressure-non-uniform temperature case, International Journal of Heat and Mass Transfer. 30 (1987) 1595–1606. https://doi.org/10.1016/0017-9310(87)90304-8.

[137] N. Ben Amar, L.M. Sun, F. Meunier, Numerical analysis of adsorptive temperature wave regenerative heat pump, Applied Thermal Engineering. 16 (1996) 405–418. https://doi.org/10.1016/1359-4311(95)00045-3.

[138] G. Maggio, A. Freni, G. Restuccia, A dynamic model of heat and mass transfer in a double-bed adsorption machine with internal heat recovery, International Journal of Refrigeration. 29 (2006) 589–600. https://doi.org/10.1016/j.ijrefrig.2005.10.005.

[139] L.Z. Zhang, A three-dimensional non-equilibrium model for an intermittent adsorption cooling system, Solar Energy. 69 (2000) 27–35. https://doi.org/10.1016/S0038-092X(00)00010-4.

[140] Y.J. Dai, K. Sumathy, Heat and mass transfer in the adsorbent of a solar adsorption cooling system with glass tube insulation, Energy. 28 (2003) 1511–1527. https://doi.org/10.1016/S0360-5442(03)00128-2.

[141] K.C. Leong, Y. Liu, Numerical study of a combined heat and mass recovery adsorption cooling cycle, International Journal of Heat and Mass Transfer. 47 (2004) 4761–4770. https://doi.org/10.1016/j.ijheatmasstransfer.2004.05.030.

[142] A. El Fadar, A. Mimet, M. Pérez-García, Modelling and performance study of a continuous adsorption refrigeration system driven by parabolic trough solar collector, Solar Energy. 83 (2009) 850–861. https://doi.org/10.1016/j.solener.2008.12.003.

[143] H. Niazmand, H. Talebian, M. Mahdavikhah, Bed geometrical specifications effects on the performance of silica/water adsorption chillers Effets des spécifications géométriques du lit sur la performance des refroidisseurs à adsorption au gel de silice/eau, International Journal of Refrigeration. 35 (2012) 2261–2274. https://doi.org/10.1016/j.ijrefrig.2012.08.017.

[144] B. Shi, A. Elsayed, S. Mahmoud, CFD Simulation of Honeycomb Adsorption Bed for Automotive Cooling System, in: Proceedings of the International Conference on Heat Transfer and Fluid Flow, Prague, Czech Republic, 2014: pp. 1–7.

[145] J. White, CFD simulation and experimental analyses of a copper wire woven heat exchanger design to improve heat transfer and reduce the size of adsorption beds, Computation. 4 (2016). https://doi.org/10.3390/computation4010008.

[146] S. Jribi, T. Miyazaki, B.B. Saha, S. Koyama, S. Maeda, T. Maruyama, CFD simulation and experimental validation of ethanol adsorption onto activated carbon packed heat exchanger, International Journal of Refrigeration. 74 (2017) 343–351. https://doi.org/10.1016/j.ijrefrig.2016.10.019.

[147] M. Mohammadzadeh Kowsari, H. Niazmand, M.M. Tokarev, Bed configuration effects on the finned flat-tube adsorption heat exchanger performance: Numerical modeling and experimental validation, Applied Energy. 213 (2018) 540–554. https://doi.org/10.1016/j.apenergy.2017.11.019.

[148] B. Golparvar, H. Niazmand, A. Sharafian, A. Ahmadian Hosseini, Optimum fin spacing of finned tube adsorber bed heat exchangers in an exhaust gas-driven adsorption cooling system, Applied Energy. 232 (2018) 504–516. https://doi.org/10.1016/J.APENERGY.2018.10.002.

[149] C. Renno, G. Landi, F. Petito, H.C. Neitzert, Influence of a degraded triple-junction solar cell on the CPV system performances, Energy Conversion and Management. 160 (2018) 326–340. https://doi.org/10.1016/j.enconman.2018.01.026.

[150] A.A. Hassan, A.E. Elwardany, S. Ookawara, I.I. El-Sharkawy, Performance investigation of a solar-powered adsorption-based trigeneration system for cooling, electricity, and domestic hot water production, Applied Thermal Engineering. 199 (2021) 117553. https://doi.org/10.1016/j.applthermaleng.2021.117553.

[151] I. Albaik, Y.A. Alamri, M.B. Elsheniti, R. Al-Dadah, S. Mahmoud, M.A. Ismail, Assessment of a novel multi-generation solar CPV/T system combining adsorption and organic rankine cycle subsystems, Solar Energy. 236 (2022) 455–472. https://doi.org/10.1016/j.solener.2022.03.024.

[152] O.Z. Sharaf, M.F. Orhan, Concentrated photovoltaic thermal (CPVT) solar collector systems: Part I - Fundamentals, design considerations and current technologies, Renewable and Sustainable Energy Reviews. 50 (2015) 1500–1565. https://doi.org/10.1016/j.rser.2015.05.036.

[153] R. Daneshazarian, E. Cuce, P.M. Cuce, F. Sher, Concentrating photovoltaic thermal (CPVT) collectors and systems: Theory, performance assessment and applications, Renewable and Sustainable Energy Reviews. 81 (2018) 473–492. https://doi.org/10.1016/j.rser.2017.08.013.

[154] J.I. Rosell, X. Vallverdú, M.A. Lechón, M. Ibáñez, Design and simulation of a low concentrating photovoltaic/thermal system, Energy Conversion and Management. 46 (2005) 3034–3046. https://doi.org/10.1016/j.enconman.2005.01.012.

[155] S. Quoilin, M. Van Den Broek, S. Declaye, P. Dewallef, V. Lemort, Techno-economic survey of organic rankine cycle (ORC) systems, Renewable and Sustainable Energy Reviews. 22 (2013) 168–186. https://doi.org/10.1016/j.rser.2013.01.028.

[156] T.C. Roumpedakis, T. Christou, E. Monokrousou, K. Braimakis, S. Karellas, Integrated ORC-Adsorption cycle: A first and second law analysis of potential configurations, Energy. 179 (2019) 46–58. https://doi.org/10.1016/j.energy.2019.04.069.

[157] F.N. Al-Mousawi, R. Al-Dadah, S. Mahmoud, Integrated adsorption-ORC system: Comparative study of four scenarios to generate cooling and power simultaneously, Applied Thermal Engineering. 114 (2017) 1038–1052. https://doi.org/10.1016/j.applthermaleng.2016.12.069.

[158] N. Chaiyat, Y. Wakaiyang, X. Inthavideth, Enhancement efficiency of organic Rankine cycle by using sorption system, Applied Thermal Engineering. 122 (2017) 368–379. https://doi.org/10.1016/j.applthermaleng.2017.05.028.

[159] L. Wang, A.P. Roskilly, R. Wang, Solar powered cascading cogeneration cycle with ORC and adsorption technology for electricity and refrigeration, Heat Transfer Engineering. 35 (2014) 1028–1034. https://doi.org/10.1080/01457632.2013.863067.

[160] K. Choon, K. Thu, Y. Kim, A. Chakraborty, G. Amy, Adsorption desalination : An emerging low-cost thermal desalination method, DES. 308 (2013) 161–179. https://doi.org/10.1016/j.desal.2012.07.030.

[161] A.S. Alsaman, A.A. Askalany, K. Harby, M.S. Ahmed, A state of the art of hybrid adsorption desalination-cooling systems, Renewable and Sustainable Energy Reviews. 58 (2016) 692–703. https://doi.org/10.1016/j.rser.2015.12.266.

[162] M. Sarai Atab, A.J. Smallbone, A.P. Roskilly, A hybrid reverse osmosis/adsorption desalination plant for irrigation and drinking water, Desalination. 444 (2018) 44–52. https://doi.org/10.1016/j.desal.2018.07.008.

[163] E.S. Ali, A.S. Alsaman, K. Harby, A.A. Askalany, M.R. Diab, S.M. Ebrahim Yakoot, Recycling brine water of reverse osmosis desalination employing adsorption desalination: A theoretical simulation, Desalination. 408 (2017) 13–24. https://doi.org/10.1016/j.desal.2016.12.002.

[164] M.W. Shahzad, K.C. Ng, K. Thu, B.B. Saha, W.G. Chun, Multi effect desalination and adsorption desalination (MEDAD): A hybrid desalination method, Applied Thermal Engineering. 72 (2014) 289–297. https://doi.org/10.1016/j.applthermaleng.2014.03.064.

[165] E.S. Ali, R.H. Mohammed, N.A.A. Qasem, S.M. Zubair, A. Askalany, Solar-powered ejector-based adsorption desalination system integrated with a humidification-dehumidification system, Energy Conversion and Management. 238 (2021) 114113. https://doi.org/10.1016/j.enconman.2021.114113.

[166] K. Harby, E.S. Ali, K.M. Almohammadi, A novel combined reverse osmosis and hybrid absorption desalination-cooling system to increase overall water recovery and energy efficiency, Journal of Cleaner Production. 287 (2021) 125014. https://doi.org/10.1016/j.jclepro.2020.125014.

[167] C. Frantz, B. Seifert, Thermal Analysis of a Multi Effect Distillation Plant Powered by a Solar Tower Plant, Energy Procedia. 69 (2015) 1928–1937. https://doi.org/10.1016/j.egypro.2015.03.190.

[168] D. Kaunga, R. Patel, I. Mujtaba, Modelling and Performance Evaluation of Humidification-Dehumidification Desalination Plant with Column Packing of Various Textures, Elsevier Masson SAS, 2020. https://doi.org/10.1016/B978-0-12-823377-1.50065-3.

[169] L.F. Greenlee, D.F. Lawler, B.D. Freeman, B. Marrot, P. Moulin, Reverse osmosis desalination: Water sources, technology, and today's challenges, Water Research. 43 (2009) 2317–2348. https://doi.org/10.1016/j.watres.2009.03.010.

[170] K. Park, J. Kim, D.R. Yang, S. Hong, Towards a low-energy seawater reverse osmosis desalination plant: A review and theoretical analysis for future directions, Journal of Membrane Science. 595 (2020) 117607. https://doi.org/10.1016/j.memsci.2019.117607.

[171] A. Subramani, M. Badruzzaman, J. Oppenheimer, J.G. Jacangelo, Energy minimization strategies and renewable energy utilization for desalination: A review, Water Research. 45

(2011) 1907–1920. https://doi.org/10.1016/j.watres.2010.12.032.

[172] J.L. Prante, J.A. Ruskowitz, A.E. Childress, A. Achilli, RO-PRO desalination: An integrated low-energy approach to seawater desalination, Applied Energy. 120 (2014) 104–114. https://doi.org/10.1016/j.apenergy.2014.01.013.

[173] K. Park, L. Burlace, N. Dhakal, A. Mudgal, N.A. Stewart, P.A. Davies, Design, modelling and optimisation of a batch reverse osmosis (RO) desalination system using a free piston for brackish water treatment, Desalination. 494 (2020) 114625. https://doi.org/10.1016/j.desal.2020.114625.

[174] J.R. Werber, A. Deshmukh, M. Elimelech, Can batch or semi-batch processes save energy in reverse-osmosis desalination?, Desalination. 402 (2017) 109–122. https://doi.org/10.1016/j.desal.2016.09.028.

[175] S. Lin, M. Elimelech, Staged reverse osmosis operation: Configurations, energy efficiency, and application potential, Desalination. 366 (2015) 9–14. https://doi.org/10.1016/j.desal.2015.02.043.

[176] S. Lin, S. Veerapaneni, Emerging investigator series: Toward the ultimate limit of seawater desalination with mesopelagic open reverse osmosis, Environmental Science: Water Research and Technology. 7 (2021) 1212–1219. https://doi.org/10.1039/d1ew00153a.

[177] J. Swaminathan, E.W. Tow, R.L. Stover, J.H. Lienhard, Practical aspects of batch RO design for energy-efficient seawater desalination, Desalination. 470 (2019) 114097. https://doi.org/10.1016/j.desal.2019.114097.

[178] Q.J. Wei, C.I. Tucker, P.J. Wu, A.M. Trueworthy, E.W. Tow, J.H. Lienhard, Impact of salt retention on true batch reverse osmosis energy consumption: Experiments and model validation, Desalination. 479 (2020) 114177. https://doi.org/10.1016/j.desal.2019.114177.

[179] Z. Wang, A. Deshmukh, Y. Du, M. Elimelech, Minimal and zero liquid discharge with reverse osmosis using low-salt-rejection membranes, Water Research. 170 (2020) 115317. https://doi.org/10.1016/j.watres.2019.115317.

[180] D.M. Davenport, L. Wang, E. Shalusky, M. Elimelech, Design principles and challenges of bench-scale high-pressure reverse osmosis up to 150 bar, Desalination. 517 (2021) 115237. https://doi.org/10.1016/j.desal.2021.115237.

[181] S. Bai, T.C. Ho, J. Ha, A.K. An, C.Y. Tso, Study of the salinity effects on the cooling and desalination performance of an adsorption cooling cum desalination system with a novel composite adsorbent, Applied Thermal Engineering. 181 (2020). https://doi.org/10.1016/j.applthermaleng.2020.115879.

[182] H. Ma, J. Zhang, C. Liu, X. Lin, Y. Sun, Experimental investigation on an adsorption desalination system with heat and mass recovery between adsorber and desorber beds, Desalination. 446 (2018) 42–50. https://doi.org/10.1016/j.desal.2018.08.022.

[183] S.Y. Woo, H.S. Lee, H. Ji, D.S. Moon, Y.D. Kim, Silica gel-based adsorption cooling cum desalination system: Focus on brine salinity, operating pressure, and its effect on performance, Desalination. 467 (2019) 136–146. https://doi.org/10.1016/j.desal.2019.06.016.

[184] I. Albaik, K. Diab, R. Al-dadah, S. Mahmoud, M.A. Ismail, Coating Thickness Effect on the Cyclic Performance of Aluminum and Zirconium Metal-Organic Frameworks for Heat Pump Application, (2021) 1–6.

[185] D.A. Nield, A. V. Kuznetsov, HEAT TRANSFER IN BIDISPERSE POROUS MEDIA, Transport Phenomena in Porous Media III. (2005) 34–59. https://doi.org/10.1016/B978-008044490-1/50006-5.

[186] M.M. Saleh, E. Elsayed, R. AL-Dadah, S. Mahmoud, Experimental testing of wire finned heat

exchanger coated with aluminium fumarate MOF material for adsorption desalination application, Thermal Science and Engineering Progress. 28 (2022) 101050. https://doi.org/10.1016/j.tsep.2021.101050.

[187] E. Elsayed, R. AL-Dadah, S. Mahmoud, P. Anderson, A. Elsayed, Experimental testing of aluminium fumarate MOF for adsorption desalination, Desalination. 475 (2020) 114170. https://doi.org/10.1016/j.desal.2019.114170.

[188] E. Elsayed, R. AL-Dadah, S. Mahmoud, P.A. Anderson, A. Elsayed, P.G. Youssef, CPO-27(Ni), aluminium fumarate and MIL-101(Cr) MOF materials for adsorption water desalination, Desalination. 406 (2017) 25–36. https://doi.org/10.1016/J.DESAL.2016.07.030.

[189] M.B. Elsheniti, A. Rezk, M. Shaaban, M. Roshdy, Y.M. Nagib, O.A. Elsamni, B.B. Saha, Performance of a solar adsorption cooling and desalination system using aluminum fumarate and silica gel, Applied Thermal Engineering. 194 (2021) 117116. https://doi.org/10.1016/j.applthermaleng.2021.117116.

[190] K. Thu, H. Yanagi, B.B. Saha, K.C. Ng, Performance analysis of a low-temperature waste heat-driven adsorption desalination prototype, International Journal of Heat and Mass Transfer. 65 (2013) 662–669. https://doi.org/10.1016/J.IJHEATMASSTRANSFER.2013.06.053.

[191] M. Kilic, M. Anjrini, Comparative performance analysis of a combined cooling system with mechanical and adsorption cycles, Energy Conversion and Management. 221 (2020) 113208. https://doi.org/10.1016/j.enconman.2020.113208.

[192] N. Ghaffour, T.M. Missimer, G.L. Amy, Technical review and evaluation of the economics of water desalination: Current and future challenges for better water supply sustainability, Desalination. 309 (2013) 197–207. https://doi.org/10.1016/J.DESAL.2012.10.015.

[193] E.M. Elsayed, A. Hussein, Numerical and Experimental Evaluation of Advanced Metal-Organic Framework Materials for Adsorption Heat Pumps Doctor of Philosophy, Univerity of Birmingham, 2018.

[194] T.Y. Qiu, P.A. Davies, Concentration polarization model of spiral-wound membrane modules with application to batch-mode RO desalination of brackish water, Desalination. 368 (2015) 36–47. https://doi.org/10.1016/j.desal.2014.12.048.

[195] Y.A. Çengel, J.M. Cimbala, Fluid mechanics, fundamentals and applications, in: McGraw-Hil, 2006.

[196] A. Ruiz-García, E. Ruiz-Saavedra, 80,000h operational experience and performance analysis of a brackish water reverse osmosis desalination plant. Assessment of membrane replacement cost, Desalination. 375 (2015) 81–88. https://doi.org/10.1016/j.desal.2015.07.022.

[197] N. Voutchkov, Energy use for membrane seawater desalination – current status and trends, Desalination. 431 (2018) 2–14. https://doi.org/10.1016/j.desal.2017.10.033.

[198] B.A. Qureshi, S.M. Zubair, Exergetic analysis of a brackish water reverse osmosis desalination unit with various energy recovery systems, Energy. 93 (2015) 256–265. https://doi.org/10.1016/j.energy.2015.09.003.

[199] W. Jantaporn, A. Ali, P. Aimar, Specific energy requirement of direct contact membrane distillation, Chemical Engineering Research and Design. 128 (2017) 15–26. https://doi.org/10.1016/j.cherd.2017.09.031.

[200] R. Singh, Analysis of high recovery brackish water desalination processes using fuel cells, Separation Science and Technology. 44 (2009) 585–598. https://doi.org/10.1080/01496390802634414.

[201] J. Kim, K. Park, S. Hong, Application of two-stage reverse osmosis system for desalination of

high-salinity and high-temperature seawater with improved stability and performance, Desalination. 492 (2020) 114645. https://doi.org/10.1016/j.desal.2020.114645.

[202] X. Chen, N.Y. Yip, Unlocking High-Salinity Desalination with Cascading Osmotically Mediated Reverse Osmosis: Energy and Operating Pressure Analysis, Environmental Science and Technology. 52 (2018) 2242–2250. https://doi.org/10.1021/acs.est.7b05774.

[203] J. Kim, K. Park, S. Hong, Optimization of two-stage seawater reverse osmosis membrane processes with practical design aspects for improving energy efficiency, Journal of Membrane Science. 601 (2020) 117889. https://doi.org/10.1016/j.memsci.2020.117889.

[204] C. Periyasamy, P. Anantharaman, T. Balasubramanian, P.V.S. Rao, Seasonal variation in growth and carrageenan yield in cultivated Kappaphycus alvarezii (Doty) Doty on the coastal waters of Ramanathapuram district, Tamil Nadu, Journal of Applied Phycology. 26 (2014) 803–810. https://doi.org/10.1007/s10811-014-0256-z.

[205] K.M. Sassi, I.M. Mujtaba, MINLP based superstructure optimization for boron removal during desalination by reverse osmosis, Journal of Membrane Science. 440 (2013) 29–39. https://doi.org/10.1016/j.memsci.2013.03.012.

[206] T. Tong, M. Elimelech, The Global Rise of Zero Liquid Discharge for Wastewater Management: Drivers, Technologies, and Future Directions, Environmental Science and Technology. 50 (2016) 6846–6855. https://doi.org/10.1021/acs.est.6b01000.

[207] E. Glueckauf, Theory of chromatography. Part 10.—Formulæ for diffusion into spheres and their application to chromatography, Transactions of the Faraday Society. 51 (1955) 1540–1551. https://doi.org/10.1039/TF9555101540.

[208] S.L. Li, J.Y. Wu, Z.Z. Xia, R.Z. Wang, Study on the adsorption isosteres of the composite adsorbent CaCl 2 and expanded graphite, Energy Conversion and Management. 52 (2011) 1501–1506. https://doi.org/10.1016/j.enconman.2010.10.015.

**Appendix A:** Experimental setup for the packed finned tube adsorption system




Figure 10-1. Two-bed packed adsorption desalination and cooling system

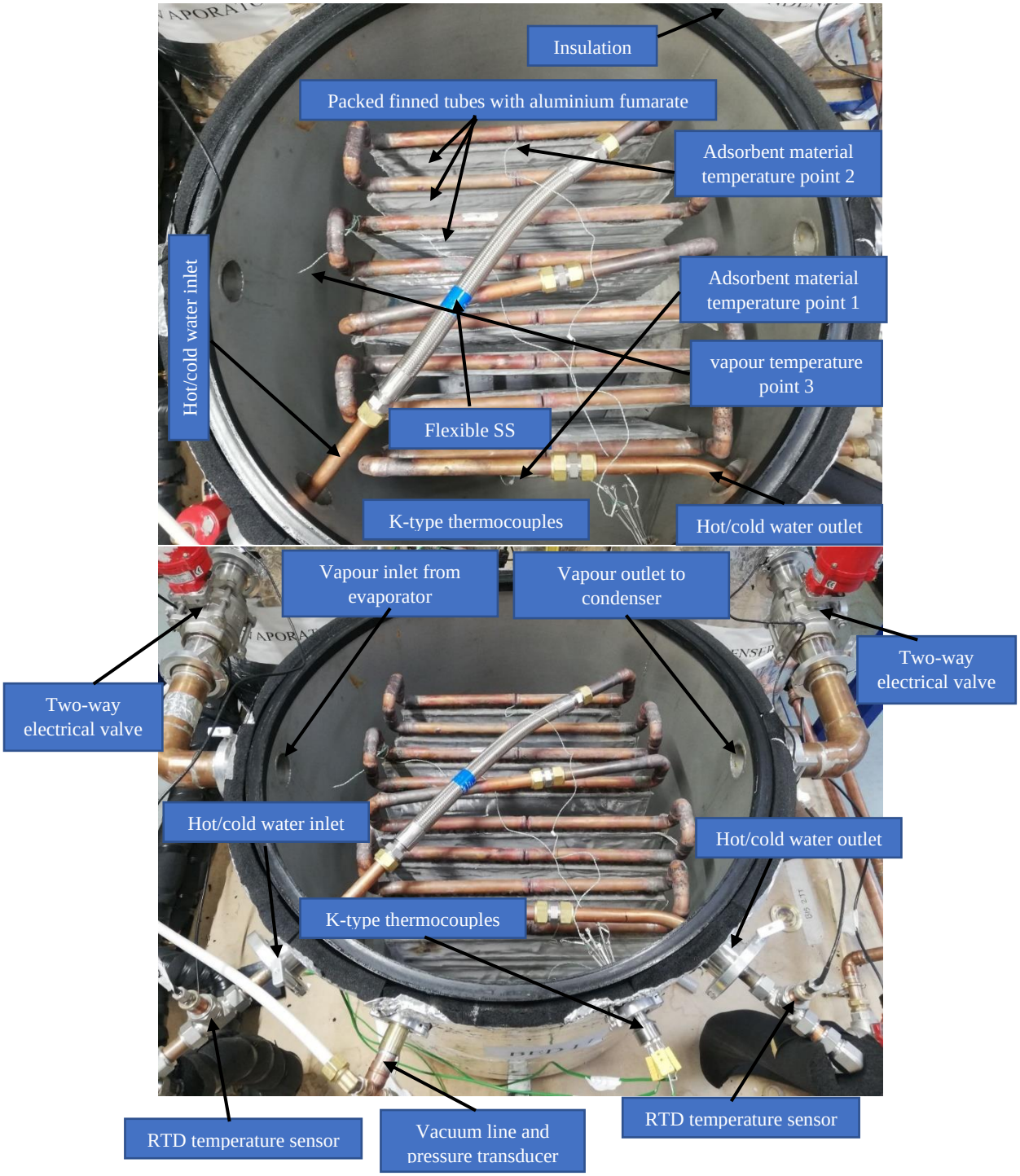



Figure 10-2. Adsorber bed and its connections in packed adsorption system




Figure 10-3. detailed water connections to the adsorber bed in packed adsorption system

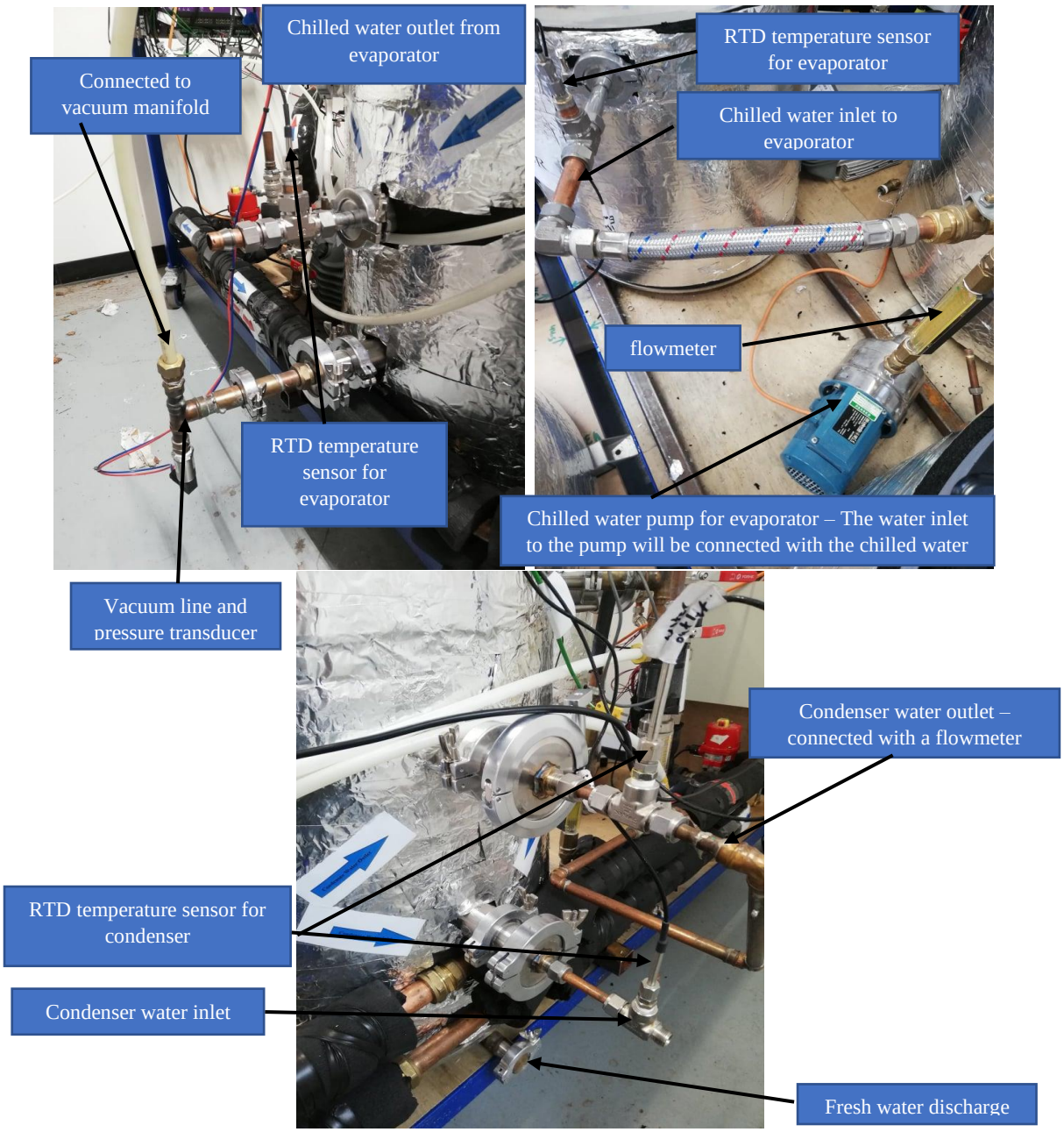



Figure 10-4. Evaporator and condenser and their connections in packed adsorption system




Figure 10-5. Datal logger, and power & control boxes in packed adsorption system

**Appendix B:** Experimental setup for the coated finned tube adsorption system

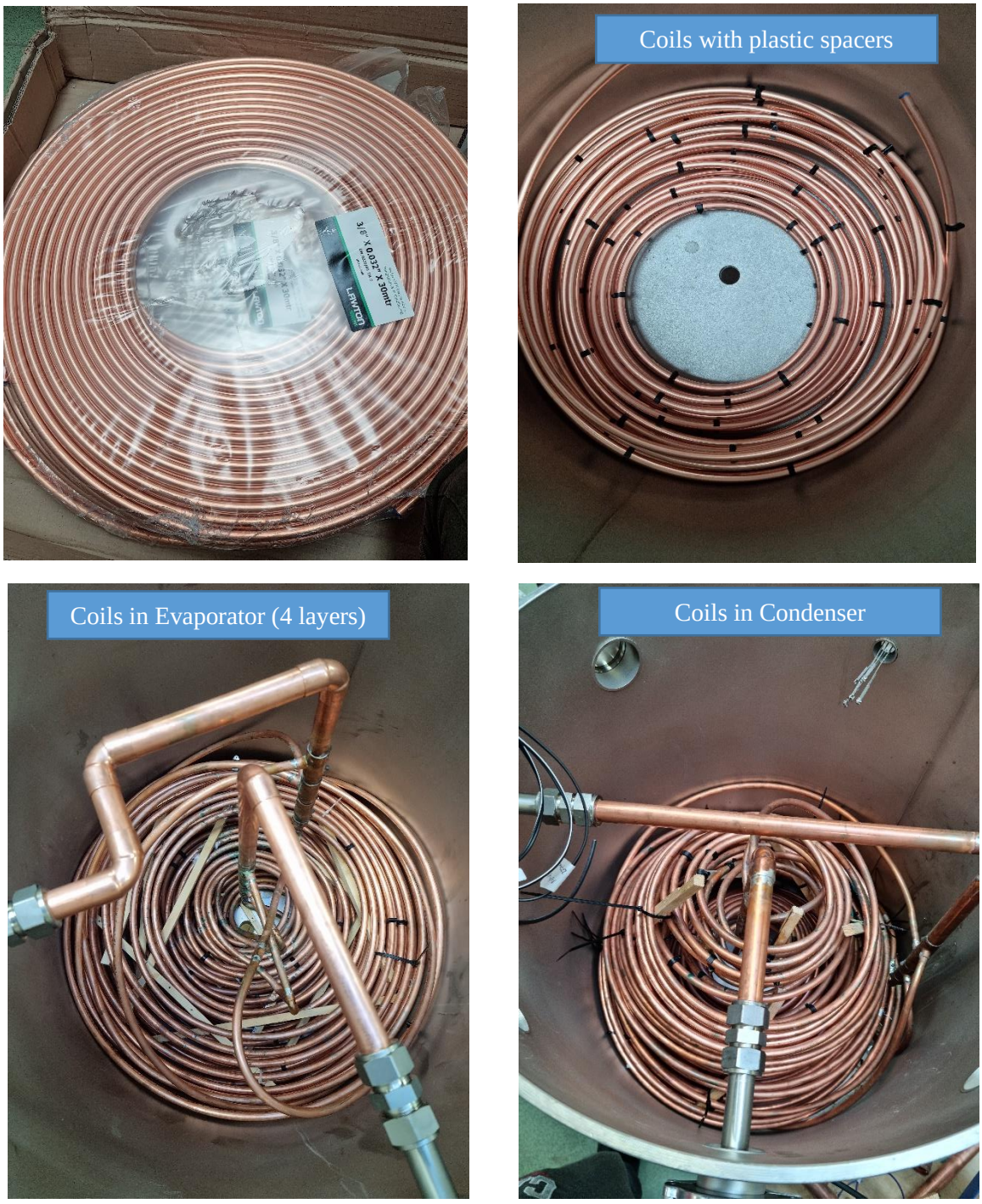



Figure 11-1 . Heat exchanger coils connections in evaporator and condenser




Figure 11-2. Hot and cold water sources for the adsorption system

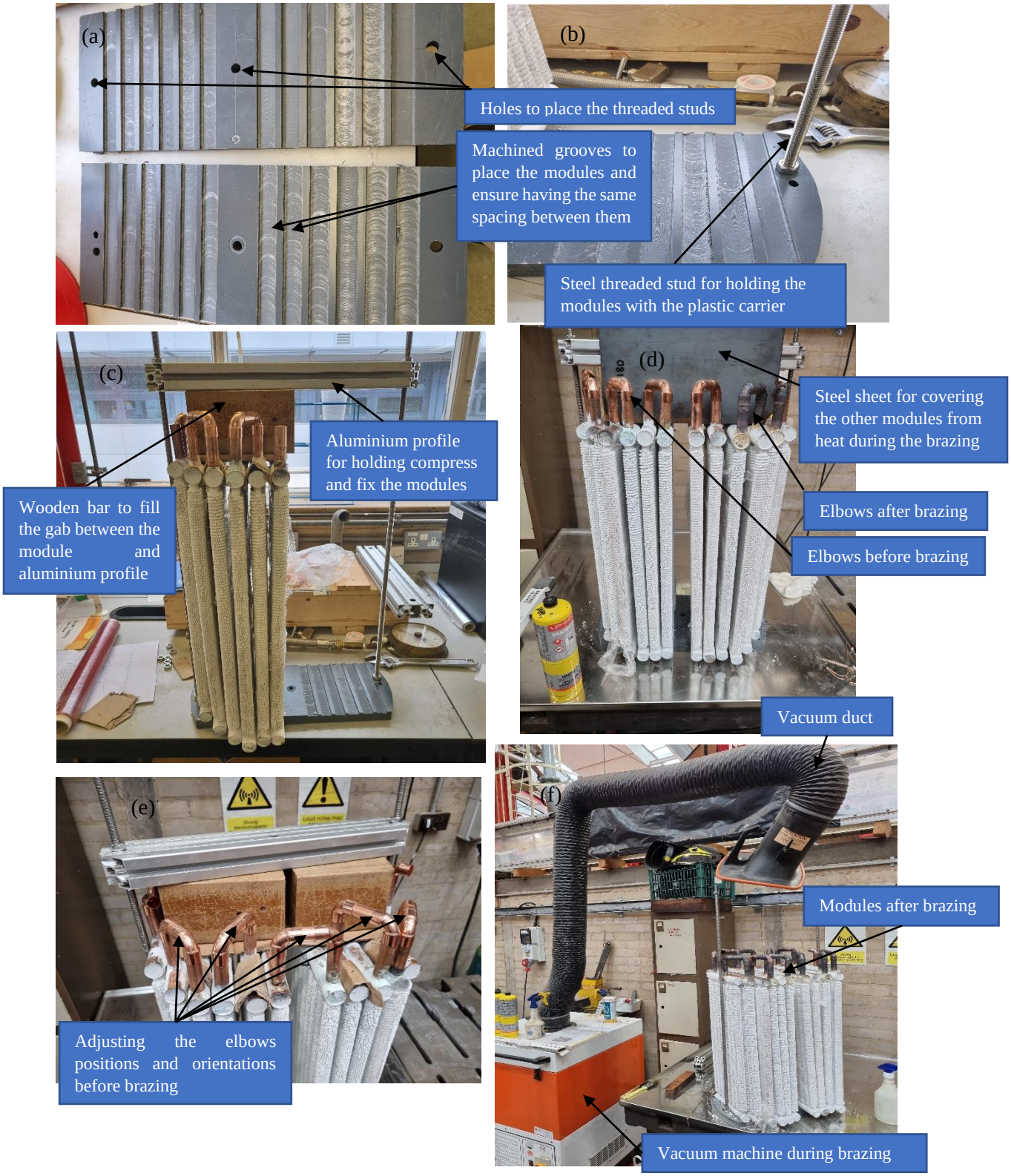



Figure 11-3. Coated wire finned tube heat exchanger modules preparations

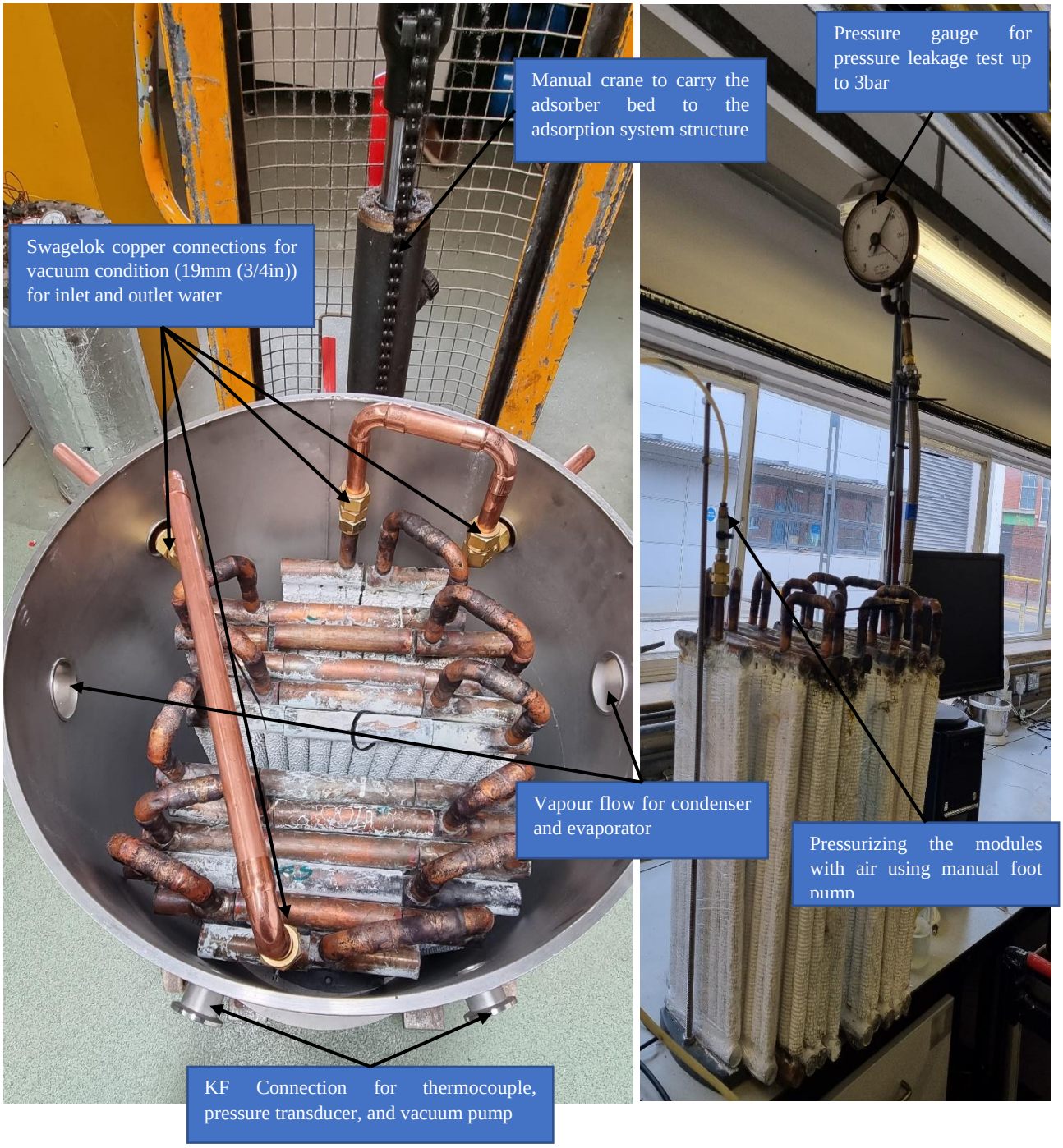



Figure 11-4. Carrying the adsorber bed and pressure test of the coated wire finned tube heat exchanger modules

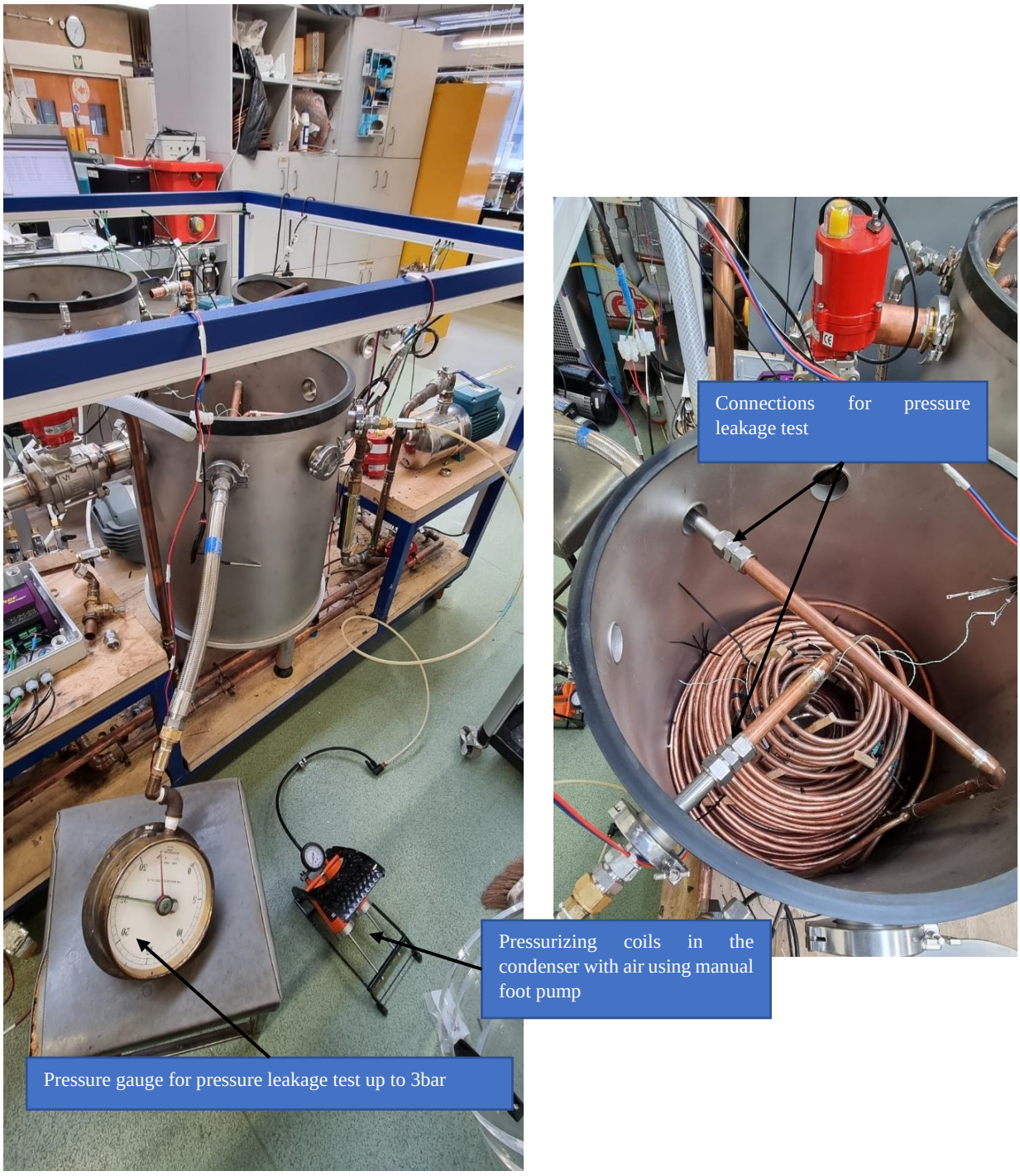



Figure 11-5. Pressure test of the heat exchanger coils of the condenser

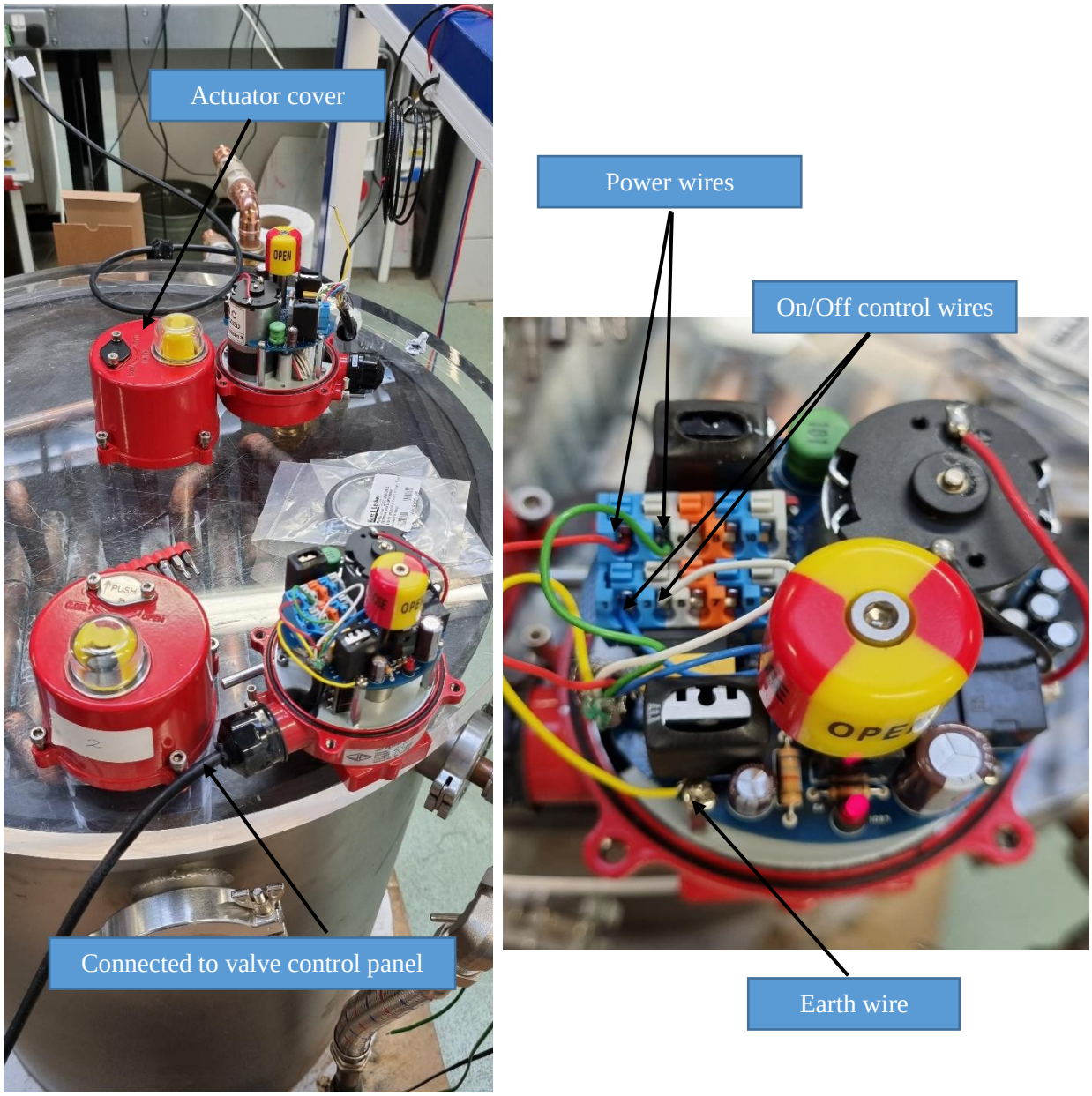



Figure 11-6. Actuator connections of the electrical solenoid ball valve

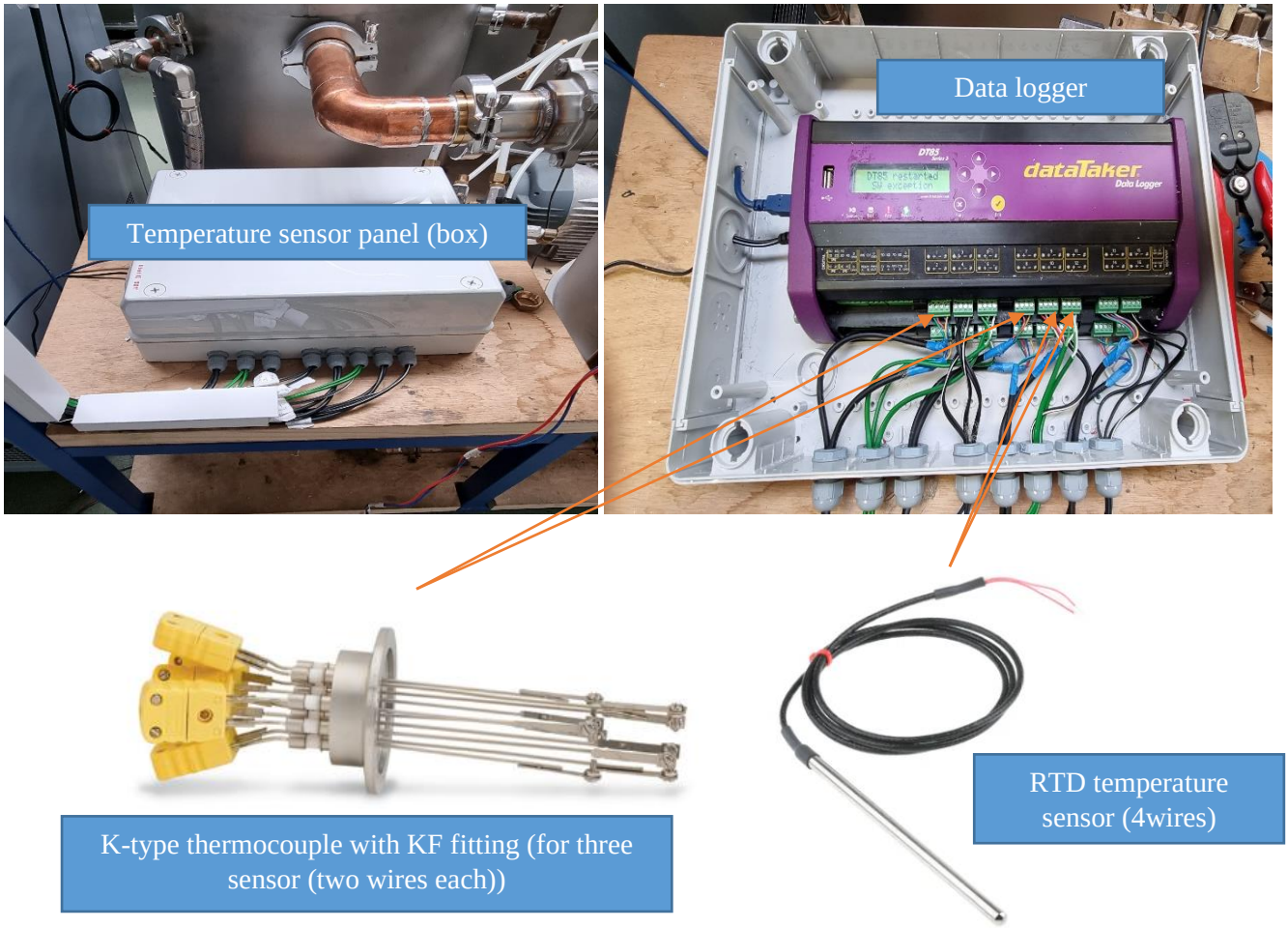



Figure 11-7. Data logger panel (box) with its connections to RTD and K-type thermocouples

# **Appendix C:** CAD Drawings

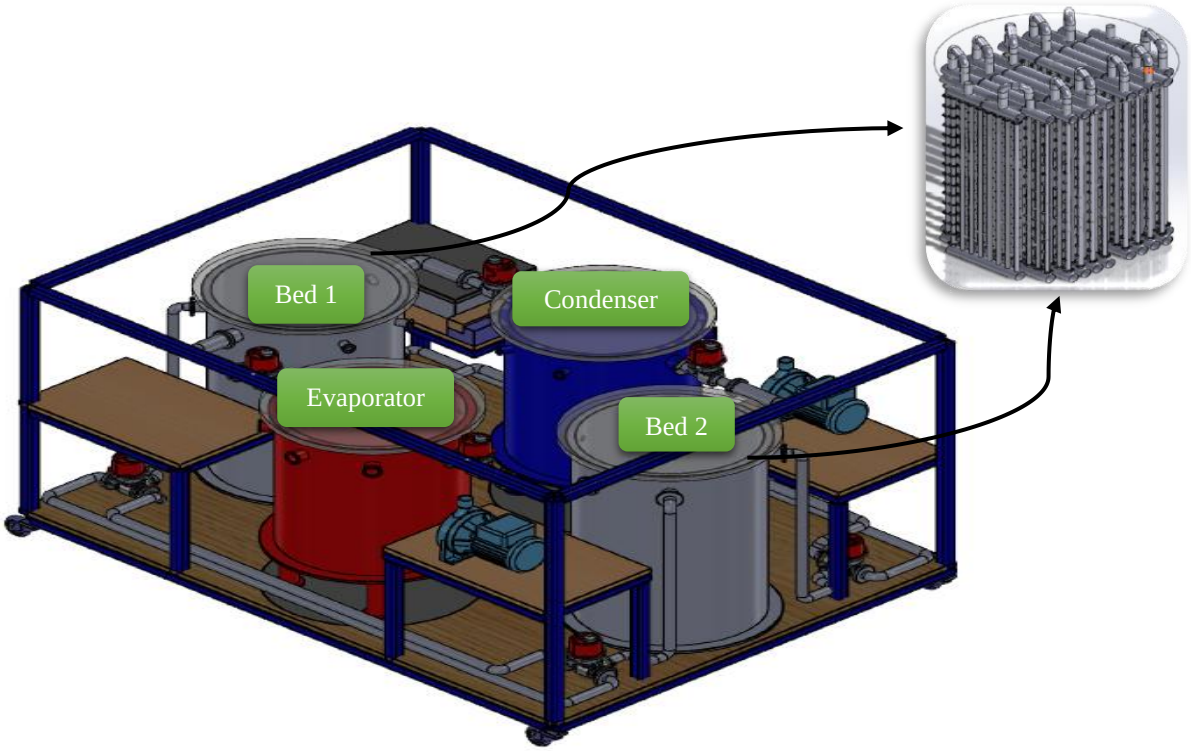



Figure 12-1. 3D isometric drawing of the adsorption system

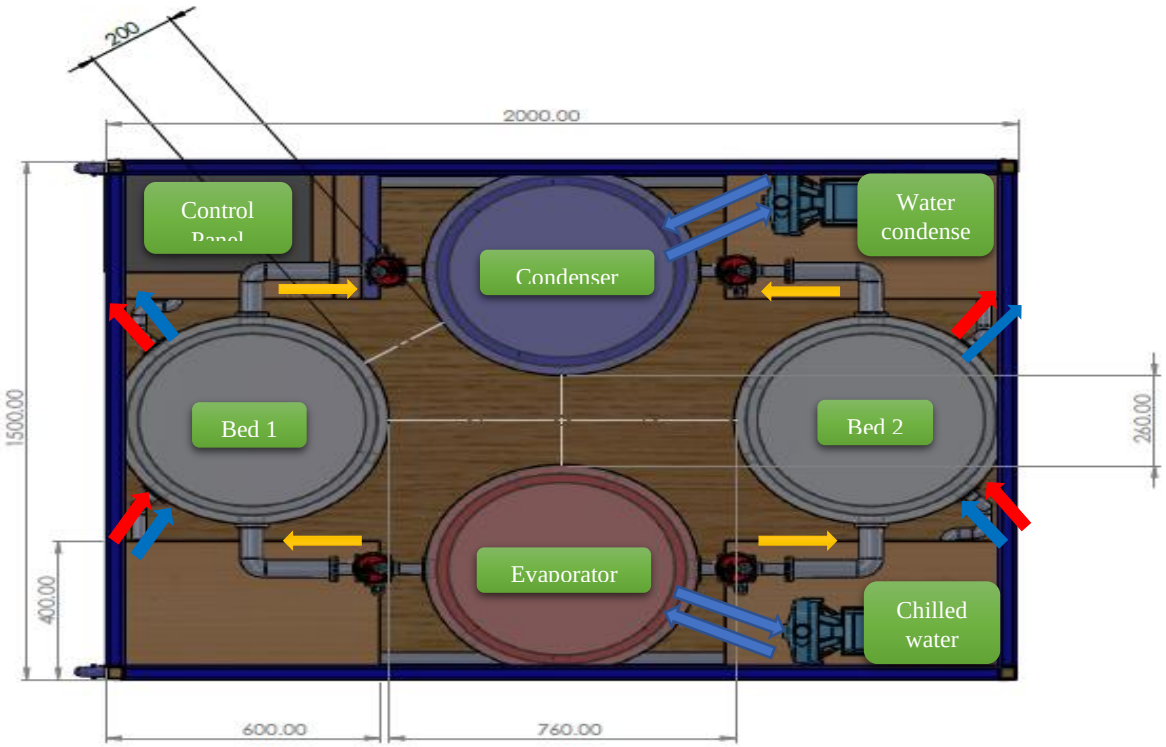



Figure 12-2. Top view of the adsorption system

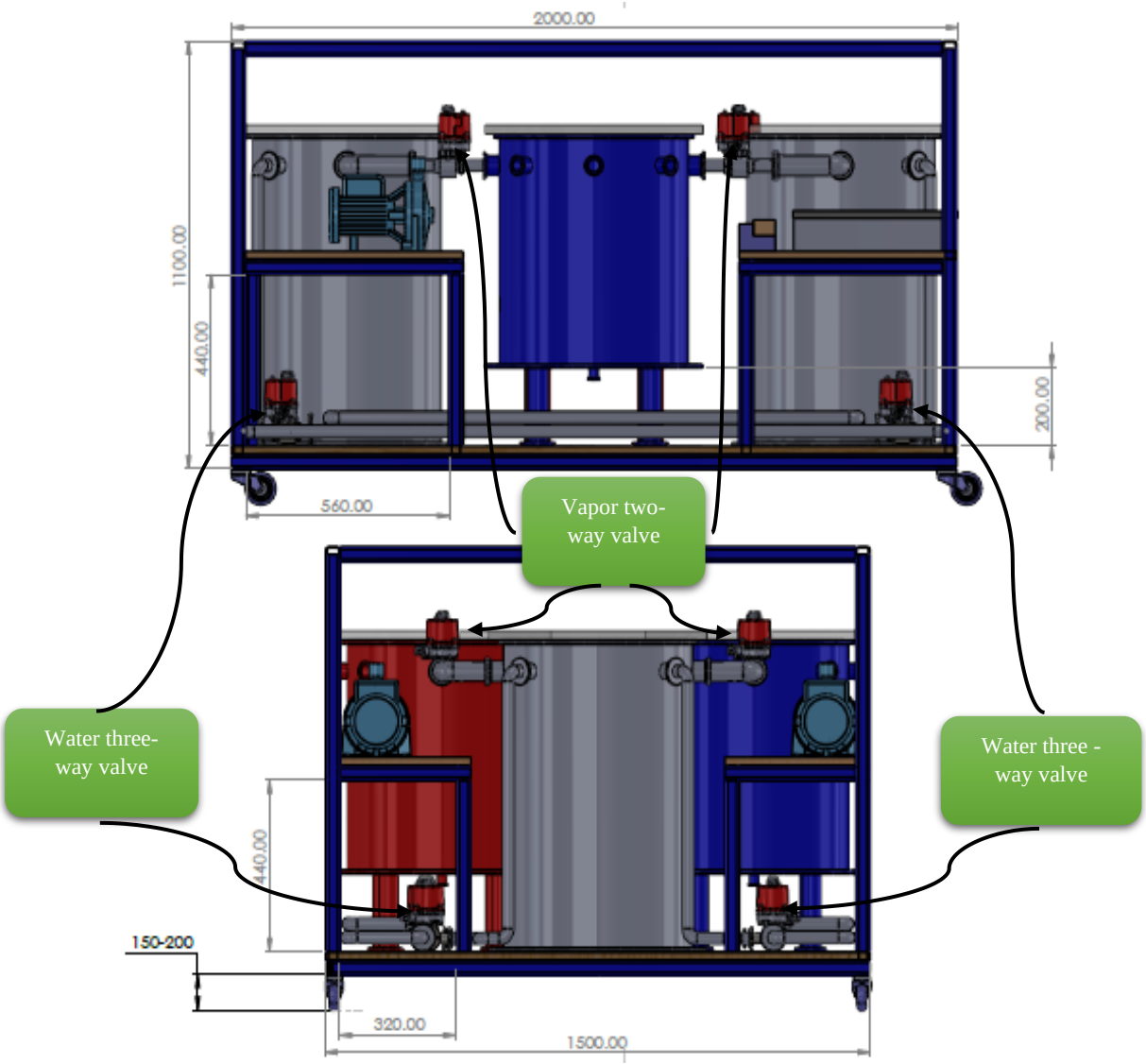



Figure 12-3. Front and side views of the adsorption system

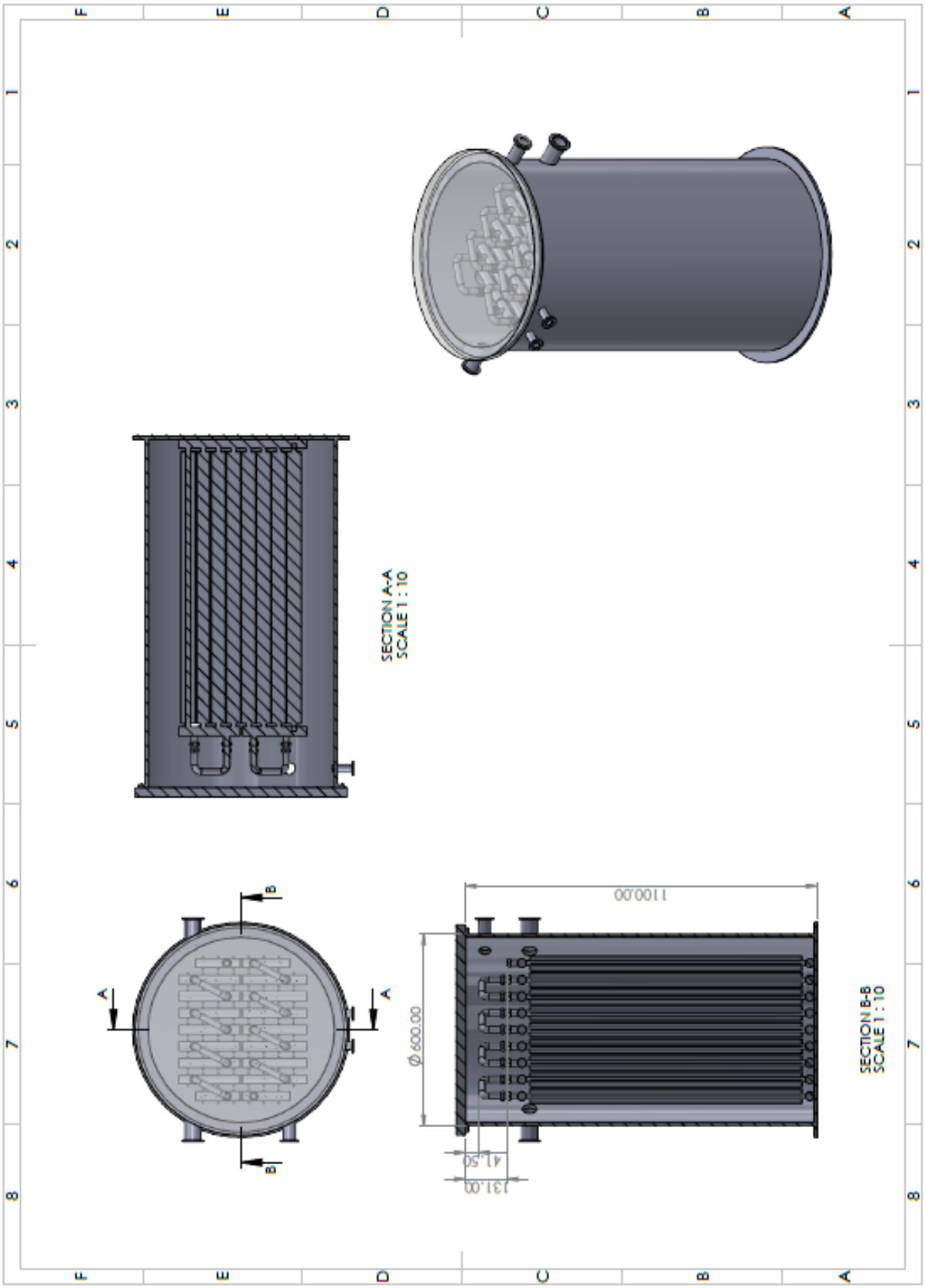



Figure 12-4. Drawing of the adsorber bed with the coated heat exchanger modules

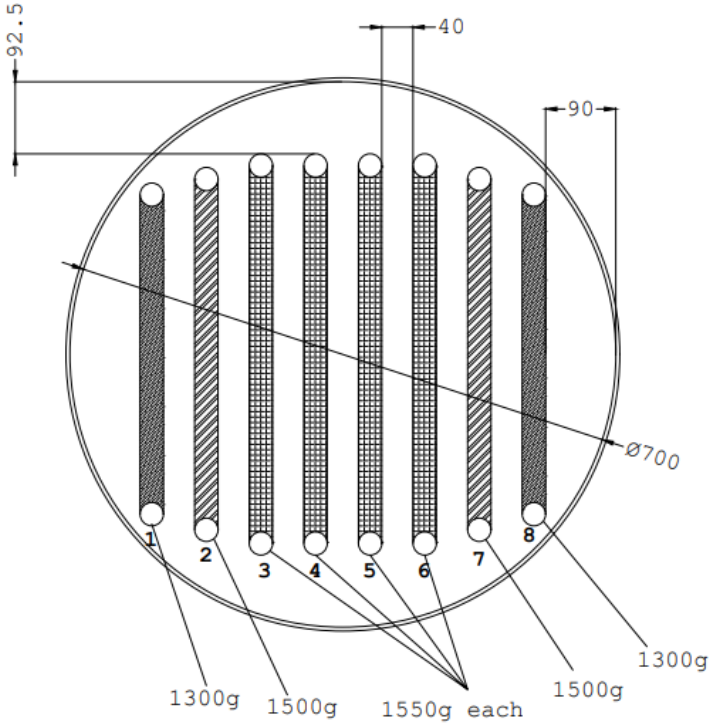



Figure 12-5. Top view of the packed rectangular finned tube heat exchanger modules in the adsorber bed

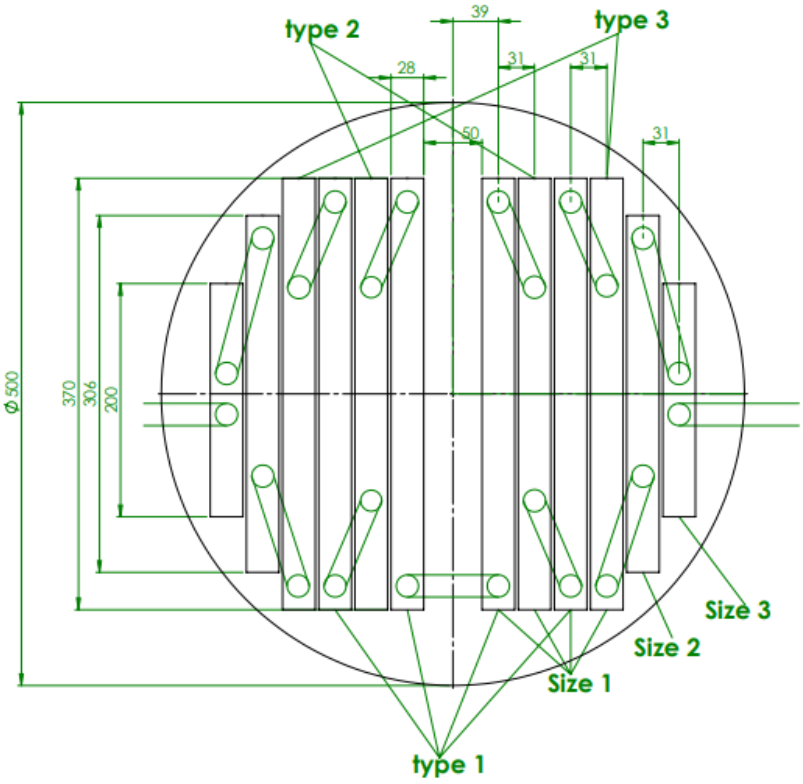



Figure 12-6. Top view of the coated wire finned tube heat exchanger modules in the adsorber bed

**Appendix D:** Electrical and control connection of the adsorption system

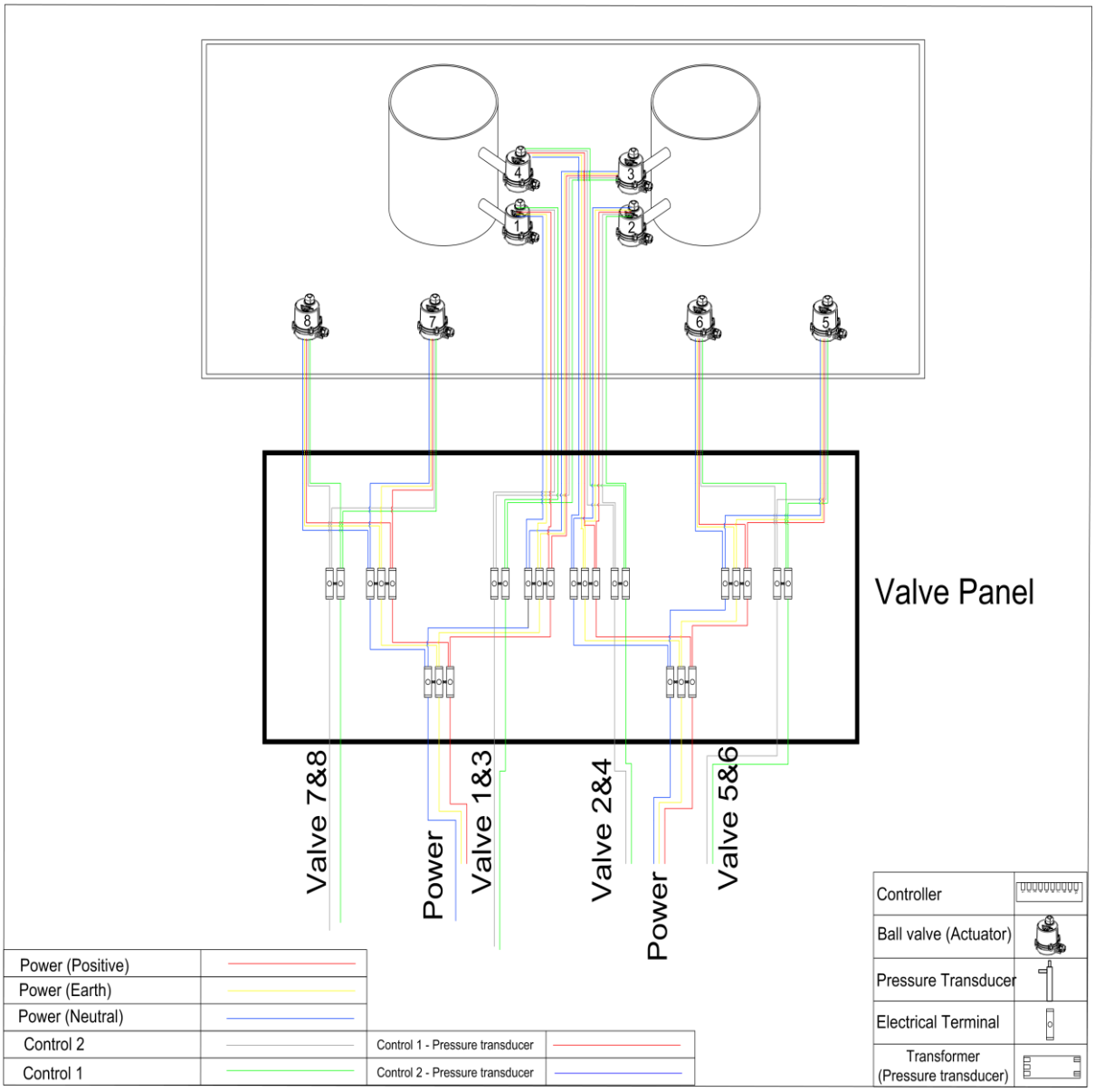



Figure 13-1. Power and control wiring of the solenoid valves

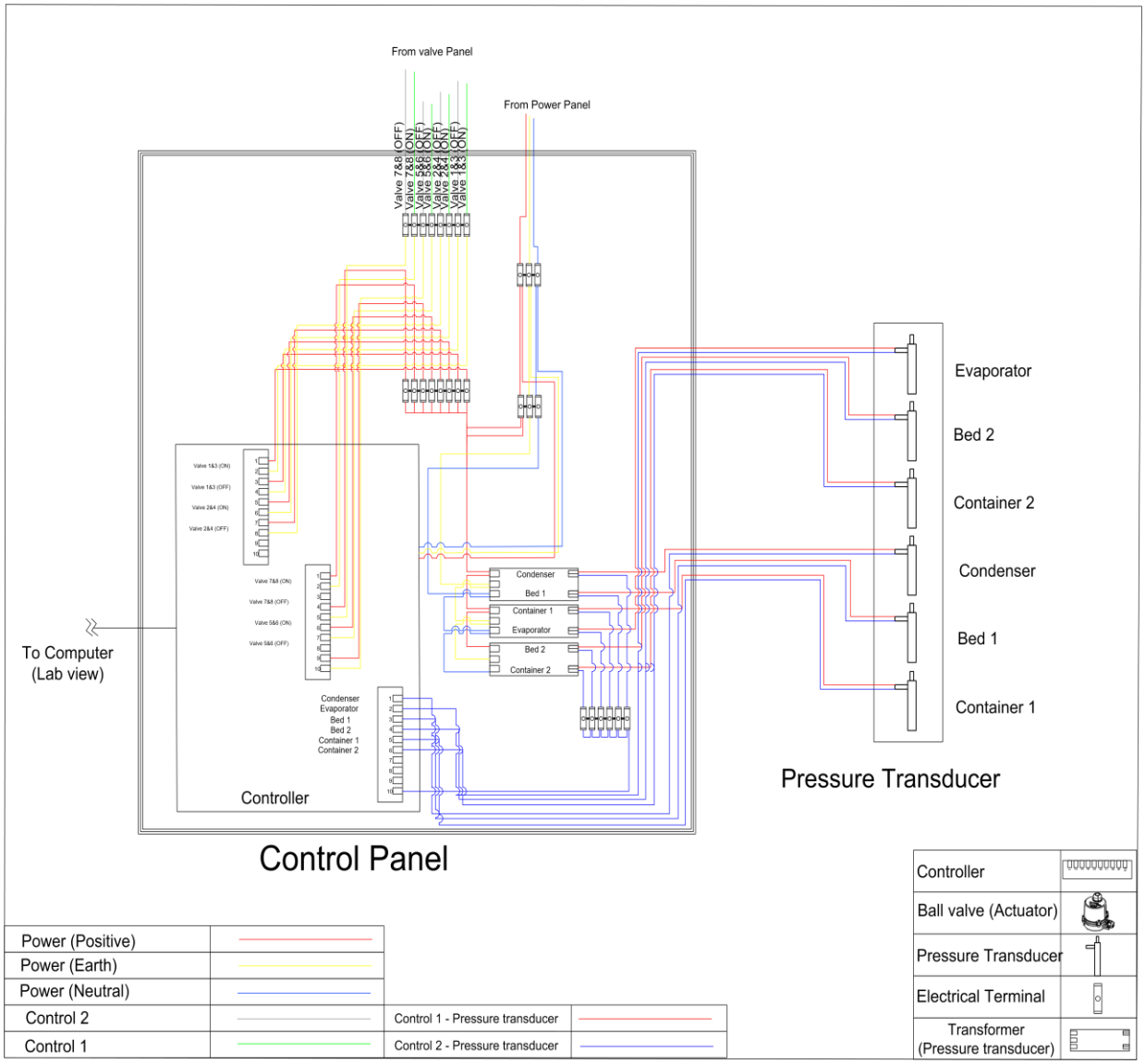



Figure 13-2. Control panel wiring with pressure transducers and solenoid valves

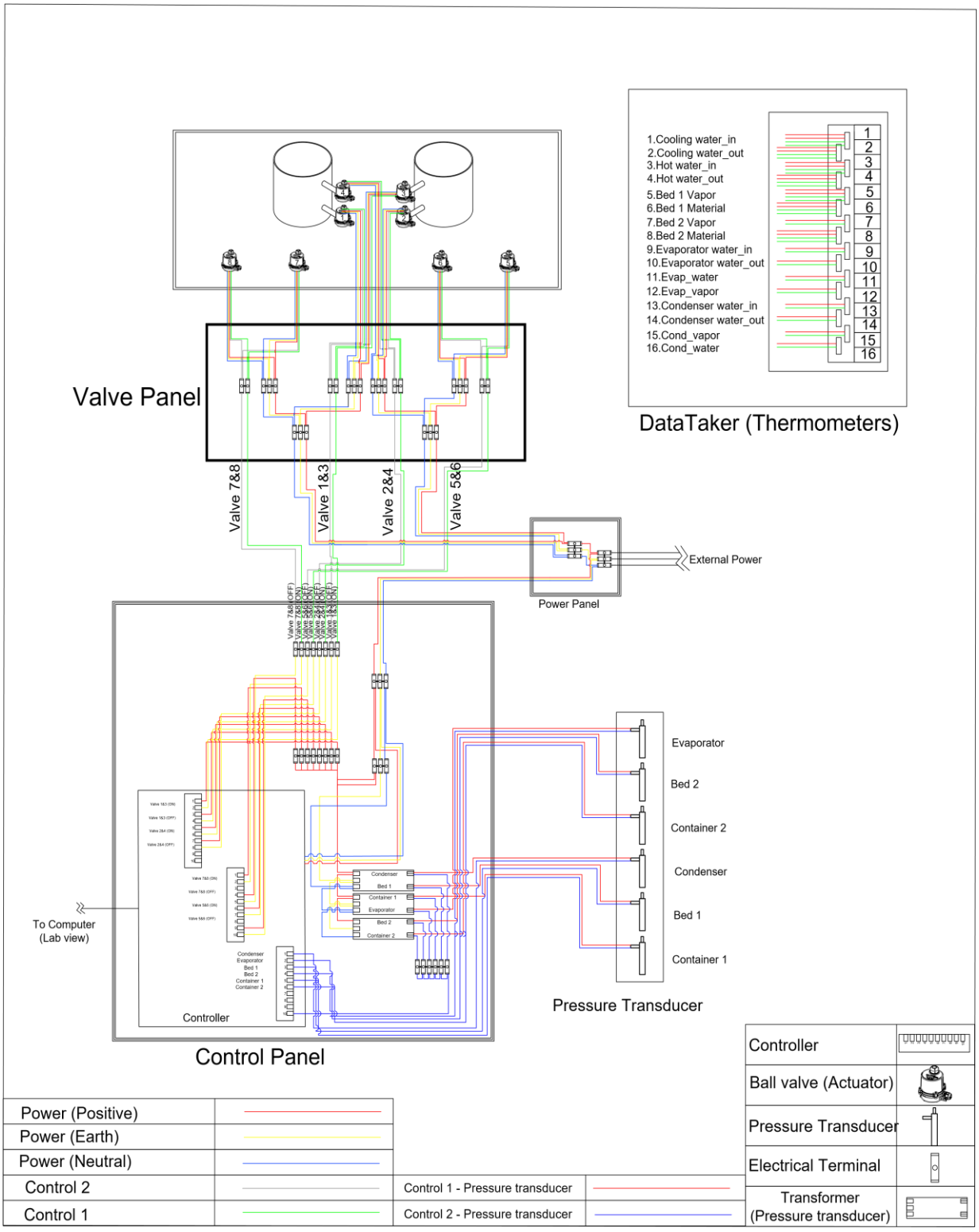



Figure 13-3. Summary of the electrical wiring of the adsorption system

# **Appendix E**: Repeatability test

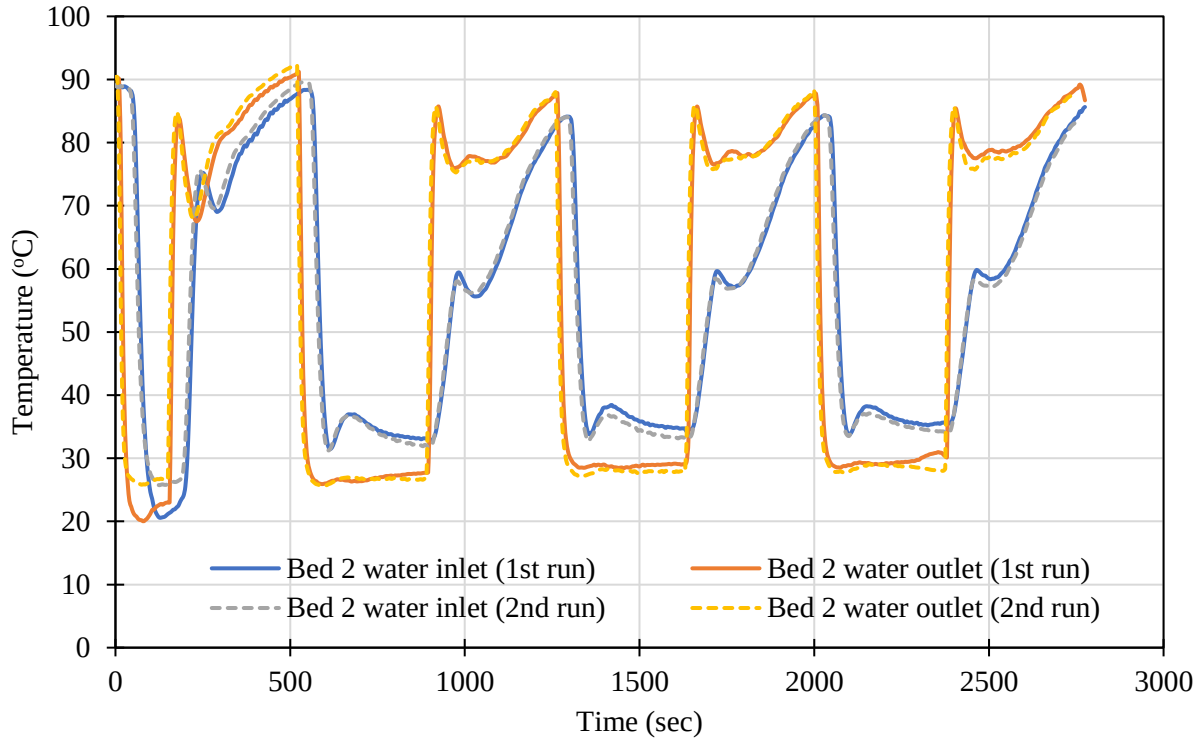



Figure 14-1. Repeatability test by measuring the inlet and outlet cold/hot water temperature to the 2nd adsorber bed

# **Appendix F:** Calibrations

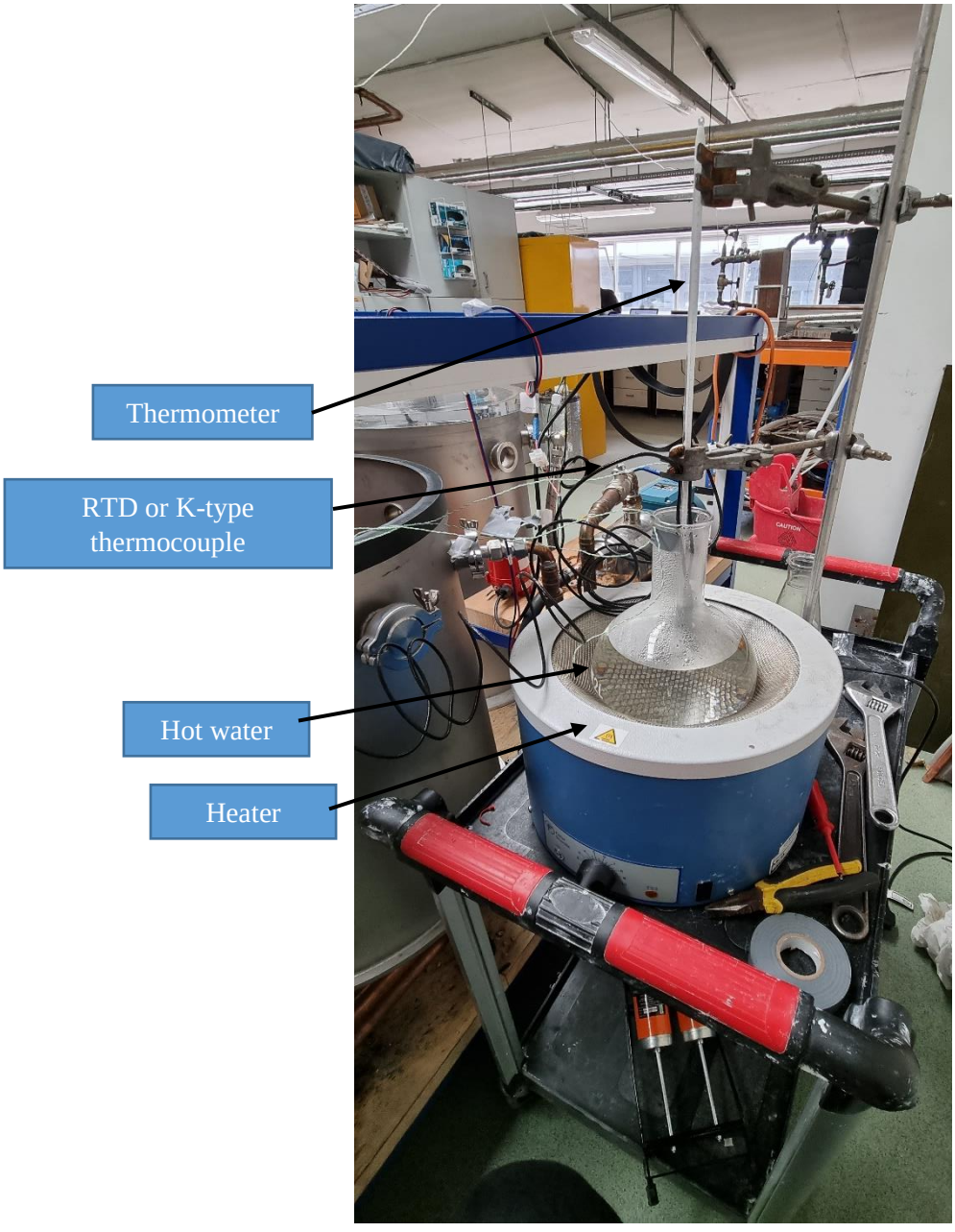



Figure 15-1. Temperature sensor calibrations

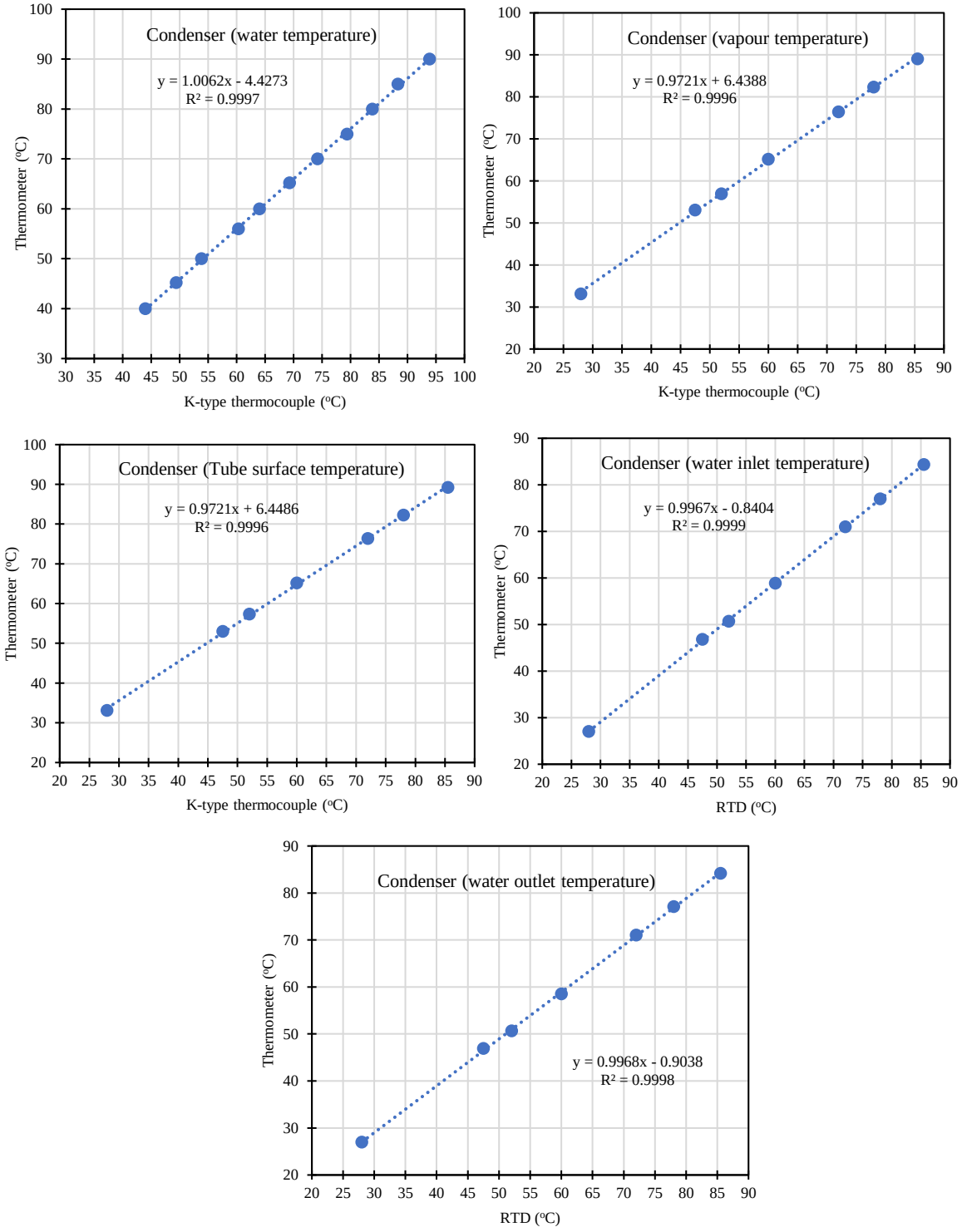



Figure 15-2. Calibration of the condenser temperature sensors

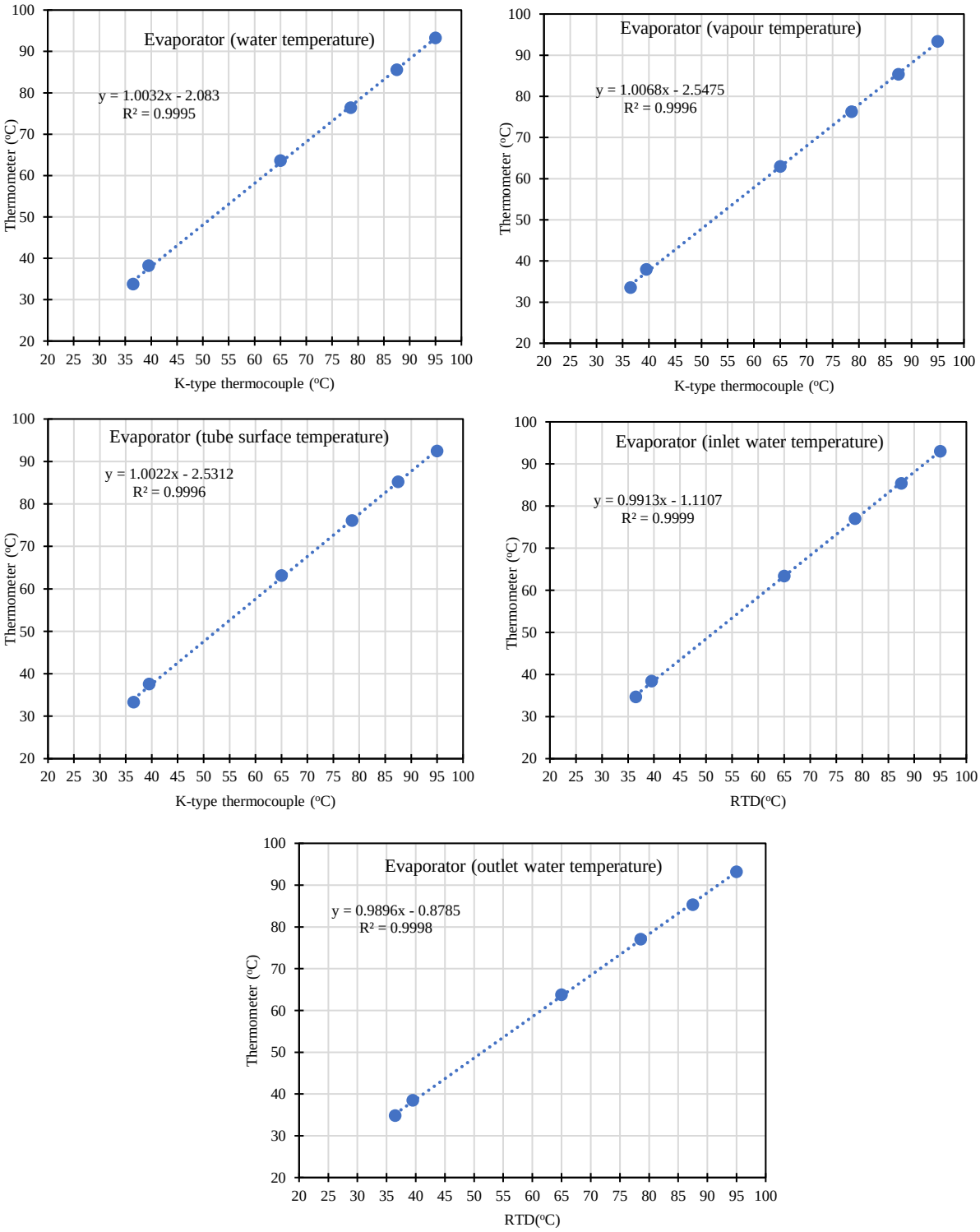



Figure 15-3. Calibration of the evaporator temperature sensors

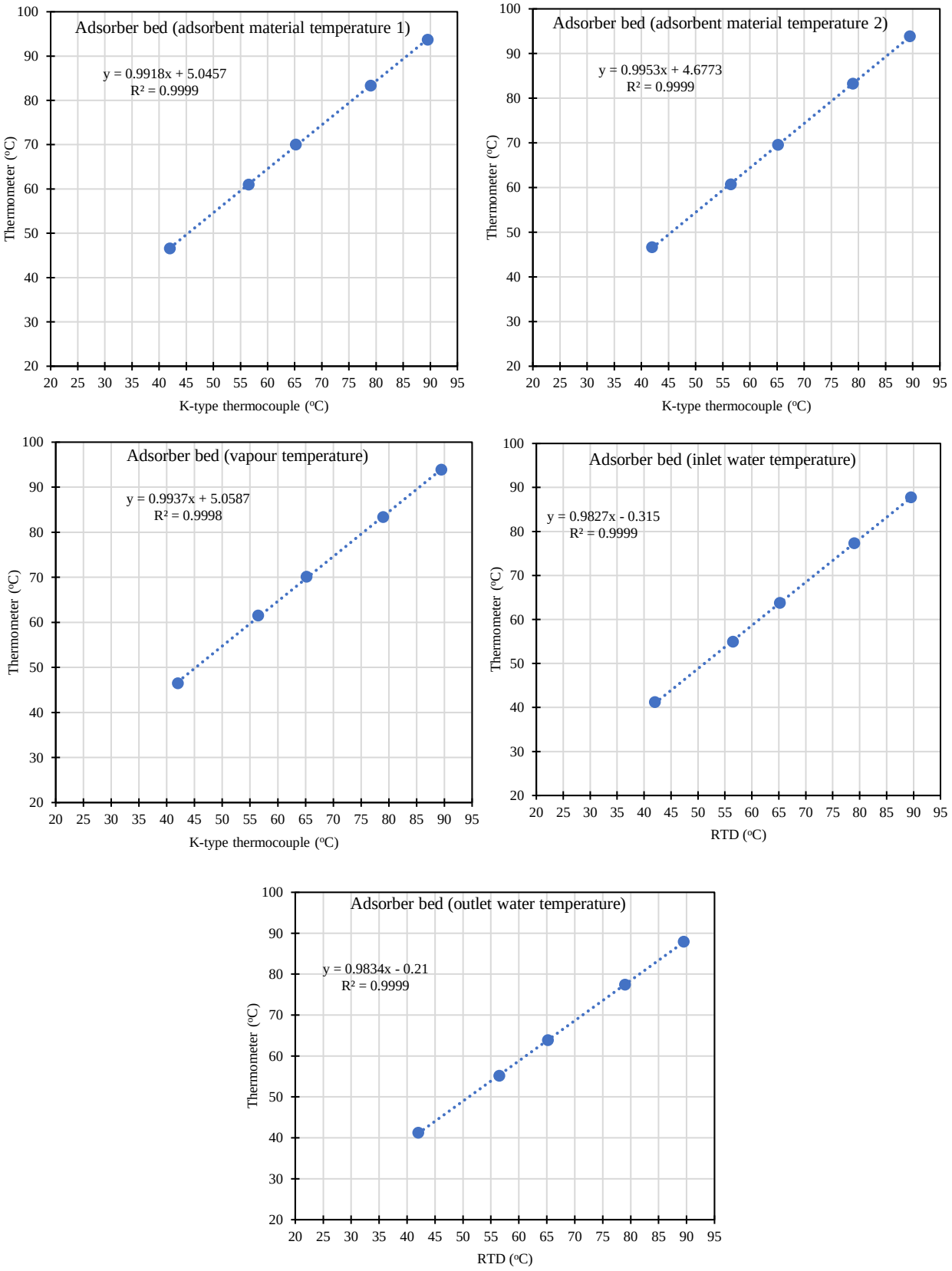



Figure 15-4. Calibration of the adsorber bed temperature sensors

# **Appendix G:** Uncertainty calculations

To estimate the uncertainty in calculating the SCP, CP, SDWP, DWP and COP of the adsorption system, the following equations are used:

$$\frac{U_{SCP}}{SCP} = \sqrt{\left(\frac{U_{Cp}}{Cp}\right)^2 + \left(\frac{U_{\dot{m}_{chilled}}}{\dot{m}_{chilled}}\right)^2 + \left(\frac{U_{T_{chilled,in}}}{T_{chilled,in} - T_{chilled,out}}\right)^2 + \left(\frac{U_{T_{chilled,out}}}{T_{chilled,in} - T_{chilled,out}}\right)^2 + \left(\frac{U_{ads\ mass}}{ads\ mass}\right)^2}$$

$$\frac{U_{CP}}{CP} = \sqrt{\left(\frac{U_{Cp}}{Cp}\right)^2 + \left(\frac{U_{\dot{m}_{chilled}}}{\dot{m}_{chilled}}\right)^2 + \left(\frac{U_{T_{chilled,in}}}{T_{chilled,in} - T_{chilled,out}}\right)^2 + \left(\frac{U_{T_{chilled,out}}}{T_{chilled,in} - T_{chilled,out}}\right)^2}$$

$$\frac{U_{SDWP}}{SDWP} = \sqrt{\left(\frac{U_{collected\ water\ amount}}{collected\ water\ amount}\right)^2 + \left(\frac{U_{ads\ mass}}{ads\ mass}\right)^2}$$

$$\frac{U_{DWP}}{DWP} = \sqrt{\left(\frac{U_{collected\ water\ amount}}{collected\ water\ amount}\right)^2}$$

$$\frac{U_{COP}}{COP} = \sqrt{\left(\frac{U_{Cp}}{Cp}\right)^2 + \left(\frac{U_{\dot{m}_{chilled}}}{\dot{m}_{chilled}}\right)^2 + \left(\frac{U_{\dot{m}_{des}}}{\dot{m}_{des}}\right)^2 + \left(\frac{U_{T_{chilled,in}}}{T_{chilled,in} - T_{chilled,out}}\right)^2 + \left(\frac{U_{T_{chilled,out}}}{T_{chilled,in} - T_{chilled,out}}\right)^2 + \left(\frac{}{T_{de}}\right.}$$

Where

| | |
|---|---|
| $U_{SCP}$ | Is the uncertainty of the calculated SCP |
| $U_{CP}$ | Is the uncertainty of the calculated CP |
| $U_{SDWP}$ | Is the uncertainty of the calculated SDWP |
| $U_{DWP}$ | Is the uncertainty of the calculated DWP |
| $U_{COP}$ | Is the uncertainty of the calculated COP |

| | |
|---|---|
| $U_{Cp}$ | Is the uncertainty in the specific heat of the water which assumed to be zero as the value is extracted from tabulated property data |
| $U_{\dot{m}_{chilled}}$ | Is the uncertainty in reading the flow rate of the chilled water in the evaporator. The flow meter has uncertainty of 0.25 L/min |
| $U_{\dot{m}_{des}}$ | Is the uncertainty in reading the flow rate of the desorption water in the adsorber bed. The flow meter has uncertainty of 0.25 L/min |
| $U_{T_{chilled,in}}$ | Is the uncertainty in reading the inlet chilled water temperature in the evaporator. It is measured using the RTD thermocouple with uncertainty of 0.179 $^{o}$C |
| $U_{T_{chilled,out}}$ | Is the uncertainty in reading the outlet chilled water temperature in the evaporator. It is measured using the RTD thermocouple with uncertainty of 0.179 $^{o}$C |
| $U_{T_{des,in}}$ | Is the uncertainty in reading the inlet desorption water temperature in the adsorber bed. It is measured using the RTD thermocouple with uncertainty of 0.179 $^{o}$C |
| $U_{T_{des,out}}$ | Is the uncertainty in reading the outlet desorption water temperature in the adsorber bed. It is measured using the RTD thermocouple with uncertainty of 0.179 $^{o}$C |
| $U_{ads\ mass}$ | Is the uncertainty in measuring the mass of the adsorbent. The mass of adsorbent is measured using digital balance with uncertainty of 0.005 kg |
| $U_{collected\ water\ amount}$ | Is the uncertainty in the reading of the measuring cylinder which has uncertainty of 25 ml. |